UNIVERSITY OF SOUTHAMPTON

FACULTY OF PHYSICAL AND APPLIED SCIENCES

Optoelectronics Research Centre

Chalcogenides for Solar Applications

by

Feras Al-Saab

Thesis for the degree of Doctor of Philosophy

January 15

UNIVERSITY OF SOUTHAMPTON

Abstract

FACULTY OF PHYSICAL AND APPLIED SCIENCES

Optoelectronics Research Centre

Thesis for the degree of Doctor of Philosophy

CHALCOGENIDES FOR SOLAR APPLICATIONS

Feras Al-Saab

In its "Strategic Research Agenda for Photovoltaic Solar Energy Technology"[1], the European Union has set a target for solar generated electricity to become competitive with conventional electricity generation by 2020–2030. Second generation thin-film chalcogenide materials are among the most promising candidates for large-scale PV manufacturing and are quickly becoming commercial products. These materials offer stable and efficient (above 10%) photovoltaic modules fabricated by scalable thin-film technologies and cell efficiencies above 20 % (CIGS).

CIGSe thin films were deposited by RF magnetron sputtering at room temperature from a single quaternary target on various substrates producing stoichiometric films. Cu_2ZnSnS_4 thin films were fabricated using a novel two stage process incorporating RF magnetron sputtering from a single target and then annealed in a rapid thermal processor without any toxic gases or reactive sulphur. GaLaS thin films were deposited by a patented high throughput PVD MBE System. The effect of the annealing temperature on the sulphur in the films was investigated. The XRD phase analysis confirms the preference of GLS to oxidise to form a more stable compound. The films were also analysed by ellipsometry, EDX and Raman.

$CuSbS_2$ thin films were fabricated using two techniques. Firstly, using an atmospheric pressure chemical vapour deposition system. $CuSbS_x$ was successfully deposited on soda lime substrates at a very fast rate of around 35 µm in 1 hour. For RF sputtering two and single stage depositions were carried out. By two stages, the films were annealed at various temperatures (250 to 325 ℃) and times (5 to 60 min). The annealing was done without any toxic gases or reactive sulphur. Single phase $CuSbS_2$ films with good adhesion, good

crystallinity and with no apparent sulphur loss can be achieved. By a single stage process, $CuSbS_2$ crystals were made in situ by depositing at 200 ℃ and 250 ℃. The grain sizes were measured by SEM imaging, and grains above 1 μm can be fabricated. The effect of etching with bromine and HCl was also investigated. The cells made showed a high current density using $CuSbS_x$ films (up to 1-2 mA/cm^2).

Table of Contents

List of Tables

List of Figures

Declaration of Authorship

I, Feras Al-Saab declare that this thesis and the work presented in it are my own and has been generated by me as the result of my own original research.

Chalcogenides for Solar Applications

I confirm that:

1. This work was done wholly or mainly while in candidature for a research degree at this University;
2. Where any part of this thesis has previously been submitted for a degree or any other qualification at this University or any other institution, this has been clearly stated;
3. Where I have consulted the published work of others, this is always clearly attributed;
4. Where I have quoted from the work of others, the source is always given. With the exception of such quotations, this thesis is entirely my own work;
5. I have acknowledged all main sources of help;
6. Where the thesis is based on work done by myself jointly with others, I have made clear exactly what was done by others and what I have contributed myself;
7. Parts of this work have been published as:

- **AL-SAAB, F**., GHOLIPOUR, B., HUANG, C. C., ANASTASOPOULOS, A., HAYDEN, B. & HEWAK, D. W. 2012. Crystallization Study of the Cu_2ZnSnS_4 Chalcogenide Material for Solar Applications. PV-SAT 8. Northumbria University, Newcastle upon Tyne.
- GHOLIPOUR, B., HEWAK, D. W., HUANG, C. C., ANASTASOPOULOS, A., **AL SAAB, F**., GUERIN, S., HAYDEN, B. & PURDY, G. 2011. Scalability and thermal stability of low current consuming, nanowire phase change memory cells for high density commercial applications. E/PCOS. Zurich, Switzerland.
- GHOLIPOUR, B., ZHANG, J., **AL SAAB, F**., GHOLIPOUR, A., MAC-DONALD, K. F., HAYDEN, B., HEWAK, D. & ZHELUDEV, N. I. 2011. Chalcogenide Phase Change

Materials in Active Plasmonic and Metamaterial Technologies. SAIT Global Research Outreach Scheme.

- GHOLIPOUR, B., ZHANG, J., **AL-SAAB, F**., MACDONALD, K. F., HAYDEN, B. E., HEWAK, D. W. & ZHELUDEV, N. I. 2012. Chalcogenide glass photonics: non-volatile bi-directional all-optical switching in phase-change metamaterials. CLEO/QELS 2012. San Jose.
- **AL-SAAB, F.**, HUANG, C. C., YAO, J., HAYDEN, B. & HEWAK, D. 2014. RTA annealed RF sputtered single phase CuSbS films. *Thin Solid films,* Submitted.
- **AL-SAAB, F.**, HUANG, C. C., HAYDEN, B. & HEWAK, D. 2014. RF sputtered single phase CuSbS thin films. *E-MRS Spring* Lille, France.
- **AL SAAB, F.**, GHOLIPOUR, B., HUANG, C. C., ANASTASOPOULOS, A., HAYDEN, B. & HEWAK, D. W. 2013. Crystallization Study of the $CuSbS_2$ Chalcogenide Material for Solar Applications. *PV-SAT 9.* Swansea University, Swansea, Wales.
- HUANG, C. C., **AL-SAAB, F.**, GHOLIPOUR, B. & HEWAK, D. W. 2011. Fabrication of thin film solar cell materials by APCVD. Low Carbon Earth Summit. Dalian, China.

Signed: .....

Date: .....

I'd like to dedicate this thesis to my Parents (Dr. Jamal Al-Saab and Mrs. Etedal Al-Saab), for always supporting, helping and standing by me…..

Acknowledgements

I'd like to thank my supervisors Professor Daniel Hewak (Head of the Novel Glass Group in the Optoelectronics Research Centre) and Professor Brian Hayden (Head of the Surface Science and Materials Discovery group in the Chemistry Department and Chief Scientist at Ilika Technologies Inc.) for their support, patience and helpful discussions.

I would like to thank all those at Ilika Technologies in particular Dr. Chris Lee, Chris Vian and Dr. Rob Noble for their help with characterization equipment. Thanks goes to Dr. Kevin Huang in the Novel Glass Group for his help with UV-VIS-NIR and FTIR training; CVD and ampoule melting training; and loads of other help throughout the project. Thanks to Kenton Knight and Chris Craig who have helped me with too many things to list; and thanks to Dr. Jin Yao for helpful discussions in PV characterisation, fabrications and device design.

Thanks to Dr. Alexandros Anastasopoulos for HT-PVD, HT-EDX and HT-XRD training, analysis and discussions and help with data presentation as well as loads of other help throughout my work in the chemistry department.

Thank you to Dr. Behrad Gholipour for help with sputtering, photolithography, heating stage, glove box training, and other useful information and help. Thanks to Khouler khan with ampoule melting, Caplain workshop for glass work, the ORC support staff, especially Robert Standish and Andrew Webb for glass work and ampoule sealing, Neil Sessions for SEM/EDX, electron beam evaporation and clean room assistance, Kevin Sumner for IT support, Ed Weatherby and Mark Lessey for gas connections and mechanical equipment, David Sager for safety, and Mandy Both for orders.

In the ECS; Neil Fagan for loads of gas stuff. Thanks to Prof. Darren Bagnall and the rest of his group especially Dr. Michael Pollard and Dr. Owain Clark for ellipsometry help and Dr. Akhtar Rind for solar characterisation training. And to all those in the Southampton Nanofabrication Centre for their help in various aspects of my project.

Thanks to Professor Ken Durose and Dr. Jon Major in the Solar Photovoltaic Research group in the University of Liverpool for CdS depositions. And a massive thank you to everyone else in the Optoelectronics Research Centre (ORC),

electronics and computer science department (ECS), chemistry department and high voltage lab that have had even the smallest effect on my work.

Finally, thank you to all my friends and family for your support and for a listening ear, when I really needed it.

Abbreviations

CIGSe	=	Copper indium gallium di-selenide
CZTS	=	Copper zinc tin sulphide
CAS or CuSbS	=	Copper antimony sulphide
PVD	=	Physical vapour deposition
HT	=	High throughput
ORC	=	Optoelectronics research centre
ECS	=	Electronics and computer science department
GLS	=	Gallium lanthanum sulphide
RTA	=	Rapid thermal annealer
RTP	=	Rapid thermal processing
SEM	=	Secondary electron Microscopy
EDX	=	Energy Dispersive X-ray spectroscopy
XRD	=	X-ray Diffraction
RF	=	Radio Frequency
CVD	=	Chemical vapour deposition
APCVD	=	Atmospheric pressure CVD
RIE	=	Reactive ion etching
UHV	=	Ultra high vacuum
I-V	=	Current – voltage
K-Cell	=	Knudsen cell
SP	=	Surface Plasmon

Chapter 1: Introduction

1.1 Motivation

One current problem in the world can be described as the 3-E trilemma [2]; that is to increase economic development, we need to increase our energy usage which on the other hand leads to more environmental issues.

These environmental issues damage our atmosphere, which causes fluctuations in the climate at the earth's surface. Cleaner energy is a must and governments have invested large sums of money in renewable energy research. This includes wind energy, geothermal energy, nuclear, solar energy, hydropower, biofuels and biomass to name a few. Now most of these can reduce the environmental issues by producing energy that would otherwise be produced from coal and natural gas, but only solar energy can on its own provide enough energy to meet the world energy demands. The advantages of solar energy are that we receive vast amounts of it, it is inexhaustible and we receive it all over the world.

The primary objective of solar research and development worldwide is to reduce the cost of modules and systems to a level that will be competitive with conventional ways of generating electricity. Until now, this has been focused on crystalline or polycrystalline silicon solar cells. But even with the strength of the material knowledge, increased production volume and reduction in cost, silicon solar cells are unlikely to meet the requirements to reach utility scale electricity standards.

Thin film solar cells on the other hand, have lower materials costs, simpler device processing and simpler manufacturing technologies for large area modules and arrays. The choice of any given technology is dictated by its highest achievable efficiency, ease of manufacturing, reliability, availability of materials and environmental sensitivity.

The leading contenders at the moment are: firstly, alloys of amorphous silicon, which have a high optical absorption, an adjustable band gap by alloying, is relatively easy to fabricate, and utilises the already massive silicon industry knowledge in place. The problem with these cells is that they degrade and their cell efficiency decreases by the Staebler-Wronski effect [3, 4]. The second

contender is cadmium telluride (CdTe) which is a p-type semiconductor; the key player with this technology is First Solar (currently holding the highest market share in thin film technology solar cells).The final contender is the ternary and the multinary variations of copper indium selenide (CIS). It requires relatively more complex processing steps than the other two, has the highest efficiency, it is very robust, stable and defect tolerant.

The CdTe and CIS materials come from a class of materials called chalcogenides. Chalcogenides are becoming more and more important for the fabrication of optoelectronic devices because of the high optical nonlinearity, strong photosensitivity, outstanding radiation hardness and several other unique properties they have. Chalcogenide glasses are normally fabricated by a conventional melt-quenching method. The glasses are then further processed to form, for example, thin films, optical fibre and optoelectronic devices.

There are many new chalcogenide materials that are continuously being proposed as materials to substitute CIS and CdTe. This is mainly because of the toxicity of cadmium and the abundance issues of indium in CIS materials.

1.2 Project Aim and Contribution to the Field

The project will focus on two key research issues. The first is the work fabrication and optimisation of $CuSbS_2$ materials for solar cell development. The second is the use of new fabrication techniques to deposit chalcogenide materials for fabricating devices and for optimisation.

For deposition, sputtering can provide good control on film composition, lower costs and is suitable for large-area, continuous and multi-component deposition. This method is already an established technique for the preparation for thin films for magnetic, optical and contact applications. In this report, we will look at the deposition of the materials using a single quaternary target; which has little previous work carried out and no literature for $CuSbS_2$.

Also, chemical vapour deposition is a widely used method for fabricating various materials for many industries. It offers better quality and comformality; along with faster deposition rates and excellent stoichiometric control. Here in this report, $CuSbS_2$ has been successfully fabricated using atmospheric pressure CVD for the first time.

For annealing, rapid thermal processing (RTP) is a method that significantly reduces the thermal budget of the sample as compared to conventional furnace annealing. In addition, two principal advantages of low thermal budget processing is the minimization of interdiffusion and impurity diffusion from the substrate as well as better control of the process kinetics. To the author's knowledge, work on the RTP of chalcogenides for solar applications without any toxic or reactive gases is very limited and, with CZTS and $CuSbS_2$ did not existent before this report; and was first reported in publications from the work in this thesis [5-8].

In addition, to speed up the synthesis and screening of potential photovoltaic materials, a new high throughput methodology will be used exploiting high-throughput physical vapour deposition [9] and appropriate optical and electronic screening for photovoltaic materials [10]. This method will be used to screen gallium lanthanum sulphide (GLS) over a wide compositional range using a single stage synthesis method utilising a new sulphur cracker. GLS has never been studied over a wide compositional range, this is used to measure the refractive index change of the material with respect to gallium content.

1.3 Photovoltaics

1.3.1 Brief History

The photovoltaic effect was first observed by Alexander-Edmond Becquerel in 1839 [11, 12]. This effect is a physical process where photons of light excite electrons to a higher energy state and current can flow. Alexander noticed that a small amount of current flowed when certain materials were exposed to light. In 1883, the first working solar cell was made by the American inventor Charles Fritts [13]. This was made possible by coating selenium with a thin layer of gold.

The solar cell was patented by Russell Ohl in 1941 [14, 15]. Although several patents were filed before this (for example by Edward Weston in 1888 [16, 17] or by Anthony H. Lamb in 1935 [18]); Russel Ohls device was the first use of the p-n junction. Another notable mention is Chapin et. al at Bell labs in 1954 [19, 20] who invented the first silicon solar cell.

1.3.2 PV Market

The PV market has been growing at a rapid rate of about 48% annually in the period from 2000 to 2012 [21]. In 2012, Bulk Si based PV accounted for around 85% of the total production with thin films accounting for the remainder.

Figure 1 shows the PV production by different technologies for different years. There was a large increase in thin film production around 1987 which later decreased again; and only started to increase again after 2004. In Figure 2, we look at the market share of thin film technologies. The boom in thin film production was a result in a-Si being used for commercial cells. This interest diminished and thin films have started to regain market share with chalcogenide technologies. An up to date chart showing the best solar cell efficiencies to date is shown in Appendix B [21]. The highest thin film solar cell efficiencies reported are: 21.0 % using CdTe and 23.3% using CIGSe

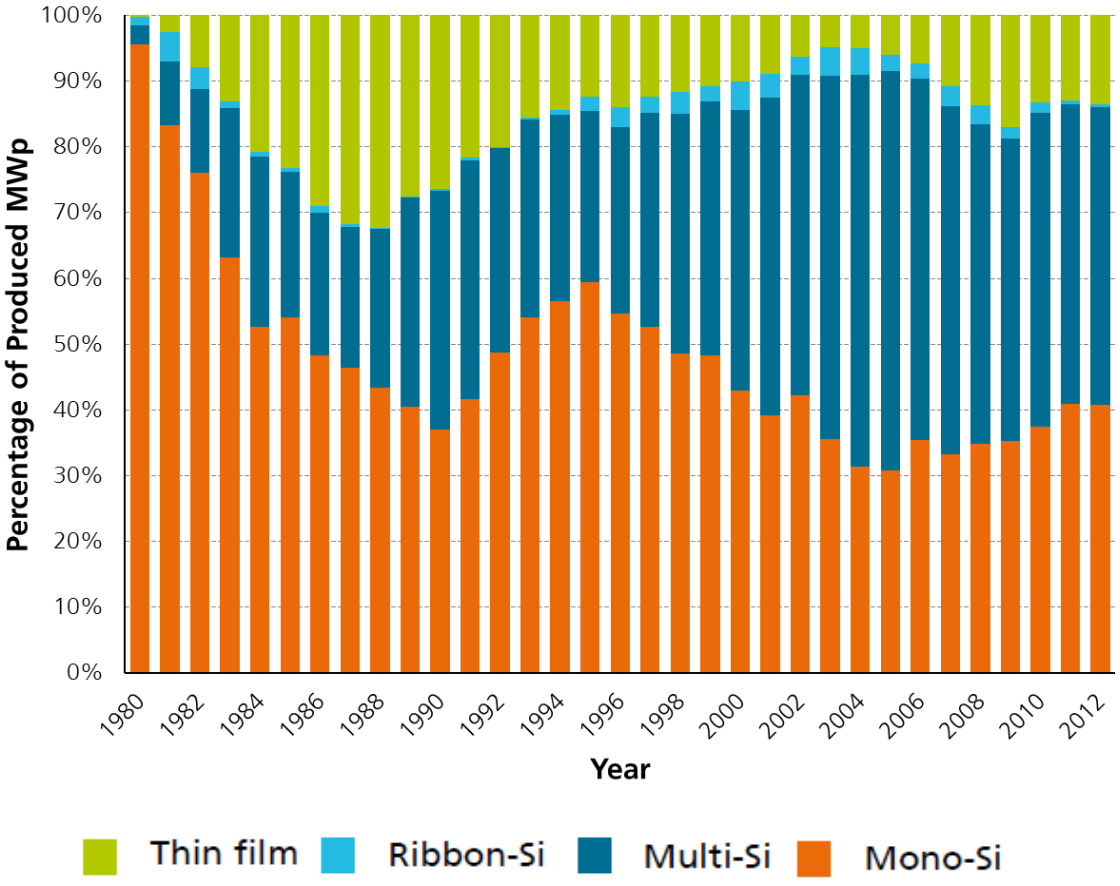

Figure 1: PV production Development by Technology. Taken from [22]

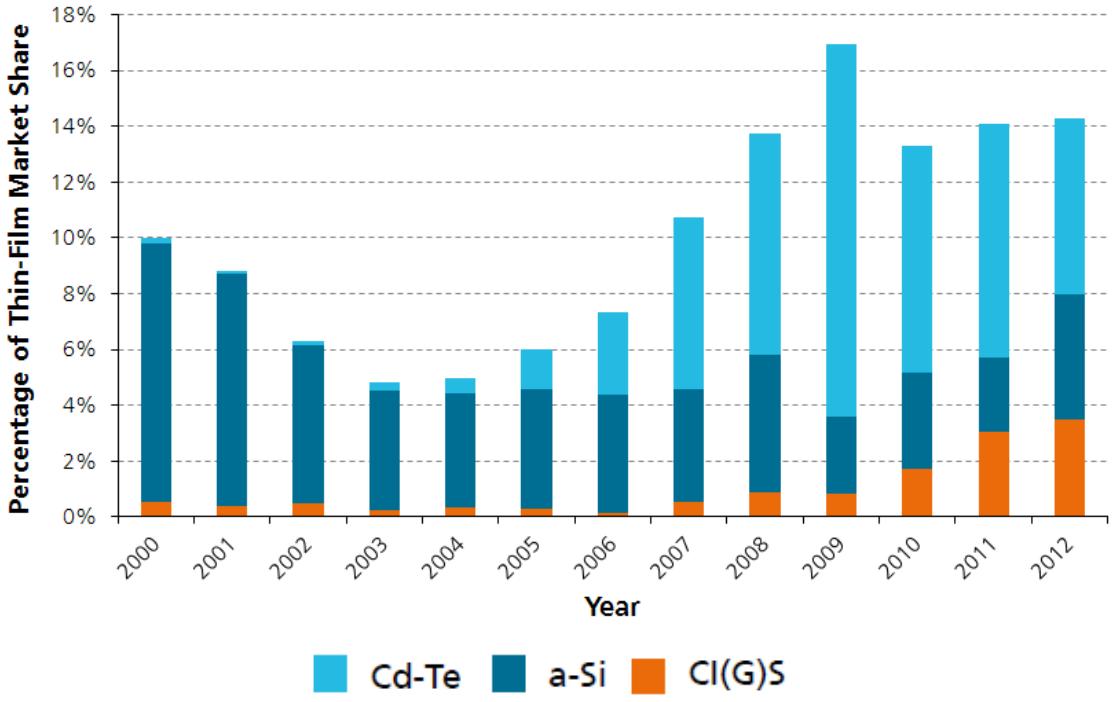

Figure 2: Market share of thin film technologies. Taken from [22]

Photovoltaic thin film materials are generally divided into three categories:

(1) First generation: this includes single and poly crystalline silicon solar cells.

(2) Second generation: this includes thin films materials such as CIGS, CdTe and amorphous Si. The scope of this thesis is on second generation solar cells and materials.

(3) Third generation: this includes novel techniques like quantum dot solar cells, polymer, dye synthesized cells and many other emerging technologies

1.4 Report Summary

After the current introduction; the chapters include:

Background theory section which goes through the basics of semiconductor physics and photovoltaic theory. It starts with equilibrium p-n junctions, reverse bias, forward bias and photovoltaic device physics. Photovoltaic loss mechanisms are also briefly introduced. Finally, the main fabrication methods (sputtering and high throughput PVD) used in this report will be introduced.

The experimental sections are split into two parts. Part A covers the work done on CIGS, CZTS and GLS.

The $CuIn_{0.7}Ga_{0.3}Se_2$ (CIGSe) chapter introduces the current literature on CIGSe, including structure, fabrication techniques, cell structure, buffer layers and back contacts. The methodology used is introduced in detail for the annealing of the CIGSe on various substrates and then the fabrication of CIGSe solar cells (including cell designs). The compositional and structural results are shown.

The Cu_2ZnSnS_4 (CZTS) chapter introduces the current literature on CZTS, including structure, fabrication techniques, and the complex phase diagram, the role of defects, instabilities, band alignment and cell structure. The methodology used, is introduced in detail for the rapid thermal annealing of the CZTS and then the fabrication of CZTS solar cells. The compositional and structural results are shown along with the device performance.

The GaLaS (GLS) chapter introduces the current literature on GLS, including structure, deposition techniques and the literature on copper doped GLS. The methodology used is introduced for the high throughput combinatorial

deposition on various substrates. The compositional, structural and optical properties measured are shown.

Part B is focused on the work carried out on $CuSbS_2$. It starts with a literature review describing the current state of the art research for this material. This includes the background, fabrication techniques, crystal structure, annealing studies and device fabrication.

Chapter 6 is the work to fabricate $CuSbS_2$ by atmospheric pressure CVD. The choice of materials is explained, including a look at the reactions taking place and the associated Gibbs free energy calculations; to determine their spontaneity. The reaction temperature is explained and why it was chosen. The results show the fabricated thin films including compositional data and morphological images.

Chapter 7 involves the fabrication of $CuSbS_2$ solar cells using a two stage process. The methodology used, is introduced in detail for the rapid thermal annealing of the $CuSbS_2$ at various temperatures and durations; and then the fabrication of $CuSbS_2$ solar cells. The compositional and structural results are shown along with the device performance.

The final experimental section is chapter 8, and this shows the work carried out to fabricate $CuSbS_2$ using a one stage in situ annealing method. A study of the effect of wet etching is also carried out on these films. The thin films are deposited at two temperatures. Then finally cells are fabricated and the compositional, morphological and electrical properties are shown.

The report concludes with further work, the project plan for the remainder of the project, a report conclusion, the appendices and references.

Chapter 2: Background Theory

2.1 Physics of Solar Cell Junction

There is a wide variety of junctions possible using semiconductors to make solar cells; here the focus is on 2- dimensional p-n junctions.

A p-n homo-junction is made by bringing together a p-type material and an n-type material (for a homo-junction both materials would be the same e.g. n-type Si and p-type Si). When combined due to the large carrier gradient between the two materials, we expect diffusion of carriers to occur. Electrons from the n-type layer diffuse towards the p-type material and vice versa. The diffusion current builds up but as it builds an opposing electric field is built up at the junction. The electrons leaving the n-type material leave positive uncompensated donor atoms; and the same with the p-type material (leaving behind uncompensated acceptor atoms). This space charge region forms an electric field which creates a drift current that opposes the diffusion current. At equilibrium these two currents must cancel out as no net charge can flow. When this condition is reached; the space charge region reaches a certain width W (depletion region) with a potential difference across it V_o (built-in potential). An equilibrium p-n junction is shown in Figure 3 and Figure 4, before and after contact, respectively. Figure 5 shows the particle flow and current at the junction.

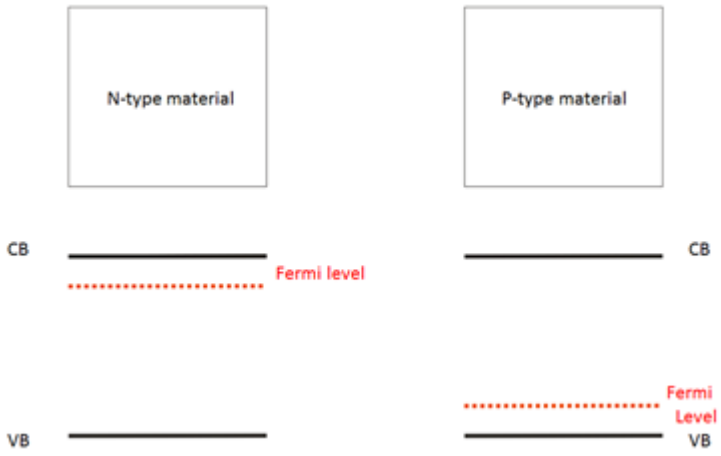

Figure 3: N-type and p-type semiconductors before contact adapted from [23]

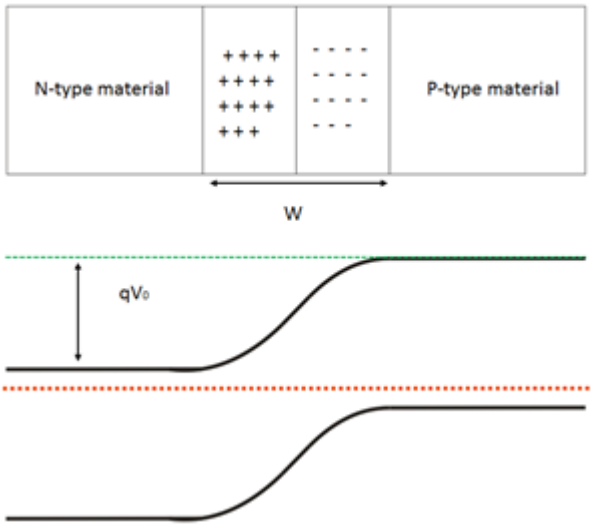

Figure 4: N-type and p-type semiconductors after contact adapted from [23]

	Particle Flow	Current
Hole Diffusion	→	→
Hole Drift	←	←
Electron Diffusion	←	→
Electron Drift	→	←

Figure 5: Particle flow and current of p-n junction at equilibrium adapted from [23]

There are usually very few carriers in the depletion region as the electric field sweeps them all out. The assumption of carrier depletion within W and neutrality outside W is called the depletion approximation. Since the dipole about the junction has an equal amount of charge in each side, the depletion region may extend into the p and n regions unequally, depending on the relative doping in each side. The maximum electric field at the junction is:

$$E = -\frac{q}{\varepsilon} N_d x_{n0} = -\frac{q}{\varepsilon} N_a x_{p0}$$

Equation 1: Electric field at junction

The built-in potential can be calculated by:

$$V_o = \frac{kT}{q} \ln \frac{N_a N_d}{n_i^2} = -\frac{1}{2} EW = \frac{1}{2} \frac{q}{\varepsilon} N_d x_{n0} W$$

Equation 2: Built-in potential

W can be calculated from:

$$W = \left[\frac{2\varepsilon V_o}{q}\left(\frac{1}{N_a}+\frac{1}{N_d}\right)\right]^{\frac{1}{2}} = \left[\frac{2\varepsilon kT}{q^2}\left(\ln\frac{N_a N_d}{n_i^2}\right)\left(\frac{1}{N_a}+\frac{1}{N_d}\right)\right]^{\frac{1}{2}}$$

Equation 3: Depletion width

And the penetration of the transition region into the n and p regions by:

$$x_{p0} = \frac{W\ N_d}{N_a + N_d}$$

$$x_{n0} = \frac{W N_a}{N_a + N_d}$$

Equation 4: Penetration of depletion region into the n and p regions

Where x_{n0} is the penetration in the n-type material, x_{p0} in the p-type material, N_a is the concentration of acceptors, N_d is the concentration of donors, ε is the permittivity of the material, q is the elementary charge ($1.60217657 \times 10^{-19}$ coulombs), n_i is the intrinsic carrier concentration, k is the Boltzmann constant ($1.3806488 \times 10^{-23}$ $m^2 kgs^{-2} K^{-1}$) and T is the temperature in Kelvin.

When the junction is biased it can allow current to flow freely (forward bias) or reduce the current to a very small amount (reverse current). This is why p-n diodes are used as rectifiers. The electrostatic potential of a junction is lowered by the forward bias$(V_o - V_f)$; and increased by the reverse bias $(V_o + V_r)$; this means that the electric field across the junction also decreases with forward bias and increases with reverse bias. This change in the electric field means that the depletion width W also decreases (forward) or increases (reverse). The separation of the energy bands is a direct function of the electrostatic potential barrier at the junction. The height of the electronic energy barrier is simply the electronic charge q times the height of the electrostatic potential barrier. Thus the bands are separated less in forward bias and more in reverse bias. Finally under bias, the Fermi levels of the two materials are separated by a value equal to the separation in energy bands. This is all shown in Figure 6 and Figure 7.

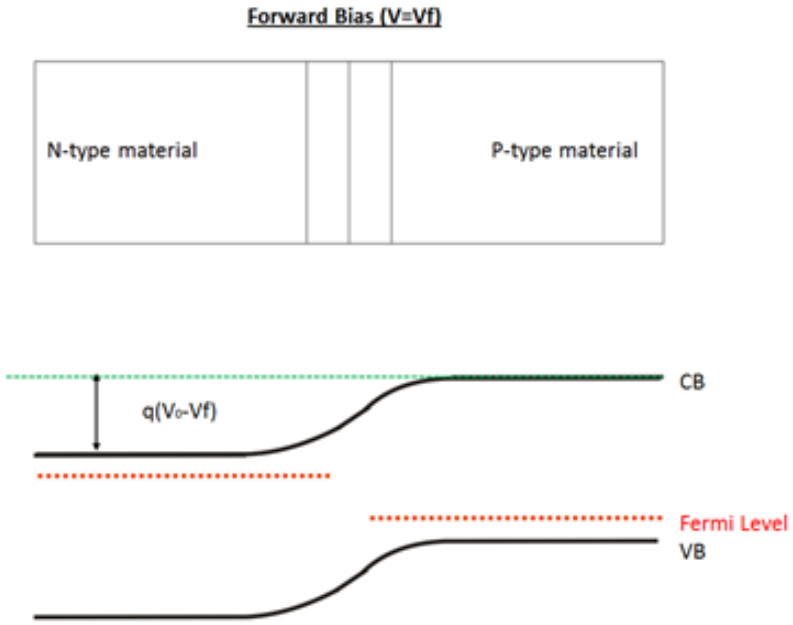

	Particle Flow	Current
Hole Diffusion	→	→
Hole Drift	←	←
Electron Diffusion	←	→
Electron Drift	→	←

Figure 6: N-type and p-type semiconductors under forward bias adapted from[23]

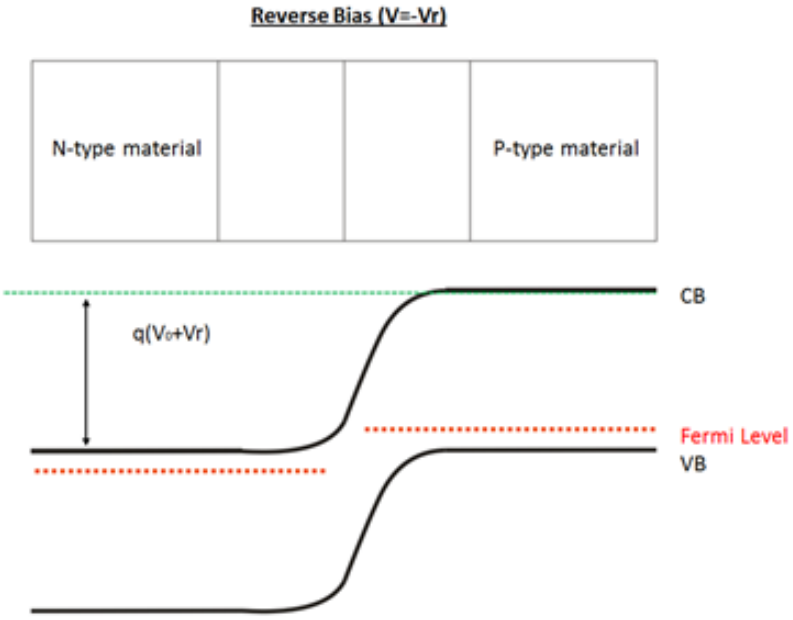

	Particle Flow	Current
Hole Diffusion	→	→
Hole Drift	←	←
Electron Diffusion	←	→
Electron Drift	→	←

Figure 7: N-type and p-type semiconductors under reverse bias adapted from [23]

The diffusion current is composed of majority carrier electrons on the n-side surmounting the potential energy barrier to diffuse to the p-side; and holes surmounting the barrier and moving from p to n. At equilibrium there is a certain number of electrons that would have enough energy to cross the barrier to the p-type material. When the junction is biased, the number of electrons with enough energy either decreases (reverse bias) or increases (forward bias); due to the change in the barrier height. On the other hand, the drift current is relatively insensitive to the barrier height. By having a stronger field, the carriers are swept faster; but this is not the limiting factor; the main limit on the drift current is how often carriers are available to be swept away. Any carrier excited thermally or optically (solar cells or photodiodes) within the diffusion length of the minority carriers will be swept by the electrical field.

The total current is equal to the diffusion current (from p to n, majority carriers) and drift current (from n to p, minority carriers) combined. In equilibrium no net

flow of current occurs. In reverse bias, only the drift current flows (from n to p) and in forward bias, the diffusion current dominates. The behaviour is described by the diode equation:

$$I = I_{gen}(e^{qV/kT} - 1)$$

Equation 5: Diode equation

There are a wide variety of devices that involve the interaction of photons with semiconductors. The response of the semiconductor junction, allows it to be used as a solar cell, to convert absorbed optical energy into useful electrical power.

If a junction is illuminated with light with energy greater than the band gap, an added generation current is produced. This illumination increases the amount of minority carriers available to be swept by the electric field. The diode equation becomes:

$$I = I_{gen}\left(e^{qV/kT} - 1\right) - I_{opt}$$

Equation 6: Diode equation with optical current

The current I_{gen} is the amount of drift current under no illumination and I_{opt} is the extra current produced by illumination. Thus the I-V curve is lowered by an amount proportional to the generation rate. When the device is short circuited (v=0), the first part of the above equation cancels out, but the optically generated drift current from n to p is still present (called the short circuit current (I_{sc})). When there is an open circuit across the device (I=0), the voltage is called the open circuit voltage (V_{oc}) and is given by:

$$V_{OC} = \frac{kT}{q} \ln\left(\frac{I_{opt}}{I_{gen}} + 1\right)$$

Equation 7: Open circuit voltage

We can modify the diode equation further to produce a one diode model; this will include the shunt resistance (this is the cells resistance to leakage and we want this to be as high as possible) and series resistance (this is the resistance of the cell, which we want to minimise in order that as little as possible power is

lost in the cell). The equation has been rearranged to make the solar cell current positive:

$$I = I_{opt} - I_{gen}\left(e^{q(V+IRs)/nkT} - 1\right) - \frac{V + IR_s}{R_{sh}}$$

Equation 8: One diode model

Where R_s is the series resistance and R_{sh} is the shunt resistance. A further diode equation can also be added to improve the model (two diode model). Something worth mentioning here is the ideality factor, it is a measure of how closely the diode follows the ideal diode equation. An ideality factor of 1 assumes that all the recombination processes are Shockley Read Hall recombinations (i.e. band to band and via traps in the bulk areas of the device). In reality there may be other recombination processes taking place (e.g. Auger or in depletion region) which cause the ideality factor to change [24].

The max power (P_{MPP}) produced by a cell is given by the equation: $P = IV$. The current at the max power (P_{MPP}) is denoted I_{MPP} and the voltage V_{MPP}. The fill factor is a measure of the square-ness of the I-V curve and is given by:

$$FF = \frac{I_{MPP}V_{MPP}}{I_{SC}V_{OC}}$$

Equation 9: Fill factor

The solar cell conversion efficiency (η) is the ratio of power generated to the power incident onto the cell and is shown in Equation 10. The quantum efficiency is the efficiency of the cell at each wavelength. It is done by illuminating the light at a certain small range of wavelengths and calculating the efficiency and then repeating to get the whole range of wavelengths.

$$\eta = \frac{P_{MPP}}{EA} = \frac{V_{MPP}I_{MPP}}{EA} = \frac{FF * I_{SC}V_{OC}}{EA}$$

Equation 10: solar cell conversion efficiency

P_{MPP} is the maximum power at the operating point; E is the irradiance (Watts/metres^2) and A is the cell area in metres^2. Figure 8 below shows V_{MPP}, I_{MPP}, I_{SC} and V_{OC} schematically.

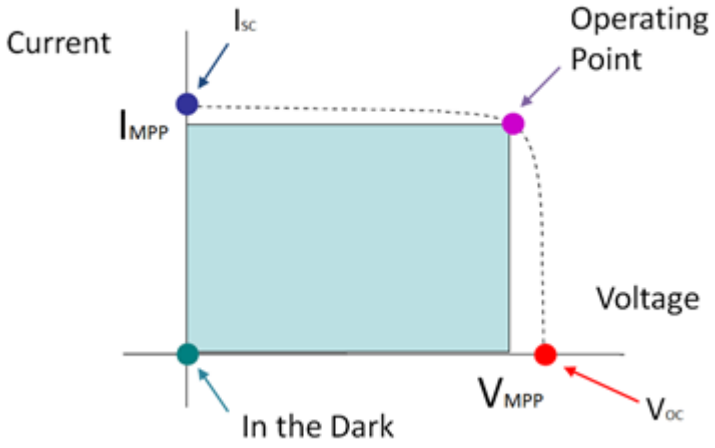

Figure 8: I-V characteristics of solar cells [25]

Figure 9 below shows some of the main loss mechanisms in solar cells.

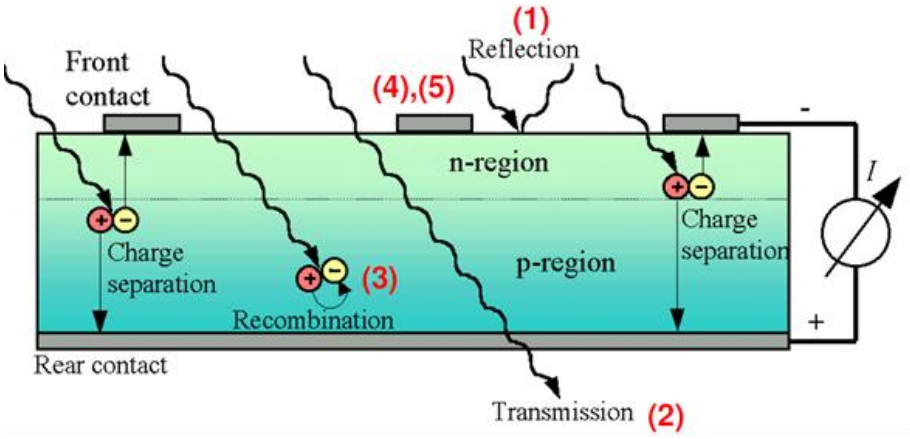

Figure 9: Solar cell loss mechanisms [25]

The losses are introduced below. Note the last three losses are not shown in Figure 9.

1. Light reflected from top surface: this can be reduced by using antireflective coatings.

2. Light passes through without absorption: here the path length of the light can be increased by scattering the light using particles, using textured surfaces on the top of the cell or on the bottom of the cell or reflecting light using back mirrors. Another approach is to use a material with higher absorption or by increasing the thickness of the cell (needs to be balanced with the next loss).

3. Electrons and holes recombine before reaching the electrodes: the thickness of the cell can be decreased or an alternative material can be used with longer carrier lifetimes. Another method is to use window or barrier layers to reduce surface recombination.

4. Shadowing by front contact grid: buried contacts can be incorporated that shadow less of the top of the material or put all the contacts on the back of the cell [26-28].

5. Small resistance losses from the contacts on the front surface: this requires better ohmic contacts to the cell by trying different contact methods or different materials. Here window or barrier layers could be used before the contacts.

6. Not all photons have sufficient energy to produce electron hole pairs: tandem or stacked solar cells could be fabricated, where materials of different band gaps are put one on top of the other in order to more efficiently make use of the spectrum (wide band gap materials on top and then decreasing band gaps going down).

7. Only the band gap energy is needed for electron-hole pair formation, the rest is lost as heat: again tandem or stacked solar cells could be fabricated or, there have been theoretical discussions where electrons are collected (hot electrons), that have not lost their energy as heat yet and therefore more energy can be extracted from the cell. [29]

8. Light is not always shining on the solar cell at the same angle: by using solar concentrators and tracking systems energy can be collected from wide angles or the sun can be tracked as it moves over the horizon (expensive).

2.2 Solar Cell Structure

Several layers are used in the basic solar cell structure. A typical structure is shown in Figure 10 below.

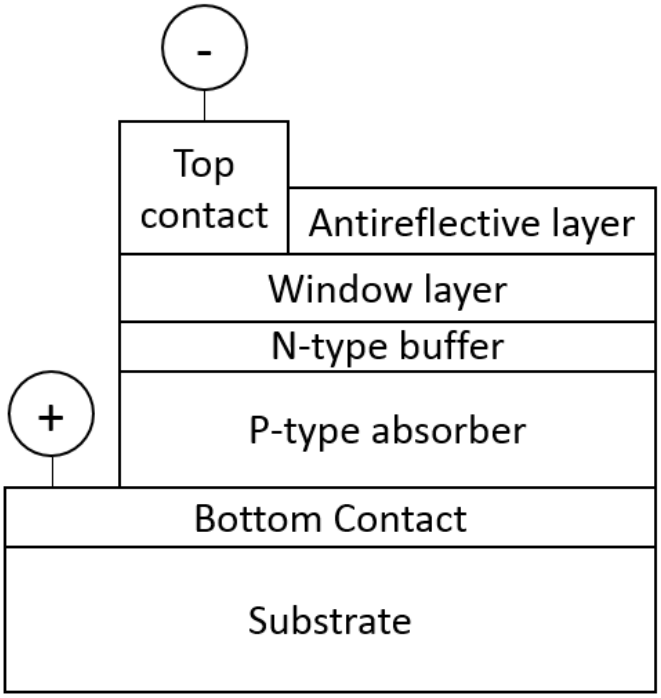

Figure 10: Typical thin film chalcogenide solar cell structure adapted from [30]

2.2.1 Absorber Material

The absorber material in chalcogenide thin film materials is the p-type layer This material absorbs most (if not all) of the incident light from the solar spectrum. The thickness ranges from 500 nm to around 2 μm depending on the absorption coefficient of the material. The main focus in this thesis is on the absorber material. The annealing of this material is of prime importance in the cell fabrication. For chalcogenides the material can be annealed in a reactive atmosphere (sulphur, selenium, H_2S or H_2Se), by annealing with a thin film of S (or Se) deposited on top or by rapid thermal processing. All of these will be discussed in the relevant sections.

2.2.2 Buffer Layers

The buffer layer here is the n-type layer that forms the p-n junction with the absorber layer mentioned above. Ideally this layer has a wide band gap and absorbs little from the spectrum allowing the photons to pass through and reach the absorber layer. Usually this layer is in the range of 50-200 nm in thickness. The current main material is CdS deposited by chemical bath deposition, and using this material, cells have achieved the greatest efficiencies. Other contenders include InS, ZnS [30-32], and many others.

2.2.3 Window Layer

This layer is in contact with the buffer layer, usually a transparent conducting oxide such as indium tin oxide or fluorine doped tin oxide is used. Since the buffer layer is very thin, the resistance laterally is very high. This layer allows for light to pass through while still allowing ohmic connections to be easily made to the cell.

Sometimes a bi-layer is used [30] for example a thin resistive undoped 50 nm ZnO layer followed by about 500 nm of the n-type more conductive Al doped ZnO. This improves the shunt resistance of the cell, although this depends on the method used for the deposition as some methods (such as high energy sputtering) can damage the surface of the buffer layer diminishing any beneficial effects [33].

2.2.4 Contacts

Contacts are deposited on either side of the above 3 layers. Depending on the window layer and the absorber layer different materials are used. In some cells a passivation layer is deposited before the contacts to decrease recombination near the contact. Good ohmic contacts are a must for high efficiency solar cells [34-37].

2.2.5 Ideal Solar Cell Parameters

Just as a quick guide the following general requirements can be deduced for an ideal solar cell:

- A p-type absorber with a band gap around 1.5 eV with a high absorption coefficient.
- An n-type layer lattice matched to the p-type layer with a wide band gap.
- Low series resistance.
- Very high shunt resistance.
- Low cost and abundant materials.
- Low fabrication costs.
- Non – toxic materials.
- Long term stability of device.

2.3 Fabrication Techniques

2.3.1 RF Sputtering

2.3.1.1 Fundamentals

Sputtering is a deposition process which has been used; plasma (argon plasma) is produced by a high electric field at low pressures (~ 1 x 10^{-5} Torr). The plasma is formed by the ionization of the argon atoms, this happens through electric discharge and is called a gas discharge process. A plasma can be defined as a gas with both neutral and charged particles, but the overall charge is neutral.

The deposition then takes place by the accelerating ions hitting the target (made of the material which will be deposited), causing some material to be knocked out and which lands on the substrate or wafer to form a film (as shown in Figure 11) [38]. The sputtering target is negatively biased, this attracts the positive argon ions, which causes the deposition to take place. As the pressure within the chamber is increased the ejected material from the target is scattered at a higher rate; therefore by optimising the ion current as well as the pressure, a stable and continuous deposition can be achieved forming films with the desired properties.

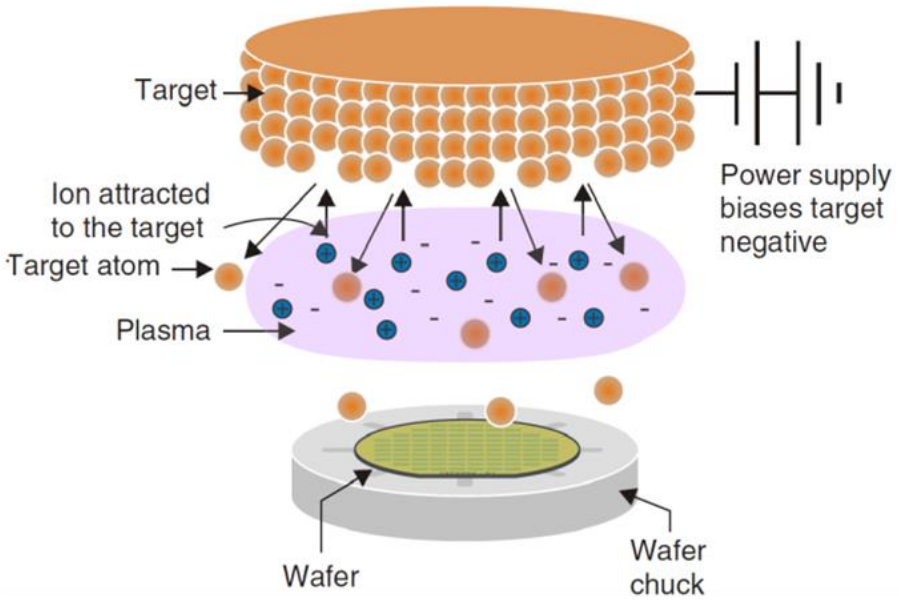

Figure 11: Fundamentals of sputter deposition [23]

Some advantages of sputtering are:

1. The high kinetic energy of the ejected atoms allow for stronger adhesion.
2. Allows simultaneous deposition from multiple sources or sequential deposition without the exposure of the deposited materials to atmosphere.
3. Good control of film composition (by controlling target composition).
4. Suitable for large area and continuous deposition.
5. An established technique for the preparation of thin films for magnetic, optical and contact applications.
6. Reactive sputtering can be achieved by introducing reactive gases to the chamber during the deposition process. Examples include oxides and nitrides.

2.3.1.2 System

The sputtering system used was a Kurt Lesker NANO-38 sputtering system. The base pressure here was maintained using a combination of a scroll pump and a turbo molecular pump (Pfeiffer). The chamber can hold two 2 inch targets facing downwards in separate guns, with separate power supplies. The sample (to be deposited on) is placed on a platen below the guns which can be rotated to achieve a homogeneous uniform deposition or can be kept stationary to achieve a deposition thickness gradient. The deposition thickness is monitored using a quartz crystal. Each material has a corresponding density, acoustic impedance and tooling factor which allows accurate thicknesses to be measured. The tooling factor accounts for the difference in distances of the monitor and the substrate.

Argon and oxygen can be flowed in into the chamber during the deposition and are introduced using mass flow controllers. A radio frequency source is used here to ionise the argon gas to produce the plasma.

2.3.2 Chemical Vapour Deposition

2.3.2.1 Fundamentals

This technique involves the deposition of materials by the reaction of vapours. CVD is a well-known method to produce high quality and high purity thin films;

the process also allows good stoichiometric control on the deposition process. Figure 12 shows an example of a CVD setup used by Dr. Huang to produce Ge-Sb-S. The precursors can be solid, liquid or gas initially and several methods can be used to vaporize them.

There are many different types of CVD methods to go into and describe each one; but the one shown below is APCVD (atmospheric pressure chemical vapour deposition). An introduction to the different types of CVD is given in ref. [39].

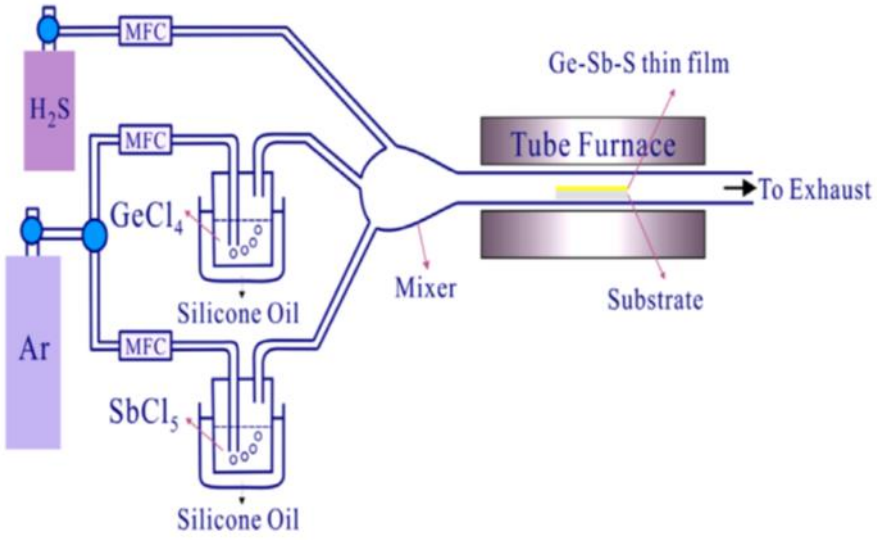

Figure 12: Typical CVD setup used for Ge-Sb-S thin film deposition. Taken from [25]

The main advantage of CVD is that it produces a very conformal deposition profile. This means that the deposition thickness on the horizontal planes is similar to the deposition on the vertical planes (in a patterned substrate).

The CVD reaction can be dominated by surface reactions and therefore the composition is sensitive to the substrate temperature and pressure. They can also be dominated by mass transport, in this case the film composition is sensitive to the ratio of the precursor partial pressures. The reaction is controlled by varying the pressure of the reaction chamber, the substrate temperature, the precursor materials and carrier gas flow rates.

With any CVD reaction, the first step is to analyse the feasibility of the reaction [40]; and this will only happen if the thermodynamics are favourable i.e. the reaction is spontaneous. A spontaneous reaction here means that the reaction is naturally favoured [41]. If the Gibbs free energy of a reaction (ΔG_r) is negative

then the reaction is spontaneous. The Gibbs free energy can be thought of as the energy stored in a system that is free to do useful work [41].

To calculate the Gibbs free energy the Gibbs free energy of formation of the reactants is subtracted from the Gibbs free energy of formation of the products, as shown in Equation 11.

$$\Delta G_r = \sum \Delta G_{f,products} - \sum \Delta G_{f,reactants}$$

Equation 11: Gibbs free energy calculation

2.3.2.2 System

The system used in this work is custom built in the Novel Glass group in the ORC by Dr. Kevin Huang. The system comprises of an Elite™ three-zone tube furnace with a quartz tube inserted (this is where the reaction takes place), custom built precursor inlets and holders (or bubblers) are used depending on the material being deposited. The system is all extracted and is held within a nitrogen purged glove box. If needed also, the system can be connected to a scroll pump to bring the pressure down to below 1 Torr.

Several gas lines are connected to the system including hydrogen and argon which are used as carrier gases as well.

2.3.3 High Throughput Physical Vapour Deposition

2.3.3.1 Fundamentals

PVD is a technique that involves the deposition of materials by the physical condensation or layering of materials onto a substrate and involves no chemical reactions. Here, we use high throughput physical vapour deposition.

High throughput materials discovery involves the fabrication and screening on a wide spread of compositionally varying materials (a library) in a single experiment. Historically, this was done sample by sample. Combinatorial methods in chemistry began with the solid state synthesis of peptides by Merrifield in 1963 [42]. Over the years, the pharmaceutical industry adopted this approach to aid in the discovery of new medicines. In terms of solid state materials, Hanak et al was the first to demonstrate high throughput approaches

[43]. Later on Schultz et al [44] used sputtering to deposit varying compositions of copper oxide thin films on a single substrate.

There are generally two methods for library generation, a sequential masking method and a continuous gradient. The masking method consists of depositing individual elements sequentially using a series of masks [45] The materials are evaporated using one of several methods including sputtering, laser ablation, thermal and electron beam evaporation. The main drawback in this method is that the deposition requires a large number of steps [10] and sometimes vacuum needs to be broken between masking steps exposing the samples to atmosphere, increasing the possibility of error and incomplete mixing of materials.

The continuous gradient method, uses sources which produce a gradient deposition relative to one another. Initially this was done sequentially for example in the study by Chang and Xiang [46, 47]. Here we still have the problem of incomplete mixing of materials. By depositing the materials at the same time we ensure complete mixing of the materials, also by heating the substrate we can form phases in situ and therefore diminishes the need for post deposition annealing. This approach is used in this work and the complete system is explained below.

2.3.3.2 System

The system used is shown in Figure 13 and a top view schematic is shown in Figure 14.

Figure 13: High throughput UHV PVD system in surface science group in chemistry [27]

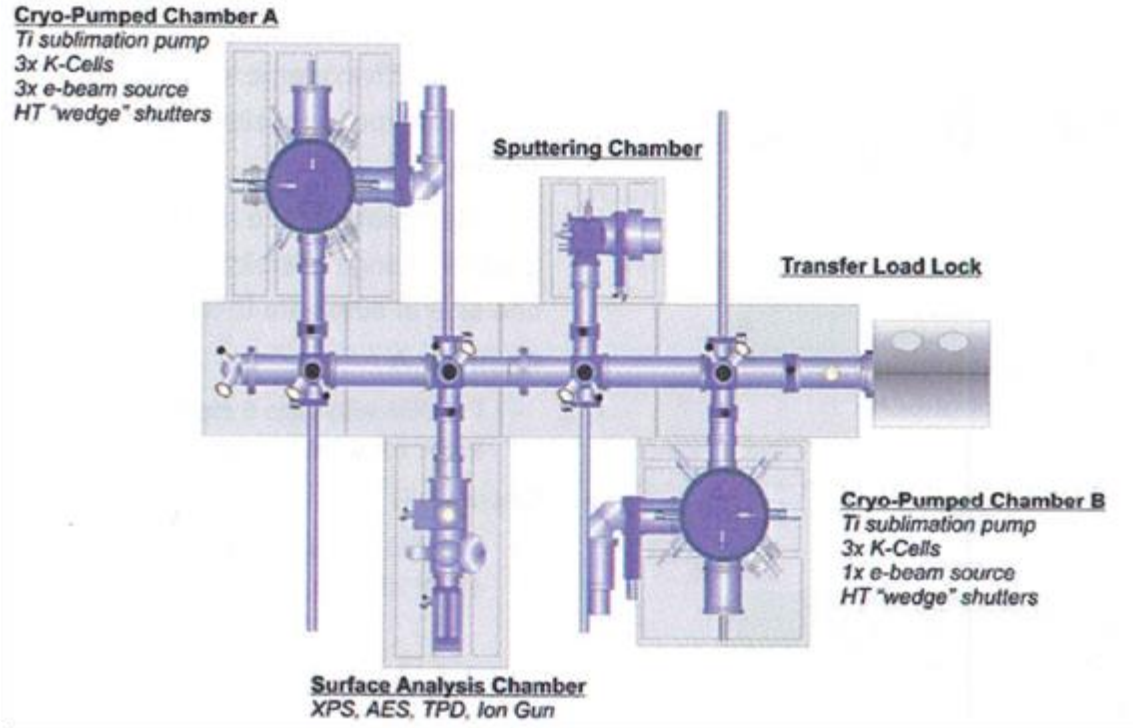

Figure 14: Top view of high throughput UHV PVD system in surface science group in chemistry [28]

The chamber used was chamber B; which comprises of 3 effusion Knudsen cells (k-cells) and one electron gun source; one advantage of this chamber is the fact that the e-gun can mimic the position of any of the 4 source positions within the

chamber. The chamber is held at a base pressure of 1 x 10^{-7} Torr by a cryogenic (CTI- Cryogenics) pump. By having multiple sources at angles from each other, spreads of different compositions across the sample can be deposited. Figure 15 shows the effect of depositing two elements from opposing sources.

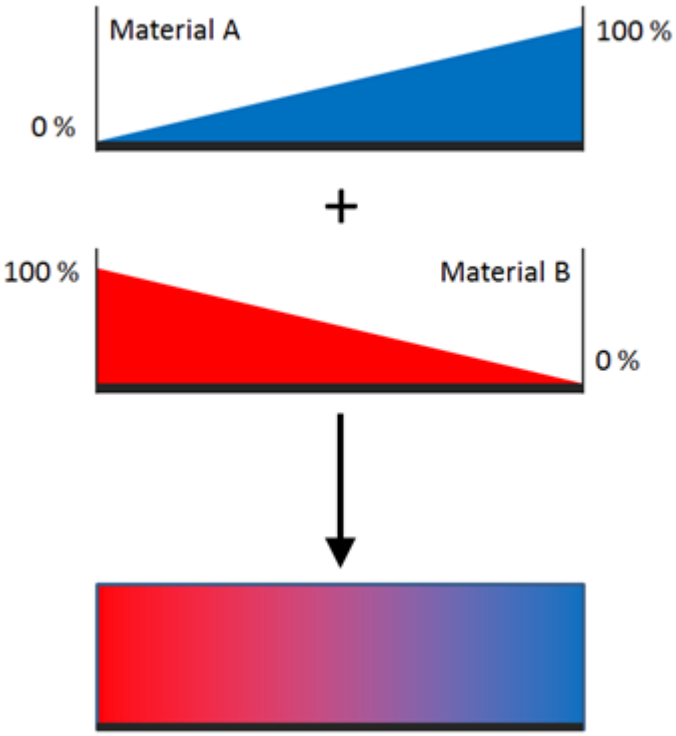

Figure 15: Example of compositional spread produced when depositing two elements from opposing sources. Adapted from [16]

The profile of each material can be controlled by inserting shutters to partly cover the 4 sources; this creates a shadow effect when the shutter is in the line-of-sight between the source and the sample. By changing the amount of coverage different deposition profiles can be achieved. A diagram of a source, shutter and the substrate inside the chamber is shown in Figure 16.

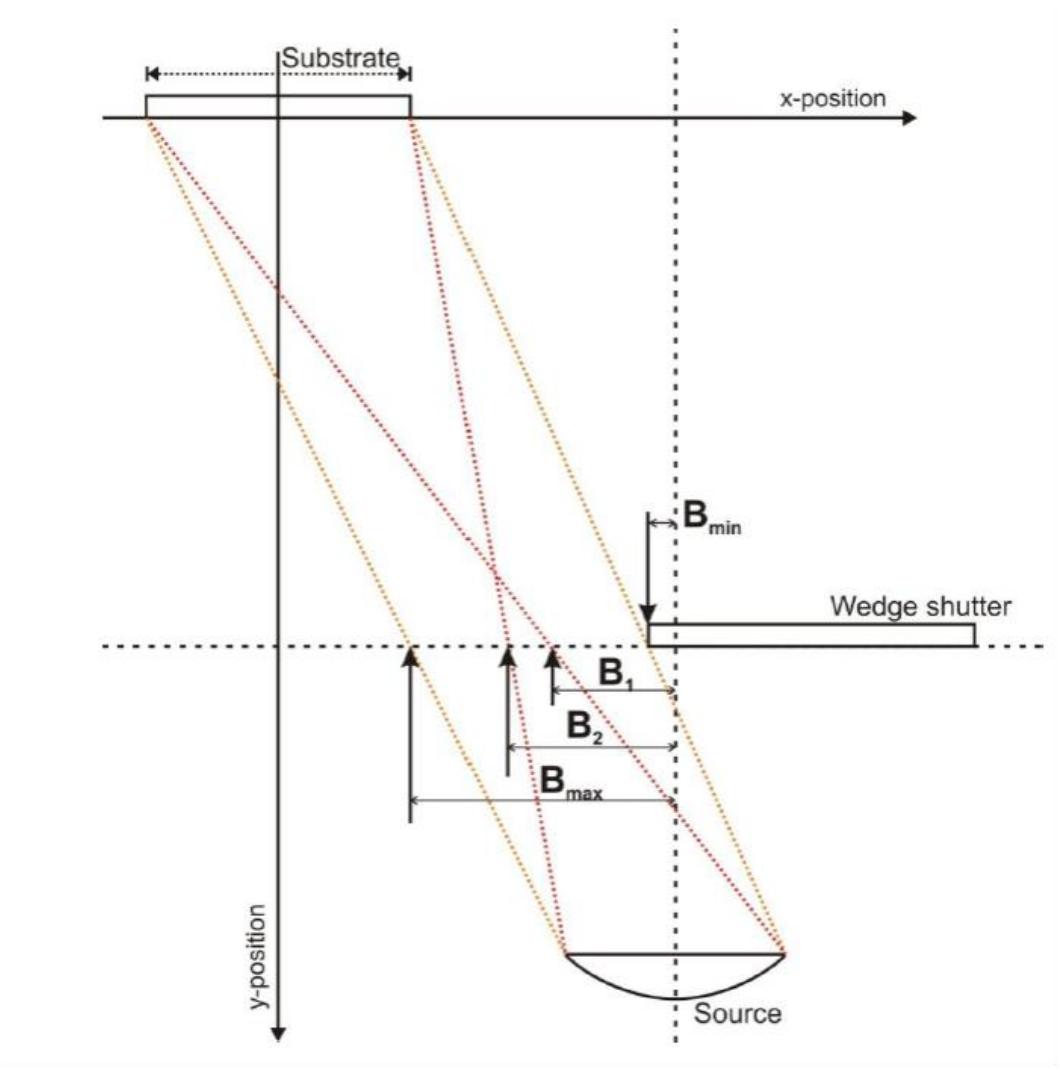

Figure 16: Diagram of a source, shutter and the substrate inside the chamber. The shutter is used to produce a gradient of the source material on the substrate [16]

The typical deposition profiles with respect to wedge shutter position between source and sample are shown in Figure 17 below.

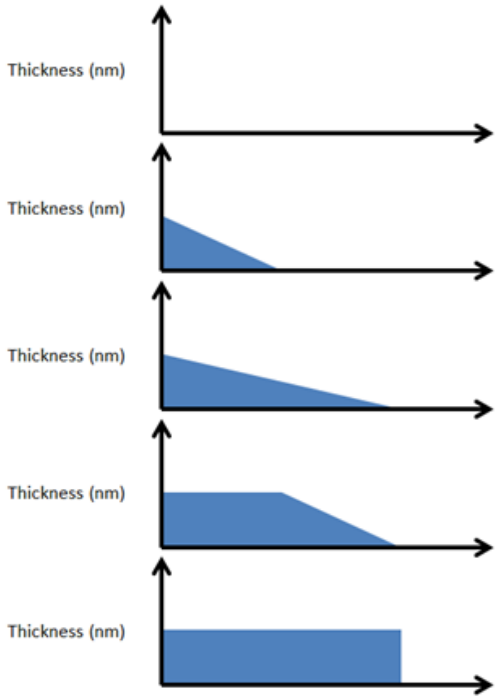

Shutter position	Deposition profile
B_{max}	No deposition
B_2 to B_{max}	Gradient + no deposition
B_1 to B_2	Linear gradient
B_{min} to B_1	Plateau + gradient
B_{min}	Plateau

Figure 17: Deposition profiles with respect to wedge shutter position between source and sample. Adapted from [16].

The shutter, source and sample positions are fixed within the chamber, along with sample size and source diameter; therefore, the compositionally graded film is highly reproducible. The setup is described in greater detail by Hayden and Guerin [9].

2.3.3.2.1 Sulphur Cracker

Chamber B is also used because it allows the deposition of sulphides. The usual PVD system utilizes electron beam evaporation and Knudsen cells to evaporate the sources. With sulphur, the problem is that it forms long chain allotropes which disrupt the deposition process. To solve the problem, this chamber has been fitted with a sulphur cracker k-cell. This cell has a second hot zone to further break down the sulphur chains. The schematics of a normal k-cell and a sulphur cracker k-cell are shown in Figure 18.

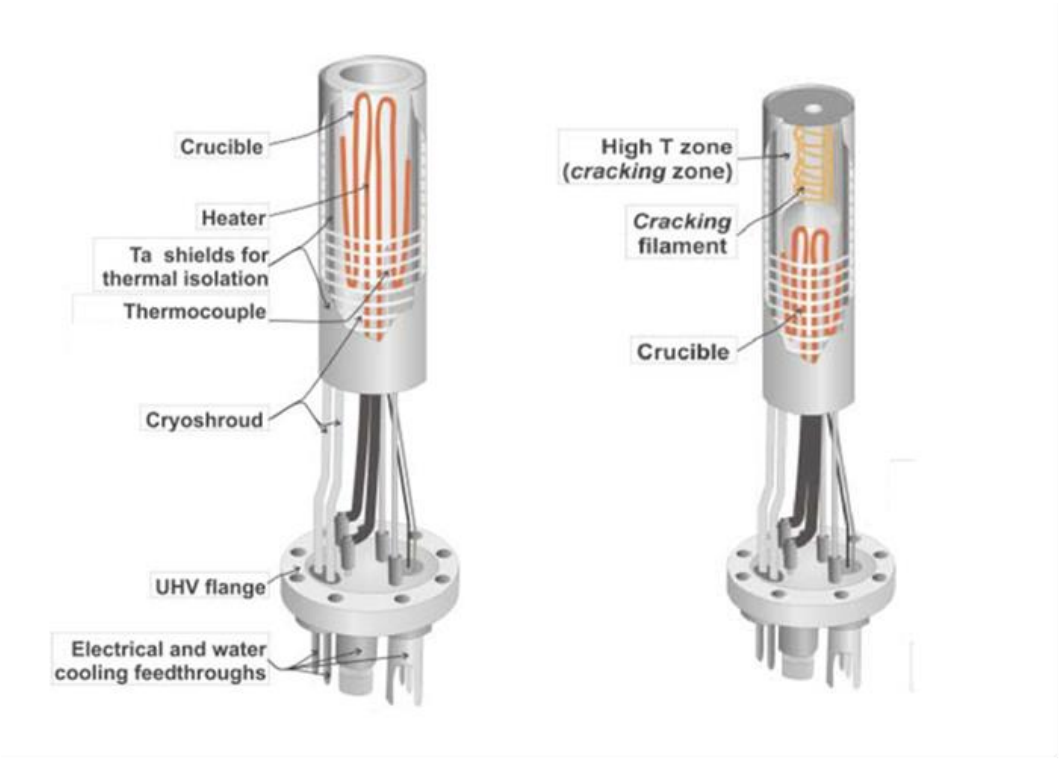

Figure 18: Knudsen and sulphur cracker Knudsen cell schematics. Taken from [48]

2.3.4 Reactive Ion Etching

2.3.4.1 Fundamentals

Reactive ion etching is a process used in micro fabrication to remove layers of a material. It is a plasma phase dry etch (in contrast to wet etching using acids for example), used for cleaning or structure formation.

Similar to a sputtering system a plasma is ignited by applying a strong RF (radio frequency) electromagnetic field. The field is set to a specific frequency and is applied to a few hundred watts. The oscillating electric field is sufficient to separate ions in the argon gas in the chamber forming the plasma. This plasma is accelerated up and down in the chamber bombarding with the substrate and sides of the chamber. As the chamber is grounded, any charged particles which collide into it will neutralise. The remainder of the ions etch the materials placed on the sample holder.

In addition to this, due to electrons being removed from the sample holder, this becomes positively biased. The plasma becomes slightly negatively charged and this attractive force speeds up the etching process. The moving ions can react

with the chemicals on the surface to etch them away or can simply sputter the material away due to the high kinetic energies of these particles [49]. A schematic of a typical reactor is shown in Figure 19.

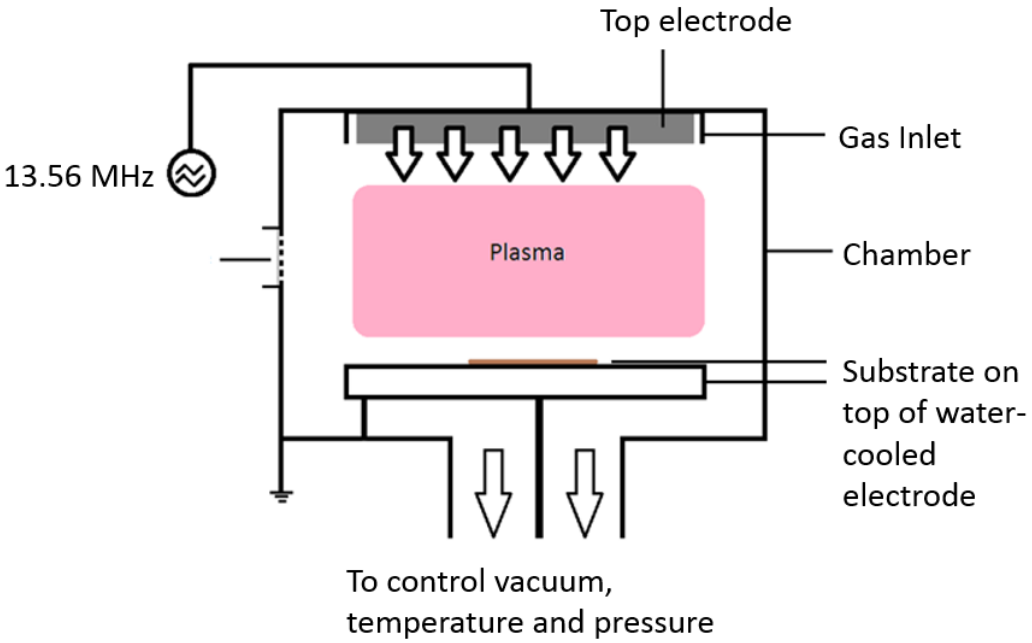

Figure 19: Sketch of a parallel plate RIE reactor. Adapted from [50]

2.3.4.2 System

The system used was an Oxford instruments PlasmaLab 80 plus system [51]. The reactor uses a 13.56 MHz radio frequency and has a substrate electrode 240 mm in size (which is water cooled). The gases are introduced using a shower head gas inlet. Several gases can be installed, in the current system this includes hydrogen, argon, oxygen and sulphur hexafluoride. The whole system is computer controlled and the etching takes place at a base pressure below 1 x 10^{-5} Torr; which as achieved using a combination of rotary and turbo molecular pumps.

2.3.5 Rapid thermal annealing

2.3.5.1 Fundamentals

Rapid thermal annealing is a manufacturing process where a material is heated up at a rapid rate. Most conventional furnaces have a max temperature ramp rate of around 20 ℃/minute, RTAs can ramp a material up to 1200 ℃ with a ramp rate of up to 100 ℃/second, and this is achieved with the use of high intensity lamps. Even though the temperature is increased rapidly, the cooling of the sample is slower as to reduce breakages and cracking of the sample and layers.

Temperature control is achieved through a mix of thermocouples and pyrometers (depending on system) and is one of the key challenges when performing anneals. Therefore for optimised rapid annealing, a balance needs to be found between the temperature profile and film stability.

2.3.5.2 System

The system used was a bench top Jipelec JetFirst rapid thermal annealer [52]. The chamber holds substrates up to 150 mm. The temperature is controlled by a PID controller with two thermocouples and a pyrometer for temperature monitoring. The annealing can be carried out under vacuum (down to 1 mTorr using a scroll pump) and three different gases can be introduced (in this case oxygen, nitrogen and argon).

2.4 Fabrication details

Many fabrication procedures were standardised across many experiments and the equipment used was the same. To avoid repetition in the methods in each chapter, here we detail the equipment, conditions, procedures and material properties that will be used in the experimental chapters – unless otherwise stated later on.

For thin film material depositions the following parameters were used for the quartz crystal monitors (to measure the thickness of the deposited film in situ):

Material	Density factor (g/cm^3)	Acoustic impedance ($g/ (cm^2 sec)$)	Tooling factor
Mo	10.2	0.5	140
CIGSe	5.91	1.2	200
ZnS	4.09	0.775	100
Al ZnO	5.61	1.58	130
Aluminium	2.7	8.2	
CZTS	5.91	1.2	200
MgF2	3.18	0.85	127

To characterise the solar cells made, an ABET Technologies Sun 3000 solar simulator [53] was used (with an AM 1.5G filter at 100 mW/cm^2), for all sputtering runs a Kurt Lesker™ NANO-38 thin film deposition system was used and for film thickness verification a KLA tensor alpha-step IQ surface profiler was used.

Also, the EDX system used was an Oxford Instruments INCA PentaFET fitted on a Carl Zeiss EVO 50 SEM using a using a working distance of 9.5 mm and a magnification of 500.

The XRD system was a Bruker C2 [54] fitted with a general area detector, allowing the simultaneous recording of all angles; the X-rays are provided by a CuKα1 source). The XRD data acquisition duration was 600 seconds, the source angle

was 11 degrees and the detector angle was 27.3 degrees. The XRD data was analysed using PDF-4+ 2010 [1] software provided by the international centre for diffraction data (ICDD), and the JCPDS file numbers are shown in the relevant figures.

SEM images (to observe grain growth from annealing) were taken using a FEI Helios 600 FIB/SEM system the images of the top morphology were taken using the Carl Zeiss EVO 50 SEM.

Four procedures were standardised for all experiments:

Procedure name	Details
Standard photolithography procedure	S1828 photoresist was spin coated onto the substrates (a SCS spin coat G3P-8 coater was used, the resist was spun with the following settings: 5 min ramp, 3000 rpm for 60 seconds). The samples were then soft baked at 100℃ for 30 min, left to cool down for 5 min and then exposed to UV light using a SUSS Microtec MA-6 aligner for 30 seconds. All substrates were exposed sequentially and then developed in a MF319 solution for one minute. The samples were then hard baked at 120 ℃ for 30 min.
Substrate cleaning procedure	The substrates were cleaned by rinsing in acetone, isopropanol, deionised water and then dried using a nitrogen gun. The samples were then etched using a reactive ion etching system (Oxford instruments PlasmaLab 80 plus) in argon for 1 min using 100 watts and a pressure of 50 mTorr.
Post deposition cleaning	Following the deposition any flakes were removed using a nitrogen gun and a 1 min reactive ion etch.
Ramp rate for heated depositions	For depositions above room temperature, the temperatures were ramped up at 5 ºC /min after the deposition was started. The interlock on the system would not allow the heaters to be turned on before the base pressure was reached and would not allow the current to flow through

	the heaters if the pressure increased abruptly (when the plasma strikes in the chamber).

2.5 Characterisation Techniques

2.5.1 Scanning Electron Microscopy

SEM is a widely used technique for the characterisation of the surface morphology of materials. It uses a focused beam of electrons which is scanned across the surface of the sample, the beam usually has an energy ranging up to 40KeV. This beam is usually generated using a thermionic or field emission electron source. The beam is focused using lenses and then a set of scanning coils are used to raster the beam across the sample. The latter is preferred as it can produce higher current density and a smaller beam size, which results in an improved signal to noise ratio and resolution.

The electron beam interacts with the surface and results in the heating of the sample, possible charging (if the sample is insulating), ejection of Auger electrons, X-ray radiation, backscattered electrons (from scattering on the surface) and plasmon production.

For imaging, the system utilises the plasmon production effect. As ionisation occurs electrons are generated (called secondary electrons), these are collected using an Everhart-Thornley detector [55], which is a type of scintillator photomultiplier device. Secondary electrons usually have low energies (<50 eV) and therefore they originate within the first few hundred nm of the samples surface. The roughness of the sample can be imaged since the amount of secondary electrons ejected from the sample changes with incident angle, areas with edges and steep angles emit more secondary electrons and so appear brighter and therefore a 3 dimensional surface image can be acquired.

The total interaction volume of the electron beam extends from under 100 nm to around 5 μm. The volume size is dependent on the material being measured (atomic mass and density), the accelerating voltage and beam size. The rest of the interaction volume (other than the first few hundred nm producing

secondary electrons) produces the other particles mentioned above. The two worth mentioning here are the X-ray radiation (which we will encounter when introducing the EDX technique) and the backscattered electrons (BSE). BSE electrons have higher energy and their number is strongly related to the atomic number of the specimen, this is because heavy elements (high atomic number) backscatter electrons more strongly. BSE detection can give information about the distribution of different elements within the sample.

2.5.2 Energy Dispersive X-ray Spectroscopy

Usually installed as part of an SEM system, EDX analyses the X-rays emitted from a sample that have been generated by the electron beam. The technique allows the quantitative measurement of relative amounts of individual elements in a sample.

The electron beam excites electrons from a neutral ground state to a higher unstable energy state, this usually occurs in the inner electron shells of the atoms. Electrons in this unstable higher energy state relax emitting energy and then return to a stable ground state. The energy is lost as an auger electron or as an emitted X-ray. EDX relies on these emitted X-rays to characterise the material. Since the energy levels of a material are unique, the energy of the X-ray directly corresponds to a specific transition. Generated X-rays are detected by a detector which converts the X-ray energy into a voltage signal (usually a SiLi detector) [56, 57].

The accuracy of EDX is dependent on:

1. Sample thickness - as the sample is made thinner we start seeing more and more signal from the substrate
2. Elements analysed – some emission peaks overlap introducing error in the calculations. A list of emission peaks used in this thesis can be found in Appendix D on page 179 [58].
3. Conductivity of sample – charging can reduce measurement accuracy

2.5.3 X-ray Diffraction

X-ray diffraction is a characterisation method used to distinguish the crystal phases in a material. The fundamentals of this technique include an X-ray source,

a sample stage, detector and the analysis software. The X-rays are generated from a metal source (e.g. Cu or Mo) by bombarding it with electrons. The metal emits X-rays which are focused onto the sample. The X-rays are diffracted from the crystal planes, and as the wavelength of the X-rays are fixed at certain angles the diffracted beams will interfere constructively. This can be written mathematically and is described by Bragg's law (Equation 12) [59]:

Equation 12: Bragg's law

$$n\lambda = 2d\sin\theta$$

Where n = the order of diffraction, λ = wavelength of X-ray radiation in meters, d = spacing between parallel crystal planes in metres and θ = angle between the incident X-rays and the crystal plane in degrees.

The constructive interference at certain angles are picked up by the detector and are then converted to a diffraction pattern. Different materials have different patterns and therefore the pattern can be used to uniquely identify the phases present.

2.5.4 Raman

Raman spectroscopy provides information on the chemical and structural information of a material. The technique relies on the inelastic scattering of light illuminated on the material. The source of the light is usually a laser with a specific wavelength. Two common wavelengths used are 632.8 nm and 785 nm.

The beam of light is absorbed by the molecules of the material and then emitted. The emitted photon is of a slightly different wavelength to the absorbed photon as the electron returns to a different ground state than it was before. The shift in frequency is called a Stokes shift (if the photon has a lower energy than the absorbed photon) or anti-Stokes shift (if the photon has a higher energy than the absorbed photon). The shift is usually in an energy range between 200 and 4000 cm^{-1}.

Different materials will shift the frequency by different amounts, by analysing the spectrum achieved we can deduce which bonds are present within the material. The benefit of using Raman for example over X-ray diffraction is that amorphous phases can be detected. Although the analysis of Raman is less

developed due to the unavailability of large databases like those available for X-ray diffraction,

2.5.5 Ellipsometry

This is an optical technique which is used to investigate the dielectric properties of thin films. The system measures the change in polarisation and intensity of a light beam as it is reflected from the surface or transmitted through from a sample. The change corresponds to the optical properties and thicknesses of the materials measured [60].

When two orthogonal waves are superimposed, one of three polarisations can be achieved: [1] if they are in phase then the light becomes linearly polarised [2] if they are 90° out of phase, the light is circularly polarised [3] if they are out of phase by any other amount, the light becomes elliptically polarised.

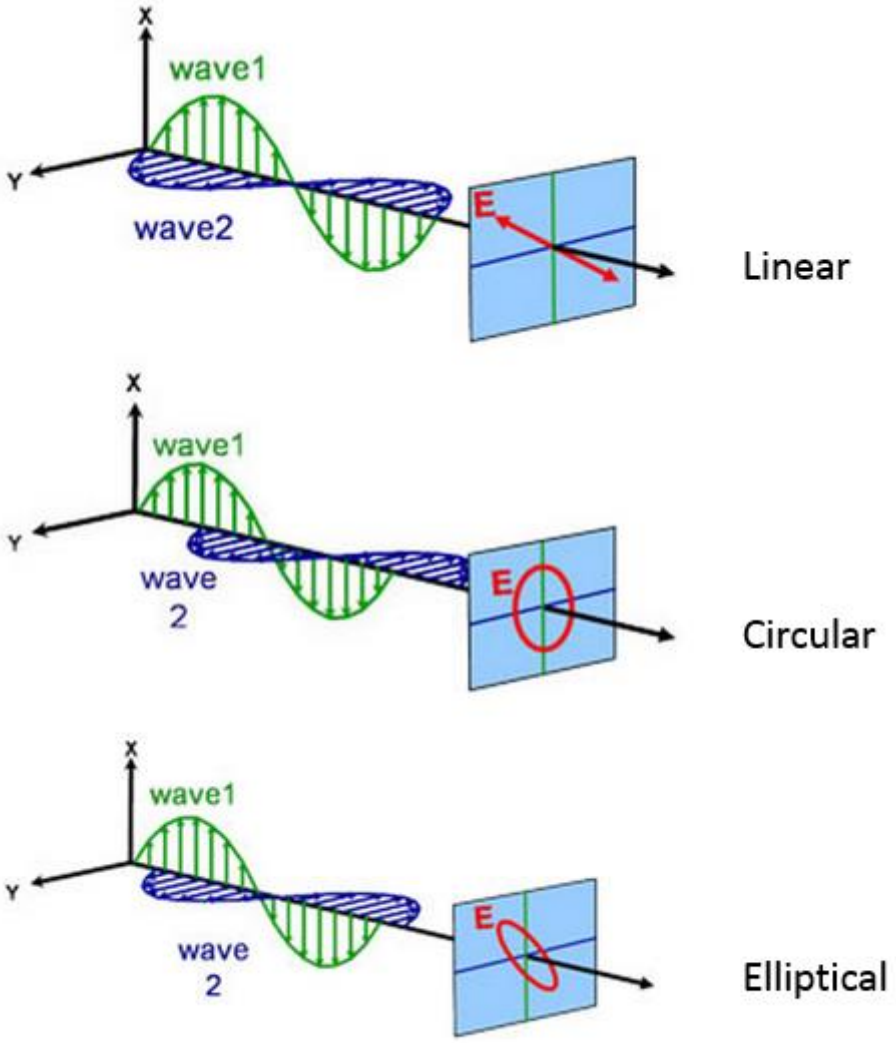

Figure 20: Superposition of two orthogonal waves. Taken from [61]

The refractive index of a material determines how light will interact with a material. It is represented by a complex number (Equation 13)

Equation 13: The complex refractive index consisting of the index and the extinction coefficient

$$\tilde{n} = n + ik$$

The index n is the ratio of the speed of light in a vacuum to the speed of light travelling within the medium. Light decrease in intensity when travelling within an absorbing material, the extinction coefficient k describes this loss and is related to the absorption coefficient α of a material by the relationship in Equation 14.

Equation 14: Relationship between absorption coefficient and extinction coefficient

$$\alpha = \frac{4\pi k}{\lambda}$$

Here λ is the wavelength of the travelling light. Snell's law gives the relationship between the angles of incidence and the angles of refraction for light at an interface of materials with differing refractive indices (Equation 15).

Equation 15: Snell's law

$$n_1 \sin \emptyset_1 \ = \ n_2 \sin \emptyset_2$$

Where $\emptyset_1$ and $\emptyset_2$ are the angles of incidence and refraction respectively. Also, n_1 and n_2 are the reactive indices of the mediums. Fresnel equations describe the amount of light reflected and transmitted at an interface (Equation 16).

Equation 16: Fresnel equations

$$r_s = \frac{n_1 \cos \emptyset_1 - n_2 \cos \emptyset_2}{n_1 \cos \emptyset_1 + n_2 \cos \emptyset_2}$$

$$t_s = \frac{2n_1 \cos \emptyset_1}{n_1 \cos \emptyset_1 + n_2 \cos \emptyset_2}$$

$$r_p = \frac{n_2 \cos \emptyset_1 - n_1 \cos \emptyset_2}{n_1 \cos \emptyset_2 + n_2 \cos \emptyset_1}$$

$$t_p = \frac{2n_1 \cos \emptyset_1}{n_1 \cos \emptyset_2 + n_2 \cos \emptyset_1}$$

Different polarisations (parallel and perpendicular to the plane of incidence, defined as p and s polarised light) will have different amounts of transmitted and reflected light intensities. In Equation 16,r_s, t_s,r_p, and t_p are the reflected and transmitted intensities for s and p polarised light respectively.

By using a polarizer to define the incident polarisation and a rotating analyser for detection; the relationship and differences between the polarisations can be measured. From these measurements and the equations above, the optical and thickness properties of the films can be derived.

2.5.6 Current-Voltage Measurements

The current-voltage curve of a solar cell is attained by sweeping a DC voltage across the cell, under a fixed illumination and measuring the current. A solar cell simulator with AM 1.5 (air mass 1.5) is the industry standard. Another measurement is taken without illumination to see the dark characteristics of the cell. The air mass coefficient take into account the attenuation of the light from the sun will experience as it passes through the earth's atmosphere at different angles.

From the I-V curve we can deduce:

1. The open circuit voltage at the x axis intercept.
2. The short circuit current at the y-axis intercept.
3. The fill factor
4. The cell efficiency

2.6 Literature Review

2.6.1 CIGSe

The current highest efficiency chalcogenide thin film solar cells are based on CIGSe ($CuIn_{0.7}Ga_{0.3}Se_2$) and its related compounds. In 1973, the first paper on CIGSe by Parkes et al. [62] was published in the Solid-State Electronics journal and interest has increased substantially with more than 1,500 papers published to date; with a peak in 2010 with over 200 papers published that year alone [63].

These semiconductors crystallize in the tetragonal chalcopyrite structure that is derived from the zinc-blende structure, in which each Se atom has two bonds to indium or gallium atoms and two bonds to copper atoms.

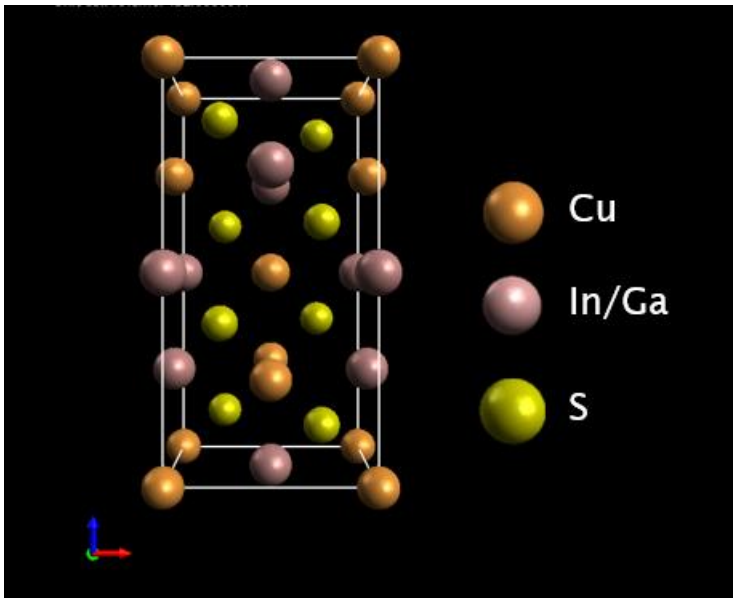

Figure 21: CIGSe chalcopyrite structure -tetragonal space group 122

The absorber is usually deposited using one of two methods as described in most recent literature, but work on new techniques is continually being developed. The first method is the co-evaporation of the individual metals in a selenium atmosphere; this process has produced the most efficient cells till now (with efficiencies exceeding 20% [64]).

Co-evaporation is complicated and precise control on the deposition of each metal is required. Films that are copper rich contain larger grains and a lower defect density, but contain many phases (are inhomogeneous). It has also been

found that copper or indium richness causes an increase in roughness in the films [65]. Control of the substrate temperature also appears to be very important in order to achieve the double-graded band gap structure which is present in the highest efficiency cells [66]. Other parameters that are important are the Ga/Ga + In and the Cu/Ga + In ratios which should be maintained between 0.35-0.37 and 0.86-0.88 respectively. Co-evaporation can take place in either a three-stage or a two-stage process. In the two-stage process, a copper rich layer is made and then the copper is decreased so that all the excess copper is consumed. The idea is to benefit from larger grains but to reduce the phases present. The three-stage process on the other hand starts with a Cu-poor layer, then a Cu-rich layer and then finally another Cu-poor layer; this process yields the highest efficiencies [67]. The temperature profile of the substrate is optimised to achieve the required absorber material properties.

The other main deposition technique for the absorber is a two-stage process where the metals are co-sputtered and then reactively annealed to form the chalcogenide material. Different methods and recipes exist for annealing CIGSe, for example Nakada et. al [68] post annealed at 550 ℃ in a 5 % H_2S-Argon mixture for up to 6 hours. Ohashi et. al [69] annealed in sulphur vapour at 580 ℃; both methods forming a CIGSSe material and changing the band gap with the incorporation of sulphur in the selenide material. Other variations include rapid thermal annealing [70] and annealing in toxic gases [71].

Other work on the deposition of the material has been done by Shi et al [65] to deposit the materials from a single quaternary sputtering target. Efficiencies of 7-8 % were achieved without anti-reflective coatings. Non-vacuum methods have also become of interest, to move away from the cost associated with vacuum technology. With efficiencies above 14% achieved so far, these may be possible alternatives [72]. Further work has been done to understand the crystallisation and phases in the films. This included the work done by Baek et al. [73]; where the phase evolution of the CIGSe compound was analysed by direct melting (sealing the materials in a quartz ampoule under vacuum and melting at different temperatures).

Cells are conventionally fabricated on soda lime glass substrates; but there have been many attempts to fabricate thin films on other substrates such as metal foils, ceramic sheets or insulating films (e.g. Kapton™). The substrates need to

satisfy certain requirements of vacuum compatibility, thermal stability, suitable thermal expansion coefficients, chemical inertness, humidity resistance, surface smoothness, cost, availability and weight. The advantages of using other materials are that they can be lighter, have better radiation hardness (ideal for space use) and can be adapted in an easier fashion to roll-to-roll deposition techniques to reduce solar cell manufacturing costs [18]. High efficiency flexible CIGSe solar cells with efficiencies similar to those fabricated on soda lime glass substrates have been achieved by developing a novel sodium incorporation technique and a 17.7 % efficient cell has been fabricated using a zirconia sheet [74] and cells with efficiencies of 17.4%, 17.7%, 14.7% on stainless steel, titanium and polyimide substrates, respectively. The presence of sodium has shown to improve the performance of cells, with a much larger improvement in cells with smaller grains [75]. Therefore the use of substrates that do not contain sodium, which can diffuse through the Mo layer to the absorber, requires the incorporation of sodium in another way [76].

Sodium seems to increase the hole carrier density, increasing the conductivity and improving the open circuit voltage, fill factor and cell efficiency. The actual mechanism of improvement is still debated upon but the literature mainly argues that Na affects the defect densities. This can be by (1) eliminating the In_{Cu} antisite (2) the formation of Na_{In} defects (3) the neutralisation of Se vacancies with oxygen which happens more readily in the presence of sodium (4) the passivation of grain boundaries. The Ga gradient in the three stage process is also found to be steeper with Na doping, which implies that the sodium inhibits elemental diffusion during absorber growth.

The basic structure of a CIGSe solar cell includes a bottom electrode (usually molybdenum), the CIGSe absorber layer, a buffer n-type layer to form the p-n junction, sometimes a window layer and a front contact (which consists of a transparent conducting oxide and a metal grid). These obviously vary by manufacturer but the basic structure remains [74].

For the back contact Mo is normally used, this is because it can be easily sputtered (usually but sometimes evaporated) under different conditions to achieve the properties required to optimise a cell, it is stable at the processing temperatures and it has low contact resistance with CIGSe. This low contact resistance is formed due to the presence of MoSe in between the layers. This

was shown by Bremaud et al. [77] to be so important that ohmic contacts could be made to other metals just by depositing $MoSe_2$ on top of them before CIGSe growth, so that cells with efficiencies similar to those having Mo as the back contact can be achieved [77]. In order to improve the Mo layer adhesion to the substrates, a study was carried out by Assmann et al. [78] in which it was shown that the Mo is under tensile stress and adheres well to the glass when deposited at high argon pressures but will have a high resistivity. On the other hand, films sputtered at low argon pressures are under compressive stress and will have a low resistivity, but will not adhere well to the surface. To gain the best of both worlds, it was shown at the NREL (National Renewable Energy Laboratory) [79] that adhesive films with high conductivity can be achieved by varying the argon pressure in two steps, initially having high argon pressures to grow high resistance adhesive films followed by a low pressure step to achieve a low resistance.

The most common buffer layer is cadmium sulphide deposited by chemical bath deposition with an intrinsic ZnO layer on top; although in some studies the ZnO is doped with boron or aluminum to decrease the resistance of the layer to improve the device. Cadmium-free alternatives are now becoming attractive due to toxicity concerns and some manufacturers (Showa, Shell and Honda) are producing commercial cells without the CdS layer. In addition, the CdS buffer layer has been argued to reduce the quantum efficiency at short wavelengths due to optical absorption losses. Nakada et al. [30-32, 66] has carried out a lot of work in this field, and has produced cells utilising ZnS (O, OH)/CIGSe with efficiencies above 17.5 %. Other materials used are InS (O,OH), InS, In(OH), SnO, ZnSe, ZnSe(OH), Zn(O,OH) and ZrO [30].The individual layers are deposited sequentially and to integrate the cells into modules; scribing processes are introduced between layers.

2.6.2 CZTS

Copper zinc tin sulfide (CZTS or Cu_2ZnSnS_4) is a promising chalcogenide material for photovoltaics. It is a variation of the CIS material where the indium is substituted by zinc and tin by equal amounts. It is found that the abundance of Zn and Sn in the earth's crust is 1500 times and 45 times greater than that of In; respectively, with In being almost two orders of magnitude more expensive than either of them [80]. Although the CIS (and variations) have higher efficiencies, the use of scarce and expensive raw materials has started a search for more abundant solar materials.

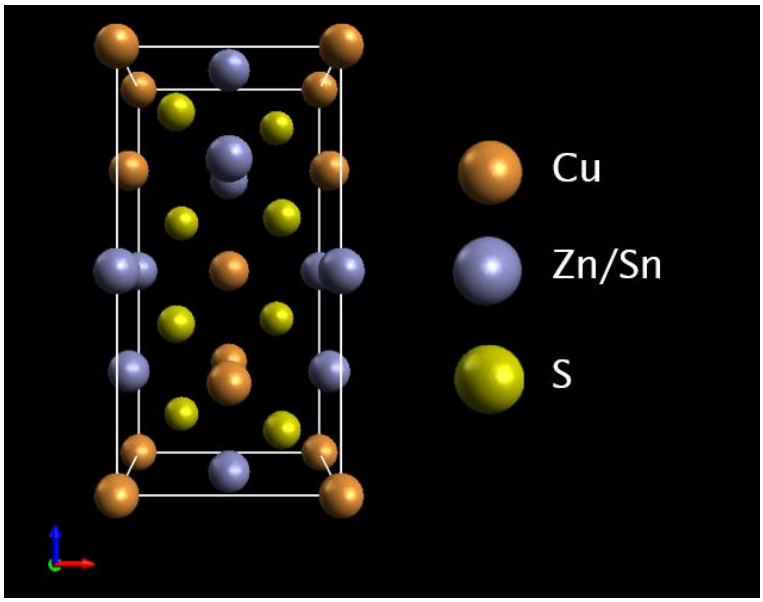

Figure 22: CZTS kesterite structure -tetragonal space group 121.

Cu_2ZnSnS_4 is a direct band gap material that uses abundant non-toxic elements; and with a band gap of around 1.5 eV and a large absorption coefficient, it stands as an ideal new photovoltaic material. Figure 23 compares the natural abundance of the raw materials and the prices for each. As can be seen clearly indium, selenium and tellurium are the most expensive (lower part of figure) and indium, cadmium, selenium and tellurium are the least abundant.

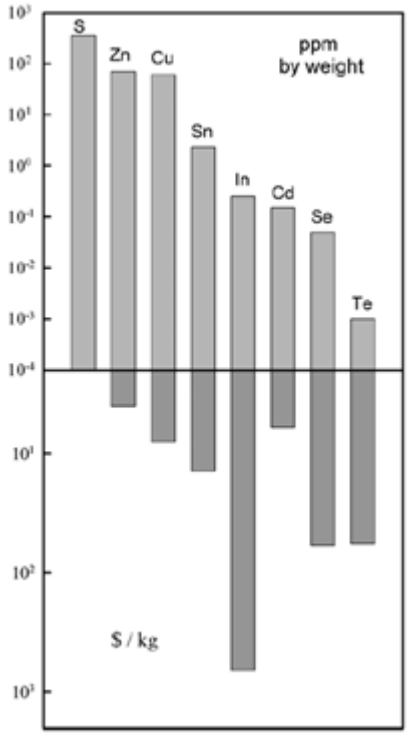

Figure 23: Natural abundance (upper part of figure) and 2007 prices of raw elemental materials (lower part of figure) for thin film PV [81]

The first paper to be published on this material used for photovoltaics was by Katagiri et al. in 1997 [81], although the material had been discovered years before this. But even after that first paper, research about CZTS did not really increase rapidly until the mid-2000's and with the greatest number published in 2011 [63]; the amount doubled that year from the year before, probably due to the abundance issues with the current highest efficiency thin film CIGSe devices.

The CZTS material forms the stannite or kesterite crystal structure, the latter more common due to it being more thermodynamically stable. The band gap can be tuned by substituting the sulphur with selenium, which reduces the band gap to around 1.0 eV with 100 percentage substitution. The investigation of the phase diagram of CZTS (Figure 24) shows that the single phase can only be formed in a very small region and the binary and ternary phases are much easier to make, which poses a significant challenge in fabricating this material [80].

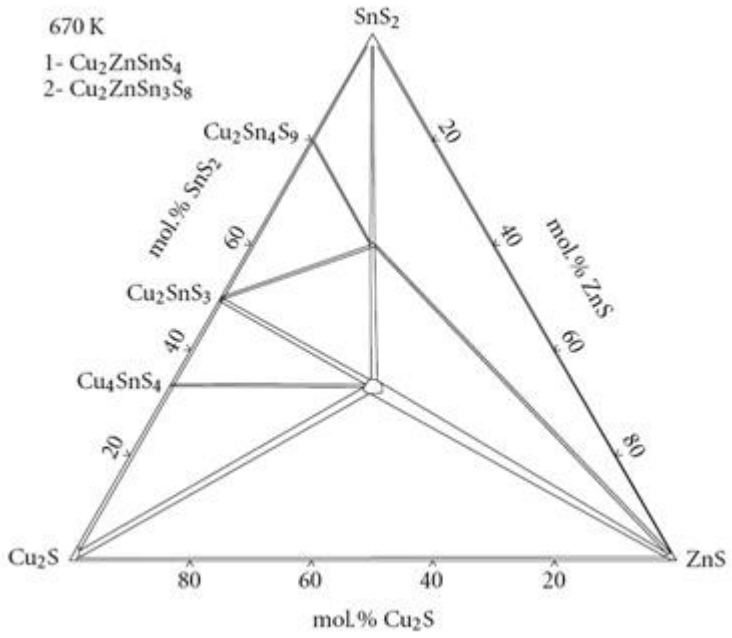

Figure 24: Phase diagram of SnS-Cu2S-ZnS solar cells adapted from [80]

Many techniques have been used to deposit CZTS over the past few years. One method used by Katagiri et al [82] was the vapor phase sulphurization of vacuum evaporated stacked metal layers (similar to the 2 stage process used in CIGSe).

Different stacking procedures were used: (1) Cu/Sn/ZnS (2) Sn/Cu/ZnS and (3) Five periods of Cu/SnS_2/ZnS which allowed the incorporation of more S in the film and better mixing of the precursors. Other stacks have been proposed such as that recently by Chalapathy et al. [83] where sputtered Cu/ZnSn/Cu layers were used. The significance of this work is the use of rapid processing to anneal the CZTS. Work done by the author on rapid processing of sputtered samples is shown in the experimental section, where unlike Chalapathy, no sulphur is utilized to successfully crystallize the CZTS and a single quaternary target is used to deposit the chalcogenide material [8]. A notable mention is the recent work by Leitao et al [84], where the rapid thermal annealing of multi-period precursors is used to fabricate CZTS. Other studies by Scragg et al. [85-87] used electroplating to make the stacked layers and then annealed them in a sulphur atmosphere. Liu et al. [88] used RF magnetron co-sputtering to make the films. Metal organic chemical vapor deposition has also been shown to produce these films recently by Ramasamy et al. [89].

Todorov et al. [90] (IBM) in 2010 using a slurry-based coating method which combined both solution processing and particle-based deposition fabricated cells with 9.6% efficiency. The only issue with the method was the use of hydrazine which requires an inert atmosphere, which may cause problems to deploy the technology on the industrial scale. Another paper has been published, using a less dangerous diluted hydrazine technique, which is more commercially acceptable [91]. Further work by the same authors have produced the current record efficiency cells at 12.6% [92]

The basic construction and module integration of the cells is similar to that of CIGSe, with Mo usually as the back contact, a CZTS absorber layer, a buffer n-type layer to form the p-n junction, sometimes a window layer and a front contact.

Defects play an important role in determining the electronic properties in semiconductors and are specifically important in CZTS because as mentioned before the CZTS only forms in a small region in the phase diagram. Even small deviations cause the formation of secondary and ternary phases. Calculations done by Asahi et al. [93] show that the most stable defect is the Cu_{Zn} defect, but the V_{Cu} defect is preferred for high efficiency cells [80].

In order to achieve cells with efficiencies as high as the CIGSe family a detailed understanding of these defects needs to be achieved. Another problem with the fabrication of CZTS is the loss of Sn as a result of the decomposition of CZTS and evaporation of SnS. Work done by Scragg et al. [94] suggests that the decomposition and evaporation of the Sn occurs after the loss of sulfur from the film and the formation of binary compounds. Sn (IV) seems to be instable and readily reduces, and with the volatility of SnS, an important problem is realized. To reduce this problem, Redinger et al. [95] shows in a study that annealing in S and SnS vapor reduces or eliminates the decomposition, yielding better films. Due to the importance of film quality on the device performance, controlling the annealing conditions for CZTS is of extreme importance.

Furthermore, another important phenomena and difference with CIGSe (the first is that CIGSe does not have material instabilities like the Sn above) is that unlike CIGSe (and its material variations) due to the defect chemistry of CZTS, it does not form n-type materials. In CIGSe at the junction, Cd can diffuse into the

material, making the junction embedded into the structure and forming a homojunction. This is not possible due to the strong preference of CZTS to form the p-type defect CuZn mentioned previously. Device simulation has indicated that a conduction band offset of 0-0.4 eV produces the best efficiencies, with obviously the lower the better [96]. Nagoya et al [96] have studied the band offsets from first principle calculations and has calculated (1) the band offset for CdS is 0.2 eV; which is this small due to the band narrowing which results from the lattice mismatch. (2) ZnS forms an offset above 0.9 eV which shows that the ZnS is an inactive high resistance insulator which will only compete with the CZTS phase. Finally a study by Haight et al [97] shows that by increasing the Se content, the CdS offset increases. But even for 100 % selenium substitution by sulfur, the CdS conduction band remains above that of CZTS.

2.6.3 GLS

Gallium lanthanum sulphide (GLS) [49] is a chalcogenide material which was first reported by Loireaulozach et al. in 1976 [98]. In the amorphous phase it is a semiconductor with a band-gap of 2.6 eV. GLS has many useful properties. Initially the low phonon energy of these glasses attracted significant interest as a host for near- and mid-infrared emitters with applications in telecommunications and sensing. In addition, its large nonlinear refractive index has also led to investigation of active waveguides, switches and routers. The relative elemental ratios can be varied to achieve ideal properties, and it has been possible to draw the glass into optical fibres. GLS has also been proposed as a rare earth host [99] for optical amplification devices; the reason for this is that because of the small phonon energies, the decay rates are small, meaning that dopants have longer excited state lifetimes. It is also has a higher solublity for rare earth ions than other sulphide glasses such as GeS [99]. GLS materials are known to be stable in both their crystalline and amorphous phases. It has been demonstrated as a photoactive medium for plasmonic switching applications [100, 101].

The structure of the glass consists of Ga-S bonds, with a length of 2.26 Å, and La-S bonds of length 2.93 Å [49, 102]. It has also been reported that the Ga-S distances in the amorphous state are identical to those in the crystalline state. It has a bulk glass transition temperature of 520 ℃ and a crystallisation

temperature of 730 ℃ [49]. The crystallisation of GLS has been studied by Ruihua Li et al. [99] and Morgan et al. [103]. These studies (and previous works) have shown that (1) GLS requires a certain amount of oxygen for stability (2) GLS has a complex phase diagram (3) sulphide and halide additives can be incorporated easily if sufficient oxygen is present (4) too much oxygen shortens rare earth lifetimes and so a compromise needs to be found.

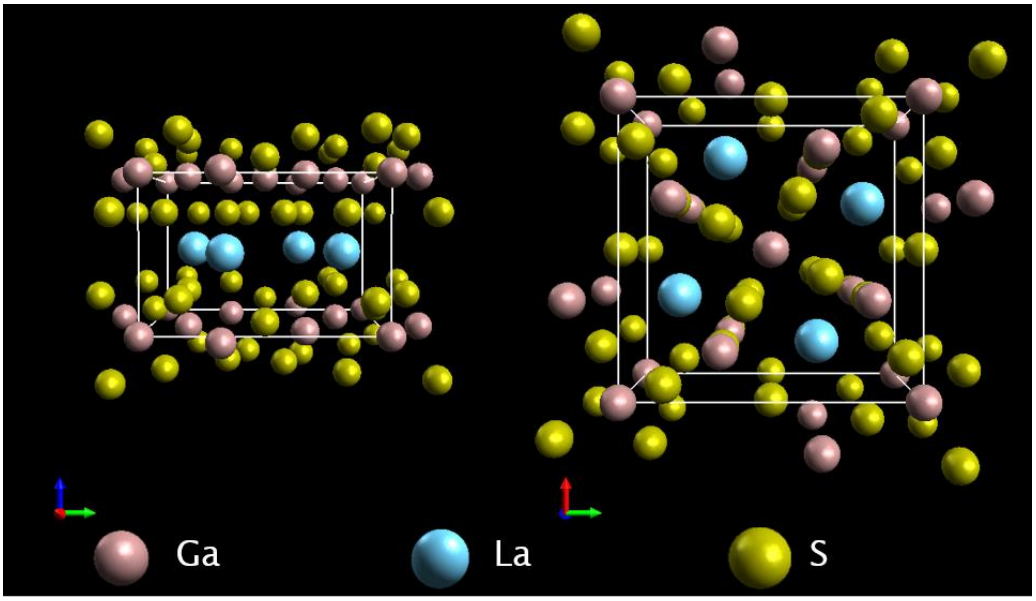

Figure 25: GLS melilite structure – tetragonal space group 113.

Further structure work has been done by Asaly et al.[104] and Benazeth et al.[105], and the work has showed that (1) the gallium and sulphur environment is such that 2 out of 3 sulphur atoms are bonded to 3 gallium atoms, with the remaining sulphur linked to 2 gallium atoms. (2) The 2 sulphur atoms that are linked to 3 gallium atoms each have 2 covalent bonds and one dative bond (covalent bond where both electrons are from the sulphur). (3) The addition of La_2S_3 adds an additional S ion; this causes the dative bond to break and produces a Ga_2S_4 environment and a negative site for the La cation. (4) Both Ga-Ga and S-S bonds occur in GLS thin films, but the La remains only bonded to sulphur.

The properties and preparation of La_2O_3-Ga_2S_3 glass ceramics were investigated by Takebe et al.[106]. The near IR optical losses of GLS and GLSO were investigated by Petrovich et al.[107]. The thermal properties were investigated by Takebe et al.[108]. The refractive index dispersion has been studied by Yayama et al.[109]. Raman and IR studies of gallium sulphide glasses were done by Barnier et al.[110].

Cu doped GLS is a material first seen in a paper by Simpson et al in 2007 [111] where the film contained up to 66% copper and were demonstrated for phase change applications. No other literature was found on this material; but an investigation on the effect of Cu doping on the electrical and optical properties of the material could yield a new material for photovoltaic applications. It is expected that the addition of Cu would lower the band gap of the material to around the optimal for photovoltaic applications (~1.5eV), increases the optical absorption and improve the electrical conductivity.

2.6.4 $CuSbS_2$

Copper antimony sulphide ($CuSbS_2$) is a chalcogenide that was discovered in 1942 as a dark grey mineral in Morocco and Tunisia [112]. $CuSbS_2$ is a relatively new material with little research published but is expected to be interesting for environmentally amenable solar cells, as its constituents are nontoxic and are relatively abundant in the earth's crust. $CuSbS_2$ (CAS) thin films show p-type conductivity, a band gap of around 1.5 eV, which is ideal to achieve the highest solar-cell conversion efficiency, and a relatively high optical absorption in the visible light range. It also has a low crystallization temperature of 250 ℃, which allows easier synthesis for flexible solar cells [113-115].

Various techniques have been developed for the synthesis of $CuSbS_2$ [116, 117]. Huilan et al [118] in 1999 fabricated nanocrystals of $CuSbS_2$ by precipitation. Soliman et al. [119] investigated the structural and electronic properties of $CuSbTe_2$, $CuSbSe_2$ and $CuSbS_2$ prepared by thermal evaporation. All three formed an orthorhombic crystal structure. Kyono and Kimata [114] along with Razmara et al [120] investigated the crystal structures of both the $CuSbS_2$ and $CuBiS_2$ material structures, which form the chalcostibite and emplectite structures, respectively; it was concluded that a complete solid solution can be synthesised between them by substituting the Sb with Bi. The relationship and substitution of In with Sb was investigated by Korzun et al [121].

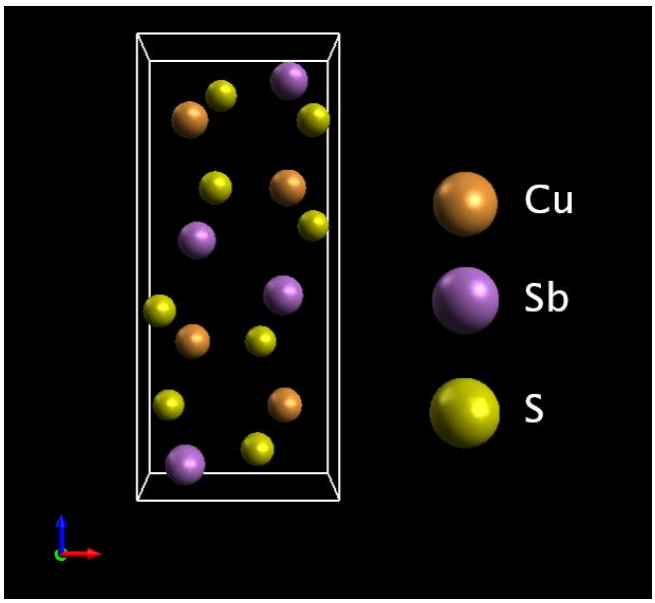

Figure 26: $CuSbS_2$ chalcostibite structure – orthorhombic space group 62.

In 2014, Ramasamy et al [122] produced films using the hot injection method [123] and produced, analysed and compared four different phases. These were $CuSbS_2$ (Chalcostibite), Cu_3SbS_4 (fematinite) [124], $Cu_{12}Sb_4S_{13}$ (tetrahedrite) and Cu_3SbS_3 (skinnerite). The latter two showing direct semiconductor behaviour. The theory predicts that the chalcostibite phase has a band gap of around 1.5 eV, here we see 1.1 eV, and this is probably caused by the irregular dimensions of the crystals along with the method of fabrication. Similarly, the formation of different phases can also be controlled if spray pyrolysis is used as the fabrication method, as shown by Popovici and Duta [117]. Ezugwu et al [125] fabricated the material using chemical bath deposition (CBD) and has suggested the use of the films in vehicle windscreens and mirrors to reduce the dazzling effect of light at night.

Deng et al. [126] doped the $CuSbS_3$ with potassium by direct melting in a fused silica ampoule, this produced an indirect semiconductor with a larger band gap of around 2.2 eV. Another doping study was carried out by Alieva et al where the material was doped with rare earth metals [127].

Rabhi et al performed several studies on $CuSbS_2$, including the effect of film thickness [128], effect of substrate temperature [129]; and the effects of vacuum [130] and air annealing [131]. It was seen that the thickness had no significant effect on the properties of the films. For vacuum annealing, amorphous films were formed when the annealing temperature was below 200℃ and higher

annealing temperatures caused the formation of polycrystalline high resistivity films (2 Ω cm) which is explained by the formation of antimony sulphide phases. The substrate temperature was varied from 100℃ to 200℃, it was observed that by increasing the temperature the band gap of the material decreased, and this is attributed to the formation of the more absorbent antimony phases. Finally air annealing caused the formation of antimony oxide phases. All the films in the studies consistently show p-type conductivity.

Colombara et al [132] fabricated the $CuSbS_2$ and $CuSbSe_2$ by the chalcognisation of Cu-Sb layers and was the first to suggest antimony instability in the films [133]. Garza et al [134] produced films by thermal diffusion of copper into Sb_2S_3. Rodriuez-Lazcano et al. [135] fabricated thin films by annealing stacked CuS/Sb_2S_3 layers in a nitrogen purged vacuum oven. The film were later used to produce some of the first CAS cells by using fluorine doped tin oxide as the window layer and CBD CdS as the n-type layer. [136]. The short circuit current density was around 0.2 mA/cm^2 and the open circuit voltage was 0.345 V.

The defect chemistry of $CuSbS_2$ was studied by Perniu et al [137] and it was suggested that by annealing the $CuSbS_2$ in a sulphur atmosphere the p-type conductivity of the material can be tailored, due to the reduction in sulphur vacancies causing less ionic conduction but improving the electronic conductivity. The defect chemistry was also studied more recently by Yang et al [138], it is shown by simulations that the dominant acceptors are copper vacancies (V_{Cu}). A hydrazine solution process was used to produce cells. The structure comprised of FTO coated glass with the chalcogenide, followed by CdS, ZnO, Al doped ZnO and gold contacts. The cells produced an efficiency of around 0.5%, a short circuit current density of 3.56 mA/cm^2 and an open circuit voltage of 0.44 V.

Although $CuSbS_2$ has mainly been studied as an absorber layer in thin film second generation cells, it has also been proposed as a material in solid state solar cells (incorporating both dense and porous TiO_2 layers)[139-141], as a thermoelectric material [142], as an electrode material in dye-sensitized solar cells [122, 143], as a two dimensional material [144] and as an electrode in lithium ion batteries [123]

Chapter 3: Copper Indium Gallium Di-Selenide Annealing Study

3.1 Methods

These experiments were done in two parts: firstly the furnace annealing of the CIGSe on different substrates, then the fabrication of CIGSe solar cells using the recipes from part 1.

3.1.1 Furnace annealing of CIGSe on titanium, borosilicate and soda lime glass:

First, 500 nm molybdenum samples were deposited on 6 borosilicate glass slides (50 mm by 50 mm in size) by RF magnetron sputtering at room temperature at a base pressure of 9.9×10^{-5} Torr. The deposition was performed using 160 W and an argon flow of 22 standard cubic centimetres (sccm); this gave a deposition rate of around 0.6 angstroms per second. During this Mo run, a CIGSe target was also mounted into the chamber, allowing for a sequential deposition without opening the chamber.

Next, 2,000 nm of CIGSe was deposited by RF magnetron sputtering at room temperature from a single quaternary target on the Mo coated substrates. The deposition was performed using 120 W and an argon flow of 30 sccm; this gave a deposition rate of around 0.67 angstroms per second.

To compare the deposition on other substrates, further substrates were prepared on titanium and soda-lime substrates. The soda lime had a 500 nm layer of Mo pre-deposited onto the substrates by another user and were provided by Dr Kevin Huang. The titanium substrates can act as a back electrode and therefore no molybdenum was deposited on these substrates.

2000 nm of CIGSe was deposited again by RF magnetron sputtering and target at a base pressure of 1.2×10^{-4} Torr. The deposition was performed using the same power and argon flow rate as the deposition above.

Figure 27 shows the initial layers put down on each substrate by sputtering. The use of titanium was noted in reference [18] as it has similar thermal expansion as the layers in a CIGSe solar cell, can act as a back connection and if thin enough (not in our case) may turn the cell into a flexible solar cell. Soda lime glass was the third substrate material and was chosen also because its thermal coefficient of expansion is closely matched to Mo and CIGSe.

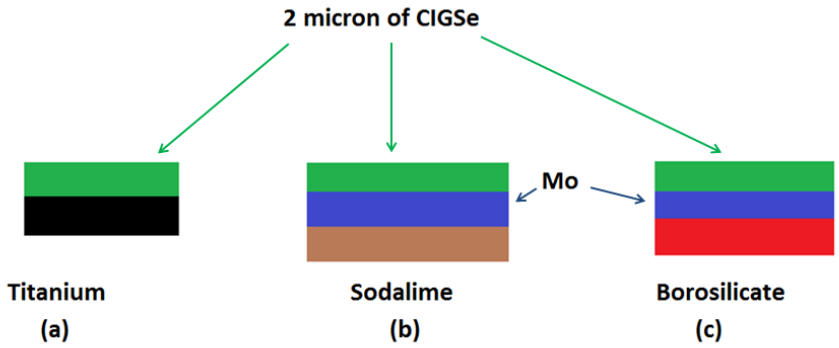

Figure 27: The depositions done on different substrates for CIGSe solar cells.

These films were annealed in an Elite™ three-zone tube furnace by Dr Kevin Huang. In the setup, selenium was evaporated at 400 ℃ in one zone in a quartz boat with argon flowing above in the direction of the substrates; the substrates were at a second and/or third zone held at the annealing temperatures. CIGSe on all three substrates were annealed at 500 ℃ for one hour and only soda lime and borosilicate substrates were annealed also at 550 ℃ for one hour. The ramp rate was 3 ℃/min.

The compositional and structural properties of the films were analysed using an energy dispersive X-ray system [145] and X-ray diffraction. SEM images (to observe grain growth from annealing) were taken by Dr Kevin Huang using an FEI Helios 600 FIB/SEM system.

3.1.2 The fabrication of CIGSe solar cells, using substrates from furnace annealing step above:

200 nm ZnS was deposited on various substrates: (1) Ti/CIGSe annealed at 500 ℃ (2) borosilicate/Mo/CIGSe annealed at 500 ℃ (3) soda lime/Mo/CIGSe annealed at 500 ℃ (4) soda lime/Mo/CIGSe annealed at 550 ℃ (5) two borosilicate slides at a base pressure of 9.7 x 10^{-5} Torr using the RF sputtering

system. The deposition was performed using a power of 45 W and an argon flow of 25 sccm; this gave a deposition rate of 0.18 angstroms per second.

The ZnS was then annealed in a Jipelec JetFirst 100 bench top rapid thermal processor using the following recipe to produce a thin oxide layer at the top of the films:

Table 1: ZnS annealing recipe

Duration (sec)	Initial Temp (°C)	Final Temp (°C)
60	0	20
180	20	20
600	20	200
600	200	200
600	200	20
180	20	20

370 nm aluminum doped zinc oxide was deposited on various substrates: (1) Ti/CIGSe annealed at 500 °C/ZnS, (2) borosilicate/Mo/CIGSe annealed at 500 °C/ZnS, (3) soda lime/Mo/CIGSe annealed at 500 °C/ZnS, (4) soda lime/Mo/CIGSe annealed at 550 °C/ZnS, (5) two borosilicate slides; at a base pressure of 5×10^{-5} Torr. The deposition was performed using 90 W and an argon flow of 15 sccm; this gave a deposition rate of 0.21 angstroms per second.

Aluminum top contacts were deposited by a BOC Edwards auto 500 system. The chamber was pumped to a base pressure of 7×10^{-6} Torr. A current between 55 and 95 mA, the current was started at 55 mA but was increased as the deposition progressed to keep the deposition rate at about 0.3 Å/s.

Figure 28, Figure 29 and Figure 30 show the final cell structures for the cells fabricated on borosilicate, titanium and soda lime respectively.

Figure 28: Cell structure for cells on float glass (borosilicate glass)

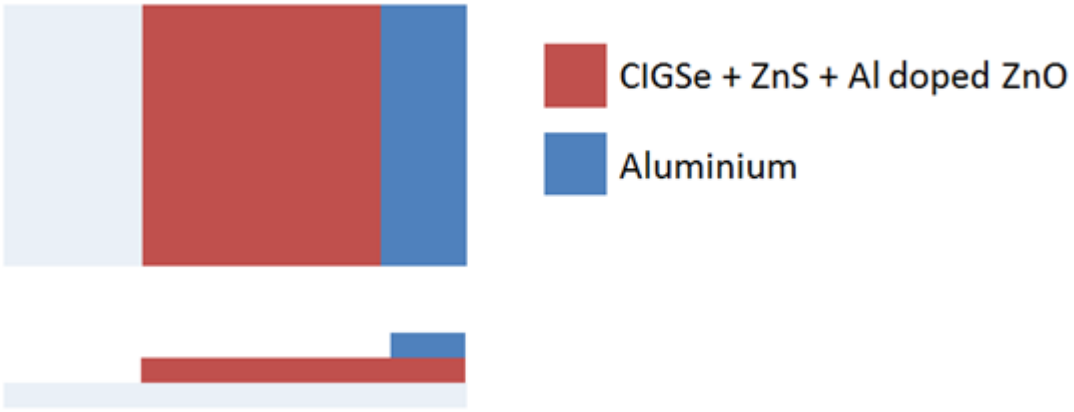

Figure 29: Cell structure for cells on titanium

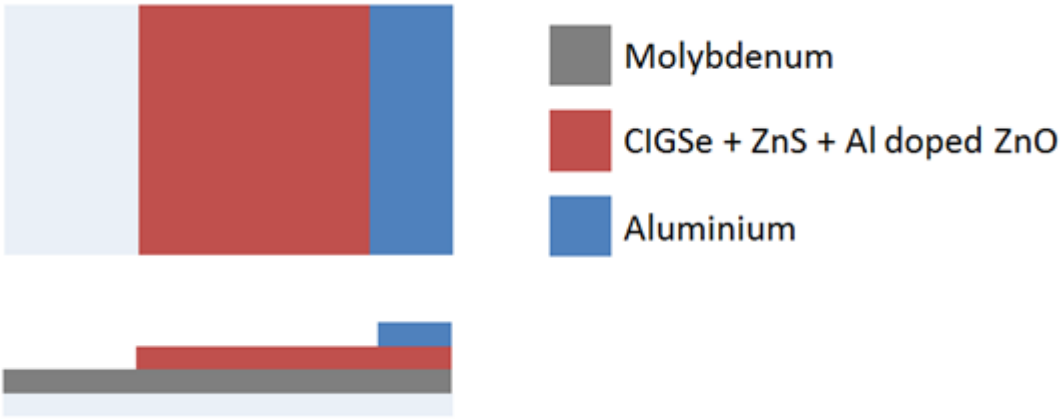

Figure 30: Cell structure for cells on soda lime glass

3.2 Results and Discussion

3.2.1 Furnace annealing of CIGSe on titanium, borosilicate and soda lime glass:

Figure 31 shows the composition of the CIGSe layer before and after the annealing in selenium. As can be seen the values change within the margin of error of the apparatus and so we can deduce that no noticeable selenium is lost. The expectation was that the sodium in the soda lime glass would diffuse into the CIGSe material, but this was not the case as no sodium was detected using the EDX. The layers on the borosilicate substrate started to peel off during the annealing and was observed on the films when taken out of the furnace.

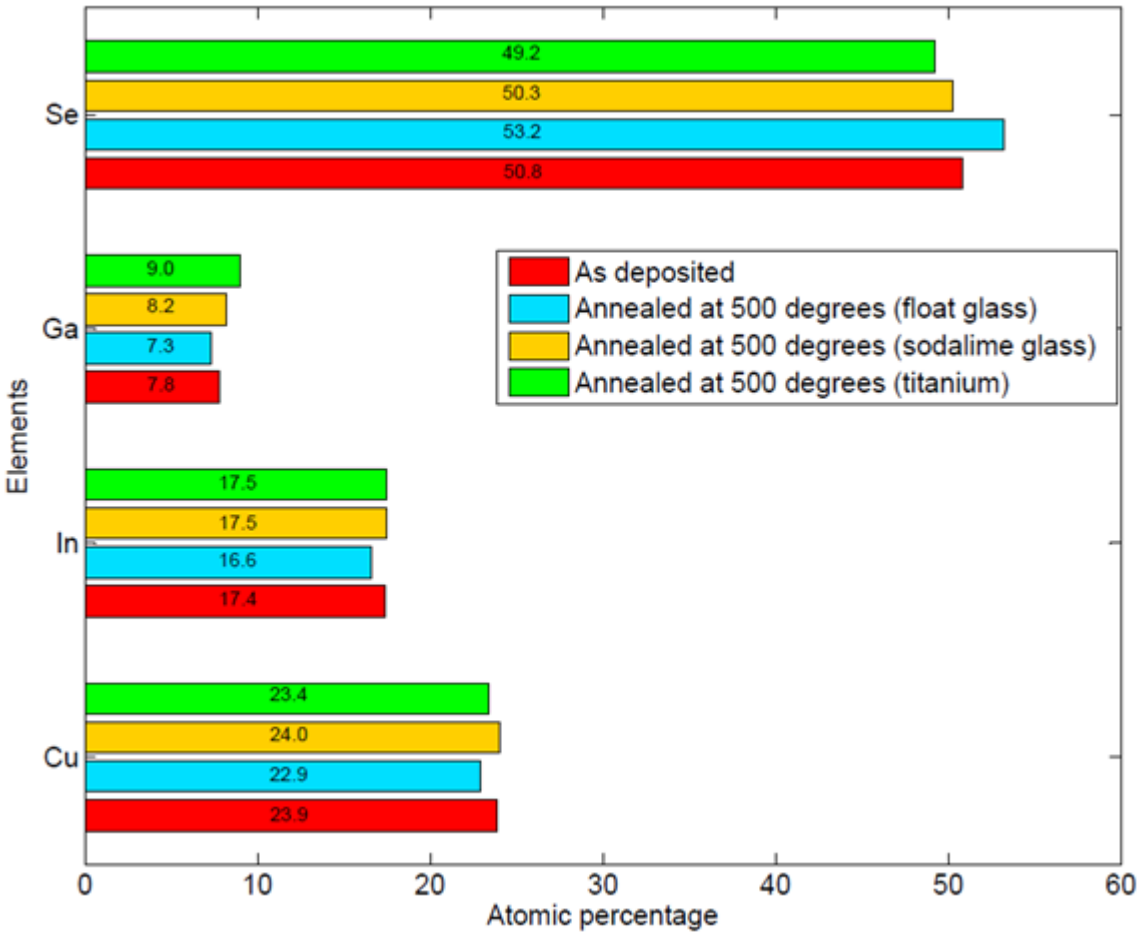

Figure 31: EDX compositional measurements before and after selenisation on all three substrates annealed at 500 ℃. The films were 2000 nm of CIGSe deposited at room temperature.

The XRD diffractograms were measured for each of the samples as shown in Figure 32 (for borosilicate), Figure 33 (for soda lime) and Figure 34 (for titanium). The PDF-4+ 2010 software was used to find the phases shown in the diffractograms; in each figure the phases along with the JCPDS file numbers are shown.

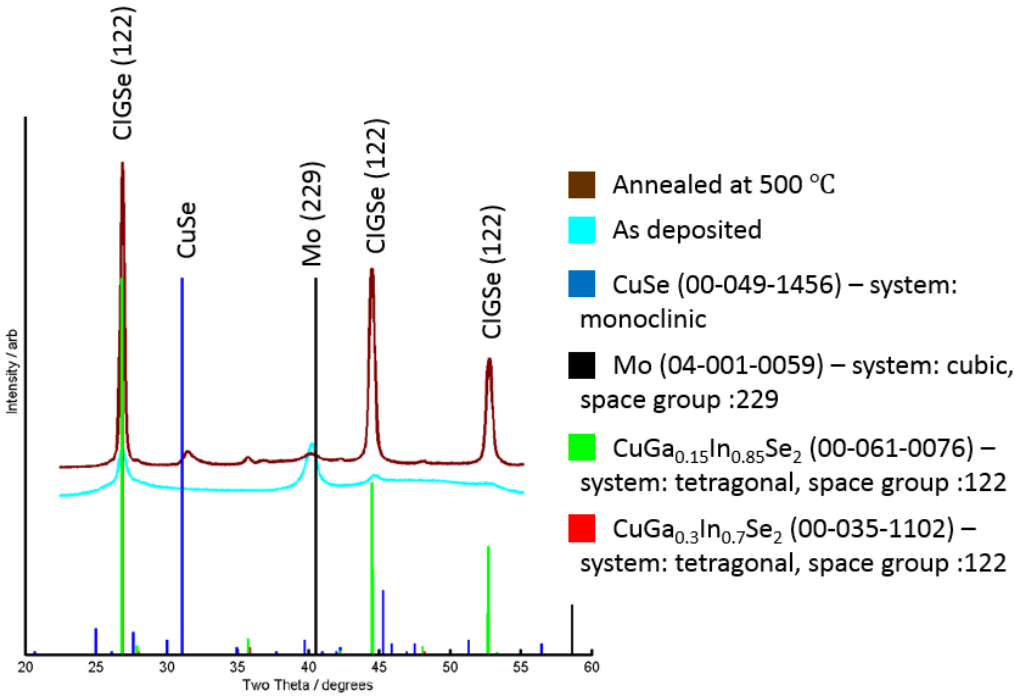

Figure 32: XRD diffractogram of samples with a borosilicate substrate and corresponding peak identification. The films were 2000 nm of CIGSe deposited at room temperature.

In Figure 32 above, the film on borosilicate annealed at 500℃ shows one CIGSe crystal structure (tetragonal - space group 122), along with a molybdenum peak and a CuSe peak as well. Ideally, the CIGSe produced in our procedure would be single phase.

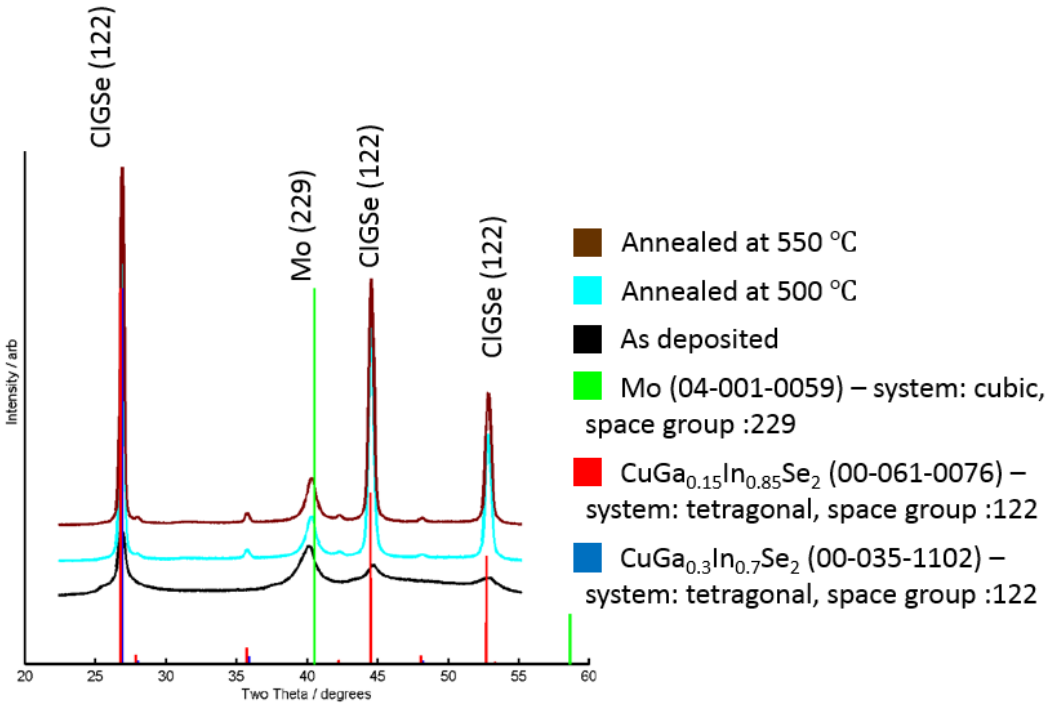

Figure 33: XRD diffractogram of samples with a soda lime substrate and corresponding peak identification. The films were 2000 nm of CIGSe deposited at room temperature.

Figure 33 shows the diffractogram for the sample on soda lime. The CIGSe phases are present along with Mo; here the CuSe is not seen in the diffractogram. This sample did not delaminate and this is probably because the thermal expansion on the soda lime is more closely matched to the CIGSe and molybdenum.

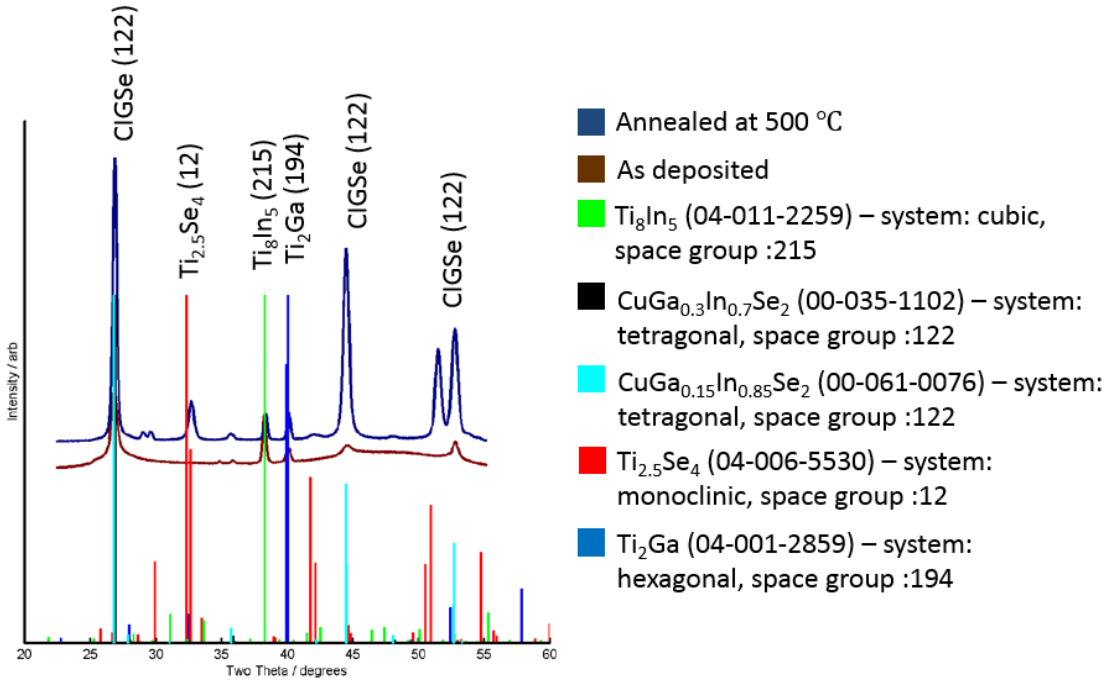

Figure 34: XRD diffractogram of samples with a Ti substrate and corresponding peak identification. The films were 2000 nm of CIGSe deposited at room temperature.

For the diffractogram for the sample on titanium (Figure 34), again the same CIGSe peaks are present. The CIGSe has also reacted with the titanium to form Ti_8In_5, $Ti_{2.5}Se_4$ and Ti_2Ga. Therefore we can deduce the molybdenum in this environment is much more inert and does not form any metallic alloys with the metals in the CIGSe and therefore, future work will need a layer of Mo between the Ti and the CIGSe. Regarding the two phases formed, this could be due to the high powers (120 W), used for sputtering. Lowering this power may produce a more uniform and homogeneous film.

SEM cross sectional images (Figure 35 and Figure 36) showed that the grain growth of the films was incomplete (ideally this would be as large as the film thickness to increase carrier mobility vertically through the cell). The grains have started to form but have not grown to the top of the film. Annealing at 550 °C produces larger grains, but still not large enough. In future work, higher temperatures or longer annealing times will be used.

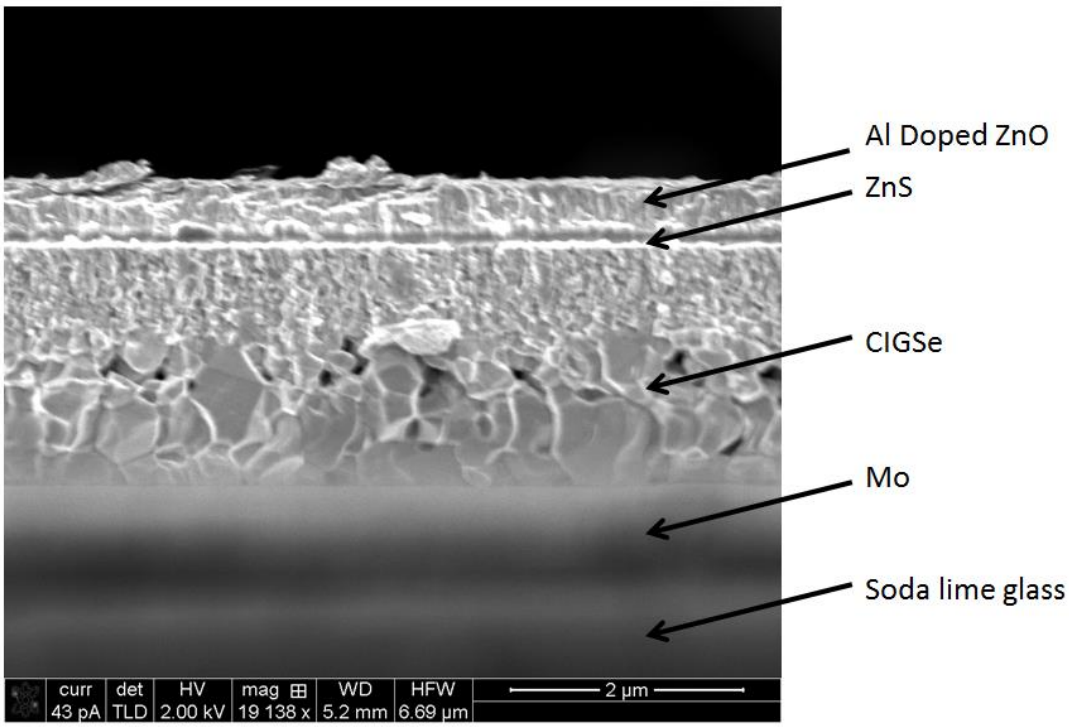

Figure 35: SEM cross section of CIGSe solar cell annealed in Se at 500 ℃ by Dr Kevin Huang. The films were 2000 nm of CIGSe deposited at room temperature.

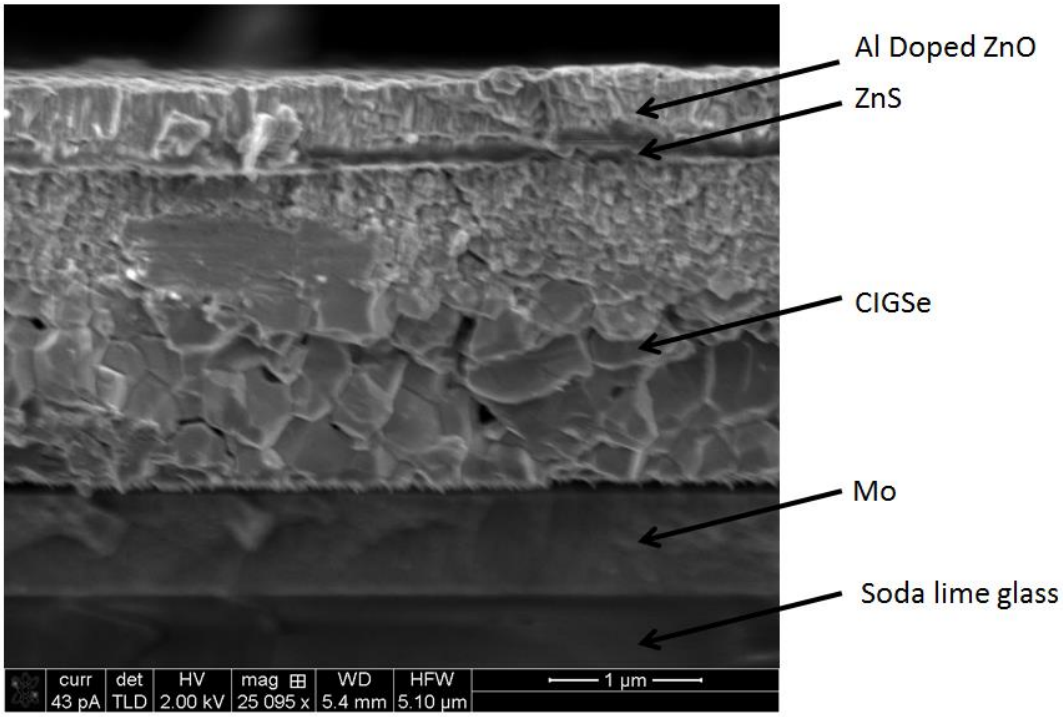

Figure 36: Cross section of CIGSe solar cell annealed in Se at 550 ℃ by Dr Kevin Huang using a FEI Helios 600 FIB/SEM system. The films were 2000 nm of CIGSe deposited at room temperature.

3.2.2 The fabrication of CIGSe solar cells, using substrates from furnace annealing step above

Unfortunately when attempting to characterise the I-V characteristics of the cells, the cells all showed short circuiting. This is probably because the cells were very large (> 1 cm^2), which means any short circuiting across the cell would short the whole cell. Another problem worth mentioning is that selenium had condensed onto the cells during the annealing process, this increased the series resistance of the cells, it also degraded the molybdenum contact on the cell, making it difficult to make ohmic contacts to the cell. Also, this selenium layer is probably non-uniform and the 200 nm of ZnS deposited on top, would have cracks and other shunting paths that would short circuit the device.

3.3 Conclusions

$CuIn_xGa_{(1-x)}Se_2$ thin films were first deposited by RF magnetron sputtering at room temperature from a single quaternary target on titanium substrates, molybdenum coated soda lime and molybdenum coated borosilicate substrates. The films were annealed in an Elite™ three-zone tube furnace at 500 and 550 degrees Celsius in a selenium rich atmosphere. The compositional and structural properties of the films were analysed using EDX and XRD, respectively. The grain sizes were measured by SEM imaging. The EDX showed a composition close to the required stoichiometry and so depositing from a single target is a possible approach to making these cells. The XRD for the films on borosilicate show a CuSe secondary phase, this disappears at 550 ℃ (shown in the film deposited on soda lime glass) and therefore it reacts at higher temperatures.

Cells were fabricated, but all showed short circuiting. Improvements can be done by designing smaller cells. The annealing carried out using selenium vapour which caused the formation of a thin layer of selenium on the top of the absorber layer which would increase the resistance greatly. An investigation of the etching of Se (without damaging the CIGSe) would be a possible step forward. The annealing should be carried out in a way that ensures homogeneous uniform films are produced with minimal roughness and minimal degradation of the contacts. A possible route is the scribing of the absorber to expose the contacts to the film, after annealing. This way the bottom contact is not damaged by the Se annealing or by the following etching.

Chapter 4: Copper Zinc Tin Sulphide Annealing Study

This work has contributed to the following:

AL-SAAB, F., GHOLIPOUR, B., HUANG, C. C., ANASTASOPOULOS, A., HAYDEN, B. & HEWAK, D. W. 2012. Crystallization Study of the Cu_2ZnSnS_4 Chalcogenide Material for Solar Applications. PV-SAT 8. Northumbria University, Newcastle upon Tyne.

4.1 Methods

These experiments were done in two parts:

4.1.1 Rapid thermal annealing of CZTS:

500 nm molybdenum samples were deposited on 8 borosilicate glass slides (50 mm by 50 mm in size) by RF magnetron sputtering at a base pressure of 1.2 x 10^{-4} Torr. The deposition was performed using 60 W and an argon flow of 22 standard cubic centimetres (sccm); this gave a deposition rate of around 0.15 angstroms per second. Photolithography was used to pattern the substrates for the CZTS depositions.

2,000 nm of CZTS was deposited by RF magnetron sputtering at room temperature from a single quaternary target on the Mo coated substrates at a base pressure of 1.2 x 10^{-4} Torr. The deposition was performed using 100 W and an argon flow of 30 sccm; this gave a deposition rate of around 0.09 angstroms per second. Following the deposition the photoresist was lifted off by soaking in acetone for around 15 min, rinsed with deionised water and then dried in glass dryer for 30 min.

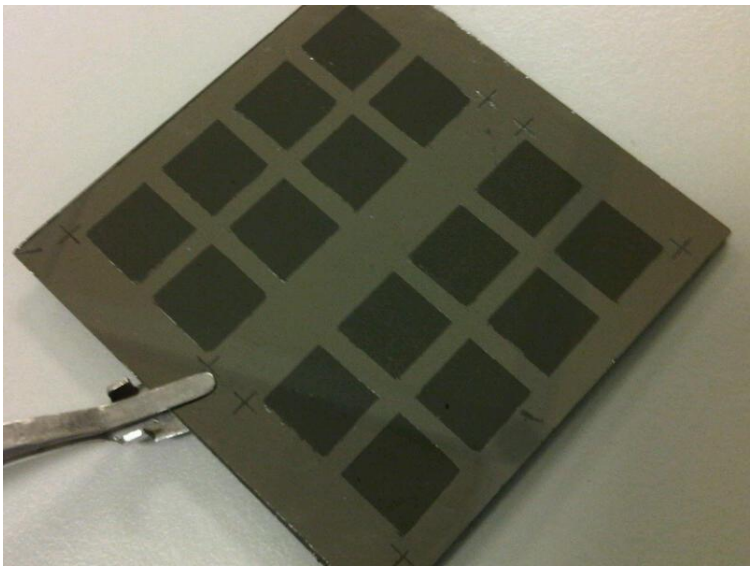

Figure 37: Image of CZTS squares on Mo after photoresist lift-of, rinsing and drying

The CZTS was then annealed in a Jipelec JetFirst 100 bench top rapid thermal processor using the following recipe:

Table 2: CZTS annealing recipe

Duration (sec)	Argon (sccm)	Initial Temp. ()	Final Temp ()
60	100	0	20
180	200	20	20
Ramp time	100	20	Annealing temperature
Duration	100	Annealing temperature	Annealing temperature
Ramp time	100	Annealing temperature	20
180	100	20	20

The ramp time, annealing temperature and annealing duration were varied according to the following table:

Table 3: Ramp times, annealing temperatures and annealing durations for CZTS

Run	Ramp time (min)	Annealing temperature (℃)	Duration (min)
1	1	540	2
2	1	520	2
3	0.5	520	2
4	1	520	5
5	1	500	5
6	1	500	10
7	1	500	20
8	1	480	20
9	1	480	40

The aim of the experiment was to achieve the fastest ramp rate and highest temperature without damaging the films. Following the starting recipe which was chosen based on annealing temperature from a paper published by Todorov et al [146] where the CZTS is annealed at 540 ℃ on a hot plate for 5 min.

The compositional and structural properties of the films were analysed using an energy dispersive X-ray system and an X-ray diffraction system. SEM images (to observe grain growth from annealing) were taken using a FEI Helios 600 FIB/SEM system.

4.1.2 The fabrication of CZTS solar cells:

500 nm molybdenum films were deposited on 10 soda lime glass slides (40 mm by 40 mm in size) by RF magnetron sputtering at room temperature at a base pressure of 6.5 x 10^{-5} Torr. The deposition was performed using 60 W and an argon flow of 22 standard cubic centimetres (sccm); this gave a deposition rate of around 0.22 angstroms per second.

Photolithography was used to pattern the substrates for the CZTS depositions. No hard baking was used here, to ensure all the photoresist was removed.

1000 nm of CZTS was deposited by RF magnetron sputtering at room temperature from a single quaternary target on the Mo coated substrates at a base pressure of 1.0 x 10^{-4} Torr. The deposition was performed using 100 W and an argon flow of 30 sccm; this gave a deposition rate of around 0.16 angstroms per second. Following the deposition the photoresist was lifted off by soaking in acetone for around 15 min, rinsed with deionised water and then dried in glass dryer for 30 min.

The CZTS was then annealed in a Jipelec JetFirst 100, using the following five recipes from the annealing study above (because these recipes produced undamaged films after annealing – see results section):

Table 4: CZTS annealing recipes used for cell fabrication

Run	Ramp time (min)	Annealing Temperature (°C)	Duration (min)
1	1	520	2
2	1	500	5
3	1	500	10
4	1	480	20
5	1	480	40

Photolithography was used to pattern the substrates for the ZnS and Al: ZnO (2% aluminum doped zinc oxide) depositions. The resist was spun with the following settings: 5 min ramp, 5000 rpm for 60 seconds. A faster speed was used to make a thinner photoresist.

120 nm of ZnS was deposited by RF magnetron sputtering at room temperature on the substrates at a base pressure of 2.0 x 10^{-5} Torr. The deposition was performed using 60 W and an argon flow of 25 sccm; this gave a deposition rate of around 0.14 angstroms per second. During this run, an Al doped ZnO target was also mounted into the chamber, allowing for a sequential deposition without opening the chamber.

400 nm aluminum doped zinc oxide was deposited on the substrates, at a base pressure of 1.3 x 10^{-4} Torr. The deposition was performed using 70 W and an

argon flow of 25 sccm; this gave a deposition rate of 0.15 angstroms per second. Following the deposition the photoresist was lifted off by soaking in acetone for around 15 min, rinsed with deionised water and then dried in glass dryer for 30 min.

Photolithography was used to pattern the substrates for the aluminum top contact depositions. The resist was spun with the following settings: 5 min ramp, 5000 rpm for 60 seconds.

Aluminum top contacts were deposited by a BOC Edwards auto 500 system. The chamber was pumped to a base pressure of 6.0×10^{-6} Torr. A current of 45 mA was used, this gave a deposition rate of about 0.3 Å/s.

Finally, 100 nm of magnesium fluoride was deposited on the substrates, at a base pressure of 1.0×10^{-5} Torr. The deposition was performed using 60 W and an argon flow of 15 sccm; this gave a deposition rate of 0.05 angstroms per second. Following the deposition the photoresist was lifted off by soaking in acetone for around 15 min, rinsed with deionised water and then dried in glass dryer for 30 min.

The 3D schematic of the cells is shown in Figure 38 and the top view of this in Figure 39.

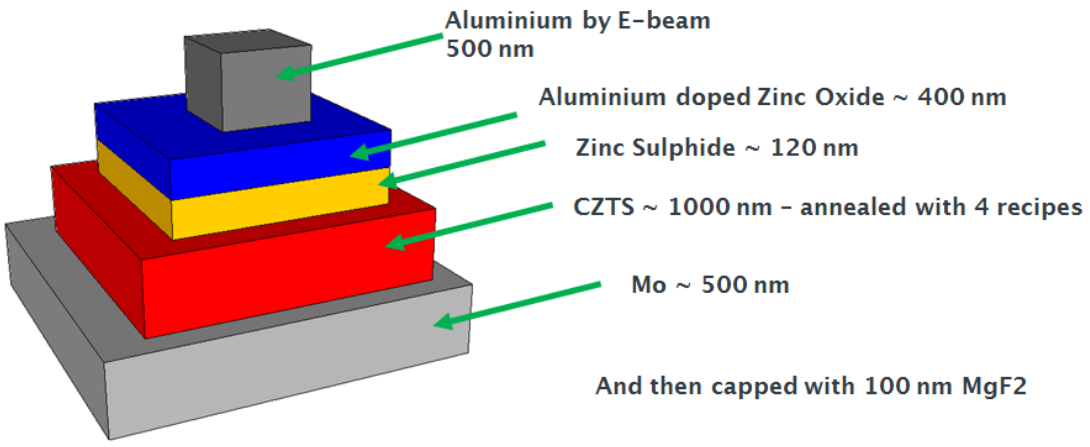

Figure 38: 3D schematic of cell design drawn using Google SketchUp [147]

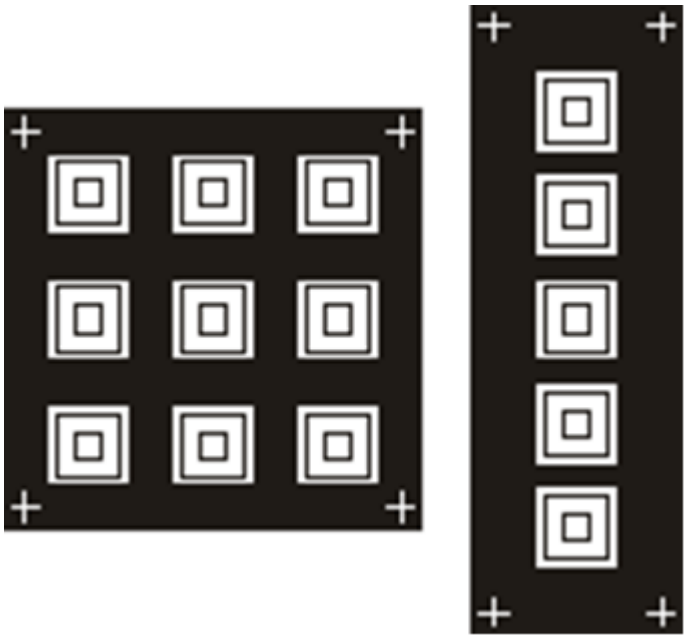

Figure 39: Top view of cell design shown schematically in Figure 38

4.2 Results and Discussion

4.2.1 Rapid thermal annealing of CZTS:

The recipes that showed no flaking or peeling are highlighted in blue in Table 5 below.

Table 5: CZTS annealing recipe results. The films were 2000 nm of CZTS deposited at room temperature.

Temp (℃)	Ramp Time (min)	Dwell at T.(min)	Comments	Characterisation
540	1	2	Flakes – probably caused by the softening of the substrate	no need
520	1	2	Film intact – Mo sulphide probably formed – change in colour - redone to confirm repeatability	EDX - first run; XRD - Both runs
520	0.5	2	Flakes – probably thermal expansion mismatch	no need
520	1	5	Flakes – Mo starts to peel off. Mo sulphide probably evaporates and SnS evaporates	no need
500	1	5	Film intact – Mo sulphide probably formed – change in colour	XRD + EDX
500	1	10	Film intact – Mo sulphide probably formed – change in colour	XRD + EDX
500	1	20	Mo removed	

480	1	20	Film intact – Mo sulphide probably formed – change in colour	XRD + EDX - CZTS ; XRD + EDX - Mo
480	1	40	Film intact – Mo sulphide probably formed – change in colour	XRD + EDX

The materials produced by these five recipes were then characterized by EDX (shown in Figure 40 below). The samples showed a composition very close to the 2:1:1:4 ratio, with around 25 % copper, 12.5 % zinc, 12.5% tin and 50 % sulphur. No recipe shows a large change in composition although the sample annealed for 40 min at 480℃ shows a small sulphur loss. A common problem is the CZTS decomposing to form SnS, which then evaporates. This is not seen here as no tin loss is observed. A change in colour was observed in most films which was probably due to the formation of a very thin layer of molybdenum sulphide. But, as no significant loss in sulphur was observed in the films, we can deduce only a small amount of sulphur evaporated and reacted with the molybdenum. If this is the case, it is assumed the molybdenum sulphide has also formed between the Mo and the CZTS which has been known to improve the performance of the junction [77, 78].

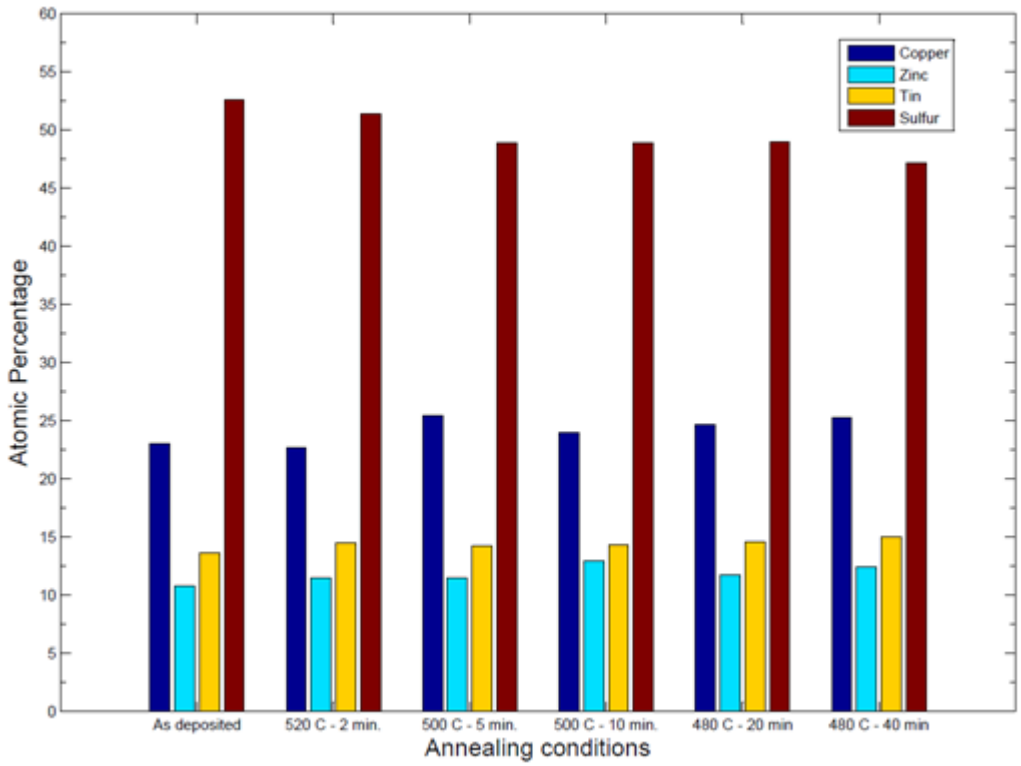

Figure 40: EDX of all working recipes that showed no flaking or peeling from Table 5. The films were 2000 nm of CZTS deposited at room temperature.

The X-ray diffractogram for the as deposited film is shown in Figure 41 below. The kesterite tetragonal CZTS phase is present along with the cubic Mo phase.

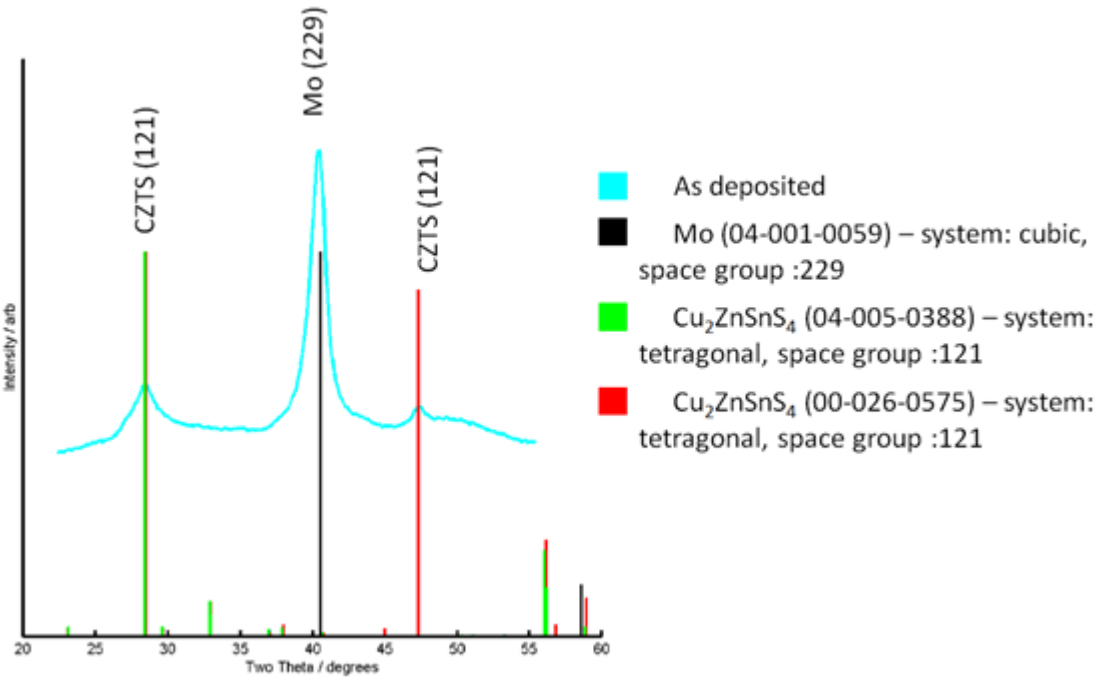

Figure 41: XRD of as deposited CZTS films before annealing. The films were 2000 nm of CZTS deposited at room temperature.

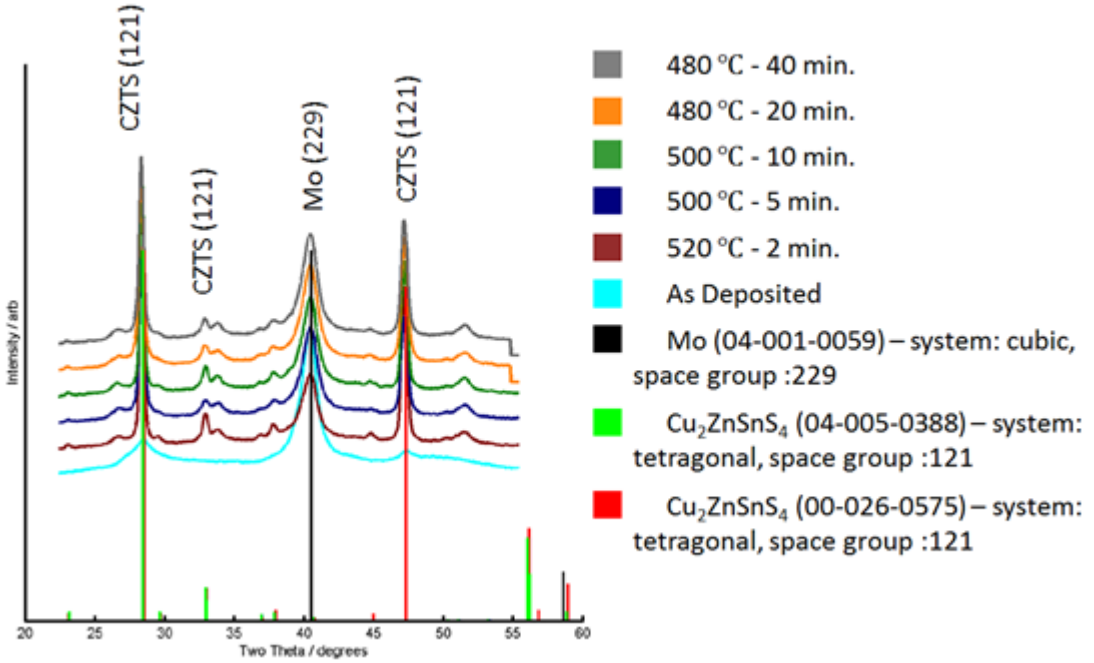

Figure 42: XRD of all films that showed no flaking or peeling from Table 5. The films were 2000 nm of CZTS deposited at room temperature.

The X-ray diffractograms for the samples annealed for all the working recipes are shown in Figure 42 above. The samples all show similar diffractograms with identical peaks. The XRD for the sample annealed at 480 ℃ for 20 minutes is shown in Figure 43 below:

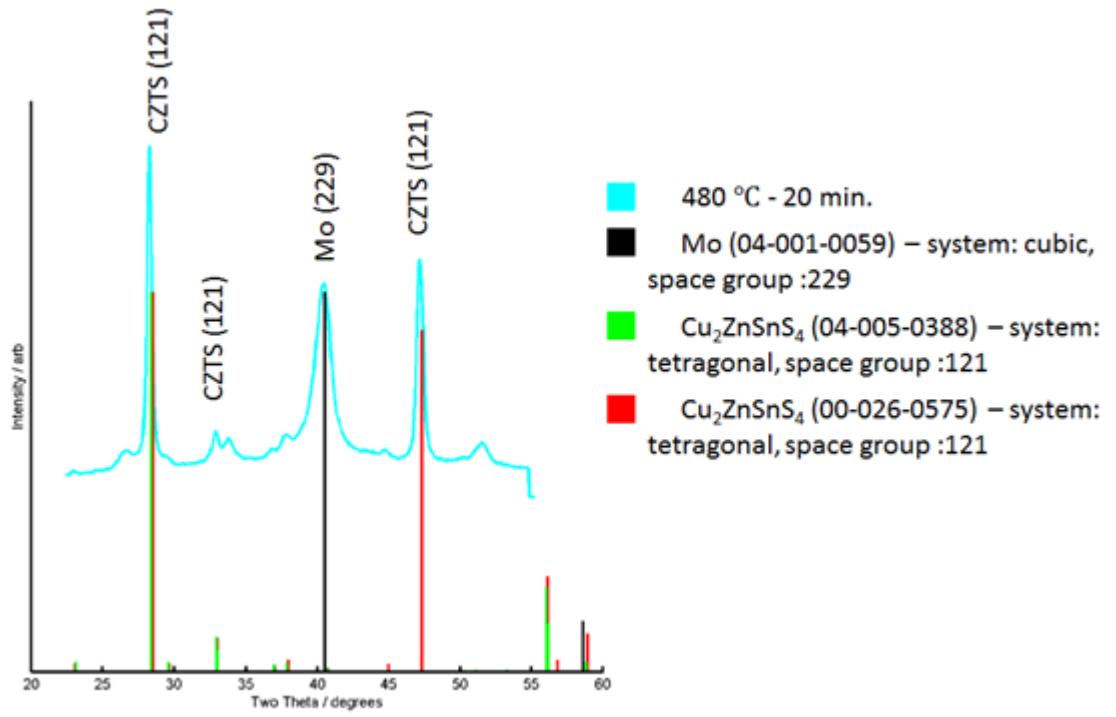

Figure 43: XRD of CZTS annealed at 480℃ for 20 min. The films were 2000 nm of CZTS deposited at room temperature.

Similar to the as deposited films, the kesterite tetragonal CZTS phase is present along with the cubic Mo phase; smaller peaks which could not be resolved with the as deposited diffractogram can now be seen clearly, such as the peak at around 32.5 degrees. Here similar to CIGSe, ideally the CZTS would be single phase, unfortunately some other peaks are present, such as that at around 53 degrees, which could not be located in the database and assigned a phase. But as we see in the SEM images below (Figure 44), the grain sizes with these annealing recipes are around 100 nm, and therefore many other amorphous phases can occur at the grain boundaries (causing recombination). By increasing the grain size, we may be able to reduce or completely eliminate these other phases. All the recipes show similar grain sizes and further work needs to be done to increase these grain sizes.

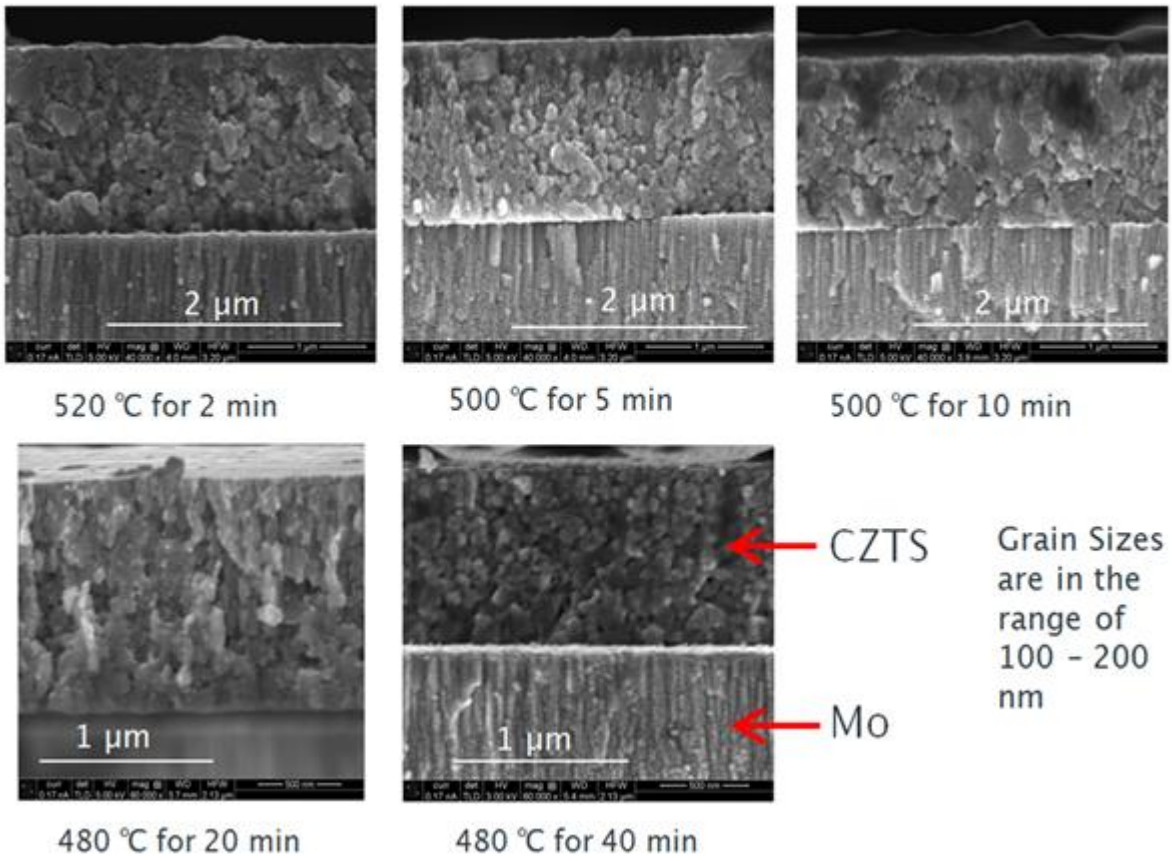

Figure 44: SEM cross sections of CZTS annealed with different recipes. The films were 2000 nm of CZTS deposited at room temperature.

4.2.2 The fabrication of CZTS solar cells

Several problems were encountered when attempting to characterise the I-V characteristics of the cells. Firstly, the probes applied too much pressure on the cells, causing a decrease in shunt resistance, and an eventual short circuit of the p-n junction with multiple measurements. Secondly, the probes were positioned over the cells and therefore shadowed the illumination on the cell, decreasing any photocurrent produced substantially. Figure 45 shows a typical substrate being characterised.

Figure 45: Cells being characterised using ABET Technologies Sun 3000 solar simulator

Three cells showed rectification. These were annealed at 480 degrees Celsius for 20 min. All 3 I-V curves are shown in Figure 46 below.

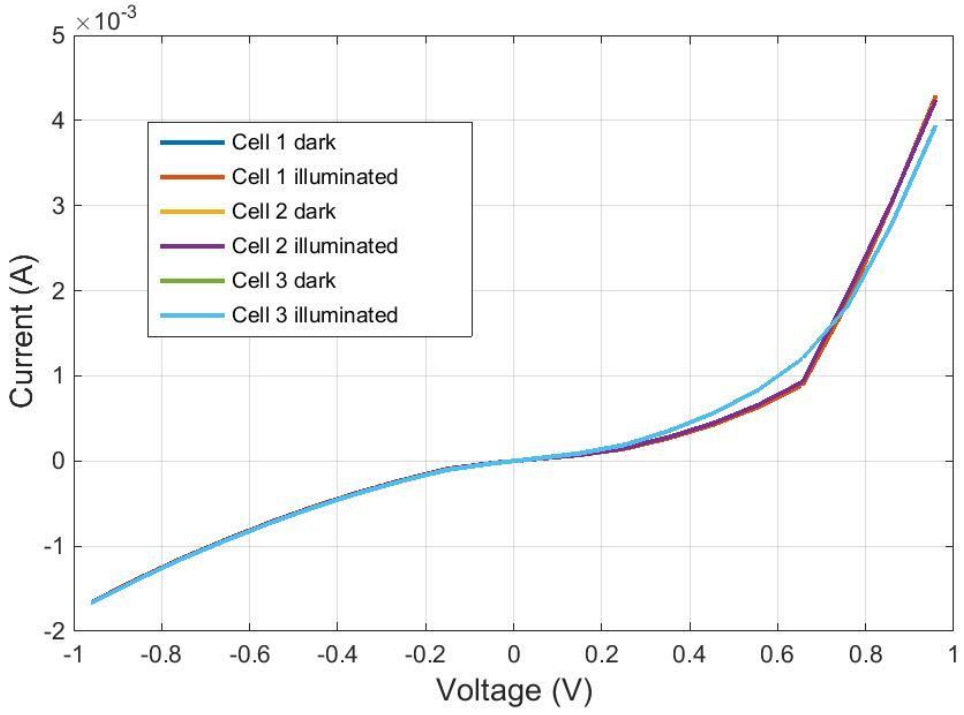

Figure 46: I-V curves of the 3 cells that showing rectification. The absorber layer was 1000 nm of CZTS deposited at room temperature and annealed at 480 ℃ for 20 min.

The photocurrent produced by the cells is shown in Figure 47 below; the graph shows a zoomed in plot around v=0, which shows the short circuit voltage.

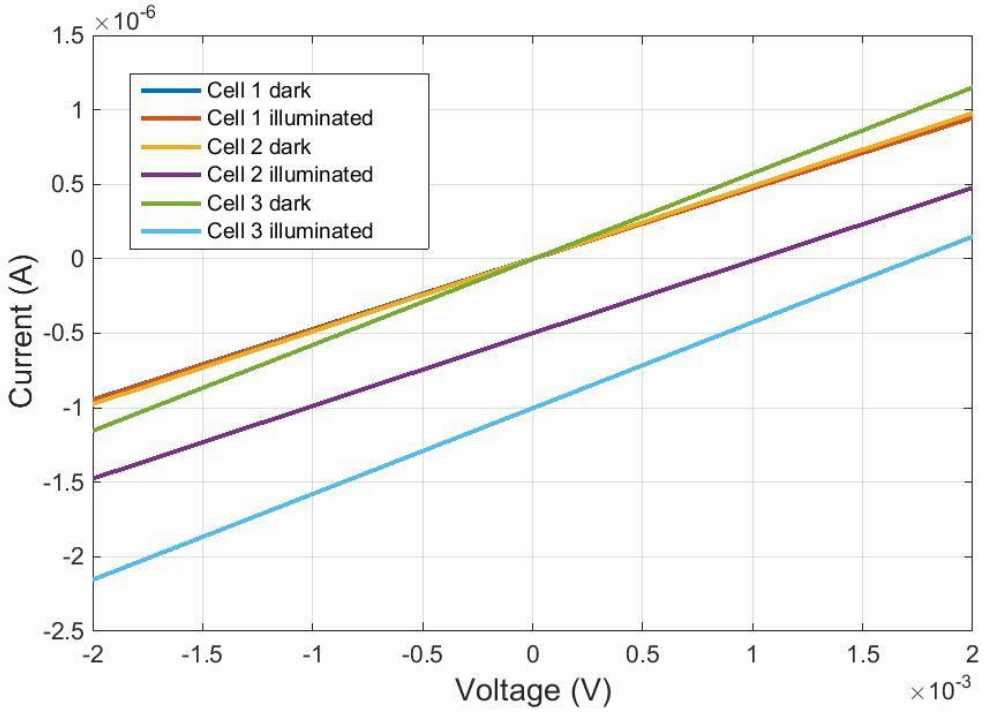

Figure 47: Photocurrent of 3 cells that showed a working p-n junction. The absorber layer was 1000 nm of CZTS deposited at room temperature and annealed at 480 ℃ for 20 min.

The maximum short circuit current seen is just above 1 μA (current density of 1 μA/cm^2) and an open circuit voltage of around 1.7 mV. The fabrication of future cells will not involve a lift off step between the p-type and n-type layers to avoid damaging the interface and therefore introducing recombination centres which would decrease the efficiency of the cells.

4.3 Conclusions

Cu_2ZnSnS_4 thin films have been deposited by RF magnetron sputtering at room temperature from a single quaternary target on to molybdenum coated substrates. The films were annealed in a rapid thermal processor with different recipes. The annealing was done without any toxic gases or reactive sulphur. The compositional and structural properties of the films have been analysed using EDX and XRD respectively and certain recipes were identified which produce films with good adhesion, good crystallinity and that show the ideal stoichiometry before and after annealing. The grain sizes were measured by SEM imaging, and grains for the films are between 100 and 200 nm in size. Similar to the previous chapter, to improve the cells we need to increase the grain size,

which could be done by annealing at a higher temperature or at a lower pressure. The EDX showed a tin rich and zinc poor material, which can be improved by melting the targets in house and having better control of the target composition. The XRD diffractograms show single phase CZTS consistently with all the annealing recipes analysed and therefore even if the films have a composition that is non stoichiometric, the crystals formed are.

Finally cells were fabricated, but only a few cells showed rectification, with a maximum short circuit current of 1 μA. The cleaning carried out in this chapter was more thorough and greater care was taken when handling the samples and in between depositions. Also the cell designs were different, they were smaller; but the design involved losing some photocurrent due to contact shading. Also, cells were fabricated several times, which lead to the conclusion that the time between the initial depositions, annealing and ZnS deposition was integral to the photocurrent produced (this needed to be minimised). The longer it was, the lower the photocurrent which is believed to be caused by oxidation of the CZTS layer, but since the oxidation probably occurs in the first 50 nm of the layer, EDX is not a reliable technique to measure this.

Chapter 5: High-Throughput Synthesis of Gallium Lanthanum Sulphide

This work has contributed to the following:

GHOLIPOUR, B., HEWAK, D. W., HUANG, C. C., ANASTASOPOULOS, A., **AL SAAB, F**., GUERIN, S., HAYDEN, B. & PURDY, G. 2011. Scalability and thermal stability of low current consuming, nanowire phase change memory cells for high density commercial applications. E/PCOS. Zurich, Switzerland.

GHOLIPOUR, B., ZHANG, J., **AL SAAB, F**., GHOLIPOUR, A., MAC-DONALD, K. F., HAYDEN, B., HEWAK, D. & ZHELUDEV, N. I. 2011. Chalcogenide Phase Change Materials in Active Plasmonic and Metamaterial Technologies. SAIT Global Research Outreach Scheme.

GHOLIPOUR, B., ZHANG, J., **AL-SAAB, F**., MACDONALD, K. F., HAYDEN, B. E., HEWAK, D. W. & ZHELUDEV, N. I. 2012. Chalcogenide glass photonics: non-volatile bi-directional all-optical switching in phase-change metamaterials. CLEO/QELS 2012. San Jose.

5.1 Methods

5.1.1 HT-PVD characterisation of GLS

A range of compositions of GaLaS were deposited using the PVD system described in chapter 2. Lanthanum was evaporated using an electron beam, while gallium and sulphur were evaporated from Knudsen cell. The sulphur cell comprises of a second stage to crack the long allotropes of sulphur to achieve a more uniform and homogenous integration of sulphur in the films. The power and wedge of each source can be controlled independently to achieve a desired gradient for each material. A shutter for each source then controls the deposition of a material. When all shutters are open and the gradients calibrated, compositional gradients can be deposited across a film with small thickness variations. All depositions were 30 minutes long. Figure 48 shows an example of a GLS sample where the compositional spread can be seen, and Figure 49

shows the compositional spread of three samples achieved after calibration. By depositing at different temperatures and in situ annealing we can control the amount of sulphur in the films. Appendix 1 shows all the depositions and characterisation done for each sample.

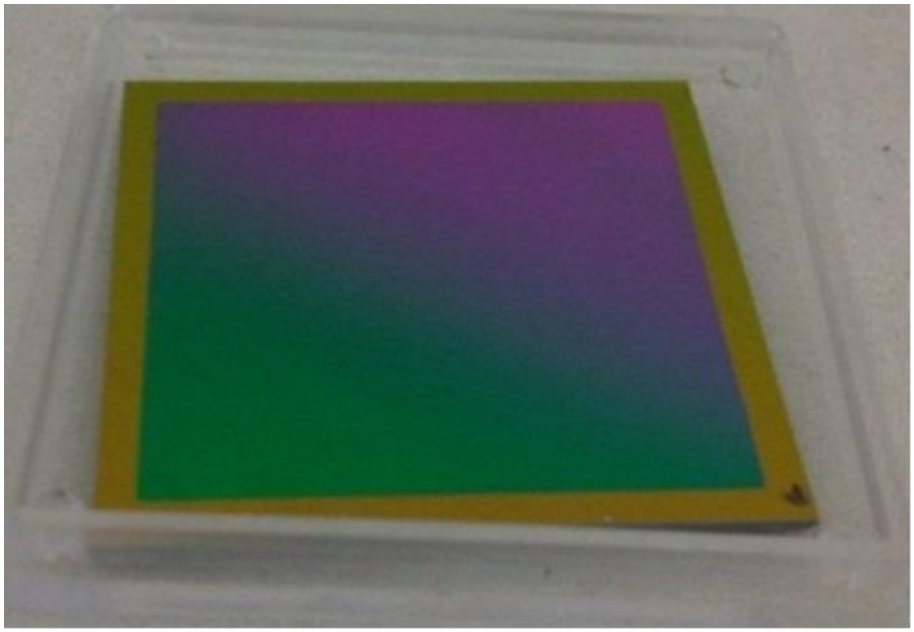

Figure 48: Example GLS sample fabricated in UHV-PVD chamber

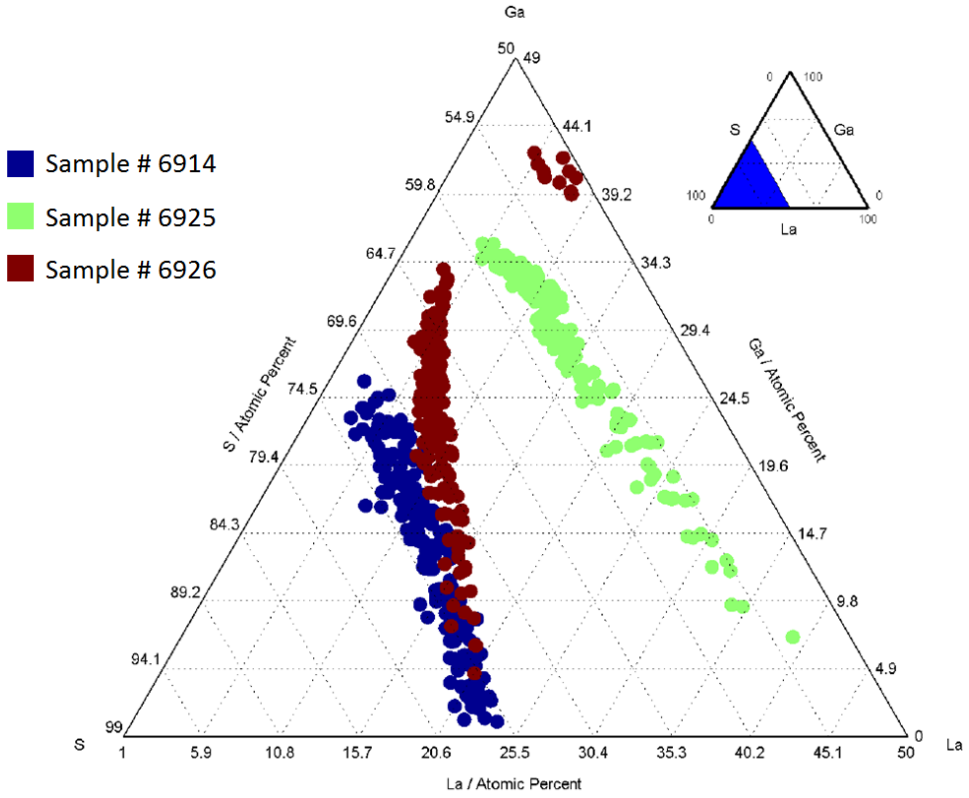

Figure 49: Typical GLS Compositional Spread – inset in top right shows the section of the complete ternary diagram in which the sample compositions are found.

To achieve 60% sulphur homogenously throughout the films, depositions were optimised by depositing at room temperature, 200 ℃ and 400 ℃. Depositions at room temperature and 200 ℃ were annealed until further annealing did not decrease the sulphur content of the films. Finally, depositions carried out with the sulphur cracker at 500 ℃ and the effusion zone at 125 ℃ were compared with depositions carried out with the effusion zone at room temperature to compare the effect of the sulphur partial pressure on the sulphur incorporated in the film.

Three different substrates were chosen for refractive index measurements, X-ray diffraction and Raman measurements. Compositional measurements were carried out on all substrates using a Jeol JSM-5910 SEM [148], fitted with an Oxford INCA 300 EDX, using a working distance of 10 mm and a magnification of 500x.

Refractive index measurements were carried out on silicon substrates using a J. A. Woollam spectroscopic ellipsometer [149]. The ellipsometer was fitted with an X-Y translational stage along with a vacuum holder for mounting the sample

vertically. Incident light was supplied by a 75 W xenon arc white light source focused into a 1 mm diameter beam through a collimator. The transmitted signal is split into individual wavelengths by a prism, and the intensity measured by a charge-coupled device (CCD) camera. The results for sample #7120 are shown in the results section. For the analysis, the CompleteEASE® software package [149] was used. In the model, the GLS film was modelled as a Tauc Lorentz oscillator.

X-ray diffraction measurements were carried out on Si3N4 coated Si substrates, the results for sample # 6955 are shown in the results section. The sample was deposited at 200 ℃ and then post annealed at 650 ℃.

Raman measurements were carried out on Pt-coated Si substrates using a Horiba Xplora Raman spectrometer and optical microscope [150]. The results for sample # 6926 are shown in the results section.

The depositions, EDX (measurement and analysis) and XRD measurements were carried out jointly with Dr Alexandros Anastasopoulos. The XRD analysis, Raman (measurements and analysis) and ellipsometry (measurement, analysis and modelling) were performed by the author.

5.2 Results and Discussion

5.2.1 Effect of annealing on sulphur content at different deposition Temperatures

GLS was deposited at room temperature and then annealed at 500℃, 635℃, 675℃ and 700℃. The sulphur content of the as deposited film was at 70 %. After annealing the sulphur decreased to 55-60 % and did not decrease further when annealing at higher temperatures. This is shown in Figure 50 below.

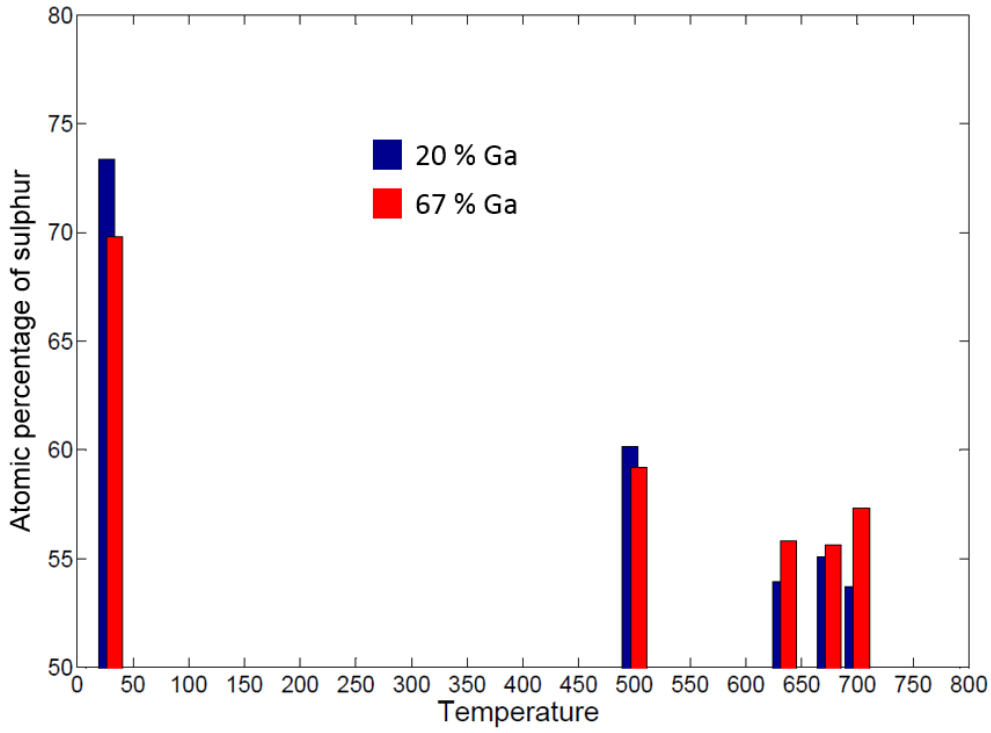

Figure 50: Effect of annealing on sulphur content for room temperature depositions. GLS was deposited at room temperature and then annealed.

GLS was then deposited with the substrate heated to 200℃ and then annealed at 650℃. The sulphur content of the as deposited film was around 55-60%. After annealing the sulphur remained the same and did not decrease further. This is shown in Figure 51 below. GLS fabricated by other groups contain around 60% sulphur (for example see ref. [103]).

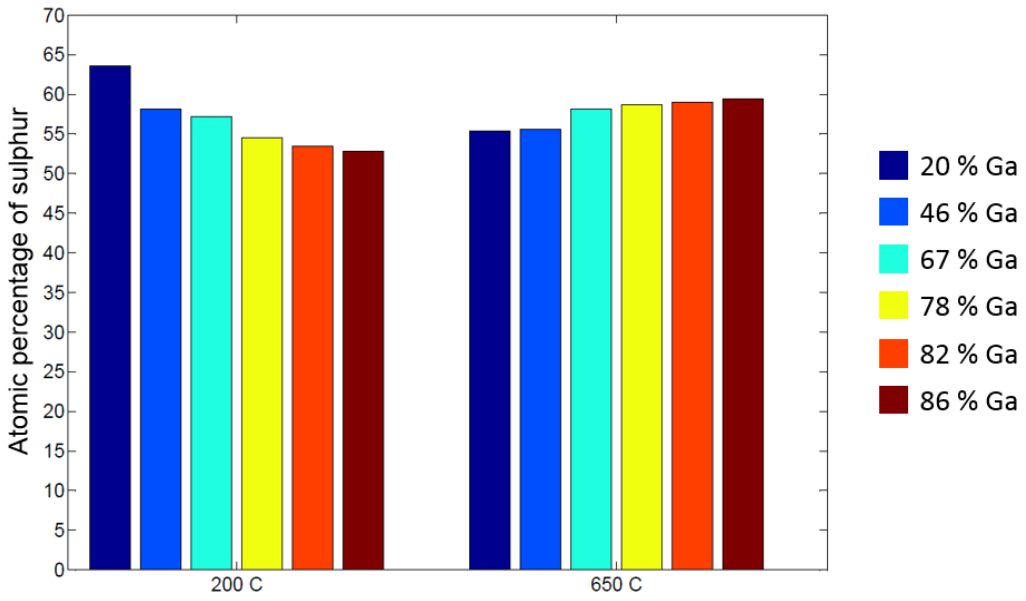

Figure 51: Effect of annealing on sulphur content for samples deposited at 200 ℃ and then annealed at 650 ℃.

5.2.2 Effect of deposition temperature on Sulphur content between cracker and native

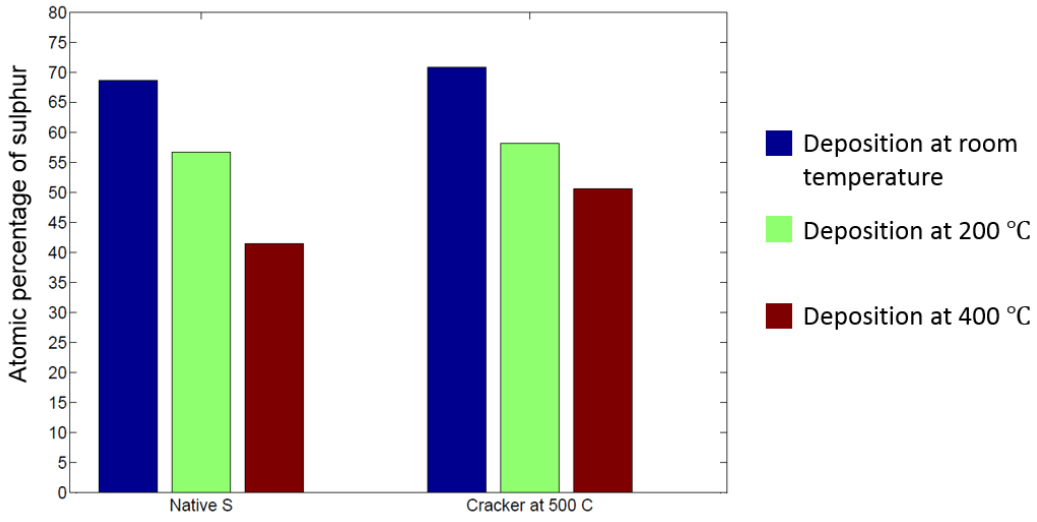

Figure 52: Effect of deposition temperature on sulphur content between depositions with a heated sulphur cracker or using the native sulphur in the chamber.

Figure 52 shows a comparison of depositions with the substrate at room temperature, 200 ℃ and 400 ℃. A comparison of depositions with the sulphur

remaining in the chamber from previous depositions and with the sulphur effusion zone at 125 ℃ and the cracker hot lip at 500 ℃ is shown as well. The sulphur content in the films only shows a significant difference with samples deposited at 400 ℃. Samples deposited at 400 ℃ using the native sulphur left in the chamber have much less sulphur.

5.2.3 X-ray Diffraction

Figure 53 shows the ratio of Gallium to Lanthanum for six points taken across the sample. The gradient is shifted towards a more gallium rich film. The entire range goes from 80 % Lanthanum to 78 % Gallium.

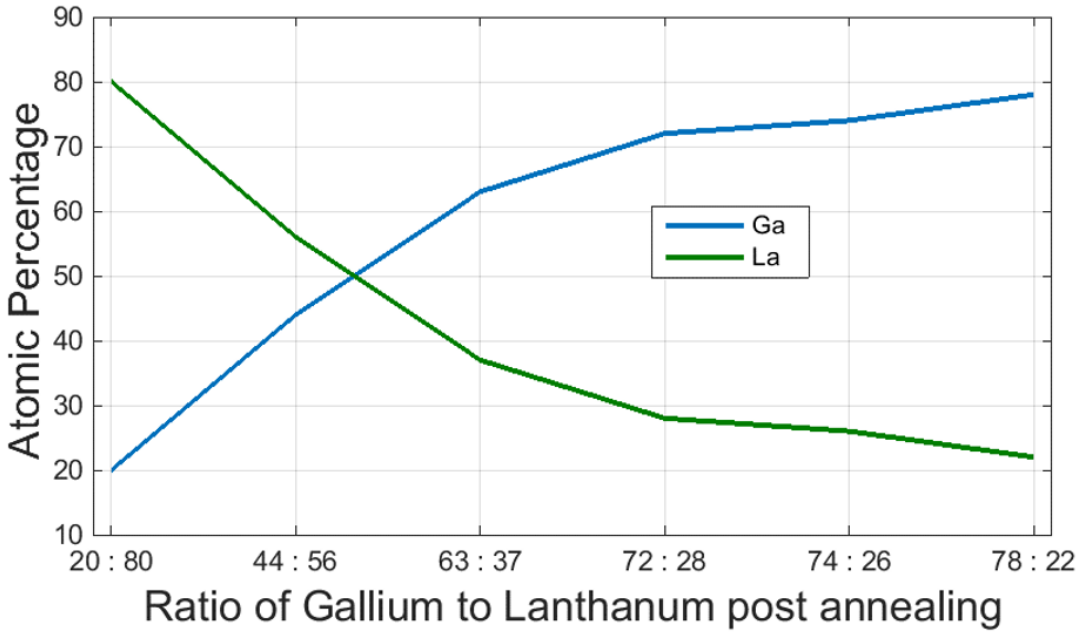

Figure 53 : The ratio of Gallium and Lanthanum post annealing for all six points measured on sample number 6955. The film was deposited at 200 ℃ and then annealed at 650 ℃.

Figure 54 shows the amount of sulphur and oxygen in the film for each of the six points. The EDX shows a very small amount of oxygen being incorporated in some of the compositions, which suggests that different compositions are more susceptible to oxygen incorporation than others.

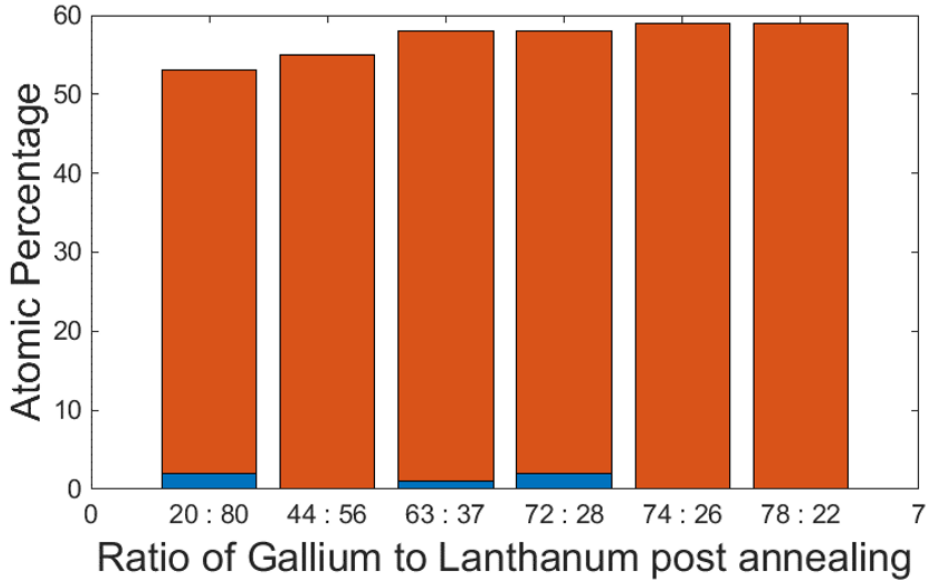

Figure 54 : The atomic percentage of sulphur and oxygen post annealing for all six points measured on sample number 6955. The film was deposited at 200 ℃ and then annealed at 650 ℃.

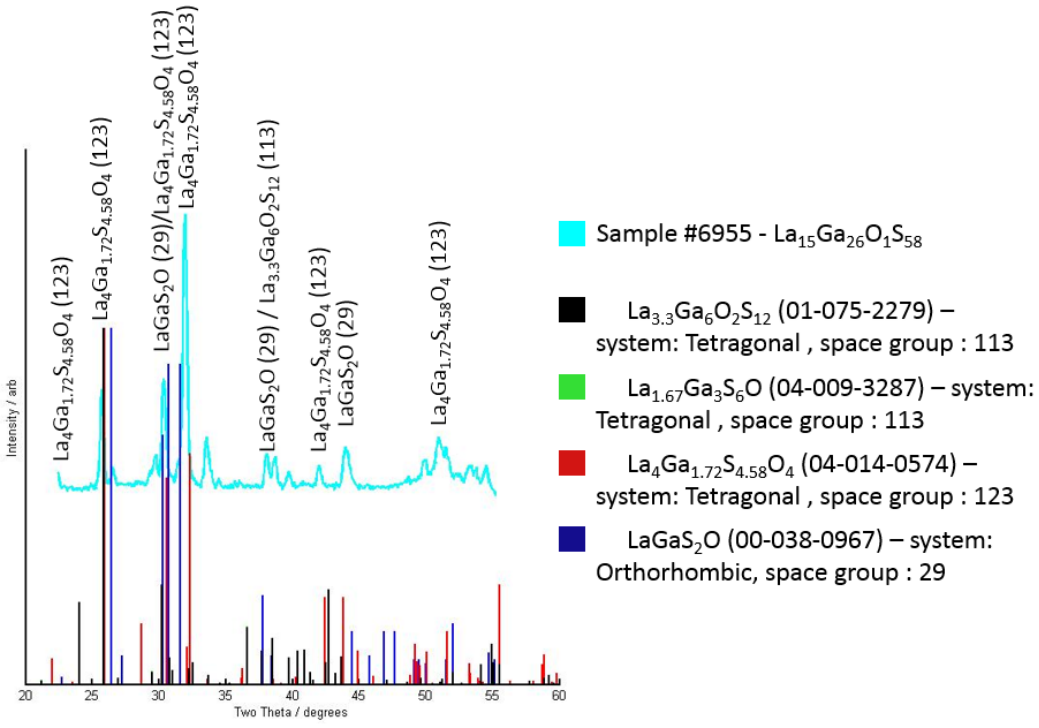

Figure 55 : XRD comparison of single point diffractogram with GLSO phases. The film was deposited at 200 ℃ and then annealed at 650 ℃.

Figure 55 shows the diffractogram of a single point X-ray diffractogram (with the composition, $La_{15}Ga_{26}O_1S_{58}$), the point was selected to have a composition near to the 70 % gallium fabricated elsewhere (for example see ref. [103]), it is also coincidently the most crystallised point in comparison to the other points measured (Figure 56 below). The XRD diffractogram is matched with a few GLSO phases, this indicates that the GLS (as mentioned previously) incorporates oxygen to stabilise, which was unexpected as no oxygen gas was introduced to the high vacuum system during the deposition.

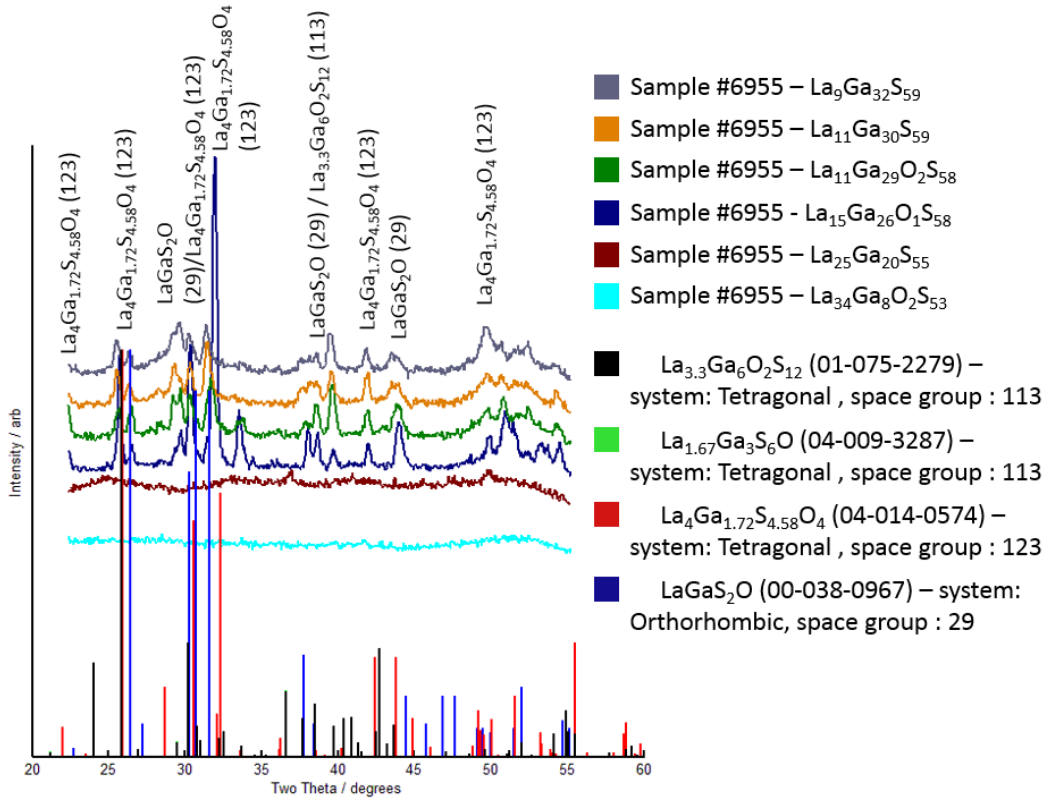

Figure 56 : XRD comparison of all six measured diffractograms with GLSO phases. The film was deposited at 200 ℃ and then annealed at 650 ℃.

In Figure 56, we see that La rich compositions do not crystallise, whereas the Ga rich compositions crystallise and with similar peaks. Although similar the intensities of each peak changes as the composition changes, this is expected because different crystals will be favourable, depending on the amount of each material present in the film. Another point to make is that the oxygen is in small amounts in the films, which means that the crystallised oxysulphide is a small portion of the film and the remainder remains as a sulphide and amorphous.

5.2.4 Raman Spectroscopy

The Raman spectra of GLS and GLSO is divided into two parts [151], the low energy part and the high energy part; separated at around 500 cm^{-1}. The low energy part is similar for both glasses with two peaks one at 150 cm^{-1} and the other at 340 cm^{-1}. In the high energy region the two glasses can be differentiated; GLS show one weak band centred at 760 cm^{-1} and GLSO has two peaks (517 and 640 cm^{-1}).

The peaks in the low energy region are present in many Ga containing sulphides and are therefore attributed to stretching and bending vibrations of the GaS_4 tetrahedral. The 760 cm^{-1} vibration is due to a strained Ga-related tetrahedral.

In GLSO, the two vibrations at 517 and 640 cm^{-1} are attributed to the Ga-O-Ga and Ga-O- bonds respectively. If the first of these bonds is broken by a La ion, we would also get a vibration at around 375 cm^{-1}. Finally a peak at 233 cm^{-1} is seen if Ga_2S_3 crystals are present and disappear if a glass if formed. LaS and LaO give vibrations at 220 cm^{-1} and between 300 and 400 cm^{-1}, respectively.

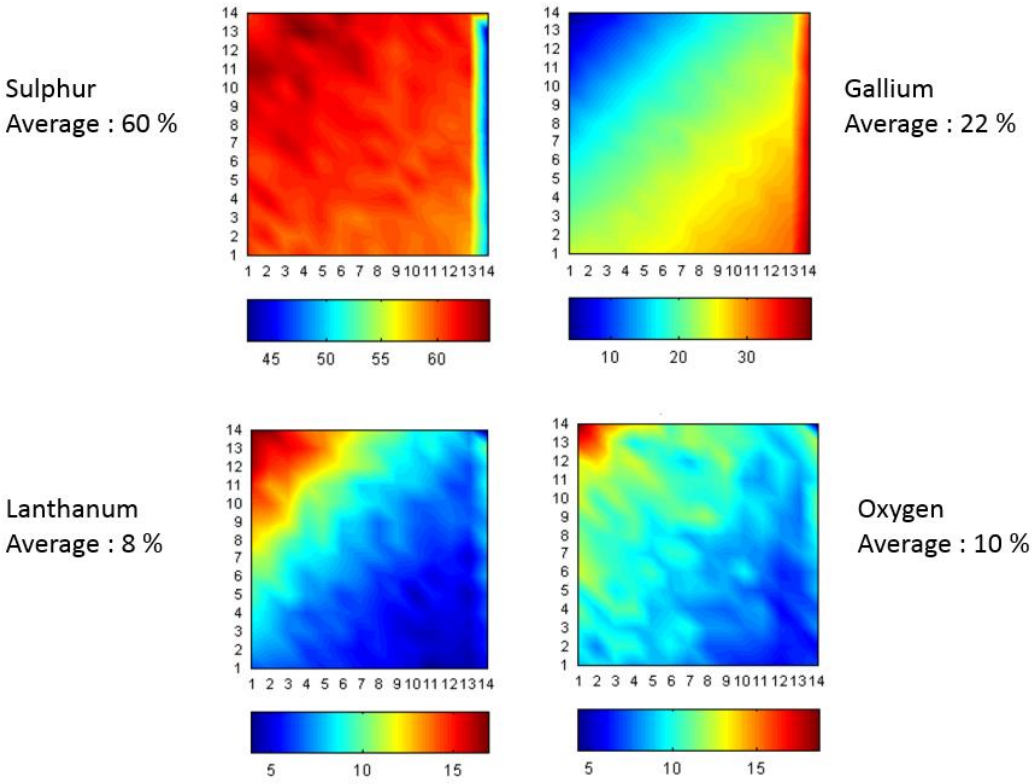

Figure 57: Wedge plots of sample 6926. Ranging from a max of 88 % Ga to 82 % La

Figure 57 shows the compositional spread of each element in the sample produced. There seems to be some shading from the mask to the right of the sample (especially visible for the sulphur and gallium plots), the spectra analysed will be from the diagonal and so this shading will not interfere with the analysis. It is promising to see that the sulphur is uniform across most of the sample with an average of about 60 %.

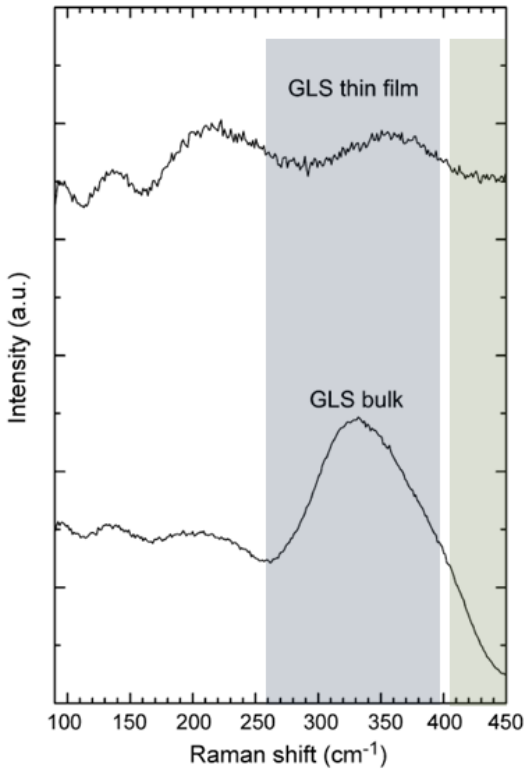

Figure 58: Raman scattering spectra of GLS bulk glass and thin PLD film adapted from [152].

When comparing to the literature (Figure 58 and ref. [152]) we see that the largest peak is between 250 and 400 cm^{-1}. Figure 59 shows the Raman spectra of different points across the diagonal of the sample. The first peak is at around 150 cm^{-1} (green peak), the second is at 220 cm^{-1} (red peak), the third peak is broad with a range between 250 and 400 cm^{-1}(orange peak) and changes from a single to a double peak (with higher gallium concentrations); finally the fourth peak (blue peak) is around 475 cm^{-1} and is the only peak that is not mentioned previously in the literature.

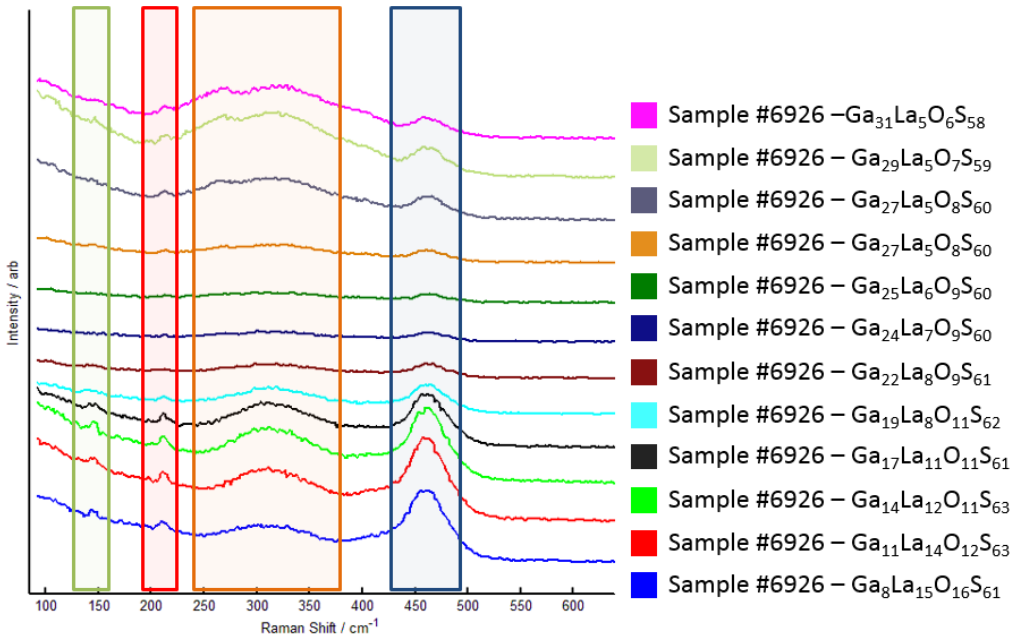

Figure 59: Raman spectra across diagonal of sample # 6926. The GLS was deposited at room temperature.

It is worth mentioning here that the peak between 250 and 400 cm^{-1} shows a double peak at high gallium concentrations, but because the two peaks are not distinct, to investigate this further, we would need a method that can differentiate between a double peak and a single peak, otherwise any trend produced could be influenced from other spectrum components.

To do this, a multivariate curve resolution algorithm was used; this was developed in a commercial informatics package used by Ilika technologies [153].

Figure 60 shows the three main components that are present in the Raman spectra. Representing a total of 94% of the 196 data point measured (ignoring the shaded region showed previously).

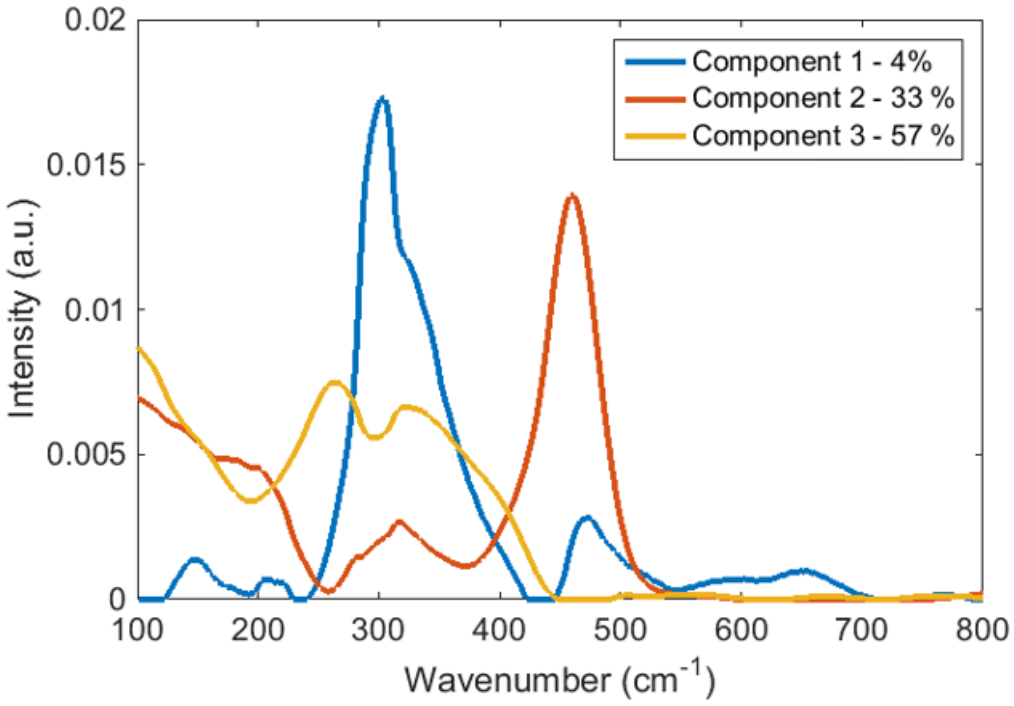

Figure 60: Multivariate curve resolution components that make up the Raman spectra

Usually for a quaternary sample, we can plot the data in a quaternary pyramid such as that shown in Figure 61.

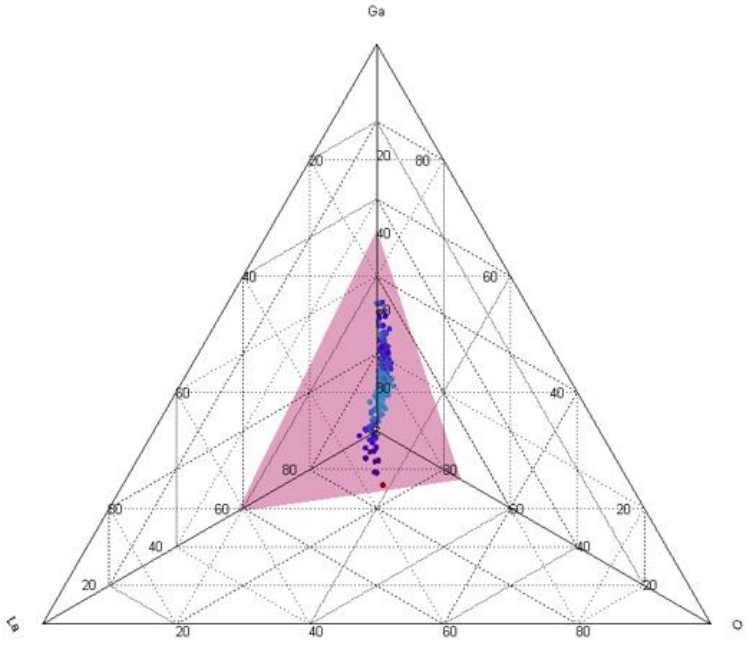

Figure 61: Quaternary plot of GaLaSO, the pink slice shows the ternary taken at 60 % sulphur.

In this case, since the sulphur is constant across the sample we can take pseudo ternary slice (also shown in Figure 61 as the pink/purple triangle).

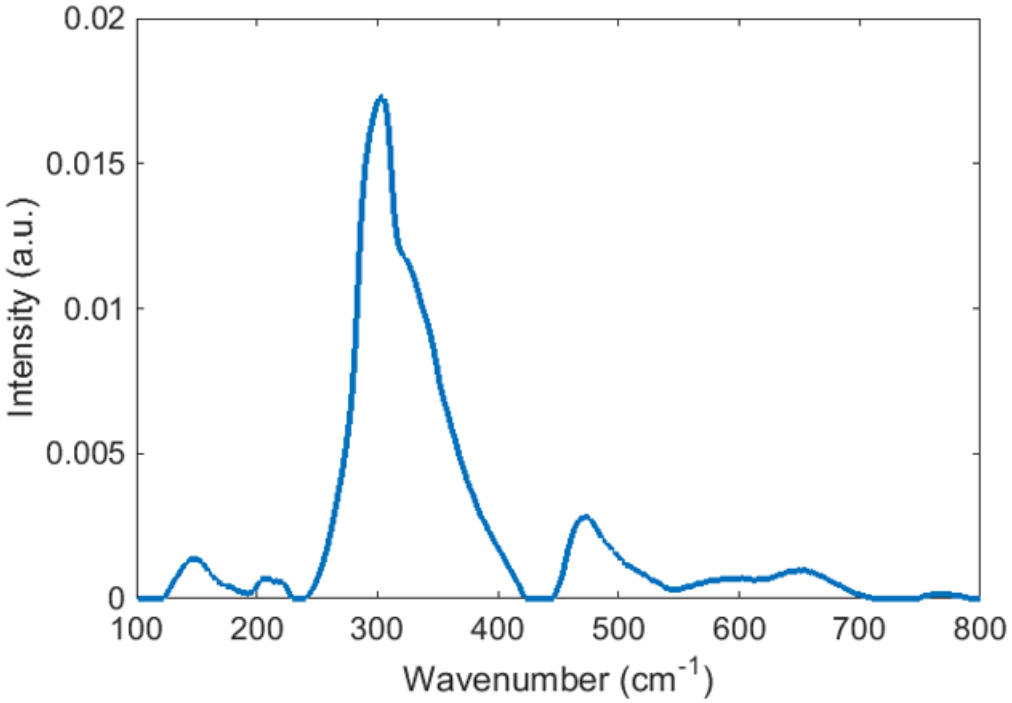

Figure 62: Component 1 from the MCR analysis of the Raman spectra of sample 6926.

Figure 62 shows the spectrum for component 1, we can see a peak at 150, 220, 300 340, 475, 640 and a small one around 760 cm^{-1}. These all match the literature except the vibration at 475 cm^{-1}, as mentioned before.

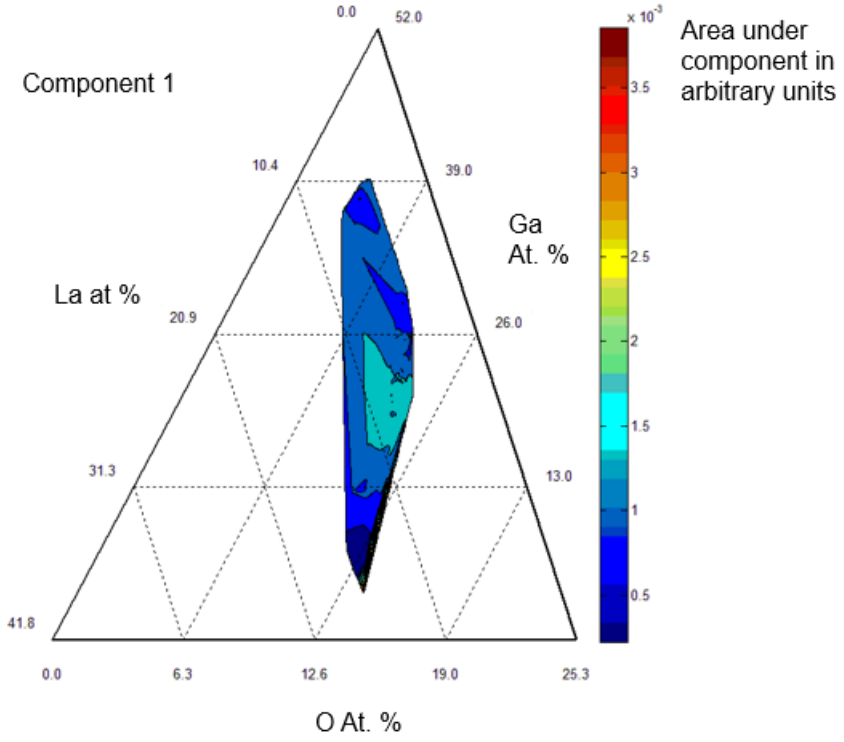

Figure 63: Ternary plot of component 1 from the MCR analysis of the Raman spectra of sample 6926.

Figure 65 shows the ternary plot of component 1, this spectrum is sharply present in the most La rich part of the sample. Also, there is a slight presence in the middle with high oxygen and low La.

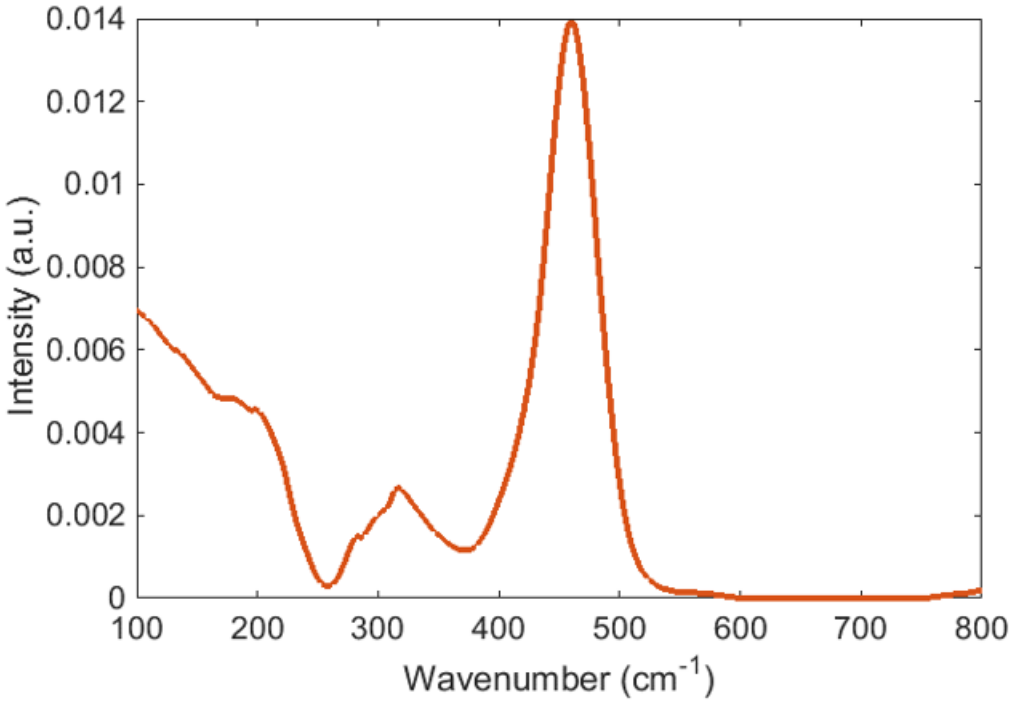

Figure 64: Component 2 from the MCR analysis of the Raman spectra of sample 6926.

Figure 64 shows the spectrum for component 2, we can see a small peak at 220, around 320 and at 475 cm^{-1}. These all match the literature except the vibration at 475 cm^{-1}, as mentioned before.

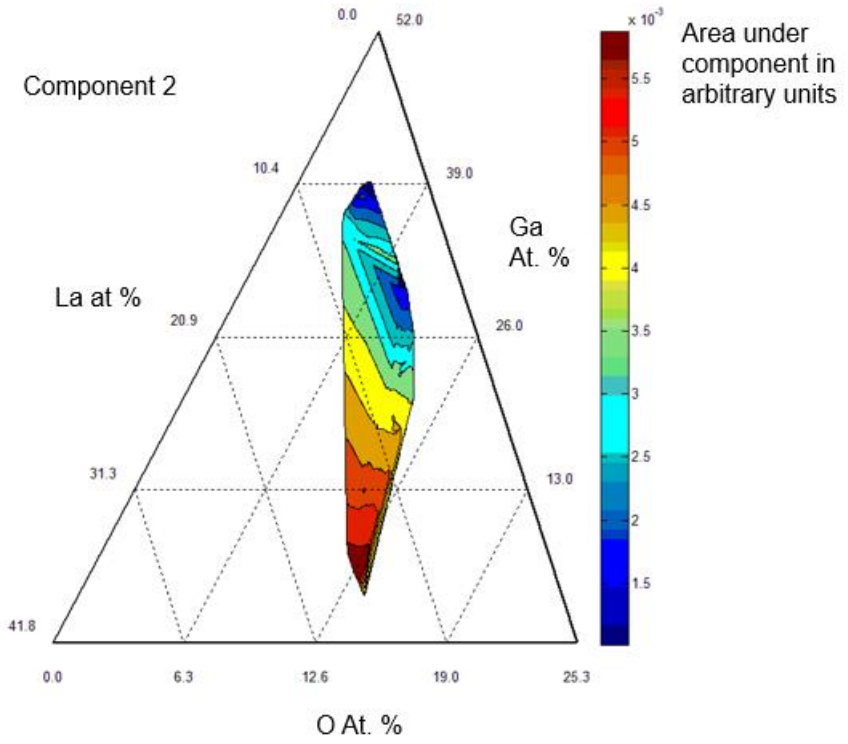

Figure 65 : Ternary plot of component 2 from the MCR analysis of the Raman spectra of sample 6926.

Figure 65 shows the ternary plot of component 2, this spectrum is present in the most La rich part of the sample, with a gradual decrease towards the Ga rich area. As this component has a large 475 cm^{-1} peak, we can assume this vibration is due to the La-O or La containing bond.

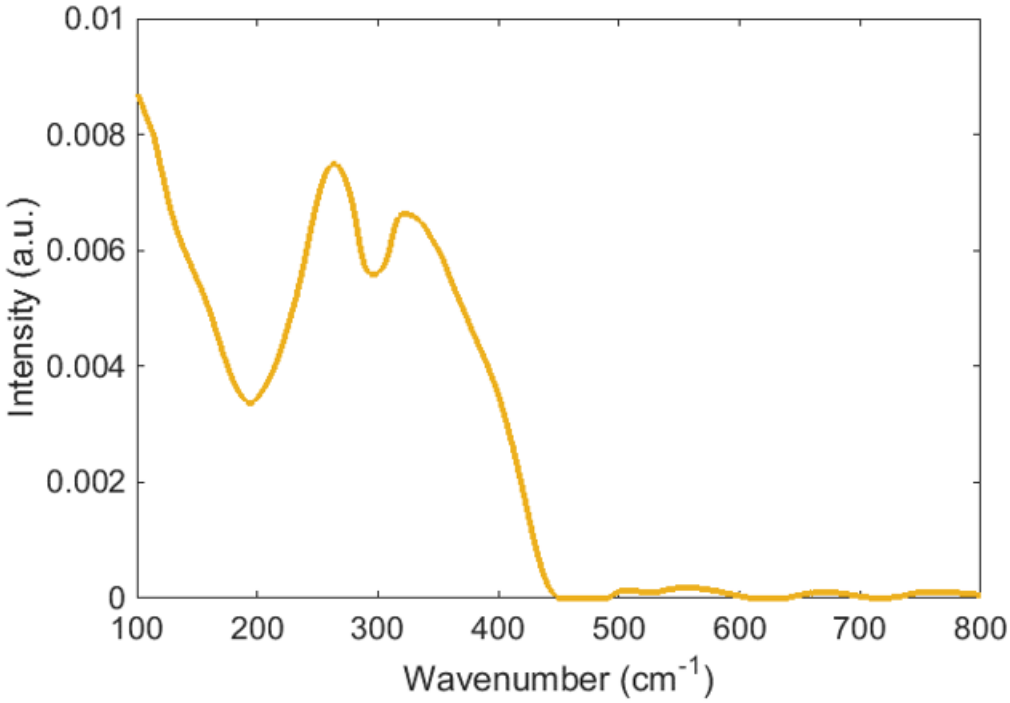

Figure 66 : Component 3 from the MCR analysis of the Raman spectra of sample 6926.

Figure 66 shows the spectrum for component 3, we can see a peak at 270 and around 320. Although this does not match a specific literature peak, we can assume that these are caused by Ga containing bands because of the many variations and environments which could slightly change the Raman shift. For example looking back at Figure 58, we can see that the peak at 340 cm^{-1} in the bulk shifts in the GLS thin films.

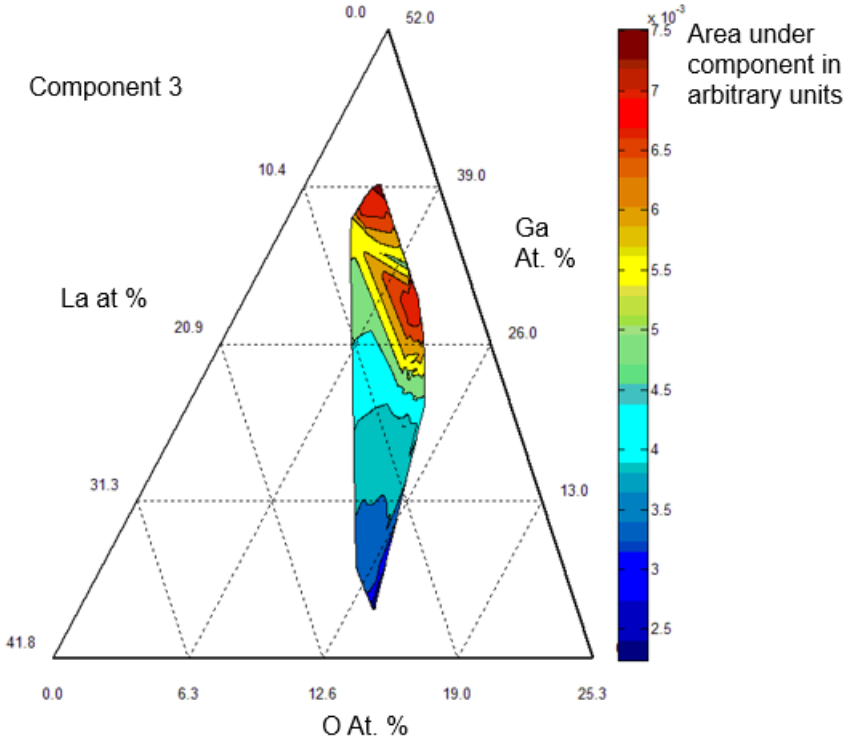

Figure 67 : Ternary plot of component 3 from the MCR analysis of the Raman spectra of sample 6926.

Figure 67 shows the ternary plot of component 3, this spectrum is present in the most Ga rich part of the sample, with a gradual decrease towards the La rich area.

5.2.5 Refractive index

Figure 68 shows a wedge plot of the sample, the composition ranges from 85% lanthanum to 75% gallium for this particular sample and with an average sulphur content of 59% and an average of 1% Oxygen (with a slight increase in the La rich region).

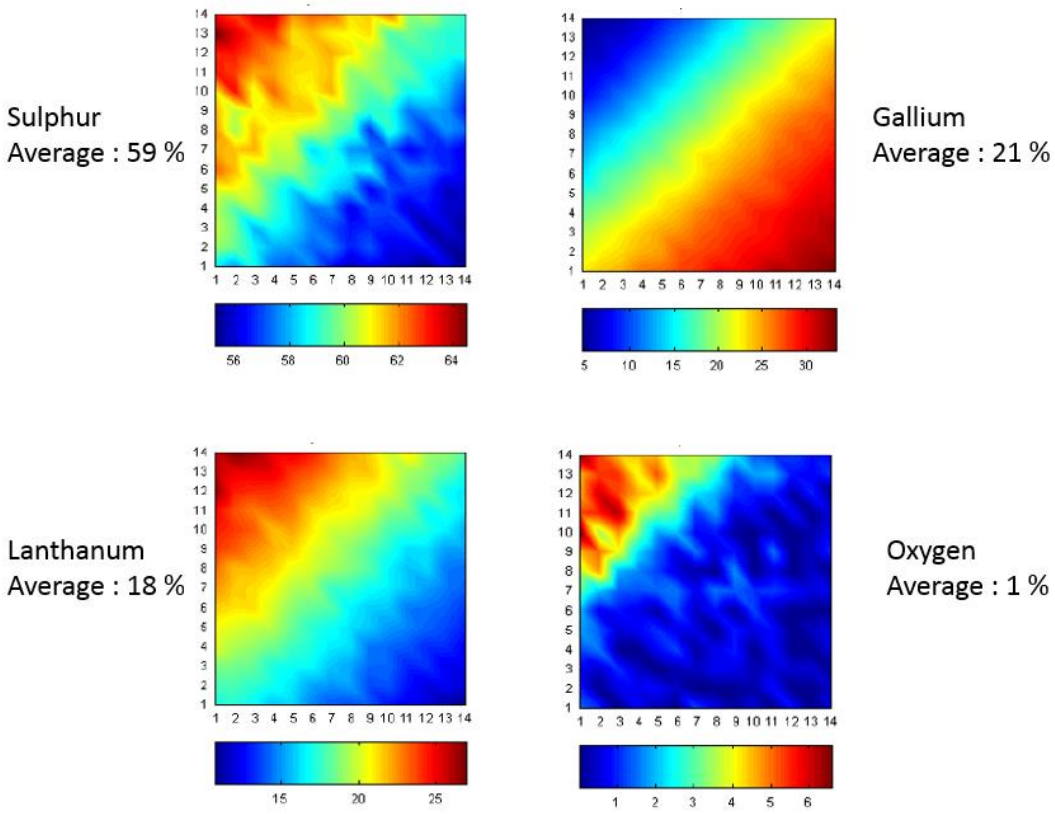

Figure 68: Wedge plot of sample ranging from 85% La to 75% Ga. The GLS was deposited was deposited at 200 ℃.

Figure 69 shows the refractive index for different compositions against wavelength. Figure 70 and Figure 71 show a zoomed in view of the refractive index at different wavelength ranges. The refractive index increases towards the gallium rich end of the sample.

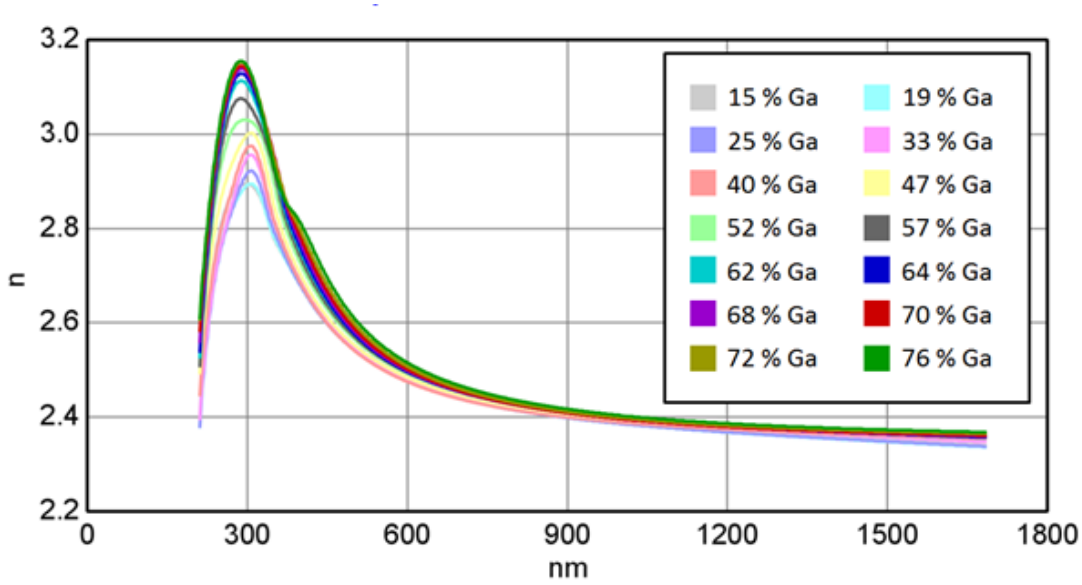

Figure 69: Refractive index against wavelength for compositionally varying GLS thin films. The GLS was deposited at 200 ℃.

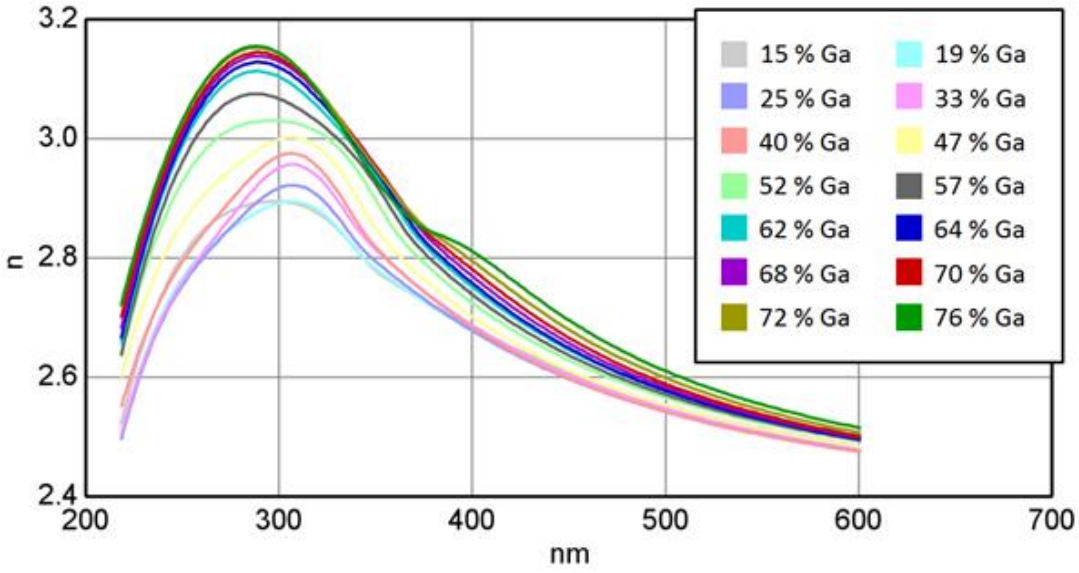

Figure 70: Refractive index from 200 nm to 600 nm for compositionally varying GLS thin films. The GLS was deposited at 200 ℃.

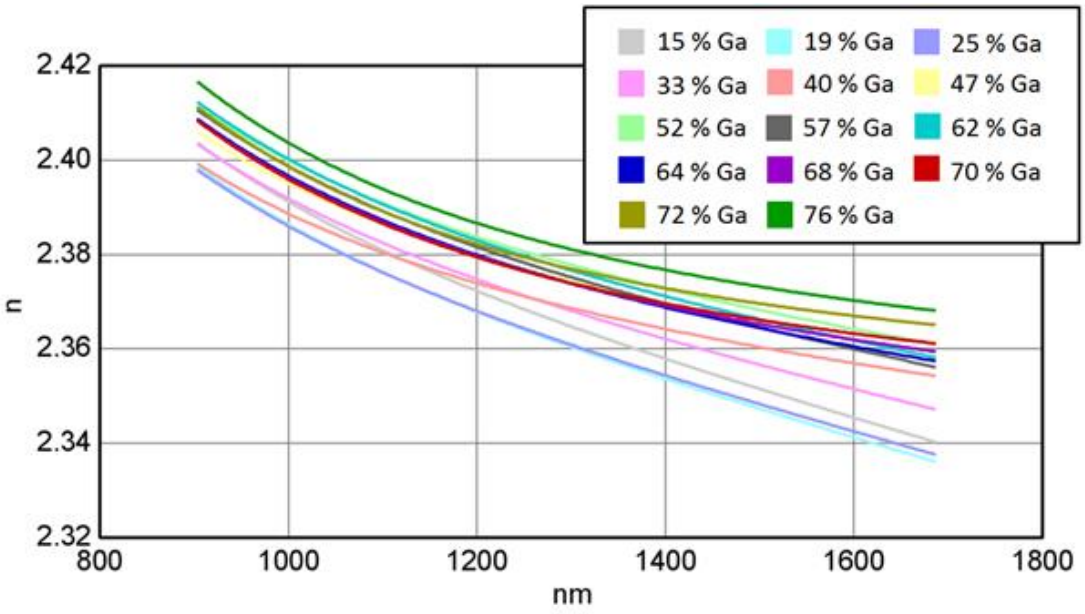

Figure 71: Refractive index from 900 nm to 1700 nm for compositionally varying GLS thin films. The GLS was deposited at 200 ℃.

Figure 72 shows the extinction coefficient for different compositions against wavelength. Figure 73 and Figure 74 show a zoomed in view of the extinction coefficient at different wavelength ranges. The extinction coefficient decreases towards the gallium rich end of the sample. The band gap is roughly around 425 nm which corresponds to around 2.9 eV.

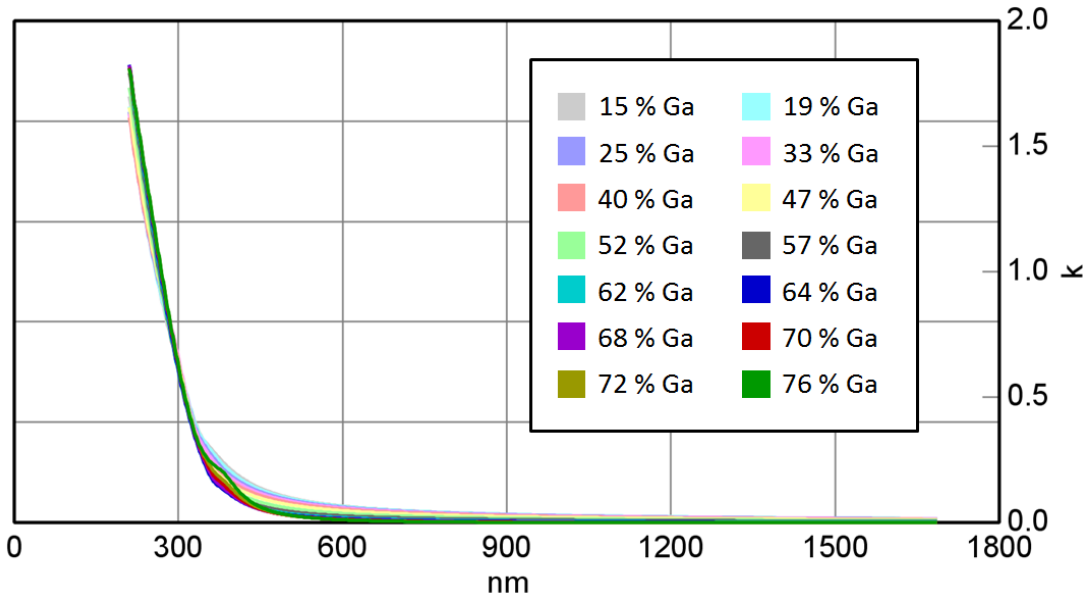

Figure 72: Extinction coefficient against wavelength for compositionally varying GLS thin films. The GLS was deposited at 200 ℃.

Hewak [154] in his book section "Chalcogenide glasses for photonics device applications" indicates that the bandgap of GLS is around 475 nm and that of GLSO is at around 425 nm. Here, it is unlikely that it is GLSO forming due to the small presence of oxygen in the films and the change is more likely to be caused by the thin film being below 200 nm in thickness.

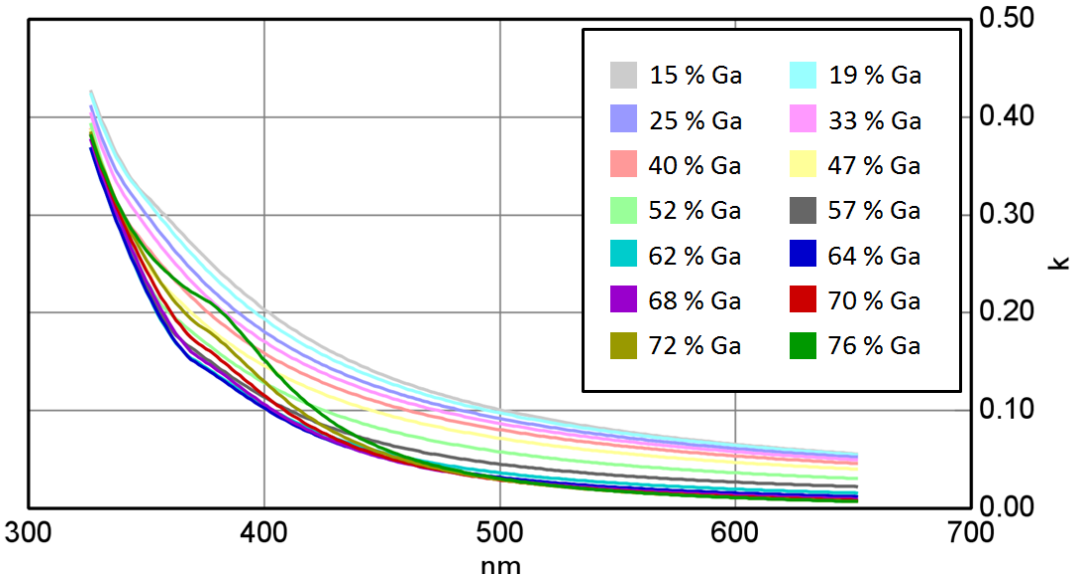

Figure 73: Extinction coefficient from 300 nm to 650 nm for compositionally varying GLS thin films. The GLS was deposited at 200 ℃.

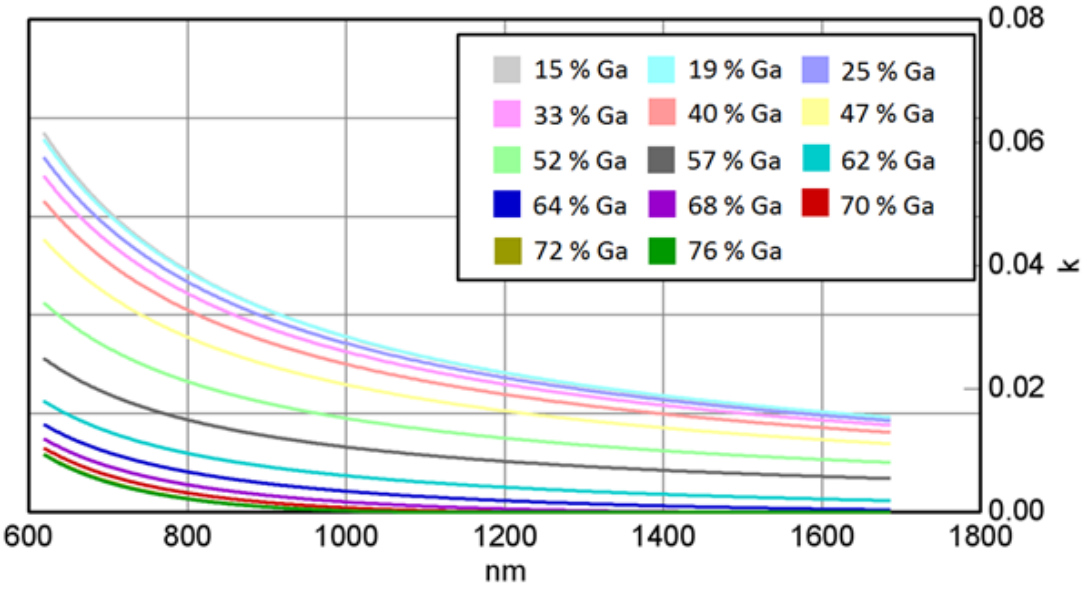

Figure 74: Extinction coefficient from 600 nm to 1700 nm for compositionally varying GLS thin films. The GLS was deposited at 200 ℃.

Figure 75 shows a ternary plot of the refractive index at 1550 nm against composition. Again the refractive index increases with gallium content.

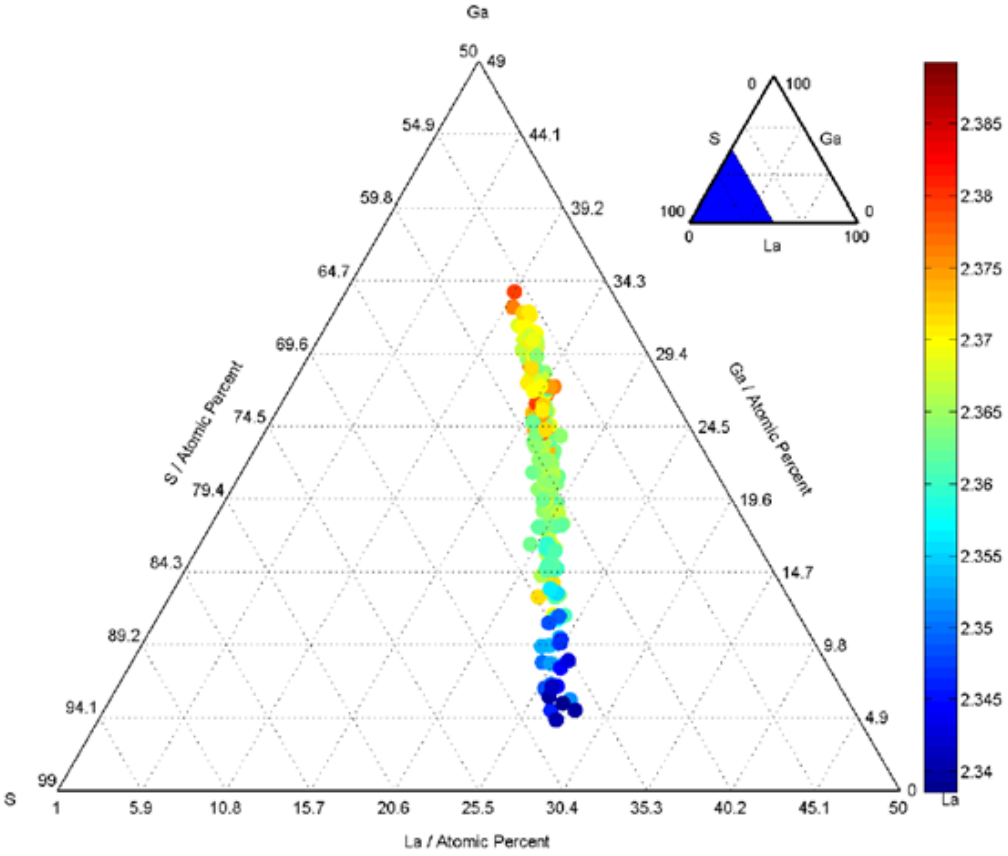

Figure 75: Refractive index against composition at 1550 nm for compositionally varying GLS thin films. The GLS was deposited at 200 ℃.

To compare with the literature, the refractive index across the diagonal of the sample is shown in Table 6 for 3 different wavelengths.

Table 6: Ellipsometry results from sample 7120. The GLS was deposited at 200 ℃.

Ga %	La %	n @ 1014 nm	n @ 1367 nm	n @ 1550 nm
14.7	85.3	2.390	2.359	2.346
19.3	80.7	2.388	2.359	2.347
25.2	74.8	2.387	2.360	2.349
32.5	67.5	2.388	2.363	2.353
39.8	60.2	2.383	2.362	2.355
46.5	53.5	2.390	2.368	2.361
51.6	48.4	2.396	2.372	2.364
56.9	43.1	2.398	2.372	2.364
61.5	38.5	2.407	2.381	2.373
64.4	35.6	2.403	2.379	2.372
67.6	32.4	2.403	2.378	2.371
69.6	30.4	2.402	2.378	2.370
71.9	28.1	2.404	2.380	2.372
75.6	24.4	2.408	2.383	2.376
Average S	60.54696			

When compared with the work by Yayama et al.[109] (Shown in Table 7), the agreement is clear for around 70 % Ga and 30 % La (shown in grey). Unfortunately no other literature is available to compare the results of the other compositions.

Table 7: Refractive index of GLS taken from [109]

Wavelength	Refractive index of $70Ga_2S_3$:$30La_2S_3$
1014 nm	2.398
1367 nm	2.379

5.3 Conclusions

GaLaS thin films were deposited in chapter 5 by a high throughput PVD MBE system on Si, Si_3N_4 coated Si and Pt coated Si substrates. Lanthanum was evaporated using an electron beam, while gallium and sulphur were evaporated from Knudsen cells. The power and wedge of each source was controlled independently, to achieve a desired gradient of each material. The compositional and structural properties of the films were analysed using EDX, Raman and XRD. The effect of the annealing temperature on the sulphur in the films was investigated, which indicated a decrease to around 55-60 atomic % with higher annealing, which then no longer changes with higher temperatures or longer anneals. It is noted that the amount of residual sulphur in the chamber when the cracker is turned off is sufficient for lower temperature depositions, but at higher temperatures (above 400℃) without the cracker the films are sulphur poor. The XRD phases do not match the literature on the XRD of GLS, GaS or LaS, they were unexpectedly matched to GaLaSO, which confirms the preference of GLS to oxidise to form a more stable compound.

The Raman measurements indicate the formation of certain bonds in different material compositions, with a certain trend forming as we move from a La rich to Ga rich compositions. Several peaks matching the literature have been distinguished along with other peaks.

Refractive index measurements were carried out using a J. A. Woollam spectroscopic ellipsometer and it is shown that the refractive index increases with gallium content. The extinction coefficient decreases with gallium content. The absorption edge is around 2.9 eV and shifts only slightly for different compositions. For GLS to be suitable for photovoltaics, we need to shift the band gap to around 1.5 eV (above 800 nm), which may be possible by doping with other materials.

The work on GLS is important as it the first time HTMBE has looked at the trends in this materials (especially in refractive index), as well as the work acting as a benchmark for GLS to be doped with different materials, to find its suitability as a photovoltaic material.

Chapter 6: Copper Antimony Sulphide by CVD

This work has contributed to the following:

HUANG, C. C., **AL-SAAB, F.**, GHOLIPOUR, B. & HEWAK, D. W. 2011. Fabrication of thin film solar cell materials by APCVD. Low Carbon Earth Summit. Dalian, China.

6.1 Methods

The materials chosen were based on previous work by Dr. Kevin Huang. Metal chlorides are a common precursor material, which are reduced to the metal sulphides with the incorporation of hydrogen sulphide gas into the system. For the copper, the precursor chosen was CuCl, this material has been used before to produce CIGS thin films by CVD [155, 156]. For the antimony precursor; $SbCl_5$ was selected, again this material has extensively been used to make other antimony containing chalcogenides for a wide range of applications [157-160]. The material choice is dictated by the cost, availability, purity, suitability for the reaction and vapour pressure. For the chalcogenide, H_2S was produced within the glove box, this is described in a little more detail later on.

The feasibility of the reaction is calculated by calculating the Gibbs free energy of the reaction. If the Gibbs free energy of the reaction is less than zero then the reaction will be spontaneous (naturally tend to occur). The calculation was carried out using the equation:

$$\Delta G_r = \sum \Delta G_{f,products} - \sum \Delta G_{f,reactants}$$

Equation 17: Gibbs free energy calculation

The data for each compound is available from references [161, 162]. The reaction equations are:

$$2\,\mathrm{CuCl} + H_2S \leftrightarrow Cu_2S + 2\,\mathrm{HCl}$$

Equation 18: Equation for the formation of Cu_2S

$$2\ \mathrm{SbCl_5} + 3\ H_2\ S \leftrightarrow\ \ Sb_2S_3\ \ + 6\ \mathrm{HCl} + 2\ Cl_2$$

Equation 19: Equation for the formation of Sb_2S_3

$$2\ \mathrm{SbCl_5} + 2\ H_2\ S \leftrightarrow\ \ 2\ \mathrm{Sb}S\ \ + 4\ \mathrm{HCl} + 3Cl_2$$

Equation 20: Equation for the formation of SbS

Table 8 shows the change in Gibbs free energy for the formation of Cu_2S at different temperatures calculated using Equation 11. The delta G for the reaction is negative around room temperature (300 K) which indicates the reaction is spontaneous (i.e. it is thermodynamically favoured), but it increases as the temperature rises (indicating the reaction become less and less spontaneous).

Table 8: Thermodynamic calculations for the formation of Cu_2S (figures rounded up to nearest thousand)

Temp (K)	Delta G (KJ)
300	-370
400	-350
500	-334
600	-318
700	-303
800	-289

Table 9 and Table 10 show the thermodynamic calculations for the formation of Sb_2S_3 and SbS respectively.

Table 9: Thermodynamic calculations for the formation of Sb_2S_3 (figures rounded up to nearest thousand)

Temp (K)	Delta G (KJ)
300	44
400	17
500	-16
600	-50
700	-84
800	-118

Table 10: Thermodynamic calculations for the formation of SbS (figures rounded up to nearest thousand)

Temp (K)	Delta G (KJ)
300	-93
400	-145
500	-195
600	-240
700	-284
800	-324

Both materials are possible products from the reaction of antimony penta-chloride with hydrogen sulphide, although the formation of Sb_2S_3 is only starts to be spontaneous around 200 ℃ (or about 500 K). From the literature it is known that antimony sulphide and copper sulphide react to form CuSbS [135]. From the above calculations and since we want to produce a 1:1 ratio of Cu:Sb) we see that a suitable temperature for these reactions would be around 700 -

800 Kelvin (425-525 ℃) as this gives a similar Gibbs free energy of formation for both materials.

We now need to look at the vapour pressures of both precursors. If the spontaneity of the reactions are similar we still need the amount of material present from each precursor to be similar. This entails having similar vapour pressures of both gases.

Table 11: Precursor vapour pressures relationship with temperature for CVD $CuSbS_2$ reactions taken from [163]

	1 Torr	5 Torr	10 Torr	20 Torr	40 Torr
CuCl	546℃	645℃	702℃	766℃	838℃
$SbCl_5$	22.7℃	48.6℃	61.8℃	75.8℃	91.8℃

Table 11 shows at what temperature we can achieve certain vapour pressures. The vapour pressure of CuCl is much lower than that of $SbCl_5$ at a similar temperature and to achieve the same vapour pressure of $SbCl_5$ at room temperature, we will need to heat the CuCl up to around 546℃. But at this temperature the spontaneity for the formation of copper sulphide is lower than that for antimony sulphide. 525℃ was chosen as a starting temperature with a balance of spontaneity and vapour pressures.

The schematic of the apparatus is shown below:

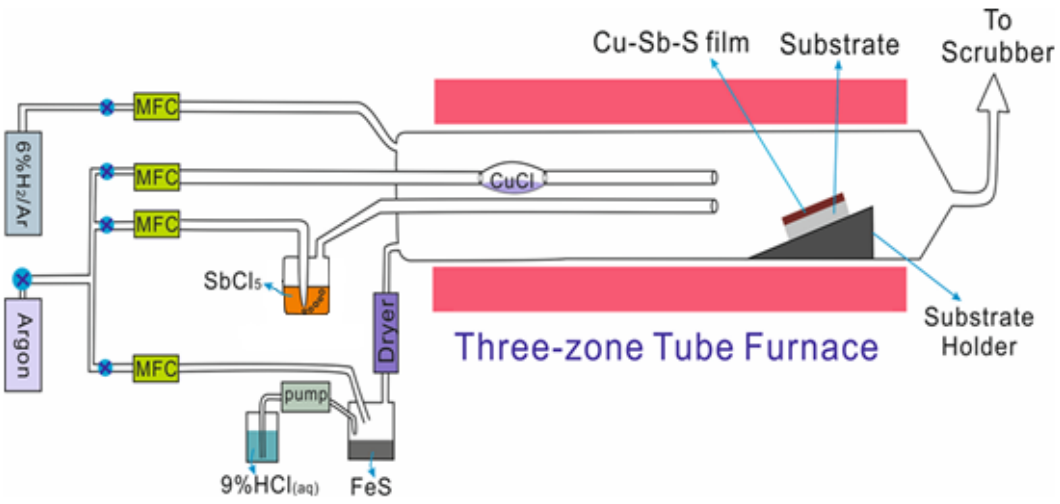

Figure 76: Schematic of CuSbS CVD setup and drawing by Dr. Kevin Huang (edited by author)

In the apparatus, the antimony chloride ($SbCl_5$) is in liquid form and the copper chloride (CuCl) is in solid form. An Elite™ three zone furnace was used to heat the copper chloride precursor and the substrates. The three zones were set at different temperatures. The whole apparatus was confined within a custom made nitrogen purged glove box for extra safety and to minimise oxidation. The CuCl was placed in a quartz injection tube. The $SbCl_5$ in a bubbler (a custom made glass apparatus that allows argon to pass through the liquid to deliver the precursor vapour into the deposition furnace without the access of air into the system).

Finally the H_2S was generated in situ by reacting 9% HCl with FeS. All precursors were introduced into the furnace using an argon carrier gas through a mass flow controller (MFC).

A glass substrate holder was used to improve the flow of gases over the substrate to ensure a more uniform deposition. The deposition was carried out on a pre-cleaned soda lime substrate (by rinsing in acetone, isopropanol, deionised water and then dried using a nitrogen gun).

The morphological and compositional properties of the films were analysed using a secondary electron microscope (SEM - a Carl Zeiss EVO 50) and energy

dispersive X-ray system (EDX system - Oxford Instruments INCA PentaFET fitted on the SEM)

6.2 Results and Discussion

The SEM images of the run are shown in Figure 77 and Figure 78. The measurement on Figure 78 shows a thickness of 35 µm for a 1 hour deposition.

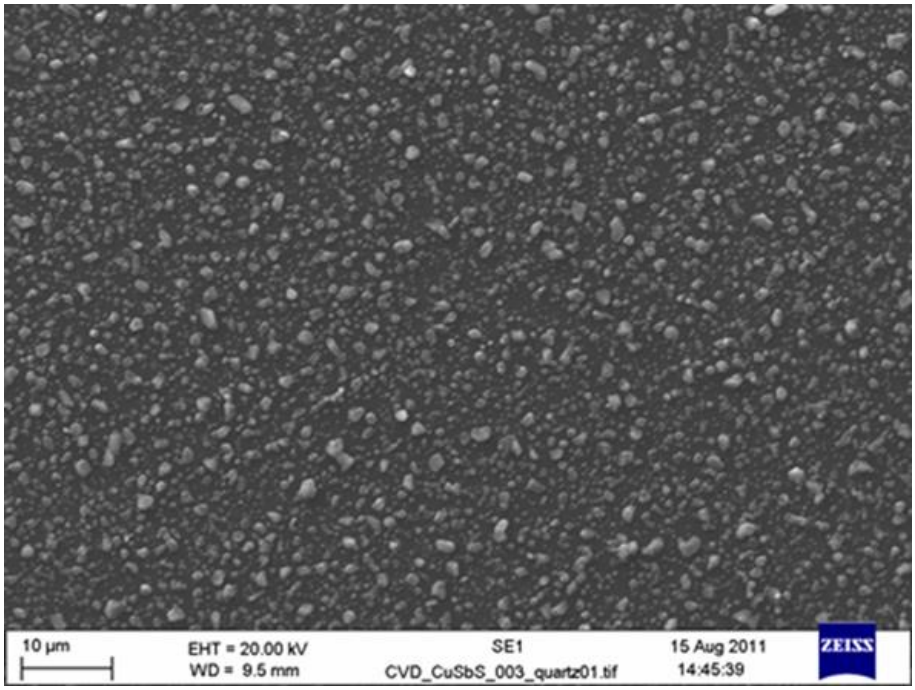

Figure 77: Top view SEM of first CuSbS deposition by CVD, deposited at 525 °C.

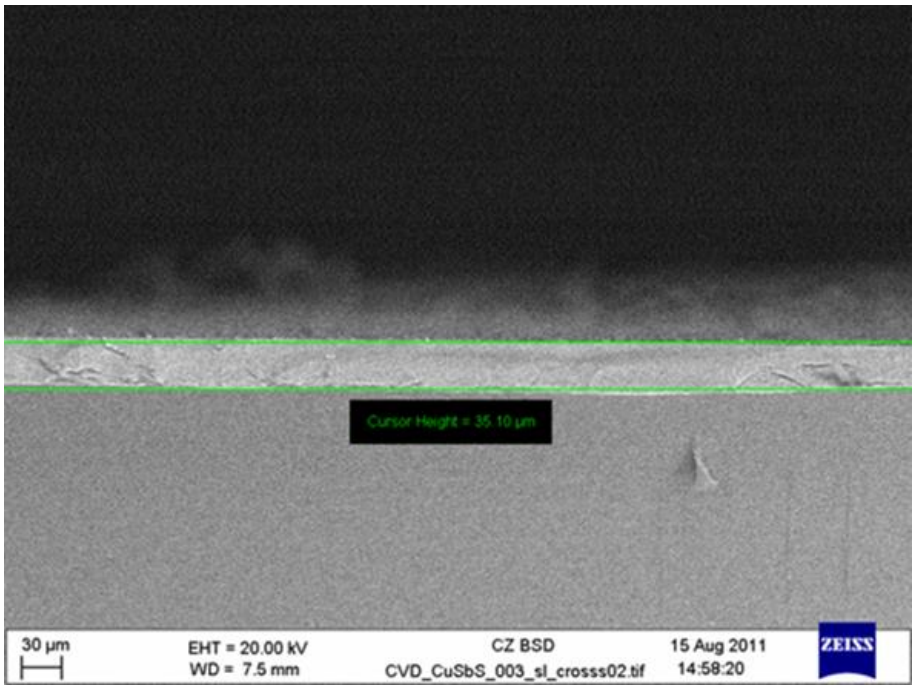

Figure 78: SEM cross section of first CuSbS deposition by CVD, deposited at 525 °C.

The EDX measurements are shown in Table 12.

Table 12: EDX of CuSbS runs – all values in atomic percentage

Substrate	Cu %	Sb %	S %
Soda lime	27.8	18.4	53.8

6.3 Conclusions

CuSbS thin films were successfully deposited using an atmospheric pressure chemical vapour deposition system. The precursors used were antimony chloride ($SbCl_5$) in liquid form, copper chloride (CuCl) and H_2S generated in situ for the reaction. The precursors were chosen from other studies undertaken to make other chalcogenide materials along with considerations of cost, availability, purity, suitability for the reaction and vapour pressure. The feasibility of the reaction is calculated by calculating the Gibbs free energy of the reaction.

$CuSbS_x$ was successfully deposited on soda lime substrates. The morphological and compositional properties of the films were analysed using SEM and EDX. The SEM images show a very fast deposition of around 35 µm in 1 hour. The EDX shows a slightly copper rich material. This chapter forms a proof of principle study suggesting the viability of producing $CuSbS_x$ films using atmospheric pressure CVD. Further work would include the fabrication of complete cells and a comparison with other techniques.

Chapter 7: Copper Antimony Sulphide by Two Stage Process

This work has contributed to the following:

AL-SAAB, F., HUANG, C. C., YAO, J., HAYDEN, B. & HEWAK, D. 2014. RTA annealed RF sputtered single phase CuSbS films. *Thin Solid films,* Submitted.

AL-SAAB, F., HUANG, C. C., HAYDEN, B. & HEWAK, D. 2014. RF sputtered single phase CuSbS thin films. *E-MRS Spring* Lille, France.

AL SAAB, F., GHOLIPOUR, B., HUANG, C. C., ANASTASOPOULOS, A., HAYDEN, B. & HEWAK, D. W. 2013. Crystallization Study of the $CuSbS_2$ Chalcogenide Material for Solar Applications. *PV-SAT 9.* Swansea University, Swansea, Wales.

7.1 Methods

These experiments were done in four parts:

- Annealing of $CuSbS_2$ at 250, 300, 325 and 350 ℃
- Annealing of $CuSbS_2$ at 250 ℃ for various durations
- Annealing of $CuSbS_2$ at 300 ℃ for various durations
- Fabrication of $CuSbS_2$ solar cell by two stage process

7.1.1 Annealing at 250, 300, 325 and 350 ℃

500 nm molybdenum samples were deposited on B270 soda lime glass (from Schott) slides (35 mm by 35 mm in size) by RF magnetron sputtering at room temperature at a base pressure of 1.0×10^{-4} Torr.

The deposition was performed using 40 W and an argon flow of 40 standard cubic centimetres (sccm); this gave a deposition rate of around 0.5 Angstroms per second.

400 nm of CuSbS was deposited by RF magnetron sputtering at room temperature from a single quaternary target on the Mo coated substrates at a base pressure of 9.1×10^{-5} Torr. The deposition was performed using 45 W and

an argon flow of 40 sccm; this gave a deposition rate of around 0.14 angstroms per second.

The CuSbS was then annealed in a Jipelec JetFirst 100 bench top rapid thermal processor (RTP) using the following recipes:

Table 13: CuSbS annealing recipe

Duration (sec)	Argon (sccm)	Initial Temp. (℃)	Final Temp (℃)
60	100	0	20
180	200	20	20
Ramp time	100	20	Annealing temperature
Duration	100	Annealing temperature	Annealing temperature
Ramp time	100	Annealing temperature	20
180	100	20	20

The ramp time (50 ℃ /min.), annealing temperature and annealing duration were varied according to the following table:

Table 14: Ramp times, annealing temperatures and annealing durations for CuSbS

Run	Ramp time (min)	Annealing temperature (℃)	Duration (min)
1	5	250	5
2	6	300	5
3	6.5	325	5
4	7	350	5

The compositional, morphological and structural properties of the films were analysed using secondary electron microscopy, energy dispersive X-ray system and an X-ray diffraction system.

7.1.2 Annealing at 250 ℃

500 nm molybdenum samples were deposited on B270 soda lime glass (from Schott) slides (35 mm by 35 mm in size) by RF magnetron sputtering at room temperature at a base pressure of 1.0 x 10^{-5} Torr. The deposition was performed using 160 W and an argon flow of 22 standard cubic centimetres (sccm); this gave a deposition rate of around 0.6 angstroms per second.

200 nm of CuSbS was deposited by RF magnetron sputtering at room temperature from a single quaternary target on the Mo coated substrates at a base pressure of 4.5 x 10^{-5} Torr. The deposition was performed using 100 W and an argon flow of 40 sccm; this gave a deposition rate of around 0.06 angstroms per second.

The CuSbS was then annealed in a Jipelec JetFirst 100 bench top rapid thermal processor using a similar recipe as Table 13 above. The difference here is that all samples were annealed at 250 ^{o}C. A similar ramp rate of 50 ^{o}C /min was used. The annealing duration was varied according to the following table:

Run	Ramp time (min)	Annealing temperature (℃)	Duration (min)
1	5 min.	250	5
2	5 min.	250	15
3	5 min.	250	30
4	5 min.	250	60

Another variation here is that the annealing chamber was pumped to a pressure of 1mTorr using a scroll pump for 10 seconds, followed by a nitrogen purge of 60 seconds. This cycle was repeated 3 times before the temperature profile was initiated.

The compositional and structural properties of the films were analysed using an energy dispersive X-ray system and an X-ray diffraction system.

7.1.3 Annealing at 300 ℃

500 nm molybdenum samples were deposited on B270 soda lime glass (from Schott) slides (35 mm by 35 mm in size) by RF magnetron sputtering at room temperature at a base pressure of 1.0×10^{-4} Torr. The deposition was performed using 160 W and an argon flow of 22 standard cubic centimetres (sccm); this gave a deposition rate of around 0.6 angstroms per second.

2000 nm of CuSbS was deposited by RF magnetron sputtering at room temperature from a single quaternary target on the Mo coated substrates at a base pressure of 6.0×10^{-5} Torr. The deposition was performed using 100 W and an argon flow of 50 sccm; this gave a deposition rate of around 0.1 angstroms per second.

The CuSbS was then annealed in a Jipelec JetFirst 100 bench top rapid thermal processor using a similar recipe as Table 13 above. The difference here is that all samples were annealed at 300 °C. A similar ramp rate of 50 °C /min was used. The annealing duration was varied according to the following table:

Run	Ramp time (min)	Annealing temperature (℃)	Duration (min)
1	6	300	15
2	6	300	30
3	6	300	60

The pump and purge cycles were used here again prior to the annealing recipe (similar to the samples annealed at 250 ℃).

The compositional, morphological and structural properties of the films were analysed using secondary electron microscopy, energy dispersive X-ray system and an X-ray diffraction system.

7.1.4 Fabrication of CuSbS solar cells

To fabricate cells, 2000 nm of CuSbS was deposited by RF magnetron sputtering at room temperature from a single quaternary target on CdS coated substrates at a base pressure of 1.0 x 10^{-5} Torr. The deposition was performed using 60 W and an argon flow of 30 sccm; this gave a deposition rate of around 0.1 angstroms per second.

The CdS was deposited by Dr. Jon Major in Professor Ken Durose's solar photovoltaic research group in the University of Liverpool. The CdS was deposited by RF magnetron sputtering at 200 ℃. The deposition was performed using 60 W for 24 minutes. Fluorine doped tin oxide coated substrates (TEC10 FTO by Pilkington) were used (covered from one side to allow for probing).

The CuSbS was then annealed in a Jipelec JetFirst 100 bench top rapid thermal processor at 300℃ for 60 min using a ramp rate of 50 ℃ /min.

Finally the substrates were masked using a stainless steel shadow mask. This was designed to have several 1mm by 1mm equally spaces gaps. 400 nm of molybdenum was deposited at 100 ℃ on top at a base pressure of 3.0 x 10^{-4} Torr. The deposition was performed using 100 W and an argon flow of 22 standard cubic centimetres (sccm); this gave a deposition rate of around 0.6 angstroms per second. A schematic of the cells is shown below in Figure 79.

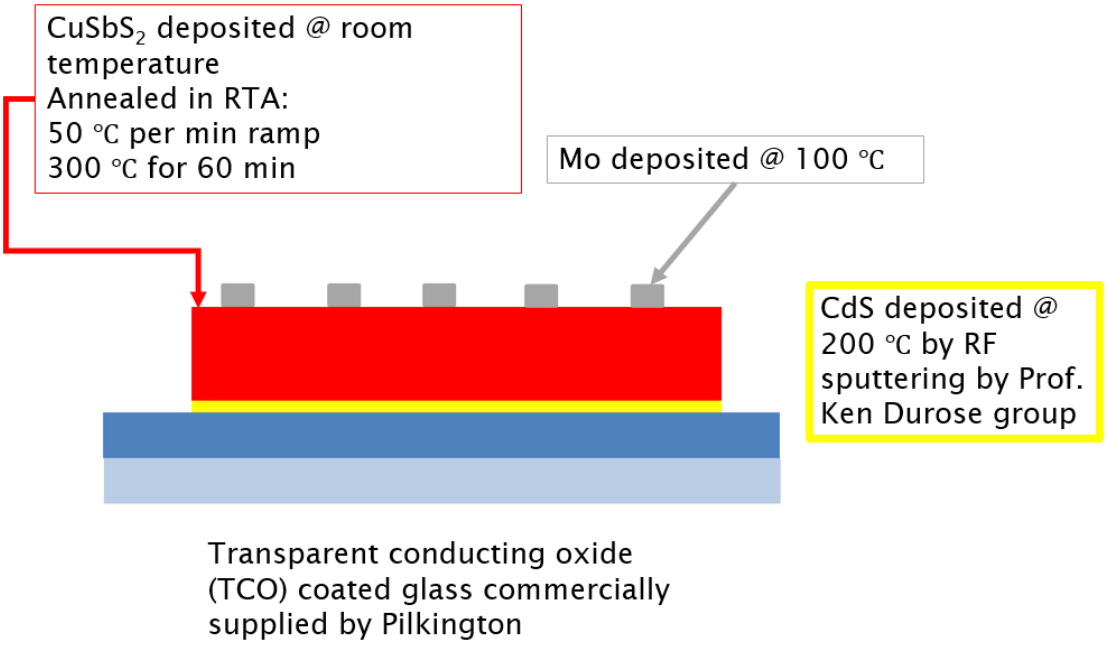

Figure 79: Schematic of CuSbS cell design fabricated by two stage process

7.2 Results and Discussion

7.2.1 Annealing at 250, 300, 325 and 350 ℃

For the samples annealed for the range of temperatures from 250 to 350 ℃. The ratio of the three elements was close to the 1:1:3 for the as deposited film and those annealed up to 300 ℃ (the stoichiometry remained within the margin of error for the technique). This is shown in Figure 80. Above this temperature it seems antimony starts to evaporate off the materials surface, this is consistent with the findings of Colombara [133], where an antimony instability is seen in $CuSbS_2$ films. In all films no flaking or peeling is observed.

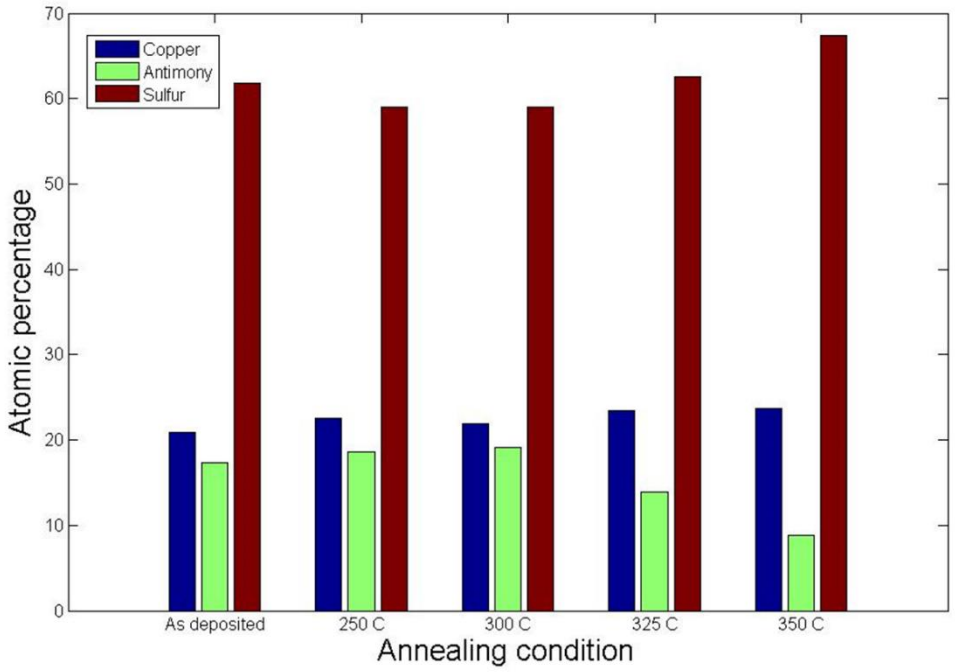

Figure 80: EDX of CuSbS annealed at 250 to 350 ℃ for 5 min. The film was 400 nm of $CuSbS_2$ deposited at room temperature.

In Figure 81, SEM images of the top surface of the films is shown. Once annealed crystal peaks are seen on the surface of the material. As we increase above 300 ℃ the rest of the film becomes rougher around these crystal peaks which can be attributed to the antimony leaving the surface of the material.

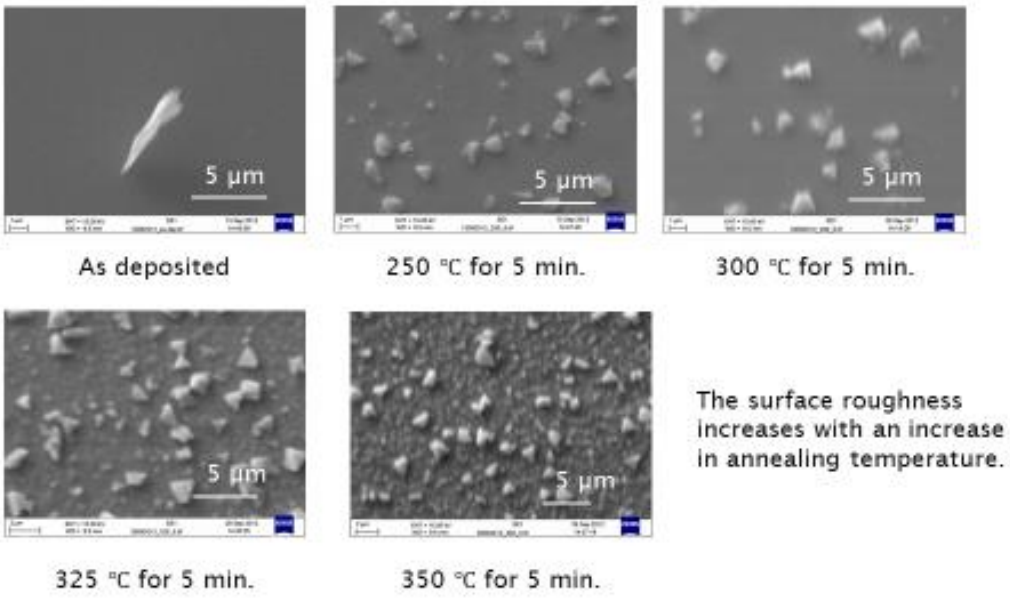

Figure 81: SEM of surface of CuSbS annealed at 250 to 350 ℃ for 5 min. The film was 400 nm of $CuSbS_2$ deposited at room temperature.

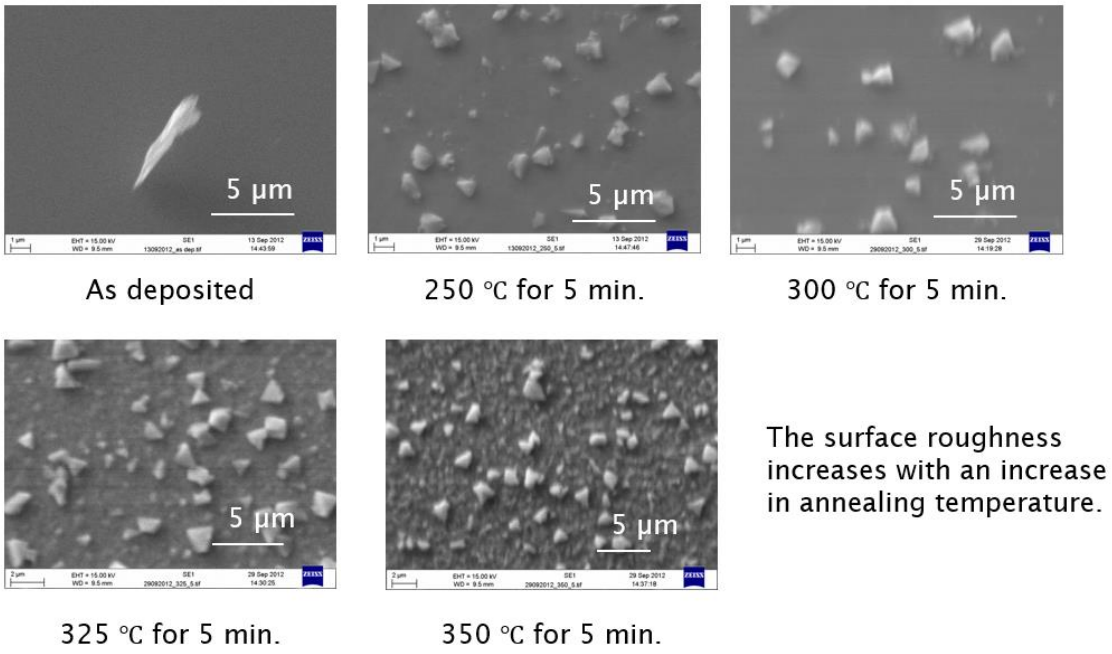

Figure 82: SEM of the cross section of CuSbS annealed at 250 to 350 ℃ for 5 min. The film was 400 nm of $CuSbS_2$ deposited at room temperature.

In Figure 82 above, the sample annealed at 250 ℃ does not show a significant change in crystal structure and therefore we can assume nucleation has occurred but the crystals have not grown yet. The sample annealed at 300 ℃ shows a large and apparent change in crystal structure. Samples annealed at higher temperatures also show a large increase in grain size, but as mentioned before at these temperatures, antimony loss is observed in the films making them Cu rich.

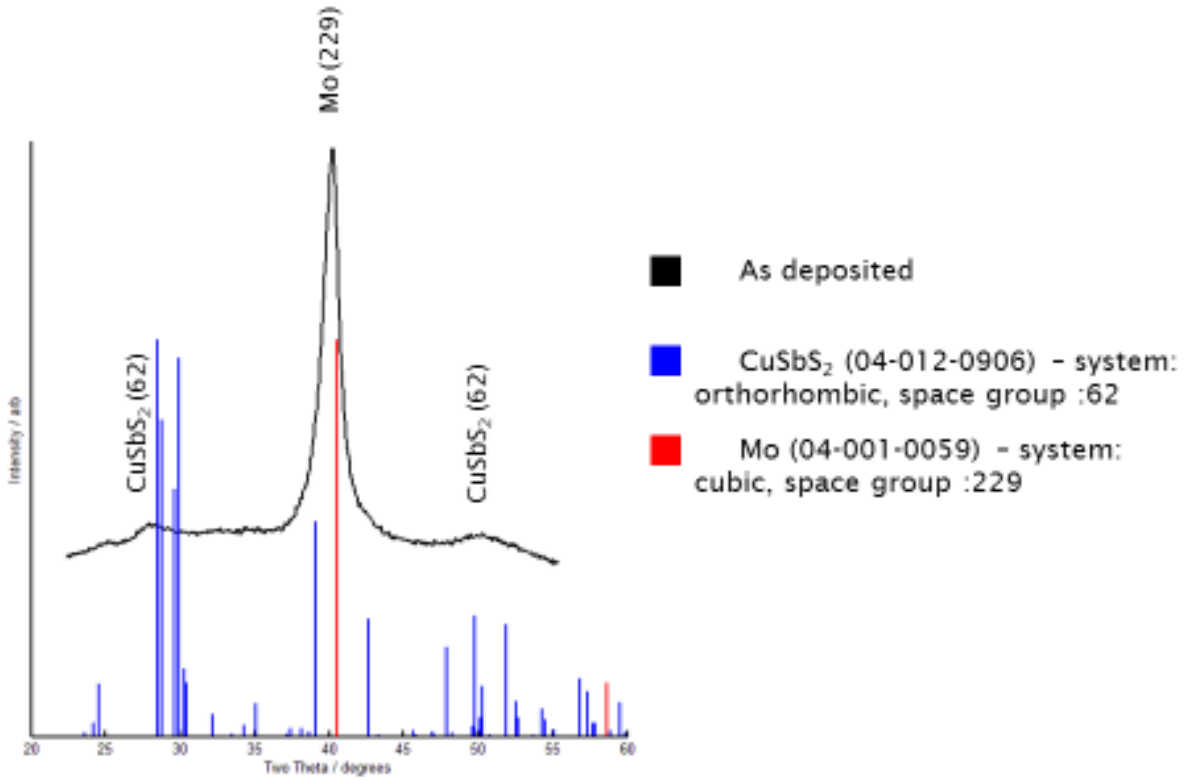

XRD diffractogram of CuSbS as deposited. The film was 400 nm of $CuSbS_2$ deposited at room temperature.

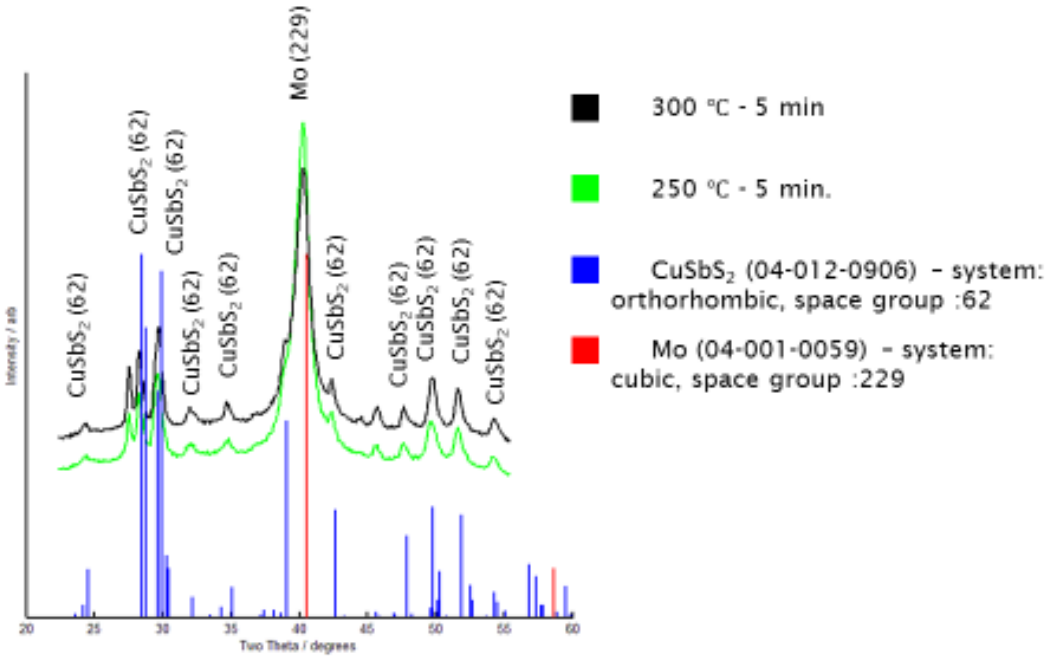

Figure 83: XRD diffractogram of CuSbS annealed at 250 °C and 300 °C. The film was 400 nm of $CuSbS_2$ deposited at room temperature.

The $CuSbS_2$ (62) orthorhombic phase is matched to the samples annealed up to 300°C (Figure 83). Above this temperature (antimony loss occurs) and the $CuSbS_2$ crystals form the Cu rich $Cu_{12}Sb_4S_{13}$ (217) cubic phase (Figure 84). In all the samples, 2 peaks are present that have been assigned to 3 possible phases: (1) $Cu_{1.8}S$ (225) cubic phase (2) Cu_2S (194) hexagonal phase (3) Cu_9S_5 (166) rhombohedral phase (Figure 85)

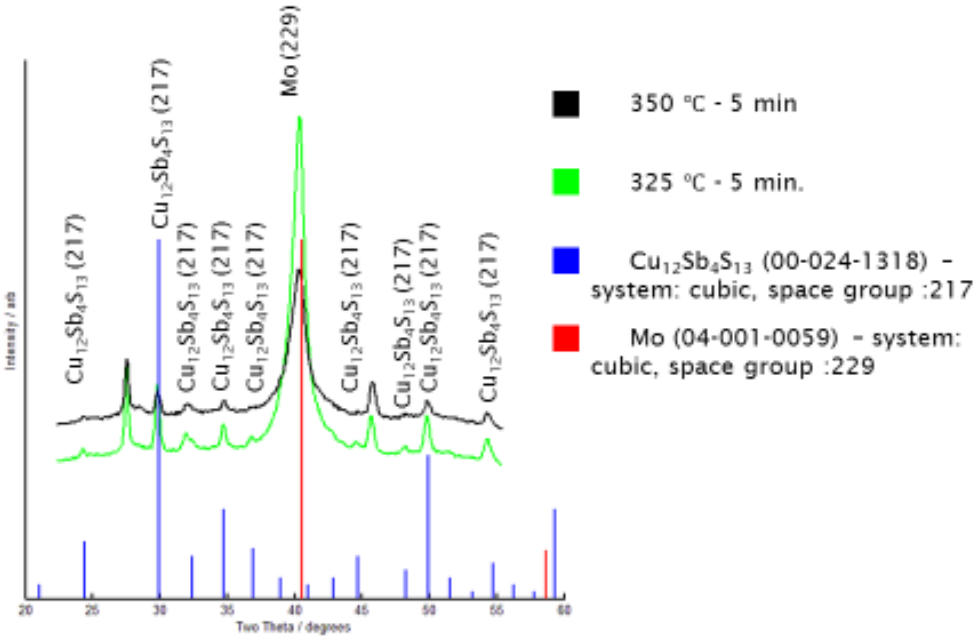

Figure 84: XRD diffractogram of CuSbS annealed at 325 and 350℃. The film was 400 nm of $CuSbS_2$ deposited at room temperature.

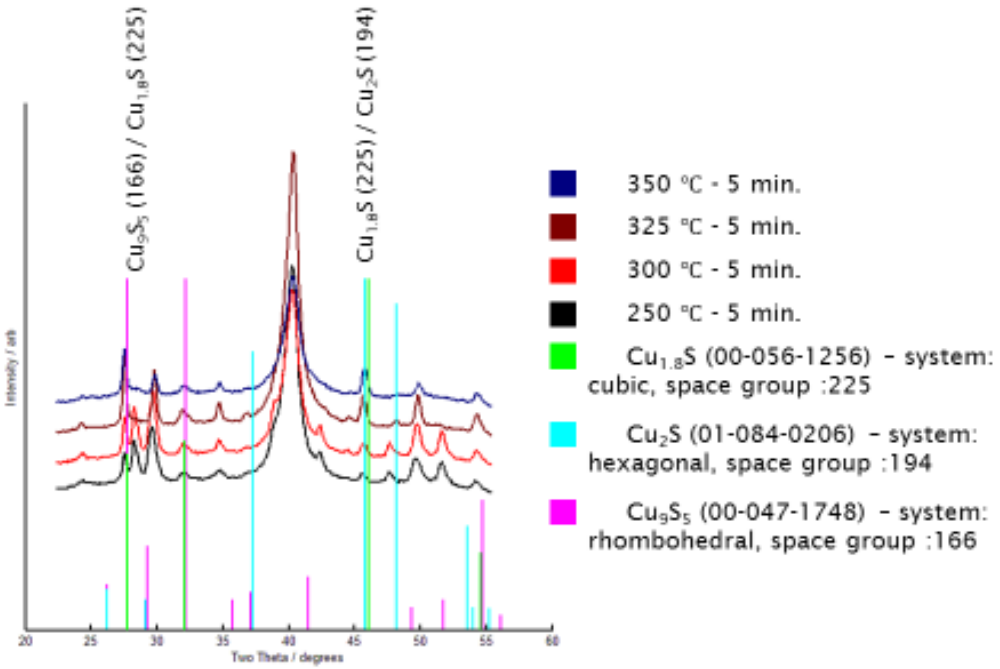

Figure 85: XRD diffractogram showing possible secondary phases. The film was 400 nm of $CuSbS_2$ deposited at room temperature.

7.2.2 Annealing at 250 ℃

Next samples were annealed at 250 ℃ for different durations. The EDX shows films with a composition close the 1:1:3 stoichiometry although with slight variations which can be attributed to the EDX apparatus margin of error.

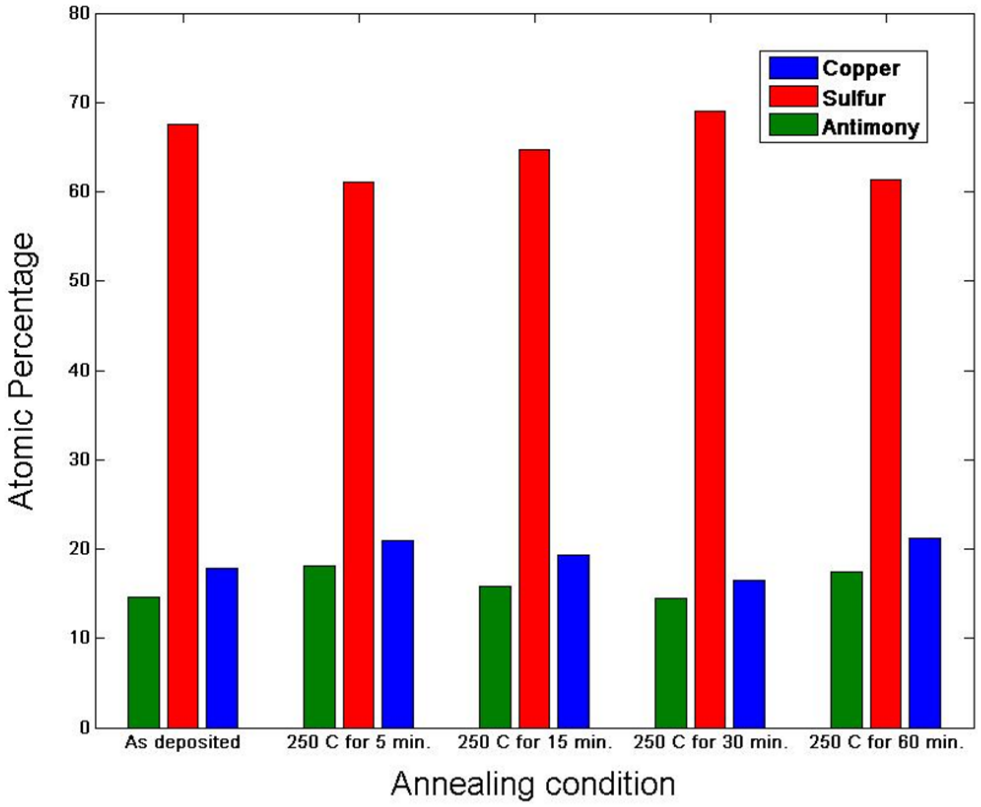

Figure 86: EDX of CuSbS annealed for varying durations at 250 ℃. The film was 200 nm of $CuSbS_2$ deposited at room temperature.

The XRD diffractograms are shown in Figure 87 below. Single phase $CuSbS_2$ appears to be present. Higher temperatures could lead to larger crystals, but it seems the changes in the recipes have resulted in single phase $CuSbS_2$ to be produced. Also, as the stoichiometry shows a 1:1:3 composition and the crystals are 1:1:2; this means there are amorphous phases still present which are sulphur rich.

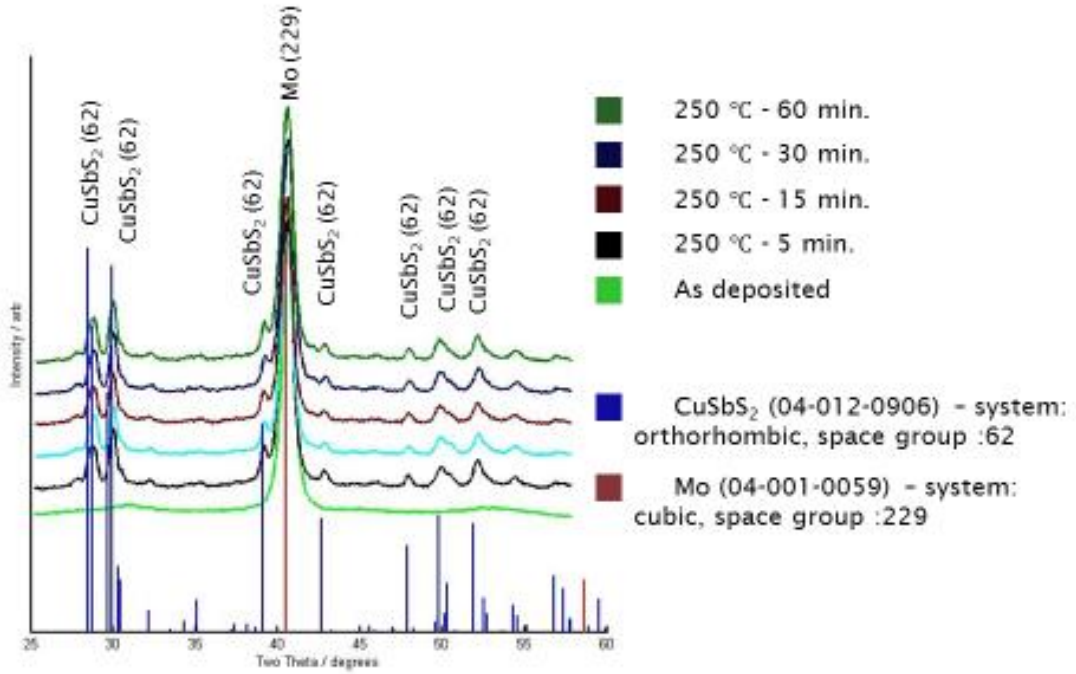

Figure 87: XRD diffractograms of CuSbS annealed for varying durations at 250 ℃. The film was 200 nm of $CuSbS_2$ deposited at room temperature.

The deposition power was increased as the deposition rate dropped significantly using the initial deposition parameters (even with the higher power the new rate was at 0.06 Å/s compared to 0.14 from the previous depositions), it seems that the higher power produces films with single phase, another explanation could be that the target is closer to the stoichiometry away from the surface and therefore the secondary phases disappear after these initial layers are removed from the target. All targets are degassed and 100 nm of material is deposited to prepare the target for experiments, which is usually sufficient, but it may be that this is not the case with these targets.

7.2.3 Annealing at 300 ℃

Samples were then annealed at 300 ℃ for different durations. The EDX shows films with a composition that has digressed from the 1:1:3 stoichiometry (the films are sulphur poor compared to those annealed at 250 ℃). The as deposited films show the 1:1:2 stoichiometry and the composition does not change with annealing and therefore it is not an effect of annealing but the deposition itself. Here 100 W was used (similar to the films annealed at 250 ℃), the argon was increased by 10 sccm as the plasma showed slight instabilities. The rate increase to 0.1 Å/s allowed for less sulphur to be incorporated into the films and therefore produces films with lower sulphur content.

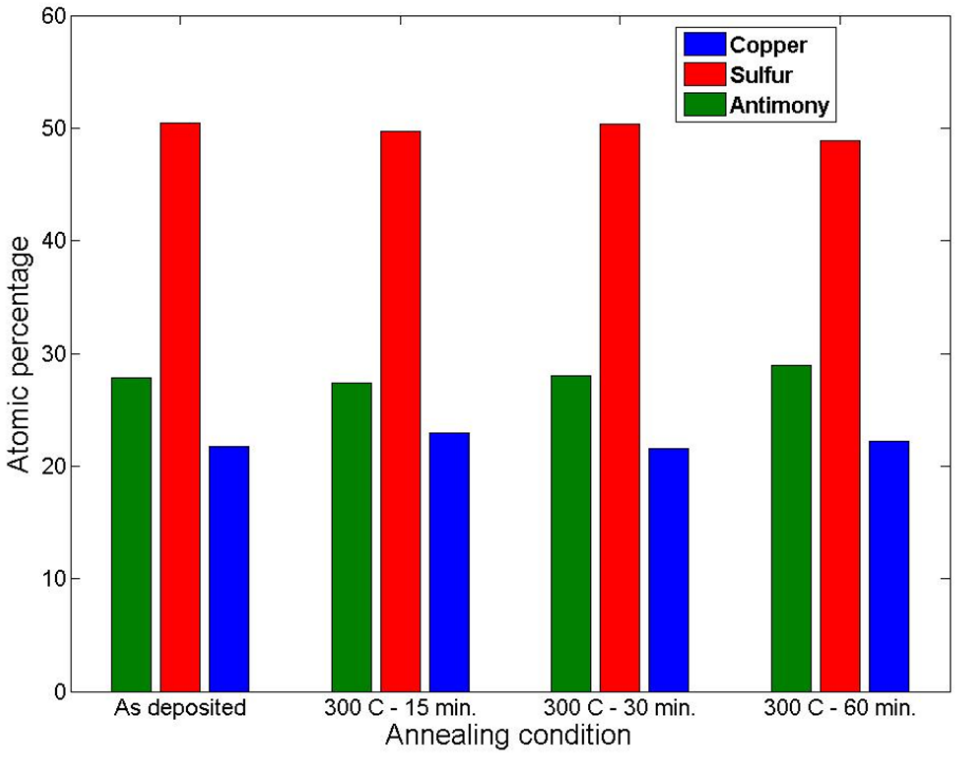

Figure 88: EDX of CuSbS annealed for varying durations at 300 ℃. The film was 2000 nm of $CuSbS_2$ deposited at room temperature.

The XRD diffractograms are shown in Figure 89 below. Single phase CuSbS appears to be present again. Also, as the stoichiometry now shows a 1:1:2 composition we can deduce that the films are predominantly $CuSbS_2$.

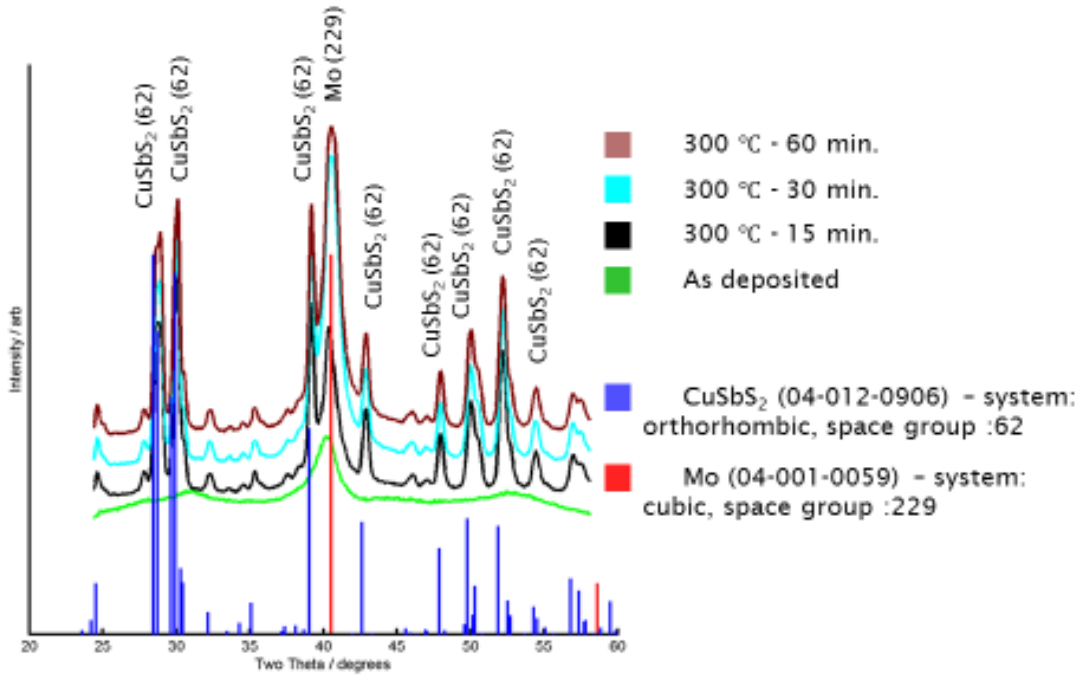

Figure 89: XRD diffractograms of CuSbS annealed for varying durations at 300 ℃. The film was 2000 nm of $CuSbS_2$ deposited at room temperature.

Figure 90 below shows the SEM cross section of the film annealed at 300 ℃ for 60 min. the crystals appear to range from 100 nm to above 500 nm. This recipe is used to fabricate cells on CdS and fluorine doped tin oxide (FTO). (See section below).

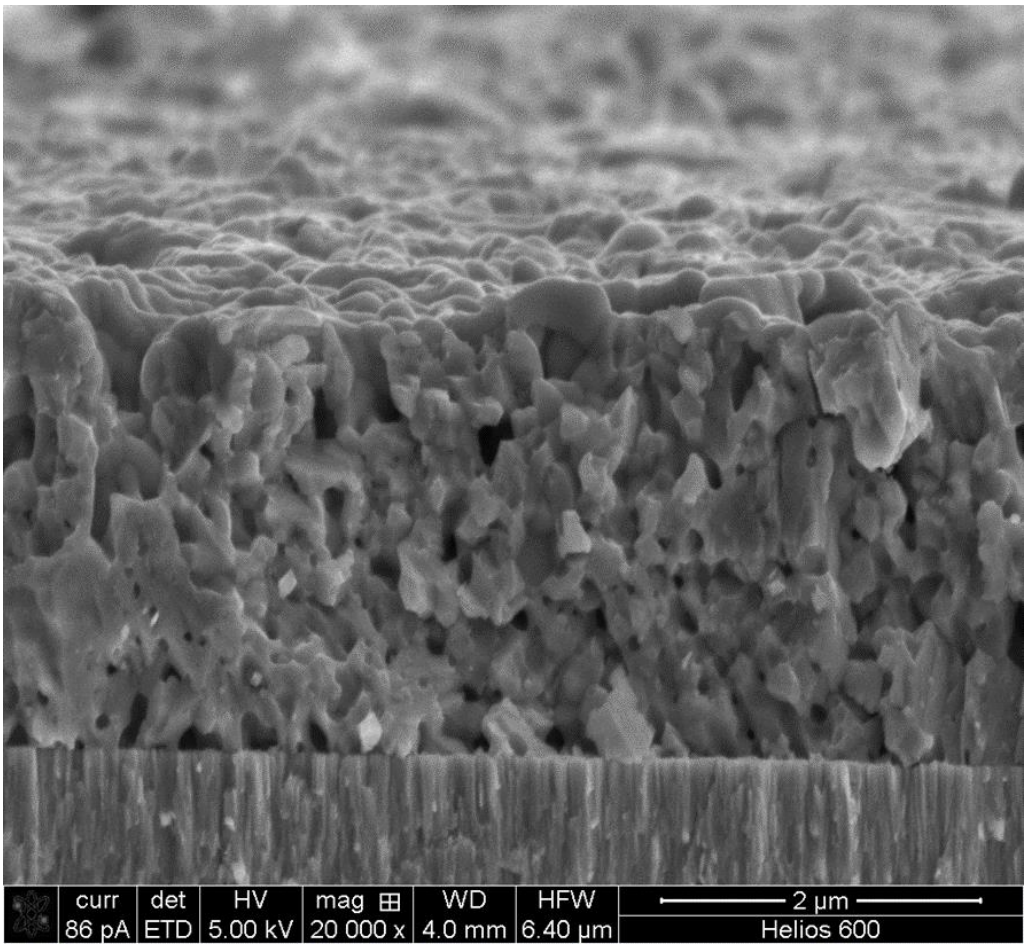

Figure 90: SEM of the cross section of CuSbS annealed at 300 ℃ for 60 min. The film was 2000 nm of $CuSbS_2$ deposited at room temperature.

7.2.4 Characterisation of $CuSbS_2$ solar cells by two stage process

Figure 91 shows the current voltage characteristics of a cell characterised. Both the dark and illuminated currents are shown. The measurement is repeated a few times to show reproducibility.

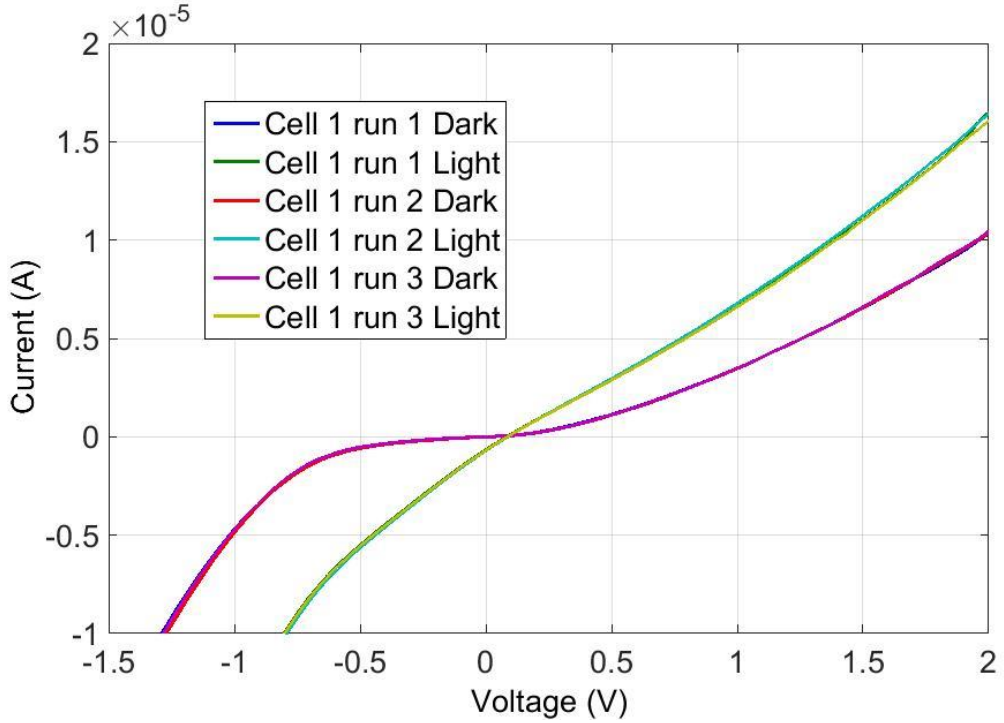

Figure 91: Current-voltage characteristics of three measurements on the same cell. The absorber layer was 2000 nm of $CuSbS_2$ deposited at room temperature and annealed at 300 ℃ for 60 min.

From the light and dark curves above, a few conclusions can be drawn. In the positive voltage region, we see an increase in the diffusion current, usually with illumination the drift current increases while the diffusion remains similar to that produced from the cell in the dark with the same bias voltage. A possible explanation for this is that the majority carriers are significantly increased with illumination – causing an increase in diffusion current.

In the negative region, the diffusion current is also increased by this phenomenon. The difference here is that as we increase the reverse bias voltage, even with the increase in majority carriers produced by illumination; the barrier height of the junction is increased to a point where the drift current dominates. This produces a high contrast between the dark and illuminated current-voltage characteristics.

The photocurrent produced by the cells is shown in Figure 92 below; the graph shows a zoomed in plot around v=0, which shows the short circuit voltage.

The maximum short circuit current seen is around 0.7 µA (which gives a current density of 0.07 mA/cm^2 as the cell area is 1 mm^2), the maximum open circuit voltage is around 0.09 V; using Equation 10, this gives a conversion efficiency of 0.007 %.

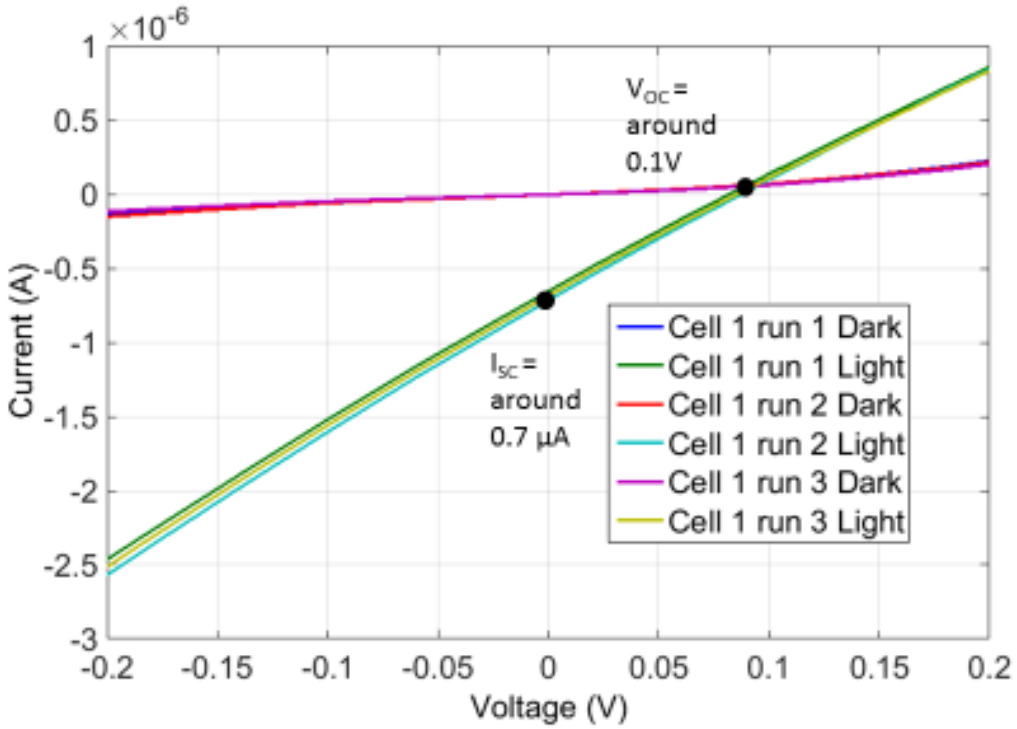

Figure 92: Photocurrent of thin film $CuSbS_2$ solar cell device. The absorber layer was 2000 nm of $CuSbS_2$ deposited at room temperature and annealed at 300 ℃ for 60 min.

7.3 Conclusion

In this work, $CuSbS_2$ thin films were first deposited by RF magnetron sputtering at room temperature from a single ternary target on molybdenum coated substrates using a Kurt Lesker NANO-38 thin film deposition system. The films were annealed in a Jipelec JetFirst 100 bench top rapid thermal processor at various temperatures (250 to 325℃) and times (5 to 60 min). The annealing was done without any toxic gases or reactive sulphur. The compositional, optical, electrical and structural properties of the films were analysed using SEM, EDX and XRD. Single phase $CuSbS_2$ films with good adhesion, good crystallinity and with no apparent sulphur loss can be achieved. The surface roughness of the films increases with an increase in annealing temperature. Above 300 ℃, an instability and loss of antimony is seen in the films. Longer anneals don't seem to change the composition of the films or the phases formed. By adding purge and pump cycles to the annealing recipe and removing any impurities in the annealing chamber, the films are improved and no secondary phases are formed.

The grain sizes were measured by SEM imaging for the films annealed at 300 ℃ for one hour, and are between 100 and 200 nm in size; although the grains are still relatively small compared to the film thickness. Smaller cells are made compared to those in the previous chapters, also the cell design is changed, and a commercial TCO is used along with commercial grade CdS supplied from collaborators. This has allowed working cells to be produced.

Current voltage characteristics of the cells showed a maximum open circuit voltage of around 0.1 V, a short circuit current of around 0.7 μA and a conversion efficiency of 0.007 %. A low efficiency, but the first cells made with this technique. Further improvements include etching the surface of the films (to remove surface defects), increasing the doping concentrations (to increase the majority carrier concentrations), producing larger grains and using a chamber with no flaking.

Chapter 8: Copper Antimony Sulphide by Single Stage Process

8.1 Methods

These experiments in this section were carried out in 4 parts:

- The deposition and characterisation of $CuSbS_2$ deposited at 200 ℃.
- Etching of $CuSbS_2$ with bromine and HCl.
- The deposition and characterisation of $CuSbS_2$ deposited at 200 ℃.
- Fabrication of $CuSbS_2$ solar cell by a single stage process.

8.1.1 Deposition at 200 ℃

1000 nm molybdenum samples were deposited on B270 soda lime glass (from Schott) slides (35 mm by 35 mm in size) by RF magnetron with a substrate temperature of 200 ℃ at a base pressure of 5.0×10^{-4} Torr. The deposition was performed using 160 W and an argon flow of 22 standard cubic centimetres (sccm); this gave a deposition rate of around 0.6 Angstroms per second.

6000 nm of CuSbS was deposited by RF magnetron sputtering with a substrate temperature of 200 ℃ from a single quaternary target on the Mo coated substrates at a base pressure of 5.0×10^{-4} Torr. The deposition was performed using 80 W and an argon flow of 25 sccm; this gave a deposition rate of around 0.45 angstroms per second.

The compositional, morphological and structural properties of the films were analysed using secondary electron microscopy, energy dispersive X-ray system and an X-ray diffraction system.

8.1.2 Etching of CuSbS with bromine and HCl

1000 nm of CuSbS was deposited by RF magnetron sputtering with a substrate temperature of 200 ℃ from a single quaternary target on the Mo coated substrates at a base pressure of 1.0×10^{-5} Torr. The deposition was performed

using 25 W and an argon flow of 20 sccm; this gave a deposition rate of around 0.2 angstroms per second.

HCl and Br_2 in methanol have been used to etch CZTS absorbers [164]. Here the effect of these two etchant on $CuSbS_2$ is investigated. The films were etched using a 0.02 molar bromine solution made up by adding about 1 ml of bromine to 81 ml of methanol. The etching was carried out for 30, 60 and 90 Seconds. The films were also etched in a solution of 36% HCl solution.

The compositional, morphological and structural properties of the films were analysed using secondary electron microscopy, energy dispersive X-ray system and an X-ray diffraction system.

8.1.3 Deposition at 250 ℃

1000 nm molybdenum samples were deposited on B270 soda lime glass (from Schott) slides (35 mm by 35 mm in size) by RF magnetron with a substrate temperature of 250 ℃ at a base pressure of 2.5 x 10^{-4} Torr. The deposition was performed using 160 W and an argon flow of 22 standard cubic centimetres (sccm); this gave a deposition rate of around 0.6 angstroms per second.

4500 nm of CuSbS was deposited by RF magnetron sputtering with a substrate temperature of 250℃ from a single quaternary target on the Mo coated substrates at a base pressure of 1.0 x 10^{-4} Torr. The deposition was performed using 100 W and an argon flow of 40 sccm; this gave a deposition rate of around 0.1 angstroms per second.

The compositional, morphological and structural properties of the films were analysed using secondary electron microscopy, energy dispersive X-ray system and an X-ray diffraction system.

8.1.4 Fabrication of cells with CuSbS deposited at 240 ℃

To fabricate cells, 800 nm of CuSbS was deposited by RF magnetron with a substrate temperature of 240 ℃ from a single quaternary target on CdS coated substrates at a base pressure of 1.0 x 10^{-5} Torr. The deposition was performed using 60 W and an argon flow of 30 sccm; this gave a deposition rate of around 0.45 angstroms per second. The temperature of 240 ℃ was used rather than 250 ℃ as the degassing of the chamber walls along with the samples caused the

interlock to trip, therefore the temperature was reduced to ensure a complete uninterrupted deposition. The power here is further decreased although this has little change on the deposition rate.

The CdS was deposited by Dr. Jon Major in Professor Ken Durose's solar photovoltaic research group in the University of Liverpool. The CdS was deposited by RF magnetron sputtering at 200 ℃. The deposition was performed using 60 W for 24 minutes. Fluorine doped tin oxide coated substrates (TEC10 FTO by Pilkington) were used (covered from one side to allow for probing).

Finally the substrates were masked using a stainless steel mask. This was designed to have several 1mm by 1mm equally spaces gaps. 400 nm of molybdenum was deposited at 100 C on top at a base pressure of 4.0 x 10^{-4} Torr. The deposition was performed using 100 W and an argon flow of 22 standard cubic centimetres (sccm); this gave a deposition rate of around 0.55 angstroms per second. A density factor of 10.2 g/cm^3, an acoustic impedance factor of 0.5 g/ (cm^2 sec) and a tooling factor of 140 was used.

A schematic of the cells is shown below in Figure 93.

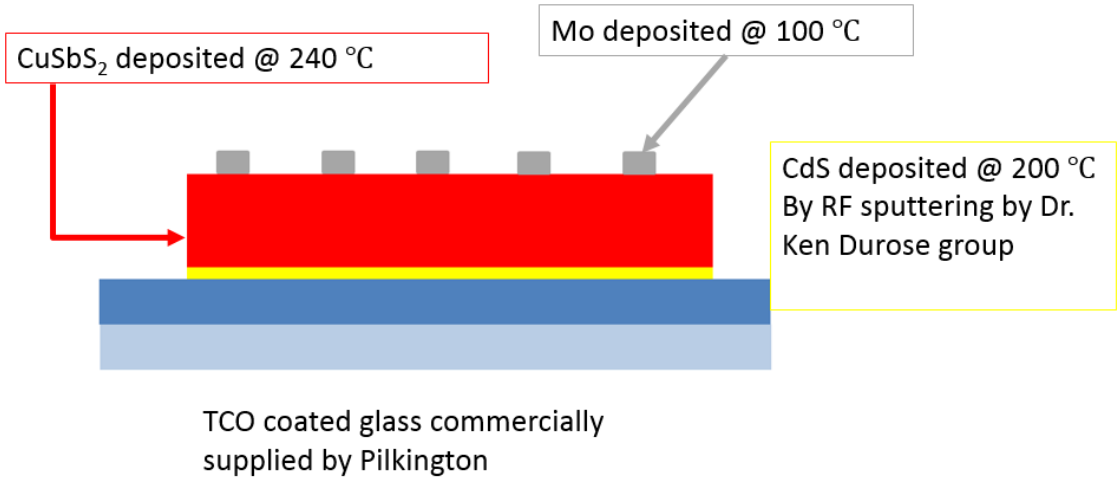

Figure 93: $CuSbS_2$ solar cell fabricated by single stage method

The compositional and structural properties of the cells films were analysed using a Nikon eclipse LV100 optical microscope, an energy dispersive X-ray system and an X-ray diffraction system (XRD system - Rigaku Smart lab; the X-rays are provided by a CuK_{α_1} source), the source angle was set at 11 degrees and the detector moved to all required angles.

8.2 Results and Discussion

8.2.1 Deposition at 200 ℃

Figure 94 shows the EDX measurement on the CuSbS deposited at 200 ℃. It is very clear that the material is Sb rich.

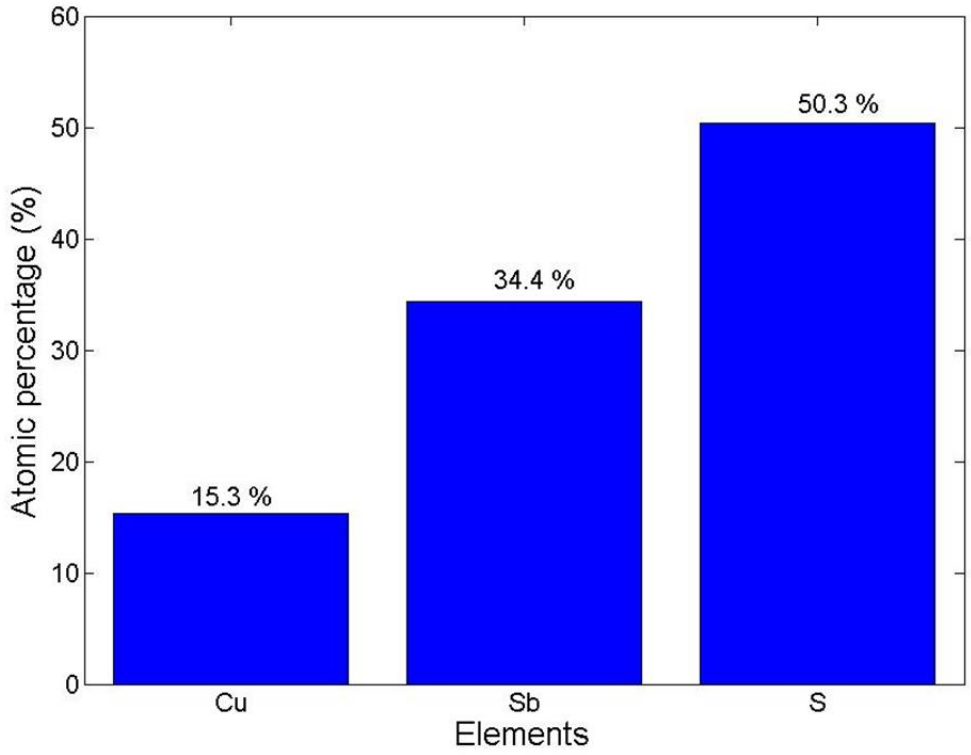

Figure 94: EDX of $CuSbS_x$ deposited at 200 ℃.. The film thickness was 6000 nm.

The rate (even though the power was lowered) increased as the chamber was heated, this is because (1) the material crystallizes becoming more conductive and therefore increasing the rate of deposition and (2) the material heats up and therefore requires less energy to be sputtered from.

In Figure 95 below (the XRD diffractogram) we can see that $CuSbS_2$ and $Cu_{1.8}S$ are formed. Although excess antimony is present in the film, no antimony containing crystals are formed.

This means that the antimony compounds formed have higher crystallisation temperatures. We can also distinguish some Mo and MoS_2 peaks from the diffractogram.

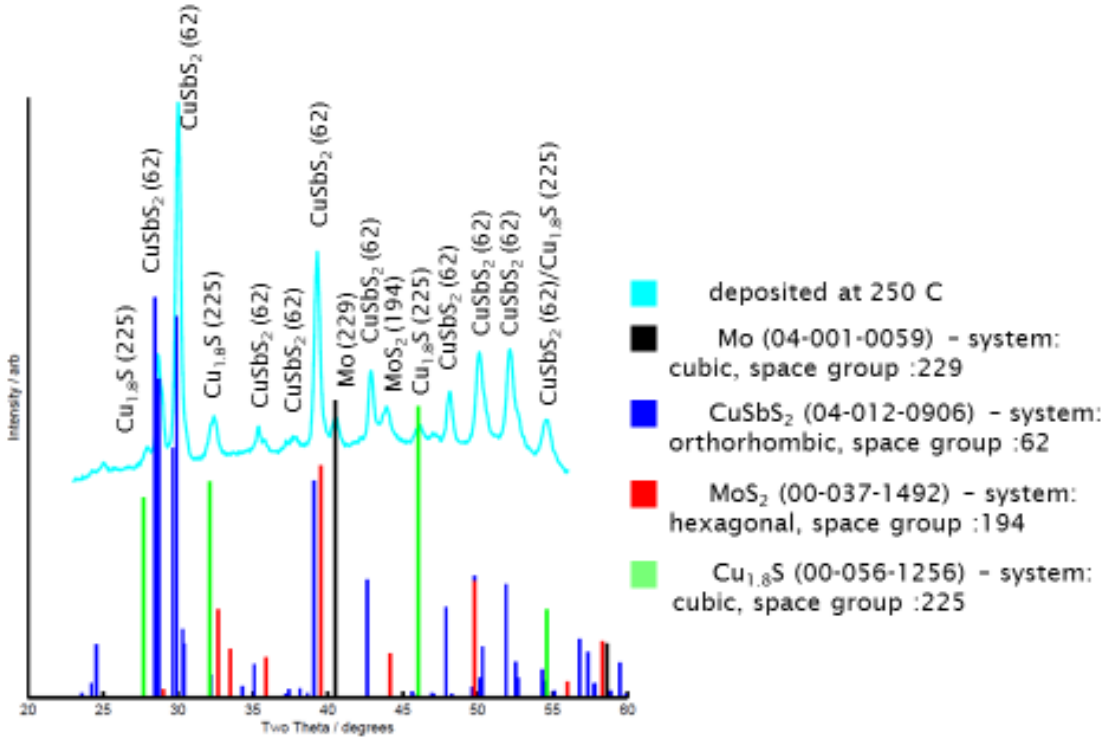

Figure 95: XRD diffractogram of the $CuSbS_x$ deposited at 200 ℃. The film thickness was 6000 nm.

In Figure 96 below, the SEM cross section for the material is shown. Large irregular crystals with sizes above 2 μm are formed. There is also a change in conductivity at the surface of the material (darker surface is caused by lower conductivity). This indicates the amorphous antimony materials have formed on the surface of the material.

The target composition therefore is inhomogeneous, being more antimony rich away from the surface; which appears later on in the deposition due to the target being used up.

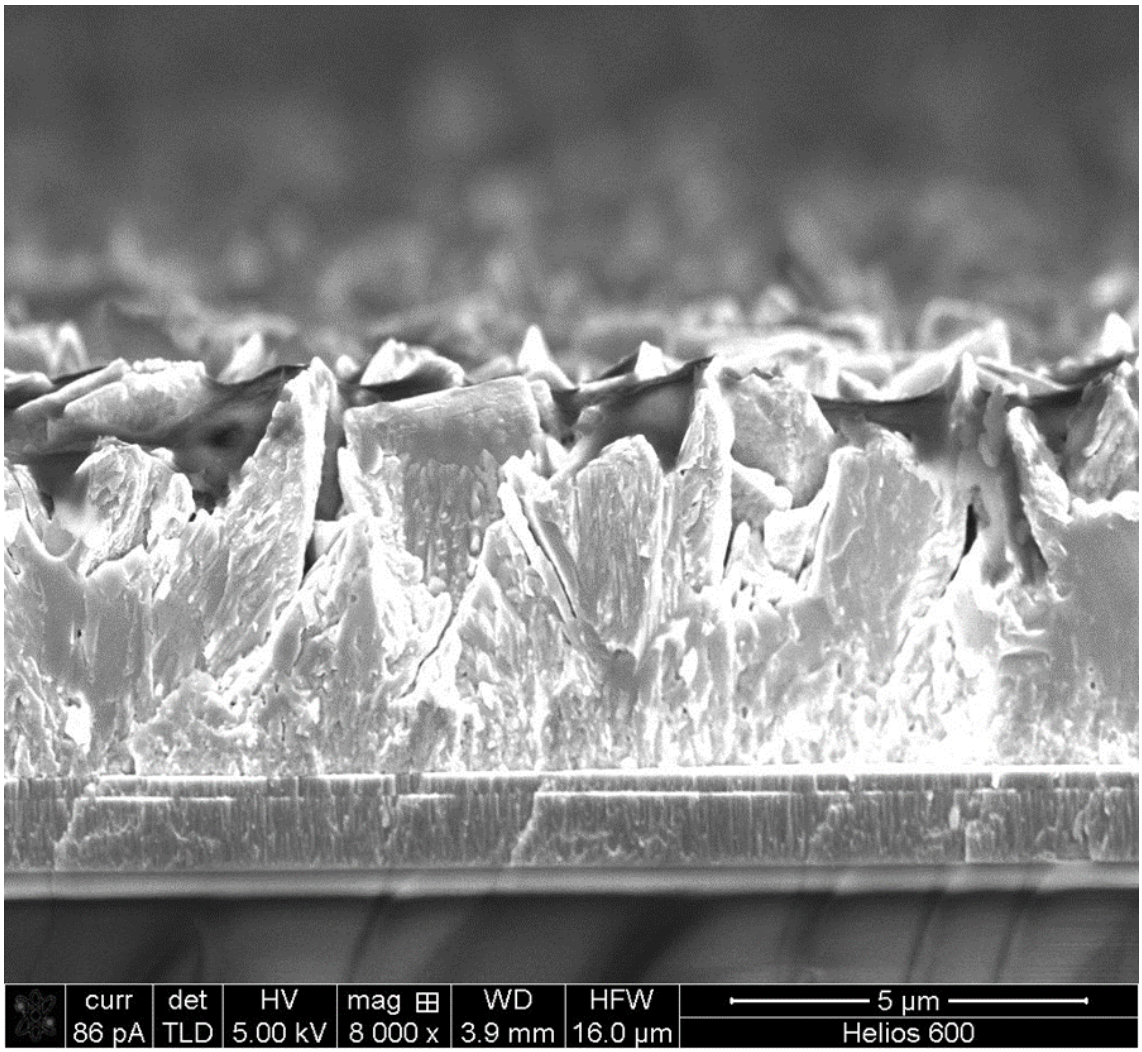

Figure 96: SEM cross section of $CuSbS_x$ deposited at 200°C. The film thickness was 6000 nm.

8.2.2 Etching of CuSbS with bromine and HCl

8.2.2.1 Bromine

Figure 97 below shows the optical microscopy images of the bromine etched CuSbS thin films. The etching is shown for all three etching durations as well as the as deposited films. As the films are produced by sputtering small flakes and residues are left on the surface of the films, the films were cleaned using a 30 sec RIE procedure, but it seems that the bromine further cleans the sample with a 90 sec etch produces the cleanest films.

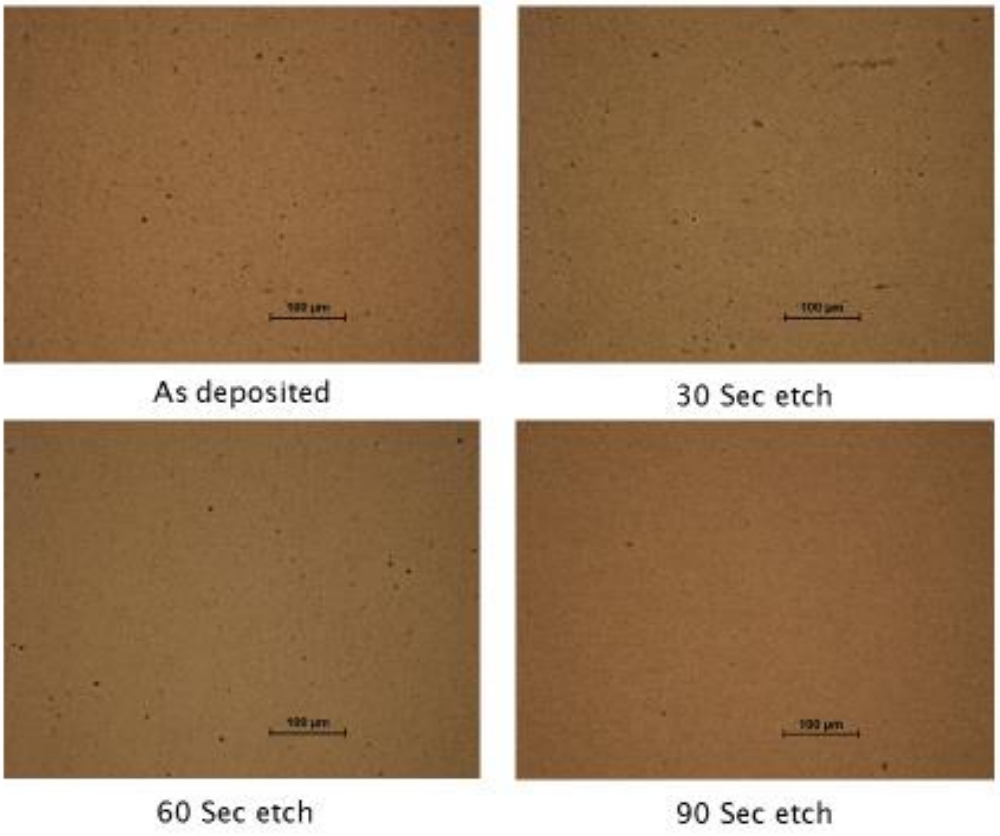

Figure 97: Optical microscopy of bromine etched $CuSbS_2$. Length bar = 100 µm. The film thickness was 1000 nm.

EDX measurements of the films (in Figure 98) shows that the composition of the films does not change with bromine etching. This means that the bromine does not etch any material preferentially. The XRD diffractogram in Figure 99 shows that the orthorhombic antimony sulphide phase is formed in addition to the CuSbS. The bromine does not etch either of the phases preferentially as both phases still exist after the etching takes place.

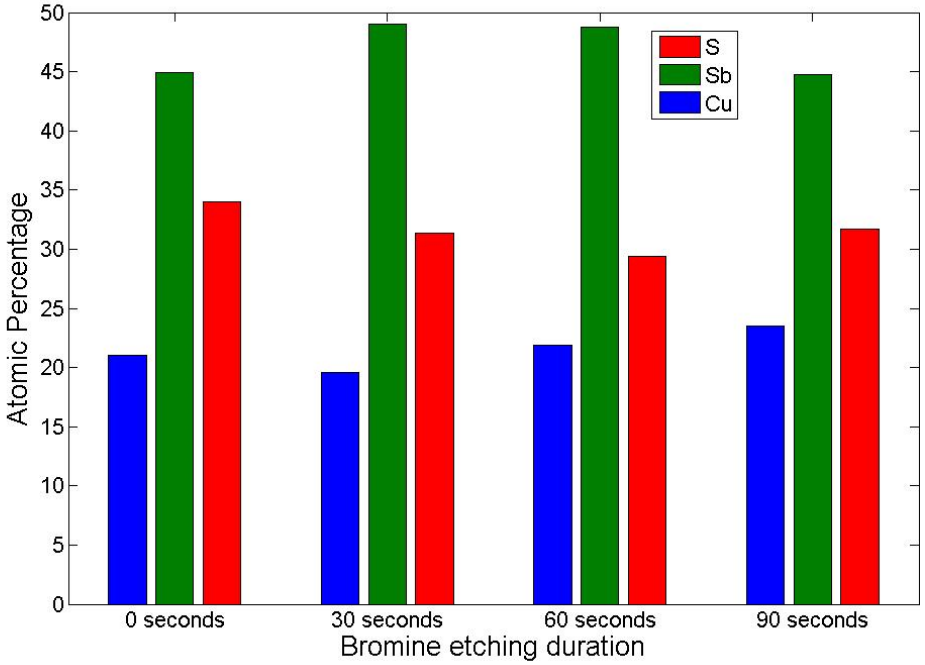

Figure 98: EDX of bromine etched $CuSbS_x$. The film thickness was 1000 nm.

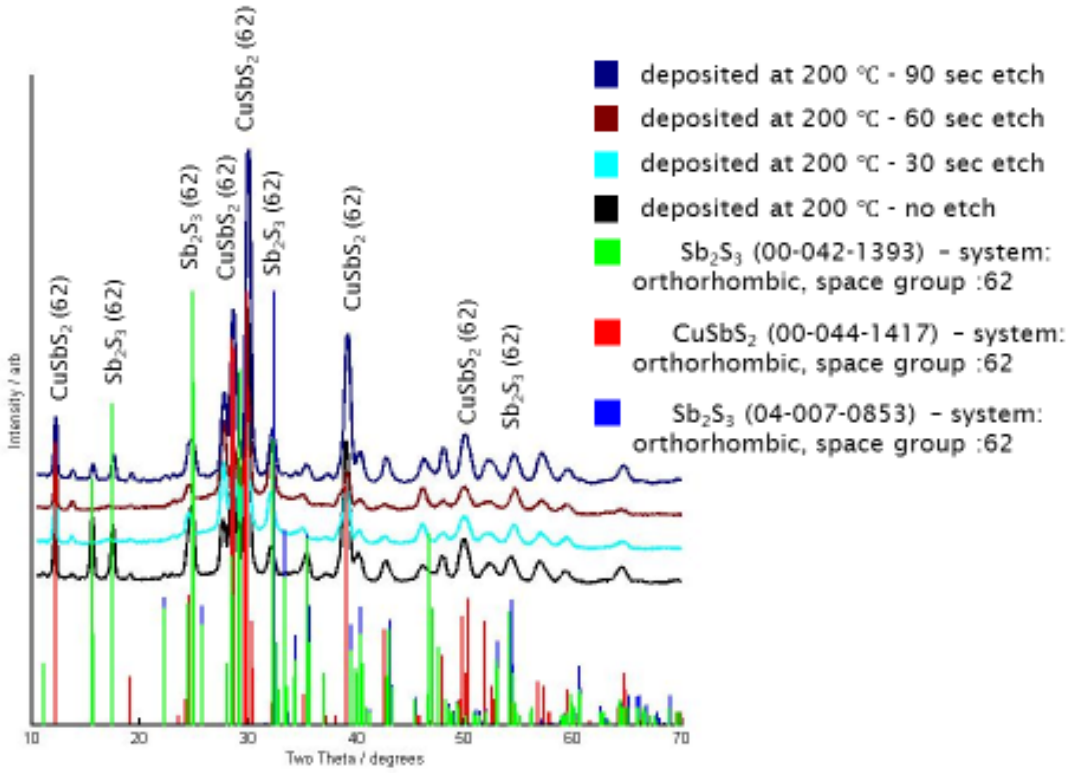

Figure 99: XRD diffractogram of bromine etched $CuSbS_x$ The film thickness was 1000 nm.

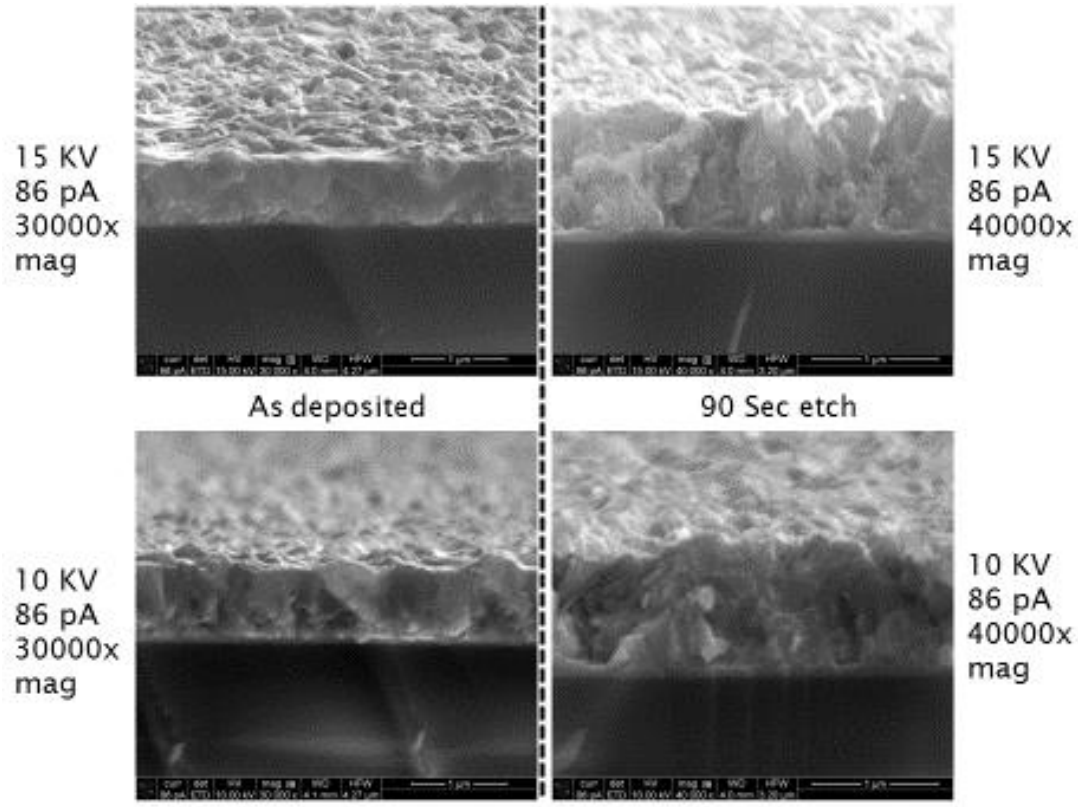

Figure 100: SEM cross section of bromine etched $CuSbS_x$. Length bar = 1 µm. The film thickness was 1000 nm.

Figure 100 shows the SEX cross sections of the films as deposited and bromine etched for 90 seconds. Accelerating voltages of 10 KV and 15 KV were used to ensure the depth of the electron current would not change the analysis of the effect of etching; the magnification was changed to achieve the best image for each. The thickness of the films remains similar, although there is a change in texture which could result from amorphous materials being removed. Figure 101 shows the top view of the film etched for 90 seconds. This shows that the bromine does not produce pin holes at the micron scale in the films.

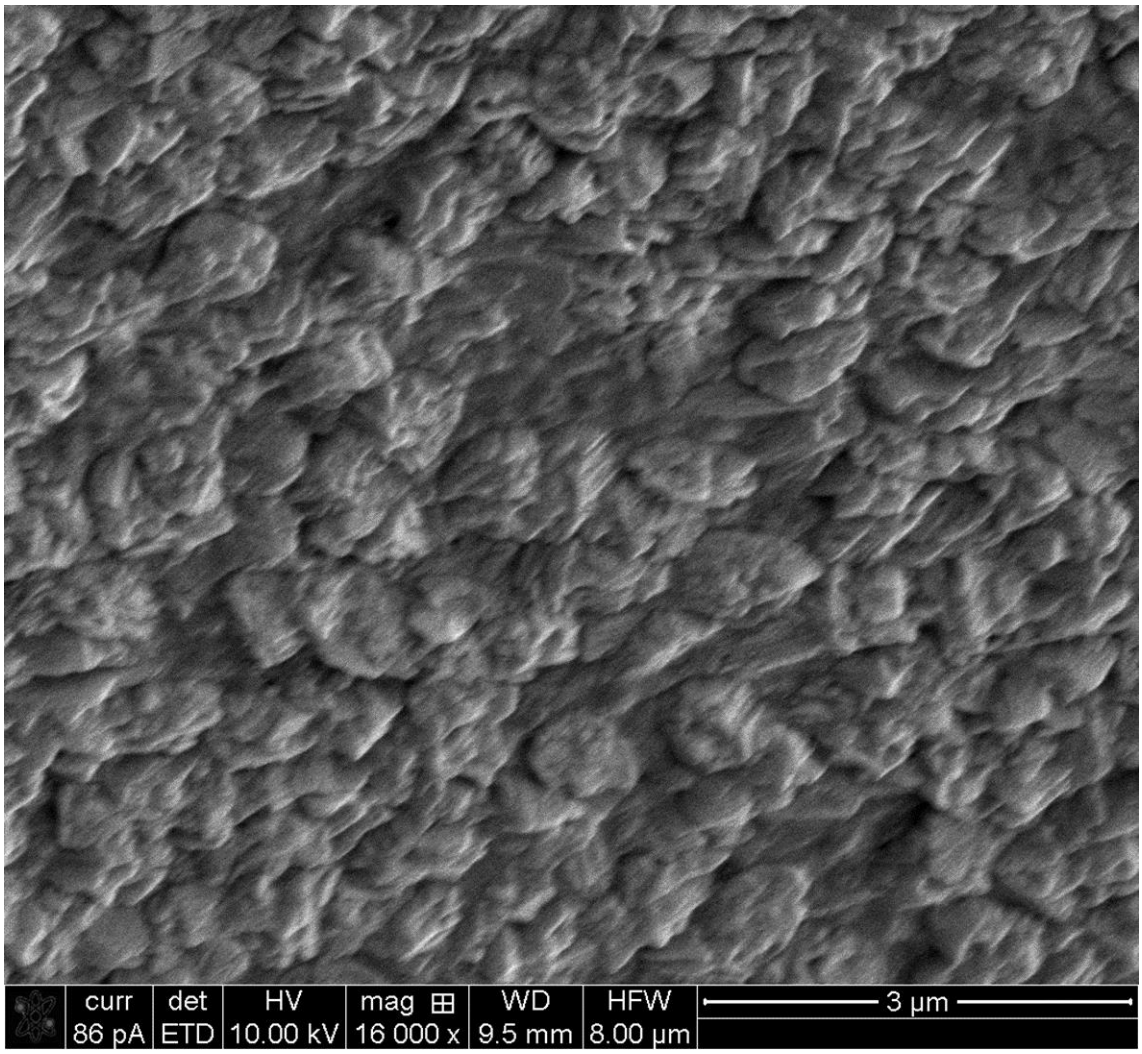

Figure 101: SEM top view of bromine etched $CuSbS_x$ for 90 sec. The film thickness was 1000 nm.

8.2.2.2 HCl etching

Similar films were etched in HCl. These films delaminated form the surface of the soda lime glass upon immersion in the acid. The etching was repeated several times at varying durations; the minimum of which was 15 seconds. It may be that an adhesion layer is needed to investigate the effect of HCl on the material without the breakage of the film. Mo may be a suitable material.

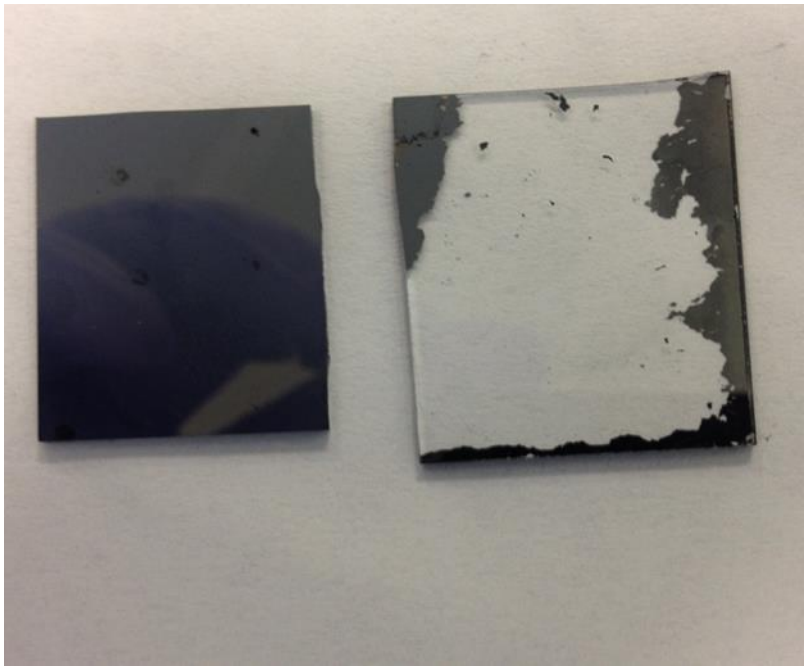

Figure 102: Optical image of samples without (left) and with (right) HCl etching. The film thickness was 1000 nm.

8.2.3 Deposition at 250 ℃

Figure 103 shows the EDX of the CuSbS deposited at 250 ℃. The composition is very close to that for the material deposited at 200 ℃ again the material is antimony rich with the sulphur just above 50 atomic %.

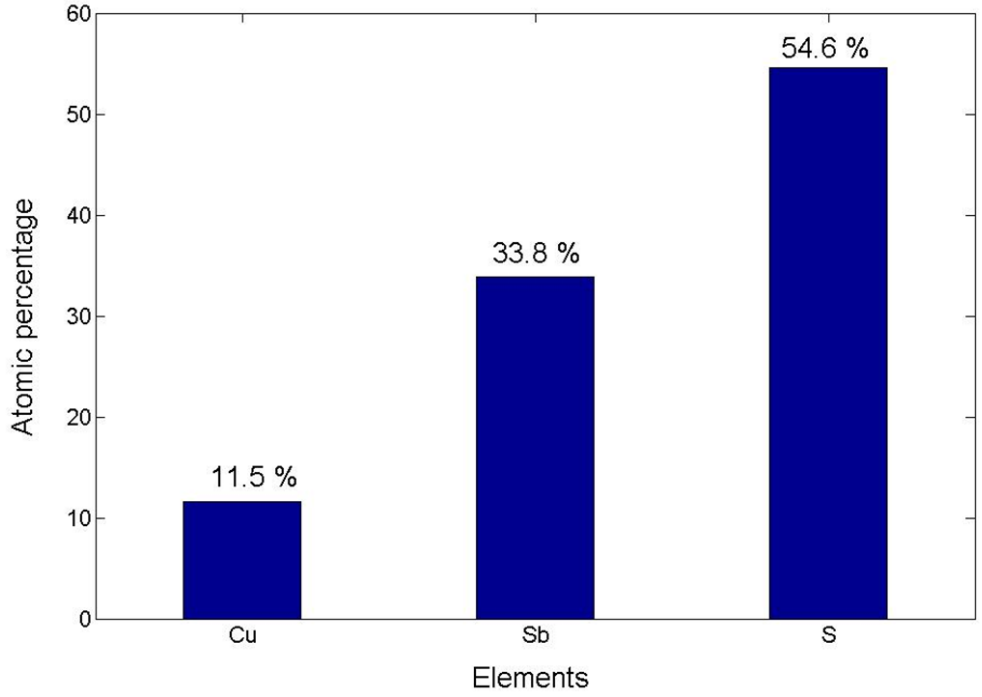

Figure 103: EDX of $CuSbS_x$ deposited at 250 ℃. The film thickness was 4500 nm.

Figure 104 shows the XRD diffractogram which shows both the $CuSbS_2$ and the Sb_2S_3 orthorhombic phases being formed. This means that the higher temperature (of 250 ℃ rather than 200 ℃) have cause the antimony phases to crystallise.

Figure 105 shows the SEM cross section of the film. Large vertical crystals with sizes a few μm in size are formed. There is also a change in conductivity at the surface of the material (darker surface is caused by lower conductivity). This indicates that there is a phase segregation during the film growth.

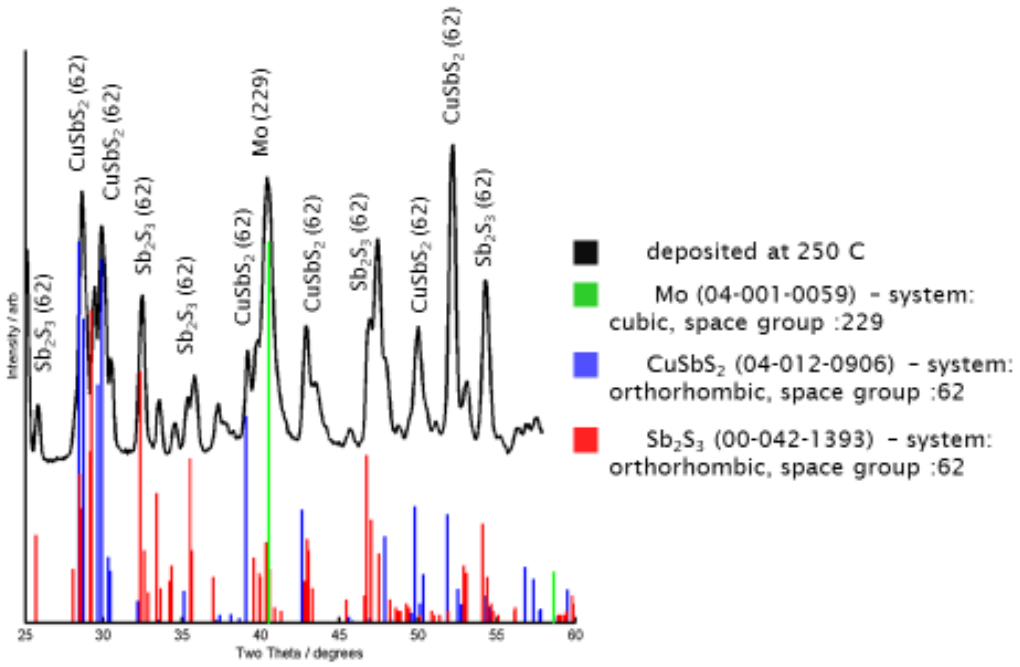

Figure 104: XRD diffractogram of $CuSbS_x$ deposited at 250 ℃. The film thickness was 4500 nm.

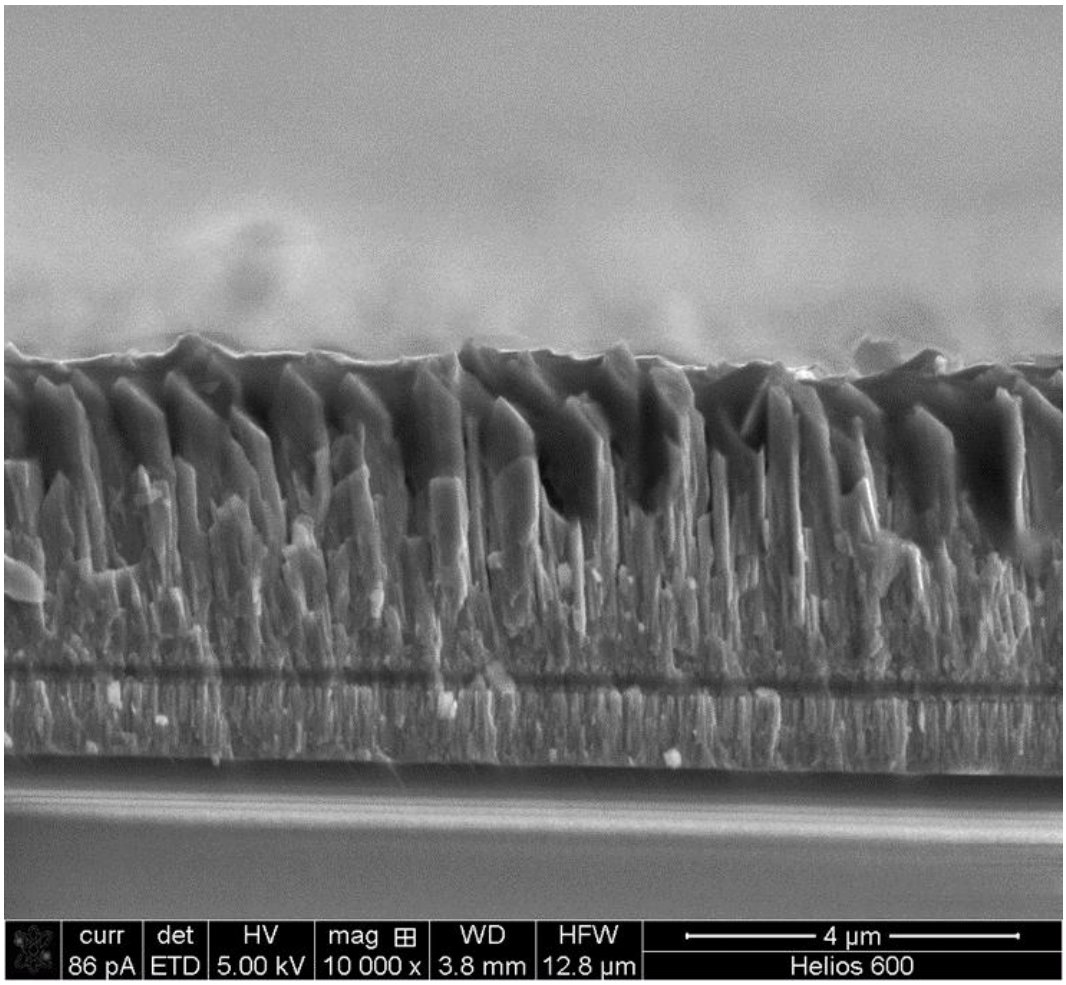

Figure 105: SEM cross section image of $CuSbS_x$ deposited at 250°C. The film thickness was 4500 nm.

8.2.4 Characterisation of cells with CuSbS deposited at 240 ℃

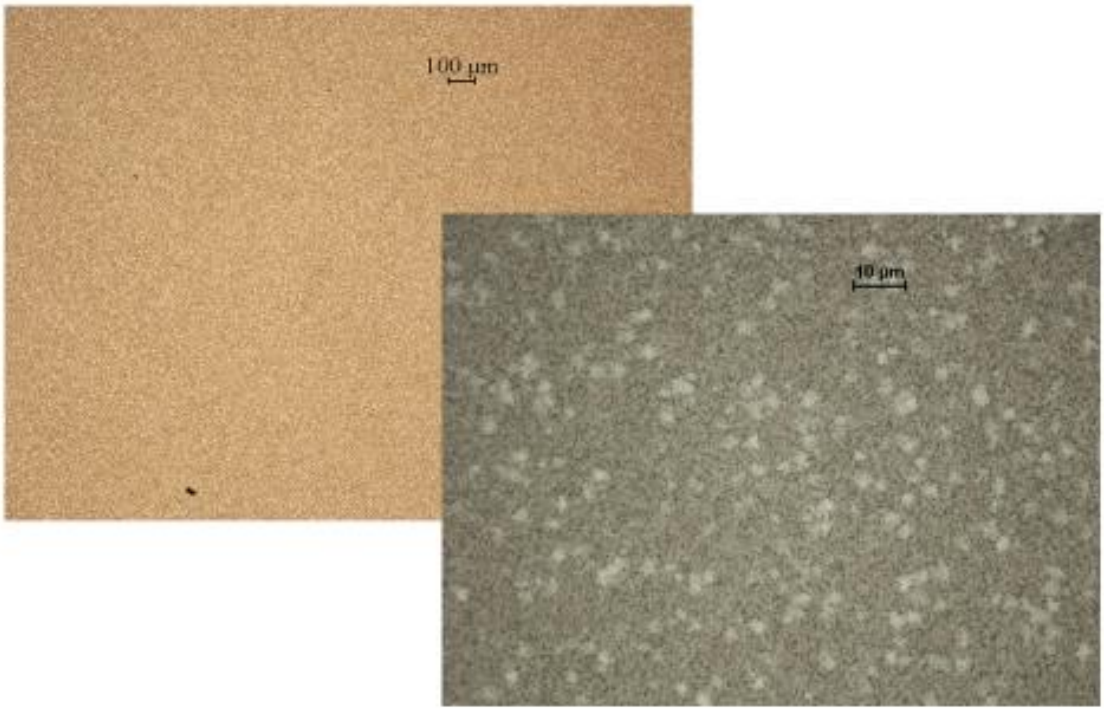

Figure 106: Optical image of CuSbSx deposited at 240 ℃ at different magnifications. The film thickness was 800 nm.

Figure 106 shows the optical microscopy of the films deposited on CdS to fabricate cells. Two magnifications are shown. At the larger magnification white specs are seen on the surface of the material, this is assumed to be the roughness and imperfections of the CdS films underneath changing the morphology of the CuSbS film deposited on top.

Figure 107 and Figure 108 shows the EDX and XRD diffractogram of the films respectively. The EDX shows that the films are antimony rich and sulphur poor. The XRD diffractogram shows that the orthorhombic antimony sulphide phase is formed in addition to the CuSbS. This is different from the phases formed in section 8.2.3 (deposition at 250 ℃) because a different target was used for the sputtering process.

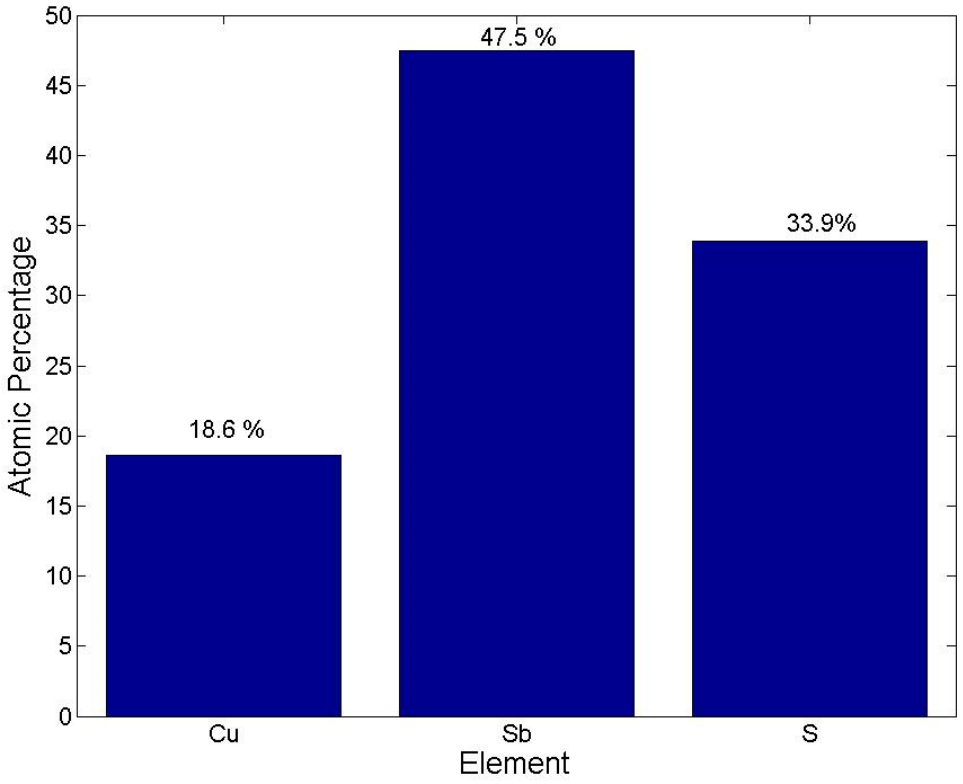

Figure 107: EDX of $CuSbS_x$ deposited at 240℃. The film thickness was 800 nm.

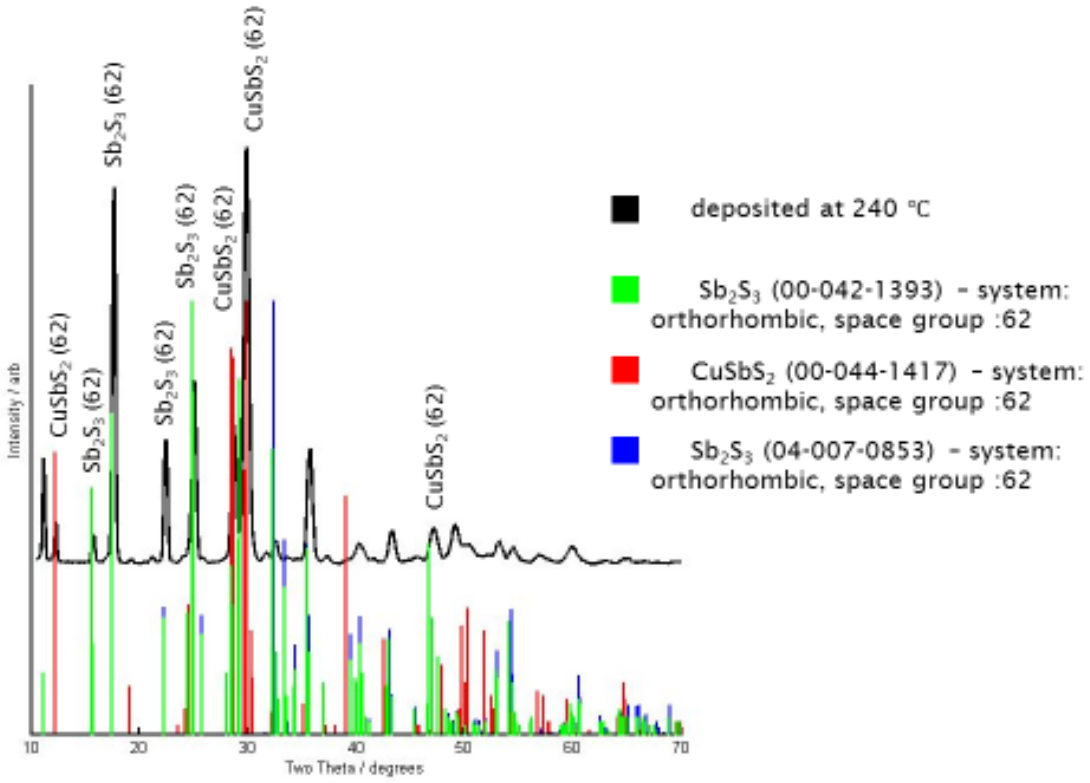

Figure 108: XRD diffractogram of CuSbS deposited at 240°C. The film thickness was 800 nm.

Figure 109 and Figure 110 show the current voltage characteristics of 3 different cells, fabricated in the same way. The photocurrent produced shows a maximum of 20 μA. The cell area is 1 mm by 1 mm (0.01 cm^2); which gives us a current density of around 1-2 mA/cm^2. The open circuit voltage is around 0.05 V, which means the cell efficiency is around 0.1 %. The curve does not show a p-n junction and short circuiting is present in the cell; nevertheless the photocurrent is the highest produced in this study.

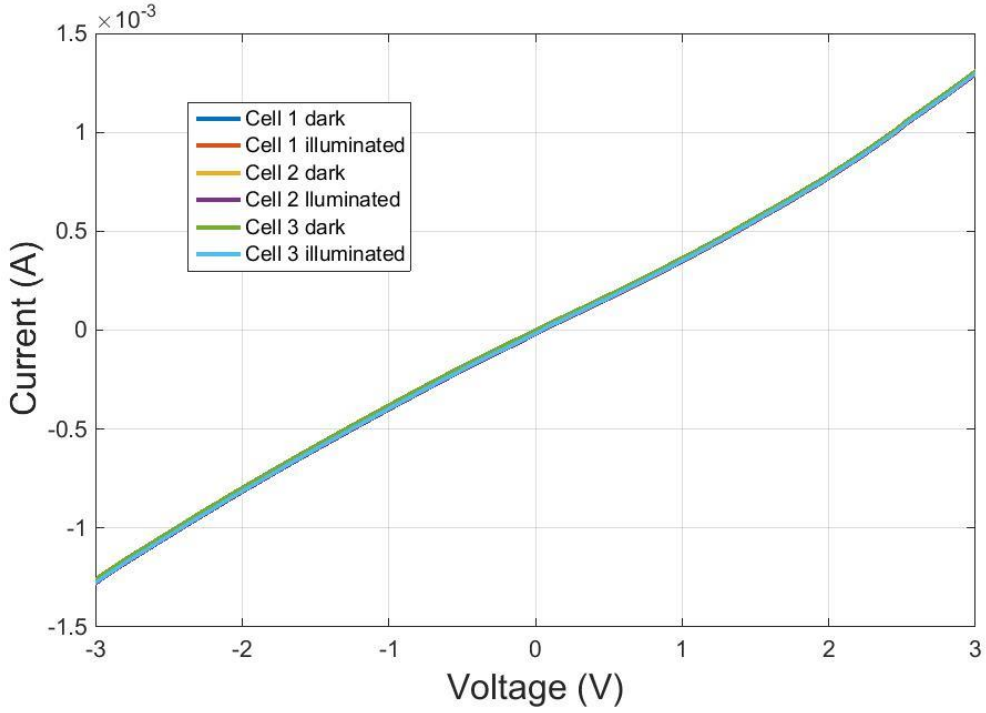

Figure 109: Current voltage characteristics of 3 cells fabricated in the same way. The absorber layer was 800 nm of $CuSbS_2$ deposited at 240 ℃.

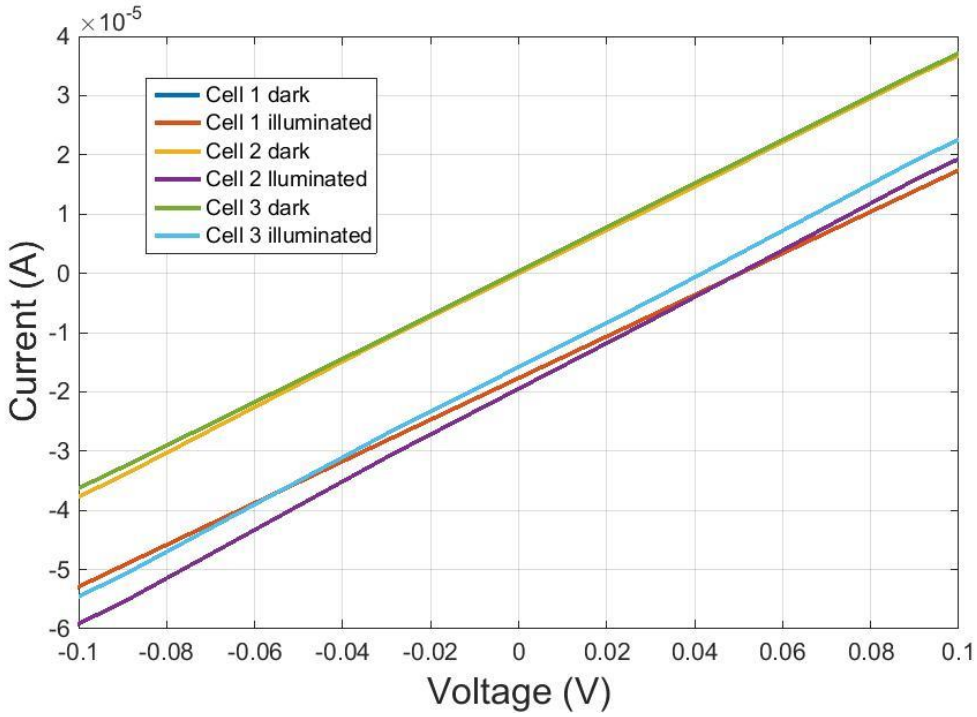

Figure 110: Current voltage characteristics of the 3 cells showing the photocurrent produced. The absorber layer was 800 nm of $CuSbS_2$ deposited at 240 ℃.

8.3 Conclusion

In this work, $CuSbS_2$ thin films were first deposited by RF magnetron sputtering at from a single ternary target on molybdenum coated substrates using a Kurt Lesker NANO-38 thin film deposition system. The crystals were made in situ by depositing at 200 and 250 ℃

The compositional, optical, electrical and structural properties of the films were analysed using optical microscopy, SEM, EDX and XRD. The grain sizes were measured by SEM imaging, and grains above 1 μm can be fabricated. The effect of etching in 0.02 molar bromine in methanol and HCl was also investigated, and this showed that the films were etched homogeneously in all directions. A problem noticed here were the targets, the targets supplied by the manufacturers were inhomogeneous producing different films with subsequent depositions, in this chapter the films were copper poor in comparison to the previous chapter and for the etching study sulphur poor. Nevertheless the reliability of these results are still intact. This is because the etching comparison is done with films from the same deposition. The films made at the two different temperatures show the properties of $CuSbS_x$ films made with this composition at this temperature.

And finally the cells made which are both copper and sulphur poor but showed a high current density (up to 1-2 mA/cm^2) using $CuSbS_2$ films. Current-voltage characteristics showed a maximum open circuit voltage of around 0.05 V, a short circuit current of up to 20 μA and a conversion efficiency of 0.1%. The open circuit of the cells along with the junction must be improved to produce high efficiency solar cells.

Chapter 9: Conclusions and Further work

To summarise the entire report, there are a few observations and points that need to be made. Also, further work that can be carried out to continue from this work is proposed here.

For the work with CIGSe, thin films were first deposited by RF magnetron sputtering at room temperature from a single quaternary target on titanium substrates, molybdenum coated soda lime and molybdenum coated borosilicate substrates. The films were annealed in an Elite™ three-zone tube furnace at 500 and 550 ℃ in a selenium rich atmosphere. The compositional and structural properties of the films were analysed using EDX and XRD, respectively. The grain sizes were measured by SEM imaging. These grains did not grow throughout the film (most ideal case), although this is not the reason the cells short circuited, it is a path for improvement. For future researchers I would recommend that the annealing is carried out at higher temperatures, lower pressures or for longer durations to increase the grain size. The EDX showed a composition close to the required stoichiometry and so depositing from a single target is a possible approach to making these cells. The XRD for the films on borosilicate show a CuSe secondary phase, this disappears at 550 ℃ (shown in the film deposited on soda lime glass) and therefore it reacts at higher temperatures. At this temperature single phase CIGSe is produced. For the phases on the Ti substrate, two Ti secondary phases are formed and therefore a buffer layer (Mo) is needed for lower resistance Ohmic contacts.

Cells were fabricated, but all showed short circuiting. Improvements can be done by designing smaller cells. The reasoning here is that due to the nature of the process (sputtering with the targets above the substrates), flaking is inevitable. This was mitigated to a certain extent by performing double depositions where possible, although even with this, the flaking occurs before each deposition when opening or closing the shutter, by making smaller cells the amount of shunting that could occur is decreased substantially, for research this is acceptable, for future production the flaking needs to be eliminated, so that larger cells can be made.

Another problem faced, was the fact that the chamber is not solely used for one compound or material and many impurities will degas into the films from the

surroundings. This was minimised by cleaning the chamber before each run and where possible coating the chamber with a relatively inert material before a deposition. This sometimes was not possible due to oxidation which can occur from opening the chamber. This theme, continues throughout the thesis and is a key limitation to achieving high efficiency solar cells.

The annealing was carried out using selenium vapour. This caused the formation of a thin layer of selenium on the top of the absorber layer which would increase the resistance greatly. An investigation of the etching of Se (without damaging the CIGSe) would be a possible step forward. The annealing should be carried out in a way that ensures homogeneous uniform films are produced with minimal roughness and minimal degradation of the contacts. A possible route is the scribing of the absorber to expose the contacts to the film, after annealing. This way the bottom contact is not damaged by the Se annealing or by the following etching.

Also, the use of in house non-optimised ZnS was another problem (an area in need of improvement), compounded by the fact that the films showed pin holes due to the flaking from the chamber, and resulted in short circuited cells. This film needs to be optimised or sourced from a collaborator with experience in the field of buffer layers for solar applications. This also applies to the window layers used.

In the Cu_2ZnSnS_4 chapter, thin films have been deposited by RF magnetron sputtering at room temperature from a single quaternary target on to molybdenum coated substrates. The films were annealed in a rapid thermal processor with different recipes. The annealing was done without any toxic gases or reactive sulphur. The compositional and structural properties of the films have been analysed using EDX and XRD respectively and certain recipes were identified which produce films with good adhesion, good crystallinity and that show the ideal stoichiometry before and after annealing. The grain sizes were measured by SEM imaging, and grains for the films are between 100 and 200 nm in size. Similar to the previous chapter, to improve the cells we need to increase the grain size, which could be done by annealing at a higher temperature or at a lower pressure. The EDX showed a tin rich and zinc poor material, which can be improved by melting the targets in house and having better control of the target composition. The XRD diffractograms show single

phase CZTS consistently with all the annealing recipes analysed and therefore even if the films have a composition that is non stoichiometric, the crystals formed are.

Finally cells were fabricated, but only a few cells showed rectification, with a maximum short circuit current of 1 μA. The cleaning carried out in this chapter was more thorough and greater care was taken when handling the samples and in between depositions. Also the cell designs were different, they were smaller; but the design involved losing some photocurrent due to contact shading. The problem with flaking is still present, which caused short circuiting paths. Also, cells were fabricated several times, which lead to the conclusion that the time between the initial depositions, annealing and ZnS deposition was integral to the photocurrent produced (this needed to be minimised). The longer it was, the lower the photocurrent which is believed to be caused by oxidation of the CZTS layer, but since the oxidation probably occurs in the first 50 nm of the layer EDX is not a reliable technique to measure this.

GaLaS thin films were deposited in chapter 5 by a high throughput PVD MBE system on Si, Si3N4 coated Si and Pt coated Si substrates. Lanthanum was evaporated using an electron beam, while gallium and sulphur were evaporated from Knudsen cells. The power and wedge of each source was controlled independently, to achieve a desired gradient of each material. The compositional and structural properties of the films were analysed using EDX, Raman and XRD. The effect of the annealing temperature on the sulphur in the films was investigated, which indicated a decrease to around 55-60 atomic % with higher annealing, which then no longer changes with higher temperatures or longer anneals. It is noted that the amount of residual sulphur in the chamber when the cracker is turned off is sufficient for lower temperature depositions, but at higher temperatures (above 400℃) without the cracker the films are sulphur poor. The XRD phases do not match the literature on the XRD of GLS, GaS or LaS, they were unexpectedly matched to GaLaSO, which confirms the preference of GLS to oxidise to form a more stable compound.

The Raman measurements indicate the formation of certain bonds in different material compositions, with a certain trend forming as we move from a La rich to Ga rich compositions. Several peaks matching the literature have been distinguished along with other peaks.

Refractive index measurements were carried out using a J. A. Woollam spectroscopic ellipsometer and it is shown that the refractive index increases with gallium content. The extinction coefficient decreases with gallium content. The absorption edge is around 2.9 eV and shifts only slightly for different compositions. For GLS to be suitable for photovoltaics, we need to shift the band gap to around 1.5 eV (above 800 nm), which may be possible by doping with other materials.

The work on GLS is important as it the first time HTPVD has been used to explain trends in this material (especially in refractive index), as well as the work acting as a benchmark for GLS to be doped with different materials, to find its suitability as a photovoltaic material.

In chapter 6, $CuSbS_2$ thin films were successfully deposited using an atmospheric pressure chemical vapour deposition system. The precursors used were antimony chloride ($SbCl_5$) in liquid form, copper chloride (CuCl) and H_2S generated in situ for the reaction. The precursors were chosen from other studies undertaken to make other chalcogenide materials along with considerations of cost, availability, purity, suitability for the reaction and vapour pressure. The feasibility of the reaction is calculated by calculating the Gibbs free energy of the reaction.

$CuSbS_x$ was successfully deposited on soda lime substrates. The morphological and compositional properties of the films were analysed using SEM and EDX. The SEM images show a very fast deposition of around 35 μm in 1 hour. The EDX shows a slightly copper rich material. This chapter forms a proof of principle study suggesting the viability of producing $CuSbS_x$ films using atmospheric pressure CVD. Further work will include the fabrication of complete cells and a comparison with other techniques.

In chapter 7, $CuSbS_2$ thin films were first deposited by RF magnetron sputtering at room temperature from a single ternary target on molybdenum coated substrates using a Kurt Lesker NANO-38 thin film deposition system. The films were annealed in a Jipelec JetFirst 100 bench top rapid thermal processor at various temperatures (250 to 325 ℃) and times (5 to 60 min). The annealing was done without any toxic gases or reactive sulphur. The compositional, optical and structural properties of the films were analysed using SEM, EDX and XRD. Single phase $CuSbS_2$ films with good adhesion, good crystallinity and with no apparent

sulphur loss can be achieved. The surface roughness of the films increases with an increase in annealing temperature. Above 300℃, an instability and loss of antimony is seen in the films. Longer anneals don't seem to change the composition of the films or the phases formed. By adding purge and pump cycles to the annealing recipe and removing any impurities in the annealing chamber, the films are improved and no secondary phases are formed.

The grain sizes were measured by SEM imaging for the films annealed at 300 ℃ for one hour, and are between 100 and 200 nm in size; although the grains are still relatively small compared to the film thickness. Smaller cells are made compared to those in the previous chapters, also the cell design is changed, and a commercial TCO is used along with commercial grade CdS supplied from collaborators. This has allowed working cells to be produced.

Current voltage characteristics of the cells showed a maximum open circuit voltage of around 0.1 V, a short circuit current of around 0.7 μA and a conversion efficiency of 0.007%. A low efficiency, but the first cells made with this technique. Further improvements include etching the surface of the films (to remove surface defects), increasing the doping concentrations (to increase the majority carrier concentrations), producing larger grains and using a chamber with no flaking.

In chapter 8, we take this work further and produce larger grains by depositing in vacuum inside the deposition chamber. $CuSbS_2$ thin films were first deposited by RF magnetron sputtering at from a single ternary target on molybdenum coated substrates using a Kurt Lesker NANO-38 thin film deposition system. The crystals were made in situ by depositing at 200 and 250 ℃.

The compositional, optical, electrical and structural properties of the films were analysed using optical microscopy, SEM, EDX and XRD. The grain sizes were measured by SEM imaging, and grains above 1 μm can be fabricated. The effect of etching in 0.02 molar bromine in methanol and HCl was also investigated, and this showed that the films were etched homogeneously in all directions. A problem noticed here were the targets, the targets supplied by the manufacturers were inhomogeneous producing different films with subsequent depositions, in this chapter the films were copper poor in comparison to the previous chapter and for the etching study sulphur poor. Nevertheless the reliability of these results are still intact. This is because the etching comparison

is done with films from the same deposition. The films made at the two different temperatures show the properties of $CuSbS_x$ films made with this technique at this temperature.

And finally the cells made which are both copper and sulphur poor but show a high (up to 1-2 mA/cm^2) current density using CuSbS films. Current voltage characteristics showed a maximum open circuit voltage of around 0.05 V, a short circuit current of up to 20 μA and a conversion efficiency of 0.1%. The open circuit of the cells along with the junction must be improved to produce high efficiency solar cells.

Complete List of Publications

1. HUANG, C. C., **AL-SAAB, F.**, WANG, Y., OU, J. Y., WALKER, J. C., WANG, S. C., GHOLIPOUR, B., SIMPSON, R. E. & HEWAK, D. 2014. Scalable High-mobility MoS_2 thin films fabricated by atmospheric pressure chemical vapour deposition at ambient temperature. Advanced Materials, Submitted.
2. **AL-SAAB, F.**, HUANG, C. C., YAO, J., HAYDEN, B. & HEWAK, D. 2014. RTA annealed RF sputtered single phase CuSbS films. *Thin Solid films,* Submitted.
3. **AL-SAAB, F.**, HUANG, C. C., HAYDEN, B. & HEWAK, D. 2014. RF sputtered single phase CuSbS thin films. *E-MRS Spring* Lille, France.
4. **AL SAAB, F.**, GHOLIPOUR, B., HUANG, C. C., ANASTASOPOULOS, A., HAYDEN, B. & HEWAK, D. W. 2013. Crystallization Study of the $CuSbS_2$ Chalcogenide Material for Solar Applications. *PV-SAT 9.* Swansea University, Swansea, Wales.
5. ISMAEEL, R., LEE, T., **AL-SAAB, F.**, JUNG, Y. & BRAMBILLA, G. 2012. A Multiport Optical Microfiber Coil Resonator. Optics Express, 20, 8568-8574.
6. ISMAEEL, R., LEE, T., **AL-SAAB, F.**, JUNG, Y. & BRAMBILLA, G. 2012. Multi-Port Optical Microfiber Coil Resonator. CLEO/QELS 2012. San Jose.
7. HEWAK, D. W., HUANG, C. C., **AL-SAAB, F.**, GHOLIPOUR, B., LEONARD, V. & MADDOCK, J. 2012. Recent advances in the application of Chalcogenide Thin Films. International Symposium on Non-Oxide and New Optical Glasses.
8. GHOLIPOUR, B., ZHANG, J., **AL-SAAB, F**., MACDONALD, K. F., HAYDEN, B. E., HEWAK, D. W. & ZHELUDEV, N. I. 2012. Chalcogenide glass photonics: non-volatile bi-directional all-optical switching in phase-change metamaterials. CLEO/QELS 2012. San Jose.
9. **AL-SAAB, F**., GHOLIPOUR, B., HUANG, C. C., ANASTASOPOULOS, A., HAYDEN, B. & HEWAK, D. W. 2012. Crystallization Study of the Cu_2ZnSnS_4 Chalcogenide Material for Solar Applications. PV-SAT 8. Northumbria University, Newcastle upon Tyne.

10. HUANG, K. C., **AL-SAAB, F.**, GHOLIPOUR, B. & HEWAK, D. W. 2011. Fabrication of thin film solar cell materials by APCV. Low Carbon Earth Summit. Dalian, China.
11. GHOLIPOUR, B., ZHANG, J., **AL SAAB, F**., GHOLIPOUR, A., MAC-DONALD, K. F., HAYDEN, B., HEWAK, D. & ZHELUDEV, N. I. 2011. Chalcogenide Phase Change Materials in Active Plasmonic and Metamaterial Technologies. SAIT Global Research Outreach Scheme.
12. GHOLIPOUR, B., HEWAK, D. W., HUANG, C. C., ANASTASOPOULOS, A., **AL SAAB, F**., GUERIN, S., HAYDEN, B. & PURDY, G. 2011. Scalability and thermal stability of low current consuming, nanowire phase change memory cells for high density commercial applications. E/PCOS. Zurich, Switzerland.

Appendices

Appendix A – GLS Depositions and Characterisations

Sample	Substrate	Material 1	Material 2	Wedge Material 1	Wedge Material 2	Power/temp Material 1	Power/temp Material 2	Substrate Temp	Mask (y/n)	sulphur cracker
6901	Silica	La	-	38	-	11.5%	-	RT	Y	-
6902	Silica	La	-	38	-	19.0%	-	RT	Y	-
6903	Silica	La	-	38	-	25.0%	-	RT	Y	-
6904	Silica	La	-	32	-	21.0%	-	RT	Y	-
6905	Silica	La	-	35	-	25.0%	-	RT	Y	-
6906	Silica	-	Ga	-	41	-	1150℃	RT	Y	-
6907	Silica	-	Ga	-	39	-	1075℃	RT	Y	-
6908	Silica	-	Ga	-	40	-	1095℃	RT	Y	-
6909	Si	La	Ga	35	40	25.0%	1096℃	RT	Y	-
6910	Si	La	Ga	34	39.5	26.0%	1097℃	RT	Y	-
6911	Si	La	Ga	37	41	26.0%	1098℃	RT	Y	-
6912	Si	La	Ga	35	41	26.5%	1099℃	RT	Y	-

Sample	Substrate	Material 1	Material 2	Wedge Material 1	Wedge Material 2	Power/temp Material 1	Power/temp Material 2	Substrate Temp	Mask (y/n)	sulphur cracker
6913	SiN	La	Ga	35	41	26.5%	1100℃	RT	Y	-
6914	SiN	La	Ga	35	41	26.5%	1101℃	RT	Y	-
6915	SiN	La	Ga	35	41	26.5%	1102℃	RT	Y	-
6916	SiN	La	Ga	35	41	26.5%	1103℃	RT	N	-
6917	SiN	La	Ga	35	41	26.5%	1104℃	RT	N	-
6918	SiN	La	Ga	35	41	26.5%	1105℃	RT	N	-
6919	silica	La	Ga	35	41	26.5%	1106℃	RT	N	-
6920	SiN	La	Ga	35	41	26.3%	1107℃	RT	N	-
6921	SiN	La	Ga	35	41	26.3%	1108℃	RT	N	-
6922	Si	La	Ga	35	41	26.3%	1120℃	RT	N	-
6923	Si	La	Ga	35	41	26.3%	1150℃	RT	N	-
6924	SiN	La	Ga	35	41	26.3%	1180℃	RT	N	-
6925	SiN	La	Ga	35	41	26.3%	1180℃	RT	N	-

Sample	Substrate	Material 1	Material 2	Wedge Material 1	Wedge Material 2	Power/temp Material 1	Power/temp Material 2	Substrate Temp	Mask (y/n)	sulphur cracker
6926	Si//Pt	La	Ga	35	41	26.3%	1180℃	RT	N	-
6934	Si	La	Ga	35	41	26.3%	1180℃	400℃	N	-
6950	Si	La	Ga	35	41	26.5%	1180℃	250℃	N	-
6955	Si	La	Ga	35	41	27.0%	1180℃	200℃	N	-
6976	SiN	La	Ga	35	41	27.0%	1180℃	200℃	N	-
6985	SiN	La	Ga	35	41	27.0%	1180℃	200℃	N	-
7001	Si	La	Ga	35	41	20.0%	1180℃	RT	N	500℃
7003	Si	La	Ga	35	41	20.0%	1180℃	200℃	N	500℃
7009	Si	La	Ga	34	41	20.5%	1180℃	400℃	N	500℃
7021	Si	La	Ga	33	42	20.5%	1220℃	RT	N	-
7024	Si	La	Ga	33	42	20.50%	1190℃	RT	N	-
7025	Si	La	Ga	33	42	20.5% going to 22%	1190℃	RT	N	-
7111	Si	La	Ga	33	42	22.00%	1190℃	RT	N	-

Sample	Substrate	Material 1	Material 2	Wedge Material 1	Wedge Material 2	Power/temp Material 1	Power/temp Material 2	Substrate Temp	Mask (y/n)	sulphur cracker
7115	Si	La	Ga	33	42	22.00%	1190℃	RT	N	-
7116	Si	La	Ga	33	42	20.00%	1190℃	RT	N	-
7117	Si	La	Ga	33	42	16.00%	1190℃	RT	N	-
7118	Si	La	Ga	33	42	16.00%	1190℃	200℃	N	500℃
7119	Si	La	Ga	33	42	16.00%	1190℃	200℃	N	500℃
7120	Si	La	Ga	33	42	16.00%	1190℃	200℃	N	500℃
7154	Si/TiW	La	Ga	33	42	16.00%	1200℃	200℃	N	500℃
7155	Si/Mo	La	Ga	33	42	16.00%	1200℃	200℃	N	500℃
7156	Si/Au	La	Ga	33	42	16.00%	1200℃	200℃	N	500℃
7157	Si/Ag	La	Ga	33	42	16.00%	1200℃	200℃	N	500℃
7158	Si/Mo	La	Ga	33	42	16.00%	1200℃	200℃	N	300℃
7159	Si/Mo	La	Ga	33	42	16.00%	1200℃	200℃	N	300℃
7160	Si/TiW	La	Ga	33	42	16.00 then to 17.7 %	1200℃	200℃	N	500℃

Sample	Substrate	Material 1	Material 2	Wedge Material 1	Wedge Material 2	Power/temp Material 1	Power/temp Material 2	Substrate Temp	Mask (y/n)	sulphur cracker
7161	Si/Mo	La	Ga	33	42	17.7%	1200℃	200℃	N	500℃
7162	Si	La	Ga	33	42	17.7%	1200℃	200℃	N	500℃
7163	Si	La	Ga	33	42	17.7%	1200℃	200℃	N	500℃

Sample		characterisation done / Notes
6901		
6902		
6903		
6904		
6905		
6906		
6907		
6908		
6909		EDX*** (DIAGONAL)
6910		EDX (DIAGONAL)
6911		EDX (DIAGONAL)
6912		EDX (DIAGONAL)
6913		

Sample		characterisation done / Notes
6914		EDX (DIAG+ 14X14)
6915		EDX (DIAGONAL)
6916		EDX (DIAGONAL)
6917		
6918		
6919		AS DEPOSITED = TRANSMISSION ELLIPSOMETRY + EDX-ORC(DIAGONAL)
6920		
6921		AS DEPOSITED, 500, 635, 675, 700 ANNEAL = XRD AND EDX (6 POINTS DIAGONAL) + EDX (RT) 14x14 + EDX - ORC (700 ANNEAL ONLY)
6922		EDX (CORNERS)
6923		EDX (CORNERS)
6924		AS DEPOSITED = ELLIPSOMETRY (14X14) + EDX (14X14) + EDX (CORNERS); AFTER HTOMPT = XRD + EDX (6 POINTS DIAGONAL) + EDX-ORC (6 POINTS DIAGONAL)
6925		AS DEPOSITED = EDX (14X14) + EDX (DIAGONAL); 500C ANNEAL = EDX (14X14)

Sample		characterisation done / Notes
6926		AS DEPOSITED = RAMAN (14X14)
6934		AS DEPOSITED, 650 ANNEAL = XRD (6 POINTS DIAGONAL) + EDX (DIAGONAL) + EDX-ORC (6 POINTS DIAGONAL)
6950		EDS (DIAGONAL)
6955		650 anneal = SEM (A FEW POINTS) ; AS DEP, 650 ANNEAL = XRD + EDX (6 POINTS DIAGONAL) + EDX SPHERES (650 ANNEAL ONLY)
6976		AS DEPOSITED = ELLIPSOMETRY (14X14)
6985		AS DEPOSITED = RAMAN (14X14)
7001		AS DEPOSITED = EDX-ORC (6 POINTS DIAGONAL); 650 ANNEAL = XRD + EDX-ORC (6 POINTS DIAGONAL)
7003		AS DEPOSITED = EDX-ORC (DIAGONAL) + ELLIPSOMETRY (14X14); 650, 700 ANNEAL = XRD + EDX-ORC (6 POINTS DIAGONAL) + ELLIPSOMETRY (14X14) + EDX (6 POINTS DIAGONAL)
7009		AS DEPOSITED = EDX-ORC (DIAGONAL); 650 ANNEAL = XRD (6 POINTS DIAGONAL) + EDX-ORC (DIAGONAL) + EDX (DIAGONAL)
7021		

Sample		characterisation done / Notes
7024		AS DEPOSITED = EDX-ORC (DIAGONAL)
7025		AS DEPOSITED = EDX (DIAGONAL) + EDX-ORC (DIAGONAL)
7111		
7115		AS DEPOSITED = EDX (2 points)
7116		AS DEPOSITED = EDX (2 points)
7117		AS DEPOSITED = EDX (DIAGONAL)
7118		AS DEPOSITED = EDX (DIAGONAL)
7119		AS DEPOSITED = EDX (DIAGONAL)
7120		AS DEPOSITED = ELLIPSOMETRY + EDX (14X14)
7154		AS DEPOSITED = EDX (14X14)
7155		AS DEPOSITED = EDX (14X14)
7156		AS DEPOSITED = EDX (14X14)
7157		

Sample		characterisation done / Notes
7158		
7159		
7160		AS DEPOSITED = EDX (14X14)
7161		
7162		AS DEPOSITED = EDX (14X14)
7163		AS DEPOSITED = EDX (14X14)

Appendix B – Best Solar Cell efficiencies [21]

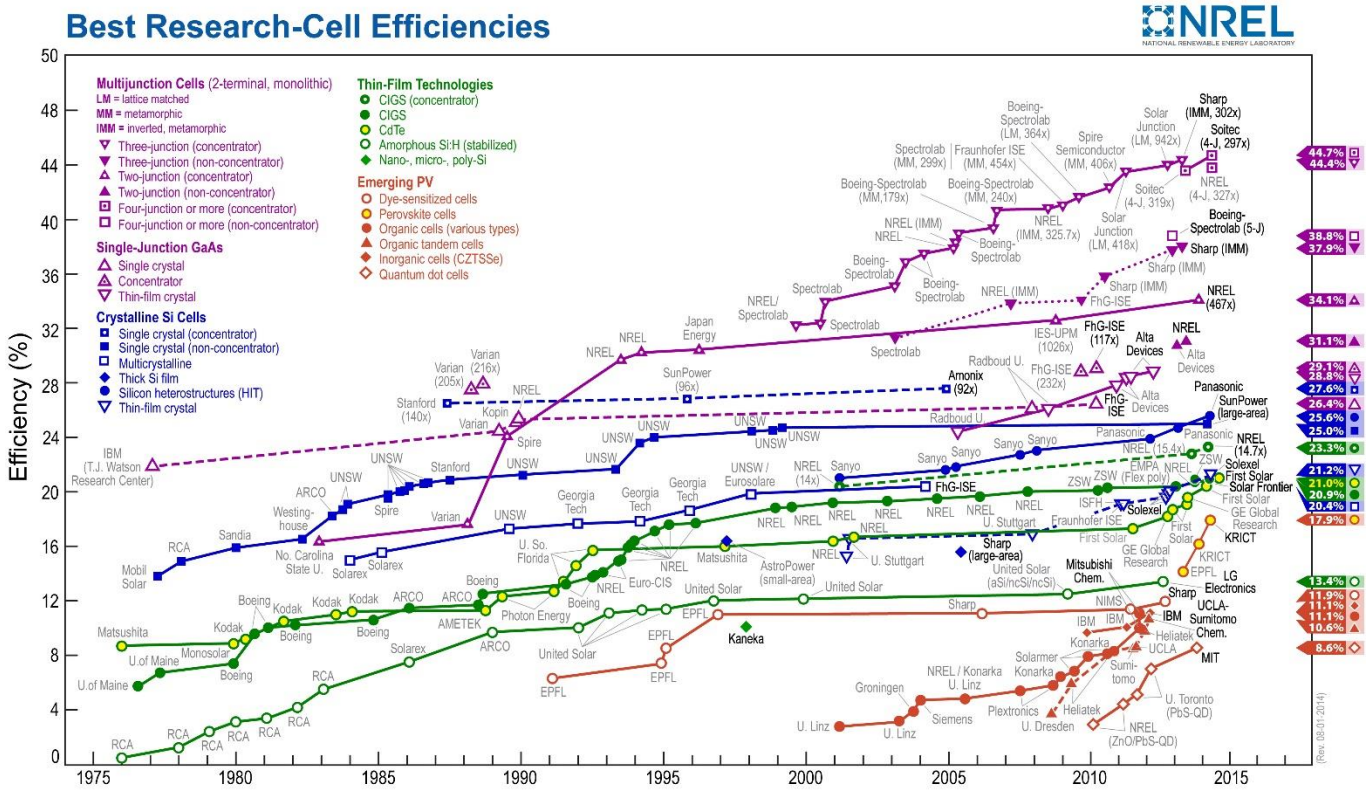

Appendix C – Conversions

1 bar = 750.061683 Torr

1 bar = 0.986923267 atm

1 bar = 100 000 Pascal

Appendix D – EDX transitions lines

Element	Kα	Lα	Mα
Carbon	0.277		
Oxygen	0.5249		
Sodium	1.0410		
Aluminium	1.4866		
Sulphur	2.3075		
Chlorine	2.6219		
Copper	8.0413	0.9297	
Zinc	8.6313	1.0118	
Gallium	9.8762	1.0979	
Selenium	11.2089	1.3791	
Molybdenum	17.4446	2.2932	
Cadmium	23.1740	3.1338	
Indium	24.2101	3.2870	
Tin	25.2718	3.4440	
Antimony	26.3595	3.6048	
Lanthanum	33.4418	4.6510	0.8332

Appendix E – Solar cell I-V curves and parameters

Here I list all the I-V curves and the associated fabrication details

	Chapter 4	Chapter 7	Chapter 8
Material	CZTS	CuSbSx	CuSbSx
Pages	74-75	130-131	153-155
Figures	Figure 46 Figure 47	Figure 91 Figure 92	**Error! Reference source not found.** **Error! Reference source not found.** **Error! Reference source not found.**
Cell structure	Figure 38 Figure 39	Figure 79	Figure 93
Fabrication details	Section 4.1.2	Section 7.1.4	Section 8.1.4
Efficiency	negligible	0.007 %	0.1 %
Current density	~ 1 $\mu A/cm^2$	~ 0.07 mA/cm^2	1-2 mA/cm^2
Open circuit voltage	< 0.1 x 10^{-3} V	0.09 V	0.05 V

References

[1] E. P. T. Platform, "A Strategic Research Agenda for Photovoltaic Solar Energy Technology," ed. Luxembourg, 2007.

[2] Y. Hamakawa, *Thin-Film Solar cells*: Springer, 2004.

[3] A. Kolodziej, "Staebler-Wronski effect in amorphous silicon and its alloys," *Opto-electronics review,* vol. 12, pp. 21-32, 2004.

[4] D. L. Staebler and C. R. Wronski, "Optically induced conductivity changes in discharge-produced hydrogenated amorphous silicon," *Journal of Applied Physics,* vol. 51, p. 3262, 1980.

[5] F. Al-Saab, C. C. Huang, B. Hayden, and D. Hewak, "RF sputtered single phase CuSbS thin films," presented at the E-MRS Spring Lille, France, 2014.

[6] F. Al-Saab, C. C. Huang, J. Yao, B. Hayden, and D. Hewak, "RTA annealed RF sputtered single phase CuSbS films," *Thin Solid films,* vol. Submitted, 2014.

[7] F. Al Saab, B. Gholipour, C. C. Huang, A. Anastasopoulos, B. Hayden, and D. W. Hewak, "Crystallization Study of the $CuSbS_2$ Chalcogenide Material for Solar Applications," presented at the PV-SAT 9, Swansea University, Swansea, Wales, 2013.

[8] F. Al Saab, B. Gholipour, C. C. Huang, A. Anastasopoulos, B. Hayden, and D. W. Hewak, "Crystallization Study of the Cu_2ZnSnS_4 Chalcogenide Material for Solar Applications," presented at the PV-SAT 8, Northumbria University, Newcastle upon Tyne, 2012.

[9] S. Guerin and B. Hayden, "Physical Vapor Deposition Method for the High-Throughput Synthesis of Solid-State Material Libraries," *J. Comb. Chem.,* vol. 8, pp. 66-73, 2006.

[10] R. M. Noble, "High Throughput Synthesis and Screening of Photovoltaic Materials," Doctor of Philosophy, School of Chemistry, University of Southampton, Southampton, 2011.

[11] R. Williams, "Becquerel Photovoltaic Effect in Binary Compounds," *The Journal of Chemical Physics,* vol. 32, pp. 1505-1514, 1960.

[12] E. Becquerel, "Mémoire sur les effets électriques produits sous l'influence des rayons solaires " *Comptes Rendus,* vol. 9, pp. 561–567, 1839.

[13] C. E. Fritts, "On a New Form of Selenium Photocell," *American Journal of Science,* vol. 26, 1883.

[14] R. Ohl, "Light-sensitive Electric Device Patent," US Patent, 1946.

[15] M. Riordan and L. Hoddeson, "The Origins of the pn Junction," *IEEE Spectrum,* pp. 46-51, 1997.

[16] E. Weston, "Apparatus for utilizing solar radiant energy," 1888.

[17] E. Weston, "Art of utilizing solar radiant energy," 1888.

[18] A. H. Lamb, "Photoelectric device," 1935.

[19] D. M. Chapin, C. S. Fuller, and G. L. Pearson, "A New Silicon p-n Junction Photocell for Converting Solar Radiation into Electrical Power," *Journal of Applied Physics,* vol. 25, pp. 676-677, 1954.

[20] J. Perlin, "The Silicon Solar cell turns 50," National Renewable Energy Laboratory 2004.

[21] *NREL Research Cell Efficiency Records*. Available: http://www.nrel.gov/ncpv/

[22] "Photovoltaics Report," Fraunhofer Institute for solar energy systems ISE, Freiburg 2013.

[23] B. G. Streetman and S. Banerjee, *Solid State Electronic Devices*: Prentice Hall, 2000.

[24] C. Honsberg and S. Bowden. *PV education : ideality factor*. Available: http://www.pveducation.org/pvcdrom/solar-cell-operation/ideality-factor
[25] N. Curson, *Solar Energy, Bandstructure and Photovoltaic Cells*. London: University College London, 2008-2009.
[26] E. V. Kerschaver and G. Beaucarne, "Back-Contact Solar Cells: a Review," *Progress in Photovoltaics: Research and Applications,* vol. 14, pp. 107-123, 2006.
[27] O. Nichiporuk, A. Kaminski, M. Lemiti, A. Fave, and V. Skryshevsky, "Optimisation of Interdigitated Back Contacts Solar Cells by Two-Dimensional Numerical Simulation," *Solar Energy Materials and Solar Cells,* vol. 86, pp. 517-526, 2005.
[28] R. Sinton and R. Swanson, "Simplified Backside-Contact Solar Cells," *IEEE Transactions on Electron Devices* vol. 37, pp. 348 - 352, 1990.
[29] J. Nelson, *The Physics of Solar cells*: Imperial College Press, 2010.
[30] T. Nakada, K. Furumi, and A. Kunioka, "High-Efficiency Cadmium-Free Cu(In,Ga)Se Thin-Film Solar Cells with Chemically Deposited ZnS Buffer Layers," *IEEE Transactions on Electron Devices,* vol. 46, 1999.
[31] T. Nakada and M. Mizutani, "18% Efficiency Cd-Free Cu(In, Ga)Se_2 Thin-Film Solar Cells Fabricated Using Chemical Bath Deposition (CBD)-ZnS Buffer Layers," *Japanese Journal of Applied Physics,* vol. 41, pp. L165-L167, 2002.
[32] T. Nakada, M. Mizutani, Y. Hagiwara, and A. Kunioka, "High-efficiency Cu(In,Ga)Se_2 thin-film solar cells with a CBD-ZnS buffer layer," *Solar Energy Materials & Solar Cells,* vol. 67, pp. 255-260, 2001.
[33] T. Kobayashi, K. Yamauchi, and T. Nakada, "Comparison of Cell Performance of ZnS(O,OH)/CIGS Solar Cells with MOCVD-ZnO:B and Sputter-Deposited ZnO:Al Window Layers " *IEEE Journal of Photovoltaics,* vol. 3, pp. 1079-1083, 2013.
[34] P. Blösch, S. Nishiwaki, T. Jaeger, L. Kranz, F. Pianezzi, A. Chirilă, *et al.*, "Alternative back contact designs for Cu(In,Ga)Se_2 solar cells on polyimide foils," *Thin Solid Films,* vol. 535, pp. 220-223, 2013.
[35] C. Gretener, J. Perrenoud, L. Kranz, C. Baechler, S. Yoon, Y. E. Romanyuk, *et al.*, "Development of MoO_x thin films as back contact buffer for CdTe solar cells in substrate configuration," *Thin Solid Films,* vol. 535, pp. 193-197, 2013.
[36] P. Blösch, S. Nishiwaki, A. Chirilă, L. Kranz, C. Fella, F. Pianezzi, *et al.*, "Sodium-doped molybdenum back contacts for flexible Cu(In,Ga)Se_2 solar cells," *Thin Solid Films,* vol. 535, pp. 214-219, 2013.
[37] V. Haug, A. Quintilla, I. Klugius, and E. Ahlswede, "Influence of an Additional Carbon Layer at the Back Contact–Absorber Interface in Cu(In,Ga)Se_2 Thin Film Solar Cells," *Thin Solid Films,* 2011.
[38] I. Knowledge. (2002, 30th March). *Fundamentals of Sputter Deposition*. Available: www.icknowledge.com/misc_technology/Sputter.pdf
[39] "Overveiw of Chemical Vapour Deposition," in *Chemical Vapour Deposition: Precursors, Processes and Applications*, A. C. Jones and M. L. Hitchman, Eds., ed: Royal Society of Chemistry, 2009, pp. 1-35.
[40] C.-C. Huang, "Development of Germanium Based Sulphide Glass By chemical Vapour Deposition (CVD)," Doctor of Philosophy, Optoelectronics Research Centre, University Of Southampton, 2005.
[41] P. Atkins, *The Laws of Thermodynamics: A Very Short Introduction*: Oxford University Press, 2010.

[42] R. B. Merrifield, "Solid Phase Peptide Synthesis. I. The Synthesis of a Tetrapeptide," *Journal of the American Chemical Society,* vol. 85, pp. 2149–2154, 1963.
[43] J. J. Hanak, "Multiple-sample-concept in materials research - synthesis, compositional analysis and testing of entire multicomponent systems," *Journal of Materials Science,* vol. 5, p. 964, 1970.
[44] X. D. Xiang, X. D. Sun, G. Briceno, Y. L. Lou, K. A. Wang, H. Y. Chang, *et al.*, "A combinatorial approach to materials discovery," *Science,* vol. 268, pp. 1738-1740, Jun 1995.
[45] I. Takeuchi, R. Bruve Van Dover, and H. Koinuma, "Combinatorial Synthesis and Evaluation of Functional Inorganic Materials Using Thin-Film Techniques," *MRS Bulletin,* pp. 301-308, 2002.
[46] H. Chang, I. Takeuchi, and X. D. Xiang, "A low-loss composition region identified from a thin-film composition spread of $(Ba_{(1-x-y)}Sr_xCa_y)TiO_3$," *Applied Physics Letters,* vol. 74, p. 1165, 1999.
[47] X. D. Xiang, "Combinatorial materials synthesis and high-throughput screening: An integrated materials chip approach to mapping phase diagrams and discovery and optimization of functional materials," *Biotechnology and Bioengineering,* vol. 61, pp. 227-241, 1998.
[48] K. Ploog, "Molecular Beam Epitaxy presentation," 27th International Conference on the Physics of Semiconductors, Tutorial Session #1—Epitaxial Growth ed. Flagstaff, 2004.
[49] B. Gholipour, "Novel Chalcogenide Optoelectronic and Nanophotonic Information Storage and Processing Devices," Doctor of Philosophy, Optoelectronics Research Centre, University Of Southampton, Southampton, 2011.
[50] C. J. Pugh, "End Point Detection in Reactive Ion Etching," Doctorate of Engineering, Electrical and Electronic Engineering University College London, 2013.
[51] *Oxford instruments Plasmalab 80 plus*. Available: http://www.oxfordplasma.de/systems/80plus.htm
[52] *Jipelec*. Available: http://www.jipelec.com/
[53] *Sun 3000 Class AAA Solar Simulator*. Available: http://www.abet-technologies.com/solar-simulators/sun-3000-class-aaa
[54] *Bruker Corporation*. Available: http://www.bruker.com/
[55] T. E. Everhart and R. F. M. Thornley, "Wide-band detector for micro-microampere low-energy electron currents," *Journal of Scientific Instruments,* vol. 37, pp. 246-248, 1960.
[56] I. M. Watt, *The Principles and Practice of Electron Microscopy*: Cambridge University Press, 1997.
[57] P. J. Goodhew, *Electron microscopy and analysis*: Taylor & Francis, 2001.
[58] *X-ray properties of the Elements*. Available: http://xdb.lbl.gov/Section1/Periodic_Table/X-ray_Elements.html
[59] W. L. Bragg, "The Diffraction of Short Electromagnetic Waves by a Crystal," *Proceedings of the Cambridge Philosophical Society,* vol. 17, pp. 43-57, 1913.
[60] H. Fujiwara, *Spectroscopic Ellipsometry: Principles and Applications*: Wiley-Blackwell, 2007.
[61] *Light & Materials - Part I tutorial*. Available: http://www.jawoollam.com/tutorial_2.html
[62] J. Parkes, R. D. Tomlinson, and M. J. Hampshire, "Electrical properties of $CuInSe_2$ single crystals," *Solid-state electronics,* vol. 16, pp. 773-777, 1973.

[63] T. Reuters. (2012, June 14th). *Web of Knowledge*. Available: http://apps.webofknowledge.com

[64] P. Jackson, D. Hariskos, R. Wuerz, W. Wischmann, and M. Powalla, "Compositional investigation of potassium doped Cu(In,Ga)Se_2 solar cells with efficiencies up to 20.8%," *Physica Status Solidi-Rapid Research Letters,* vol. 8, pp. 219-222, Mar 2014.

[65] J. H. Shi, Z. Q. Li, D. W. Zhang, Q. Q. Liu, Z. Sun, and S. M. Huang, "Fabrication of Cu(In, Ga)Se_2 thin films by sputtering from a single quaternary chalcogenide target," *Progress in Photovoltaics: Research and Applications,* vol. 19, pp. 160-164, 2011.

[66] T. Yagioka and T. Nakada, "Cd-Free Flexible Cu(In,Ga)Se_2 Thin Film Solar Cells with ZnS(O,OH) Buffer Layers on Ti Foils," *Applied Physics Express,* vol. 2, p. 072201, 2009.

[67] J. Poortmans and V. Arkhipov, Eds., *Thin Film Solar Cells: Fabrication, Characterization and Applications* (Wiley series in materials for electronic and optoelectronic applications. John Wiley and Sons Ltd, 2006, p.^pp. Pages.

[68] T. Nakada, H. Ohbo, T. Watanabe, H. Nakazawa, M. Matsui, and A. Kunioka, "Improved Cu(In,Ga)$(S,Se)_{(2)}$ thin film solar cells by surface sulfurization," *Solar Energy Materials and Solar Cells,* vol. 49, pp. 285-290, Dec 1997.

[69] D. Ohashi, T. Nakada, and A. Kunioka, "Improved CIGS thin-film solar cells by surface sulfurization using In_2S_3 and sulfur vapor," *Solar Energy Materials and Solar Cells,* vol. 67, pp. 261-265, Mar 2001.

[70] F. Karg, V. Probst, H. Harms, J. Rimmasch, W. Riedl, J. Kotschy*, et al.*, "Novel Rapid-thermal-processing for CIS thin film solar cells " *IEEE,* 1993.

[71] U. P. Singh, W. N. Shafarman, and R. W. Birkmire, "Surface sulfurization studies of Cu(InGa)Se_2 thin film," *Solar Energy Materials and Solar Cells,* vol. 90, pp. 623-630, Mar 2006.

[72] C. J. Hibberd, E. Chassaing, W. Liu, D. B. Mitzi, D. Lincot, and A. N. Tiwari, "Non-vacuum methods for formation of Cu(In,Ga)$(Se,S)_{(2)}$ thin film photovoltaic absorbers," *Progress in Photovoltaics: Research and Applications,* vol. 18, pp. 434-452, 2010.

[73] E. R. Baek, V. Astini, A. Tirta, and B. Kim, "Phase evolution of CIGS Alloyed Compound Synthesis by Direct Melting Method," *Current Applied Physics,* vol. 11, pp. S76-S80, 2010.

[74] S. Niki, M. Contreras, I. Repins, M. Powalla, K. Kushiya, S. Ishizuka*, et al.*, "CIGS absorbers and processes," *Progress in Photovoltaics: Research and Applications,* vol. 18, pp. 453-466, Sep 2010.

[75] D. Rudmann, A. F. da Cunha, M. Kaelin, F. Kurdesau, H. Zogg, A. N. Tiwari*, et al.*, "Efficiency enhancement of Cu(In,Ga)Se_2 solar cells due to post-deposition Na incorporation," *Applied Physics Letters,* vol. 84, pp. 1129-1131, 2004.

[76] P. Blosch, S. Nishiwaki, L. Kranz, C. M. Fella, F. Pianezzi, T. Jager*, et al.*, "Sodium-doped molybdenum back contact designs for Cu(In,Ga)Se_2 solar cells," *Solar Energy Materials and Solar Cells,* vol. 124, pp. 10-30, May 2014.

[77] D. J. L. Bremaud, "Investigation and Development of CIGS Solar Cells on Flexible Substrates and with Alternative Electrical Back Contacts," PhD, Physics, ETH, Zurich, 2009.

[78] L. Assmann, J. C. Bernede, A. Drici, C. Amory, E. Halgand, and M. Morsli, "Study of the Mo thin films and Mo/CIGS Interface Properties," *Applied Surface Science,* vol. 246, pp. 159-166, 15 June 2005.

[79] H. A. Al-Thani, F. S. Hasoon, J. L. Alleman, M. M. Al-Jassim, and D. L. Williamson, "The Deposition and Characterization of Mo/CuInGaSe$_2$/CdS/ZnO Solar Cells," presented at the Sharjah Solar Energy Conference, Sharjah, UAE, 2001.

[80] H. Wang, "Progress in Thin Film Solar Cells Based on Cu_2ZnSnS_4," *International Journal of Photoenergy,* vol. 2011, pp. 1-10, 2011.

[81] H. Katagiri, M. Nishimura, T. Onozawa, S. Maruyama, M. Fujita, T. Sega*, et al.*, "Rare-metal free thin film solar cell," presented at the Power Conversion Conference, Nagaoka, 1997.

[82] H. Katagiri, "Cu_2ZnSnS_4 thin film solar cells," *Thin Solid Films,* vol. 480-481, pp. 426-432, 2005.

[83] R. B. V. Chalapathy, G. S. Jung, and B. T. Ahn, "Fabrication of Cu_2ZnSnS_4 films by sulfurization of Cu/ZnSn/Cu precursor layers in sulfur atmosphere for solar cells," *Solar Energy Materials and Solar Cells,* vol. 95, pp. 3216-3221, 2011.

[84] M. G. Sousa, A. F. da Cunha, P. A. Fernandes, J. P. Teixeira, R. A. Sousa, and J. P. Leitao, "Effect of rapid thermal processing conditions on the properties of Cu_2ZnSnS_4 thin films and solar cell performance," *Solar Energy Materials and Solar Cells,* vol. 126, pp. 101-106, July 2014.

[85] J. J. Scragg, P. J. Dale, L. M. Peter, G. Zoppi, and I. Forbes, "New routes to sustainable photovoltaics: evaluation of Cu_2ZnSnS_4 as an alternative absorber material," *Physica Status Solidi B-Basic Solid State Physics,* vol. 245, pp. 1772-1778, Sep 2008.

[86] J. J. Scragg, "Studies of Cu_2ZnSnS_4 Films prepared by sulfurisation of electrodeposited Precursors," PhD, Department of Chemistry, University Of Bath, Bath, 2010.

[87] J. J. Scragg, T. Ericson, X. Fontané, V. Izquierdo-Roca, A. Pérez-Rodríguez, T. Kubart*, et al.*, "Rapid annealing of reactively sputtered precursors for Cu_2ZnSnS solar cells," *Progress in Photovoltaics: Research and Applications,* vol. 22, pp. 10-17, 2014.

[88] F. Liu, Y. Li, K. Zhang, B. Wang, C. Yan, Y. Lai*, et al.*, "In situ growth of Cu_2ZnSnS_4 thin films by reactive magnetron co-sputtering," *Solar Energy Materials and Solar Cells,* vol. 94, pp. 2431-2434, 2010.

[89] K. Ramasamy, M. A. Malik, and P. O'Brien, "The chemical vapor deposition of Cu_2ZnSnS_4 thin films," *Chemical Science,* vol. 2, p. 1170, 2011.

[90] T. K. Todorov, K. B. Reuter, and D. B. Mitzi, "High-Efficiency Solar Cell with Earth-Abundant Liquid-Processed Absorber," *Advanced Materials,* vol. 22, pp. E156-E159, 2010.

[91] T. Todorov, O. Gunawan, S. J. Chey, T. G. de Monsabert, A. Prabhakar, and D. B. Mitzi, "Progress towards marketable earth-abundant chalcogenide solar cells," *Thin Solid Films,* vol. 519, pp. 7378-7381, 2011.

[92] W. Wei, M. T. Winkler, O. Gunawan, T. Gokmen, T. K. Todorov, Z. Yu*, et al.*, "Device Characteristics of CZTSSe Thin-Film Solar Cells with 12.6% Efficiency," *Advanced Energy Materials,* vol. 4, pp. 1301465 (5 pp.)-1301465 (5 pp.), 13 2014.

[93] A. Nagoya and R. Asahi, "Defect formation and phase stability of Cu_2ZnSnS_4 photovoltaic material," *Physical Review B,* vol. 81, 2010.

[94] J. J. Scragg, T. Ericson, T. Kubart, M. Edoff, and C. Platzer-Björkman, "Chemical Insights into the Instability of Cu_2ZnSnS_4 Films during Annealing," *Chemistry of Materials,* vol. 23, pp. 4625-4633, 2011.

[95] A. Redinger, D. M. Berg, P. J. Dale, and S. Siebentritt, "The Consequences of Kesterite Equilibria for Efficient Solar Cells," *Journal of the American Chemical Society,* pp. 3320–3323, 2011.

[96] A. Nagoya, R. Asahi, and G. Kresse, "First-principles study of Cu_2ZnSnS_4 and the related band offsets for photovoltaic applications," *Journal of Physics: Condensed Matter,* vol. 23, p. 404203, 2011.

[97] R. Haight, A. Barkhouse, O. Gunawan, B. Shin, M. Copel, M. Hopstaken, *et al.*, "Band alignment at the $Cu_2ZnSn(S_xSe_{(1-x)})_4$/CdS interface," *Applied Physics Letters,* vol. 98, p. 253502, 2011.

[98] A. M. Loireaulozach, M. Guittard, and J. Flahaut, "Glass Formed By Rare-earth Sulfides (L_2S_3) with Gallium Sulfide (Ga_2S_3)," *Materials Research Bulletin,* vol. 11, pp. 1489-1496, 1976.

[99] Ruihua Li and A. B. Seddon, "Gallium lanthanum sulphide glasses: a review of recent crystallisation studies," *Journal of Non-Crystalline Solids,* vol. 256 & 257, pp. 17-24, 1999.

[100] Z. L. Sámson, S.-C. Yen, K. F. MacDonald, K. Knight, S. Li, D. W. Hewak, *et al.*, "Chalcogenide glasses in active plasmonics," *physica status solidi (RRL) - Rapid Research Letters,* vol. 4, pp. 274-276, 2010.

[101] Z. L. Sámson, K. F. MacDonald, F. De Angelis, B. Gholipour, K. Knight, C. C. Huang, *et al.*, "Metamaterial electro-optic switch of nanoscale thickness," *Applied Physics Letters,* vol. 96, p. 143105, 2010.

[102] R. Asal, P. E. Rivers, and H. N. Rutt, "A structural study of gallium lanthanum sulphide glass bulk and thin films by x-ray absorption fine structure spectroscopy," *J. Phys.: Condens. Matter,* vol. 9, pp. 6217–6230, 1997.

[103] S. P. Morgan, I. M. Reaney, R. Buckley, D. Furniss, and A. B. Seddon, "Crystallization of Gallium Lanthanum Sulfide Glasses," *J. Am. Ceram. Soc.,* vol. 81, pp. 1913–18, 1998.

[104] R. Asaly, P. E. Rivers, and H. N. Rutt, "A structural study of gallium lanthanum sulphide glass bulk and thin films by x-ray absorption fine structure spectroscopy," *J. Phys.: Condens. Matter,* vol. 9, pp. 6217–6230, 1997.

[105] S. Benazeth, M. H. Tuilier, A. M. Loireaulozach, H. Dexpert, P. Lagarde, and J. Flahaut, "An EXAFS Structural Approach of the Lanthanum Gallium Sulfur Glasses," *Journal of Non-Crystalline Solids,* vol. 110, pp. 89-100, Jul 1989.

[106] H. Takebe, T. Murakami, M. Kuwabara, and D. Hewak, "Preparation and properties of La_2O_3–Ga_2S_3 glass-ceramics for IR materials," *Journal of Non-Crystalline Solids,* vol. 352, pp. 2425-2429, 2006.

[107] M. Petrovich, A. Favre, D. W. Hewak, H. N. Rutt, A. C. Grippo, and M. D. Shinn, "Near-IR absorption of Ga:La:S and Ga:La:S:O glasses by free-electron laser-based laser calorimetry," *Journal of Non-Crystalline Solids,* vol. 326-327, pp. 93-97, 2003.

[108] H. Takebe , D. J. Brady, D. W. Hewak, and K. Morinaga, "Thermal properties of Ga_2S_3-based glass and their consideration during fiber drawing," *Journal of Non-Crystalline Solids,* vol. 258, p. 239±243, 1999.

[109] H. Yayama, S. Fujino, K. Morinaga, H. Takebe, D. W. Hewak, and D. N. Payne, "Refractive index dispersion of gallium lanthanum sulfide and oxysulfide glasses," *Journal of Non-Crystalline Solids,* vol. 239, pp. 187-191, 1998.

[110] S. Barnier, M. Guittard, M. Palazzi, M. Massot, and C. Julien, "Raman and infrared studies of the structure of gallium sulphide based glasses," *Materials Science and Engineering,* vol. B14, pp. 413-417, 1992.

[111] R. E. Simpson, A. Mairaj, R. J. Curry, C. C. Huang, K. Knight, N. Sessions, *et al.*, "Electrical phase change of Ga:La:S:Cu films," *Electronics Letters,* vol. 43, p. 830, 2007.

[112] J. T. Dufton, A. Walsh, P. M. Panchmatia, L. M. Peter, D. Colombara, and M. S. Islam, "Structural and electronic properties of $CuSbS_2$ and $CuBiS_2$: potential absorber materials for thin-film solar cells," *Phys Chem Chem Phys,* vol. 14, pp. 7229-33, May 28 2012.

[113] M. Versavel and J. Haber, "Structural and optical properties of amorphous and crystalline antimony sulfide thin-films," *Thin Solid Films,* vol. 515, pp. 7171-7176, 2007.

[114] A. Kyono and M. Kimata, "Crystal structures of chalcostibite ($CuSbS_2$) and emplectite ($CuBiS_2$): Structural relationship of stereochemical activity between chalcostibite and emplectite," *American Mineralogist,* vol. 90, pp. 162-165, 2005.

[115] M. Kumar and C. Persson, "$CuSbS_2$ and $CuBiS_2$ as potential absorber materials for thin-film solar cells," *Journal of Renewable and Sustainable Energy,* vol. 5, p. 031616, 2013.

[116] C. Yan, Z. Su, E. Gu, T. Cao, J. Yang, J. Liu*, et al.*, "Solution-based synthesis of chalcostibite ($CuSbS_2$) nanobricks for solar energy conversion," *RSC Advances,* vol. 2, p. 10481, 2012.

[117] I. Popovici and A. Duta, "Tailoring the Composition and Properties of Sprayed $CuSbS_2$ Thin Films by Using Polymeric Additives," *International Journal of Photoenergy,* vol. 2012, pp. 1-6, 2012.

[118] H. Su, Xie, Yi., S. Wan, B. Li, and Y. Qian, "A novel one-stop solvothermal route to nanocrystalline $CuSbS_2$ and Ag_3SbS_3," *solid state ionics,* vol. 123, pp. 319-324, 1999.

[119] L. Soliman, A. Abo el Soad, H. Zayed, and S. El Ghfar, "Structural and electrical properties of $CuSbTe_2$, $CuSbSe_2$ and $CuSbS_2$ chalcogenide thin films," *Fizika A,* vol. 11, pp. 139-152, 2002.

[120] M. F. Razmara, C. Henderson, R. Pattrick, A. Bell, and J. Charnock, "The crystal chemistry of the solid solution series between chalcostibite ($CuSbS_2$) and emplectite ($CuBiS_2$)," *Mineralogical magazine,* vol. 61, pp. 79-88, 1997.

[121] B. V. Korzun, A. N. Gavrilenko, A. A. Fadzeyeva, O. V. Ignatenko, I. I. Maroz, V. R. Sobol*, et al.*, "T(x) phase diagram of the $CuSbS_2$-$CuInS_2$ system and solubility limit of Sb in $CuInS_2$," *Crystal Research and Technology,* pp. n/a-n/a, 2013.

[122] K. Ramasamy, H. Sims, W. H. Butler, and A. Gupta, "Selective Nanocrystal Synthesis and Calculated Electronic Structure of All Four Phases of Copper-Antimony-Sulfide," *Chemistry of Materials,* vol. 26, pp. 2891-2899, May 2014.

[123] Z. A. Zhang, C. K. Zhou, Y. K. Liu, J. Li, Y. Q. Lai, and M. Jia, "$CuSbS_2$ Nanobricks as Electrode Materials for Lithium Ion Batteries," *International Journal of Electrochemical Science,* vol. 8, pp. 10059-10067, Jul 2013.

[124] J. van Embden and Y. Tachibana, "Synthesis and characterisation of famatinite copper antimony sulfide nanocrystals," *Journal of Materials Chemistry,* vol. 22, p. 11466, 2012.

[125] S. C. Ezugwu, F. I. Ezema, and P. U. Asogwa, "Sythesis and characterisation of ternary $CuSbS_2$ thin films: effect of deposition time," *Chalcogenide Letters,* vol. 7, pp. 341-348, 2010.

[126] B. Deng, G. H. Chan, D. E. Ellis, R. P. Van Duyne, and J. A. Ibers, "Synthesis, structure, and electronic structure of K_2CuSbS_3," *Journal of Solid State Chemistry,* vol. 178, pp. 3169-3175, Oct 2005.

[127] R. A. Alieva, S. T. Bairamova, V. M. Ragimova, O. M. Aliev, and M. R. Bagieva, "Phase diagrams of the $CuSbS_2$-MS (M = Pb, Eu, Yb) systems," *Inorganic Materials,* vol. 46, pp. 703-706, 2010.

[128] A. Rabhi and M. Kanzari, "Structural, Optical and electrical properties of $CuSbS_2$ these amorphous films: effect of the thickness variation " *Chalcogenide Letters,* vol. 8, pp. 383-390, 2011.
[129] A. Rabhi, M. Kanzari, and B. Rezig, "Optical and structural properties of $CuSbS_2$ thin films grown by thermal evaporation method," *Thin Solid Films,* vol. 517, pp. 2477-2480, 2009.
[130] A. Rabhi, M. Kanzari, and B. Rezig, "Growth and vacuum post-annealing effect on the properties of the new absorber $CuSbS_2$ thin films," *Materials Letters,* vol. 62, pp. 3576-3578, 2008.
[131] A. Rabhi and M. Kanzari, "Effect of Air Annealing on $CuSbS_2$ thin films grown by vacuum thermal evaporation," *Chalcogenide Letters,* vol. 8, pp. 255-262, 2011.
[132] D. Colombara, L. M. Peter, K. D. Rogers, J. D. Painter, and S. Roncallo, "Formation of $CuSbS_2$ and $CuSbSe_2$ thin films via chalcogenisation of Sb–Cu metal precursors," *Thin Solid Films,* vol. 519, pp. 7438-7443, 2011.
[133] D. Colombara, "Investigation of Chalcogenide Absorber Materials for Photovoltaic Applications," PhD, Department of Chemistry, University Of Bath, 2012.
[134] C. Garza, S. Shaji, A. Arato, E. Perez Tijerina, G. Alan Castillo, T. K. Das Roy*, et al.*, "p-Type $CuSbS_2$ thin films by thermal diffusion of copper into Sb_2S_3," *Solar Energy Materials and Solar Cells,* vol. 95, pp. 2001-2005, 2011.
[135] Y. Rodríguez-Lazcano, M. T. S. Nair, and P. K. Nair, "$CuSbS_2$ thin film formed through annealing chemically deposited Sb_2S_3-CuS thin films," *Journal of Crystal Growth,* vol. 223, pp. 399-406, 2001.
[136] Y. Rodríguez-Lazcano, M. T. S. Nair, and P. K. Nair, "Photovoltaic p-i-n Structure of Sb_2S_3 and $CuSbS_2$ Absorber Films Obtained via Chemical Bath Deposition," *Journal of The Electrochemical Society,* vol. 152, p. G635, 2005.
[137] D. Perniu, A. Duta, and J. Schoonman, "Defect chemistry of $CuSbS_2$," *IEEE,* 2006.
[138] B. Yang, L. Wang, J. Han, Y. Zhou, H. B. Song, S. Y. Chen*, et al.*, "$CuSbS_2$ as a Promising Earth-Abundant Photovoltaic Absorber Material: A Combined Theoretical and Experimental Study," *Chemistry of Materials,* vol. 26, pp. 3135-3143, May 2014.
[139] S. Manolache, M. Nanu, A. Duta, A. Goossens, and J. Schoonman, "Improvements in the quality of $CuSbS_2$ films used in solid state solar cells," *IEEE,* 2005.
[140] S. Manolache, A. Duta, L. Isac, M. Nanu, A. Goossens, and J. Schoonman, "The influence of the precursor concentration on $CuSbS_2$ thin films deposited from aqueous solutions," *Thin Solid Films,* vol. 515, pp. 5957-5960, 2007.
[141] S. Manolache, L. Andronic, A. Duta, and A. Enesca, "The influence of the deposition condition on crystalgrowth and on the band gap of $CuSbS_2$ thin film absorber used for Solid State Solar Cells (SSSC)," *Journal of optoelectronics and advanced materials* vol. 9, pp. 1269-1272, 2007.
[142] V. Kumar Gudelli, V. Kanchana, G. Vaitheeswaran, A. Svane, and N. E. Christensen, "Thermoelectric properties of chalcopyrite type $CuGaTe_2$ and chalcostibite $CuSbS_2$," *Journal of Applied Physics,* vol. 114, p. 223707, 2013.
[143] K. Ramasamy, B. Tien, P. S. Archana, and A. Gupta, "Copper antimony sulfide ($CuSbS_2$) mesocrystals: A potential counter electrode material for

dye-sensitized solar cells," *Materials Letters,* vol. 124, pp. 227-230, Jun 2014.
[144] K. Ramasamy, H. Sims, W. H. Butler, and A. Gupta, "Mono-, few-, and multiple layers of copper antimony sulfide ($CuSbS_2$): a ternary layered sulfide," *Journal of the American Chemical Society,* vol. 136, pp. 1587-98, Jan 29 2014.
[145] *Zeiss United Kingdom*. Available: http://www.zeiss.co.uk/
[146] K. Wang, O. Gunawan, T. Todorov, B. Shin, S. J. Chey, N. A. Bojarczuk, *et al.*, "Thermally evaporated $CuZnSnS_4$ solar cells," *Applied Physics Letters,* vol. 97, p. 143508, 2010.
[147] *SketchUp*. Available: http://www.sketchup.com/
[148] *Joel USA*. Available: http://www.jeolusa.com/
[149] *J.A. Woollam Co.* Available: http://www.jawoollam.com/
[150] *HORIBA Scientific*. Available: http://www.horiba.com/scientific/
[151] T. Schweizer, F. Goutaland, E. Matrins, D. Hewak, and W. S. Brocklesby, "Site-selective spectroscopy in dysprosium-doped chalcogenide glasses for 1.3-m optical-fiber amplifiers," *Journal of the Optical Society of America B* vol. 18, 2001.
[152] P. Němec, V. Nazabal, M. Pavlišta, A. Moreac, M. Frumar, and M. Vlček, "Gallium–lanthanum–sulphide amorphous thin films prepared by pulsed laser deposition," *Materials Chemistry and Physics,* vol. 117, pp. 23-25, 2009.
[153] *Ilika Technologies*. Available: http://www.ilika.com/
[154] D. Hewak, D. Brady, R. J. Curry, G. Elliot, C. C. Huang, M. Hughes, *et al.*, "Chalcogenide glasses for photonics device applications," in *Photonic glasses and glass-ceramics*, G. S. Murugan, Ed., ed: Research Signpost, 2010, pp. 29-102.
[155] C. C. Huang, K. Knight, and D. Hewak, "Deposition and Characterisation of Copper Indium Gallium Sulphide Thin Films Fabricated by Chemical Vapour deposition with Metal Chloride Precursors," presented at the PVSAT-6 proceedings, Southampton, United Kingdom, 2010.
[156] D. Hewak, K. Knight, and C. C. Huang, "Towards deposition of copper indium gallium sulphide/selenide materials by chemical vapour deposition," presented at the IoP: Thin Film Photovoltaics, London, 2009.
[157] C. C. Huang, B. Gholipour, J. Y. Ou, K. Knight, and D. W. Hewak, "Electrical phase change of CVD-grown Ge-Sb-Te thin-film device," *Electronics Letters,* vol. 47, p. 288, 2011.
[158] C. C. Huang, K. Knight, and D. W. Hewak, "Antimony germanium sulphide amorphous thin films fabricated by chemical vapour deposition," *Optical Materials,* vol. 29, pp. 1344-1347, Jul 2007.
[159] C. C. Huang, C. Y. Tai, C. J. Liu, R. E. Simpson, K. Knight, and D. W. Hewak, "Germanium antimony sulphide nano wires fabricated by chemical vapour deposition and e-beam lithography," *Nsti Nanotech 2008, Vol 3, Technical Proceedings,* 2008.
[160] C. C. Huang, C. C. Wu, K. Knight, and D. W. Hewak, "Optical Properties of CVD Grown Amorphous Ge-Sb-S Thin Films," *Journal of Non-Crystalline Solids,* vol. 356, pp. 281-285, 15 February 2010.
[161] I. Barin, *Thermochemical Data of Pure Substances*, Third ed.: CVH, 1995.
[162] C. W. Bale. (2005). *Reaction - Web*. Available: http://www.crct.polymtl.ca/reacweb.htm
[163] D. Stull, "Vapour pressure of Pure substances," *Industrial and engineering chemistry,* vol. 39, pp. 517-550, 1947.

[164] M. Mousel, A. Redinger, R. Djemour, M. Arasimowicz, N. Valle, P. Dale, *et al.*, "HCl and Br_2-MeOH etching of $Cu_2ZnSnSe_4$ polycrystalline absorbers," *Thin Solid Films,* vol. 535, pp. 83-87, 2013.